UNIVERSITÀ DEGLI STUDI DI PADOVA
Sede amministrativa: UNIVERSITÀ DEGLI STUDI DI PADOVA
DIPARTIMENTO DI ASTRONOMIA

Dottorato di ricerca in Astronomia
Ciclo XVI

Supernovae as probes of the cosmological Star Formation Rate and distance scale

Coordinatore: Ch.mo Prof. Giampaolo Piotto
Supervisori: Ch.mo Prof. Roberto Barbon
Dott. Enrico Cappellaro
Dott. Massimo Turatto

Dottorando: Giuseppe Altavilla

31 dicembre 2003

Contents

List of Tables

List of Figures

Sommario

Ed io qui solingo,
che mi aggiro tra le stanze vuote
di questo santuario tecnologico
dove un ciclopico occhio vitreo,
degno di un Polifemo alluminato,
scruta i misteri reconditi del cosmo infinito
per restare accecato talvolta dall'abbagliante lampo
di una stella morente che esala
in un ultimo fulgido urlo azzurro di luce
quella che fu la sua gloria lucente
e le tenebre squarciate si richiudono poi,
lugubre sudario, sulle sue misere spoglie atomiche,
fertile concime...
G.A., *Pensieri diVersi*

Lo studio delle Supernovae (SNe) presenta innumerevoli risvolti in diversi ambiti dell'Astronomia, dall'Astrofisica alla Cosmologia. Le SNe rappresentano, in generale, un "laboratorio" privilegiato dove la materia è soggetta a condizioni estreme e non riproducibili sulla Terra. Le SNe possono fornire informazioni sull'evoluzione stellare, sui processi di perdita di massa e di accrescimento, sulla fisica delle esplosioni stellari. A loro volta le esplosioni di SNe sono strettamente legate alla cinematica ed all'arricchimento chimico del mezzo interstellare. Le SNe possono inoltre far luce sullo studio delle pulsar, dei raggi cosmici, dei neutrini, delle onde gravitazionali e dei *γ-ray bursts*. D'altro canto, grazie alla loro elevata luminosità, le SNe rappresentano anche un importante strumento per sondare l'Universo a distanze cosmologiche, fornendo informazioni sulle sue proprietà.
In questa Tesi non discuteremo la fisica delle Supernovae ma focalizzeremo la nostra attenzione proprio sulla loro utilità come "sonde" per investigare l'Universo. In particolare discuteremo l'uso delle SNe di tipo Ia come indicatori di distanza, con le loro implicazioni cosmologiche, e il loro utilizzo, insieme alle Supernovae di tipo II ed Ib/c (*Core collpase*

SNe, CCSNe), come indicatori del tasso di formazione stellare.
Lo studio dell'evoluzione dell'Universo è uno degli scopi fondamentali della cosmologia, ed uno degli esperimenti concettualmente più semplici che si possono effettuare per indagarne le proprietà è studiare come la luminosità apparente di una candela standard varia con il *redshift*. Le SNe di tipo Ia, dopo una appropriata calibrazione, sono sono particolarmente adatte a questo scopo e possono fornire indicazioni sulle proprietà globali dell'Universo, come la costante di Hubble H_0 (Rust 1974; Hamuy et al. 1996b; Tripp and Branch 1999; Freedman et al. 2001), ed i parametri cosmologici q_0, Ω_m, Ω_Λ (Schmidt et al. 1998; Perlmutter et al. 1999; Riess et al. 1998). In particolare le SNe vicine possono dare indicazioni sull'attuale tasso di espansione dell'Universo mentre SNe più lontane permettono di evidenziare gli effetti dovuti alla sua curvatura e danno informazioni sull'evoluzione del tasso di espansione con il tempo.
La presente Tesi è strutturata in due parti: nella prima analizzeremo un campione di SNe vicine mentre nella seconda studieremo un campione di SNe a *redshift* intermedio. In particolare discuteremo i seguenti argomenti:

- Le proprietà spettrofotometriche relativamente omogenee e l'elevata luminosità ha subito suggerito l'uso delle SNe di tipo Ia come indicatori di distanza. Tuttavia, come discusso nel Capitolo 2, studi successivi hanno evidenziato una grande varietà di oggetti, caratterizzati da luminosità al massimo significativamente diverse. Allo stesso tempo si è evidenziata l'esistenza di una correlazione tra la magnitudine al massimo e la forma della curva di luce, tramite la quale è possibile calibrare le SNe Ia. Per questo, anche se non perfettamente omogenee, le SNe di tipo Ia, dopo una appropriata calibrazione, rappresentano forse il più accurato indicatore di distanze, anche su scale cosmologiche. Nel Capitolo 2 utilizzeremo dati raccolti dalla letteratura e nostri nuovi dati, non ancora pubblicati, per stimare i parametri della relazione che lega la magnitudine al massimo e la forma della curva di luce. Esamineremo inoltre come differenti calibrazioni delle stelle variabili Cefeidi, ottenute tenendo conto degli effetti dovuti a diverse metallicità, si ripercuotono sulla calibrazione delle SNe Ia e di conseguenza sulla stima della costante di Hubble. Discuteremo inoltre il problema dell'assorbimento cui sono soggette le SNe, che risulta giocare un ruolo cruciale nella calibrazione della loro magnitudine assoluta.

- Fino ad oggi le stime del tasso di esplosione delle SNe ad alto redshift si sono basate sui dati ricavati da osservazioni di SNe di tipo Ia, finalizzate a ricerche di tipo cosmologico, e non sono mai state fornite stime sul tasso di esplosione relativo alle CCSNe al di fuori dell'Universo locale. Partendo da questa considerazione nel 1999 è stata intrapresa una ricerca di SNe il cui scopo principale era quello di fornire una stima del tasso di esplosione delle CCSNe, oltre che delle SNe di tipo Ia, a *redshift* intermedio ($z \sim 0.3$). Nel Capitolo 3 presenteremo la nostra **S**outhern In**T**ermediate **R**edshift **E**SO **S**upernova **S**earch (**STRESS**), descrivendo la strumentazione utilizzata, la strategia di osservazione, l'analisi dei dati ed il *software* sviluppato appositamente per i nostri scopi. Presenteremo infine le Supernovae confermate spettroscopicamente e i sottoprodotti della nostra ricerca.

  Nel Capitolo 4 calibreremo le SNe scoperte nel corso della nostra ricerca a *redshift* intermedio tramite i risultati ottenuti nel Capitolo 2. Il campione di SNe così ottenuto è stato utilizzato per stimare i parametri comologici Ω_M, Ω_Λ. Per una stima migliore di tali parametri abbiamo combinato le nostre SNe a *redshift* intermedio con i dati presenti in letteratura, ottenendo un campione significativamente più esteso, sia per quanto riguarda il numero di oggetti considerati, sia per quanto riguarda la loro estensione in *redshift*. In entrambi i casi le Supernovae ad alto *redshift* sembrano essere meno luminose di quanto ci si aspettava, come se l'Universo fosse soggetto ad una espansione accelerata e non costante. Questo effetto, già evidenziato alla fine degli anni '90, può essere spiegato, nel contesto cosmologico standard dato dal modello Friedmann-Robertson-Walker, attribuendo al vuoto dell'energia (*"dark energy"* o costante comologica). Interpretazioni alternative sono comunque discusse.

Il tasso di esplosione delle Supernovae (SNR) è importante per diversi motivi. In una data galassia, questa grandezza è legata ai processi di formazione stellare, all'evoluzione stellare (che dipende dalla metallicità e quindi dall'età delle galassie) ed alla popolazione di sistemi binari.Per questo motivo lo studio del tasso di esplosione di SNe a diversi *redshift* può fornire importanti indicazioni sui progenitori e sul tasso di formazione stellare (SFR). In particolare il tasso di esplosione delle CCSNe, a causa della veloce evoluzione dei loro massicci progenitori($M > 8M_{\odot}$), rispecchia direttamente il tasso instantaneo di formazione stellare. Le SN di tipo Ia invece, avendo origine in sistemi binari evoluti, possono dare delle indicazioni sulla storia dell'evoluzione stellare. Studiare il tasso di esplosione delle SNe è importante anche perchè esse sono tra i maggiori responsabili dell'evoluzione chimica delle galassie. Nel Capitolo 5 sfrutteremo i dati raccolti nel corso della nostra ricerca di SNe per dare una stima del tasso di esplosione a redshift intermedio ($z \sim 0.3$) sia per quanto riguarda le SNe di tipo Ia che per le CCSNe. La nostra è la prima stima del tasso di esplosione delle CCSNe al di fuori dell'Universo locale. I nostri dati mostrano un incremento del tasso di esplosione delle SNe al crescere del *redshift*, soprattutto per quanto riguarda le CCSNe, in accordo con l'andamento del tasso di formazione stellare. Altri studi sul tasso di esplosione delle SNe Ia suggeriscono un'evoluzione meno accentuata col *redshift*, tuttavia le incertezze sono così grandi che i due risultati non sono inconciliabili. Ulteriori studi sono quindi necessari per avere una risposta definitiva.

I risultati ottenuti in questa Tesi e le prospettive future di questo tipo di studi sono riassunti nel Capitolo 6.

Summary

I could be bounded in a nutshell
and count myself king of infinite space,
were it not that I have bad dreams.
Shakespeare, *Hamlet*

Supernovae (SNe) can give useful hints in a variety of studies spanning different astrophysical and cosmological issues. SNe in general represent in fact useful "laboratory" where matter experiences extreme conditions that cannot be produced in terrestrial laboratories. SNe can give information on stellar evolution, mass loss processes or accretion mechanisms, explosions physics. Supernovae explosions are tight related to the kinematics and enrichment of the interstellar matter. SNe can also shed light on the study of pulsars, cosmic rays, neutrinos, gravitational waves and γ-ray bursts. Besides, because of their brightness, SNe are also an important tool to investigate the Universe to very large distances, providing us with information on its properties.
In this Thesis we will not discuss the physics of Supernovae but we will focus our attention on the last issue mentioned, i.e. role of SNe as probes. In particular we will discuss the use of Type Ia SNe as distance indicator, their use as cosmological tool for determining the cosmological parameters and, together with Core Collapse SNe, we will discuss their role as star formation rate tracers.
Understanding the global history of the Universe is a fundamental goal of cosmology and one of the conceptually simplest test is observing how a standard (or standardizable!) candle dims as a function of redshift. Type Ia SNe in particular are invaluable cosmological tool that can be used to measure global properties of our Universe, like the Hubble constant H_0 (e.g. Rust 1974; Hamuy et al. 1996b; Tripp and Branch 1999; Freedman et al. 2001), the cosmological parameters q_0, Ω_m, Ω_Λ (e.g. Schmidt et al. 1998; Perlmutter et al. 1999; Riess et al. 1998). The nearby SNe in particular provides the current expansion

rate, while more distant objects allow us to search for the effects of cosmic curvature and the Universe expansion history.
The thesis is made up of two parts: in the first one we will analyse a sample of nearby SNe, while in the second part we will study an intermediate redshift SN sample. In particular, the topics discussed in this Thesis are the following:

- The intrinsic brightness, the relatively uniform light curves and spectral evolution of SNe Ia suggested very soon their use as standard candles. Yet, as it will be discussed in Chapter 2, observations of an increasing number of SNe showed a great variety of objects also inside SN Ia. Fortunately for their use as distance indicators, correlations between observables and absolute magnitude at maximum seem to exist. So, although not strictly homogeneous, after proper calibration, SNe Ia represent the most accurate distance indicators on cosmological scales. In Chapter 2 we use data from literature and new unpublished data of nearby SNe Ia to estimate the parameters of the luminosity-width relation and we examine how different metallicity-dependent calibrations of the Cepheid absolute magnitude affect the type Ia calibration and, in turn, the Hubble constant. We also focus the attention on the absorption estimate and correction, which turn out to play a crucial role in the SN absolute magnitude calibration.

- To date observational estimates of the SN rate at high redshift have been based on the SN searches aimed to use SN Ia as cosmological probes and no estimates for CCSNe rate are available. For this reason in 1999 we started a SN search mainly aimed to estimate the supernovae rate at intermediate redshift ($z \sim 0.3$) for both Thermonuclear SNe (SNe Ia) and Core Collapse SNe. In Chapter 3, after a brief overview on SN searches in general, we describe our **S**outhern In**T**ermediate **R**edshift **E**SO **S**upernova **S**earch (**STRESS**). The technical details of the instrumentation used, the observations scheduling and strategy, the data collection as well as the software development and the data reduction of the STRESS project are reported. The spectroscopically confirmed SNe as well as the byproducts of the search are also presented.

  In Chapter 4 we combine our intermediate redshift SNe with the local sample used in Chapter 2, exploiting the results found in the same chapter to calibrate the whole sample. The resulting Hubble diagram is then used to estimate the cosmological parameters Ω_M, Ω_Λ. In order to get better constraints on the cosmological parameters, we also combine our intermediate redshift SN sample with data from literature, obtaining a significantly larger sample and extending the hubble diagram to higher redshifts. In both cases Supernovae at high redshift seem to be fainter than expected, as if the rate of expansion of the Universe is accelerating. This behavior, already noticed a few years ago, can be explained in the framework of the standard Friedmann-Robertson-Walker cosmology through the presence of a vacuum energy ("dark energy" or a cosmological constant), but alternative hypotheses are presented too.

  The explosion rate of Supernovae (SNR) is important for several reasons. Supernova rates in galaxies depend on the star formation processes, on stellar evolution (which depends on metallicity and hence on the galaxy age), and on the binary system population. A comparison between SN explosion frequencies at different redshifts may provide important constraints on the evolutionary scenario of the SN progenitors and on the star formation rate (SFR). In particular, because of the short lifetime of massive progenitors ($M > 8M_{\odot}$), the rate of Core Collapse SNe (CCSNe) is correlated with the instantaneous SFR, while the rate of Type Ia SNe, originating in evolved binary system, can give information about the long term star formation history. Moreover Supernovae are among the main drivers of the chemical evolution of a galaxy, it is thus important to follow the temporal evolution of their rates as accurate as possible. In Chapter 5 we exploit the data collected during our SN search to estimate the SN rates at intermediate redshift ($z \sim 0.3$), for both type Ia and CCSNe. This is the first attempt to measure the CCSNe rate beyond the local Universe! Our data show an increase of the supernova explosion frequencies with z for both SN classes, but much more steeper for Core Collapse Supernovae, in agreement with the expected star formation rate evolution in the same redshift range. Other modern studies on type Ia SN rates suggest a shallower evolution with redshift, but the large uncertainties do not allow to claim a disagreement and leave the problem open to further study.

The results obtained in this Thesis and future perspectives are summarized in Chapter 6.

Chapter 1

Supernovae

He passed the flaming bounds of space and time
the living throne, the sapphire-blaze
where angels tremble while they gaze,
He saw; but blasted with excess of light
closed his eye in endless night.
Milton, *Progress of poetry*

1.1 Introduction

Supernovae (SNe) are the result of the instantaneous release of $\sim 10^{51}$ erg of energy that occurs at the end of a star's lifetime and represent one of the most energetic explosive event in the Universe. Although only a small fraction of the energy is released in the form of visible light, the exploding star becomes as bright as the whole galaxy in which it is embedded. In our own galaxy, the Milky Way, a supernova might even be visible in broad daylight, as if a new star has appeared in the sky. A few such events were seen in historical times in the Milky Way, and apparently no one occurred in the last 300 years. Ancient european, chinese, japanese, korean and arabian chronicles report the observation of these "new stars". Seven or eight events have been confirmed from historical records in the last 2000 years, with apparent magnitudes in the range between 0 (SN 1181 AD) and -9 (SN 1006 AD). The last two events were recorded by Tycho Brahe in 1572 and by Johannes Kepler in 1604. After that there were no other unambiguous naked eye events until SN 1987A, which exploded in the Large Magellanic Cloud, a satellite galaxy of the Milky Way. Modern estimates predict that one supernova should occur in a galaxy like the Milky Way every few decades, and, if not heavily obscured by interstellar matter, it should become a very spectacular events in the sky. The astronomers are eagerly waiting for the next such event.

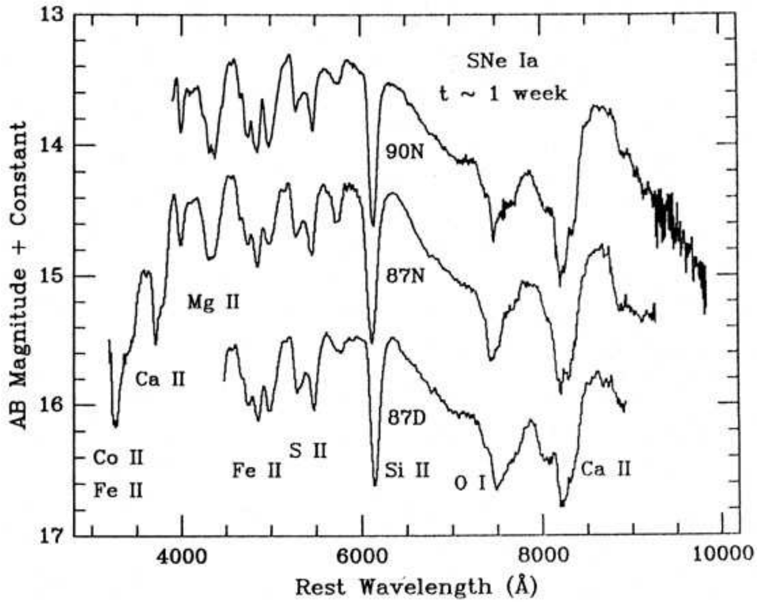

Figure 1.1: Typical Type Ia SN spectra close to maximum. Figure from Filippenko (1997).

Supernovae owe their name to astronomers Baade and Zwicky, who, in the 1930's, disentangled extragalactic SNe from the galactic novae, realizing that the former are much more luminous.
The attractiveness of supernovae lies in their astrophysical potential in exploring issues like stellar evolution, stellar mass loss, collapse and explosion physics, radiative hydrodynamics, shock physics, galactic structure and chemical evolution, and cosmology.

1.2 Supernova Taxonomy

Supernova explosions are not all the same, but they can be grouped in different types. The classification of SNe is an observational one, based on their spectral features and light curves (plot of luminosity vs. time). Classification of SNe was first introduced by Minkowski (1941), who separated SNe into two groups based on the presence or absence of Hydrogen Balmer lines in their spectra at maximum brightness. Those without Balmer lines were classified as Type I SNe and those with Balmer lines were classified as Type II. Typical spectra of Type Ia and Type II SNe are shown in Fig. 1.1, 1.2 This simple scheme evolved with time to the present one, in which supernovae of Type I are further divided into Type Ia (with Si absorption near 6150Å due to Si II), Ib (with He lines instead of the Si II feature) and Ic (similar to Ib but with faint or absent He lines). Type II SNe are divided in IIL (linear), IIP (plateau), according to their light curve shape (linear or with a plateau). Type II SNe with narrow emission lines in their spectra are classified as Type IIn (narrow). There are also "intermediate" objects which show a metamorphosis from a classic Type II SN at early phases, with hydrogen lines in its spectrum, to a Type Ib/c in the nebular phase. This is the case of SNe 1993J (Filippenko et al., 1994; Barbon et al.,

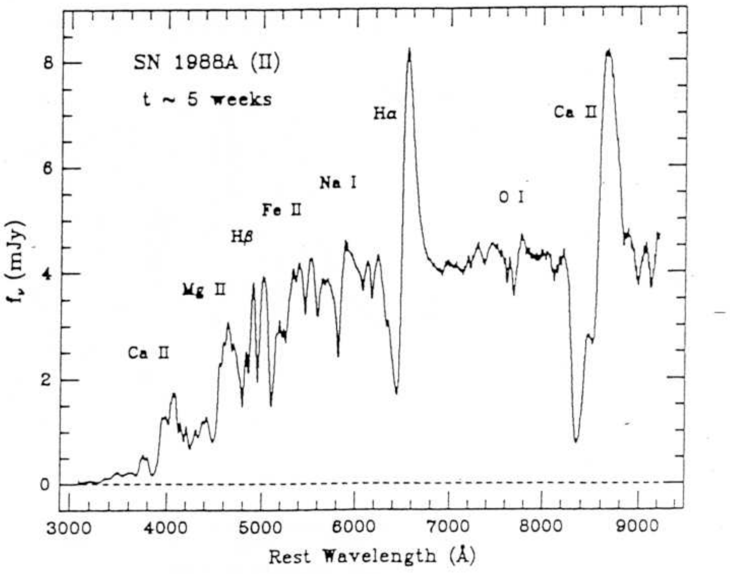

Figure 1.2: Typical Type II SN spectrum a few weeks post maximum.

1995) and 1987K (Filippenko, 1988). The new subclass Type IIb has been proposed for these transition objects, which suggest a continuity between Type Ib/c and Type II SNe and a similar explosion mechanism. For this reason Type II and Type Ib/c SNe can be all referred to as Core Collapse Supernovae (CCSNe).
Although the classification is a purely observational one, it traces the physical similarity of the progenitor stars. In fact according to the explosion mechanisms, SNe can be divided into two main groups (Fig. 1.3), as described below.

- **Thermonuclear Supernovae**
  Type Ia Supernovae (SNe Ia) are the result of the thermonuclear explosion of a C-O white dwarf (WD) in a binary system. The spectra of SNe Ia are characterized by the absence of hydrogen lines. The light curves show a sharp rise followed by a steady, gradual decline, steeper in the first ~ 30 days after maximum (decline rate in the B band: $\beta_B \sim 0.1 mag/day$) and shallower later on (the decline rate decrease to $\beta_B \sim 0.015 mag/day$).
  Despite the efforts (Branch et al., 1995; Renzini, 1996; Iben, 1997; Ruiz-Lapuente et al., 1997), progenitor systems and hydrodinamical models are still controversial. Two main scenarios have been proposed:
  - the single degenerate (SD) scenario, where the SN Ia progenitor is a WD in a close binary system and the companion is a main sequence or a red giant star (Whelan and Iben, 1973);
  - the double degenerate (DD) scenario, where also the companion is also a white dwarf (Iben and Tutukov, 1984).
  In the SD scenario it is believed that the strong gravitational attraction of the WD overcomes the weaker gravity of the companion, causing mass from the outer envelope of the companion star to be accreted onto the WD. For intermediate accretion

SN type	Characteristics	Progenitor
I	**No hydrogen in spectrum**	
Ia	• Strong absorption at 6150Å near max light. • Iron-group emission lines in late-time spectrum	• Detonation or deflagration of an accreting white dwarf or of two white dwarf colliding.
	THERMONUCLEAR SUPERNOVAE	
	CORE COLLAPSE SUPERNOVAE	
Ib	• Absorption near 5700Å, due to He (plus other He lines). • O-I, Ca-II emission lines in late-time spectrum.	• Core collapse of massive star stripped of the H envelope before explosion by strong wind (Wolf-Rayet stars) or binary interactions.
Ic	• No He in spectrum. •O-I, Ca-II emission lines in late-time spectrum.	• Core collapse of massive star stripped of the H & He envelope before explosion by strong wind (Wolf-Rayet stars) or binary interactions.
II	**Hydrogen in spectrum**	
IIP	• P-Cygni profile. • After maximum light curve shows a plateau for 30-90 days.	• Massive red supergiant.
IIL	• Weak or no P-Cygni profile. • Light curve falls linearly (0.05 mag/day) after max light.	• Massive red supergiant. • Some envelope lost?
IIb	• Weak H lines in spectrum. • He lines in spectrum. • O-I, Ca-II, H emission lines in late time spectrum.	•Massive star which has lost most, but not all, of its H envelope by tidal stripping.
IIn	• Narrow emission lines on top of broad emission features. • Slow decline in light curve at late times.	•Massive Star which explode in the middle of massive stellar outflow?

Figure 1.3: Supernovae Taxonomy.

rates (i.e. $10^{-8} M_\odot\, yr^{-1} < \dot{M} < 3 \times 10^{-6}\ M_\odot\, yr^{-1}$) the process continues until the WD mass reaches the Chandrasekhar limit ($1.4\, M_\odot$, where $M_\odot$ is the solar mass) beyond which the electron degeneracy pressure is no longer able to balance the gravitational force. For slower accretion rates, hydrogen shell burning is unstable and most of the accreted matter is periodically ejected in "flash" (the strongest flash leading to *nova* explosion); for higher accretion rates the new material forms a common envelope, which is eventually lost by the system. A debated issue is whether such SD systems exist in sufficient number to account for the observed SN Ia frequency, and whether the WD grows enough to reach the critical mass for ignition. In this scenario, a significant amount of circumstellar matter is expected to be in the vicinity of the explosion but so far, no convincing evidence for narrow circumstellar hydrogen or helium lines in SN Ia spectra has been found (Ho and Filippenko, 1995; Cumming et al., 1996), with the exception of SN 2002ic (Wood-Vasey, 2002; Hamuy et al., 2003a,b). Nor has X-ray (Schlegel and Petre, 1993) or radio (Eck et al., 1995) emission from circumstellar interaction been seen. These non-detections are not yet quite stringent enough, however, to rule out single-degenerate progenitor system.

In the DD scenario the Chandrasekhar limit is reached when the two WDs, with a combined mass exceeding $1.4\, M_\odot$, merge after spiraling together as a consequence of the emission of gravitational waves. We know that most stars end up as white dwarf and that a major fraction of stars are in binary systems, hence DDs must be common among WDs. But we do not know if a significant number of these systems is able to merge in less than one Hubble time and those researchers who have made recent attempts to model the merging process (Mochkovitch and Livio, 1990; Benz et al., 1990; Rasio and Shapiro, 1995; Mochkovitch et al., 1997) are not optimistic about producing SNe Ia in this way. In the DD model it is not clear if there should be a significant amount of circumstellar matter in the vicinity of a merger SN Ia, but if so, it would be carbon and oxygen rather than hydrogen and helium. In this regard, the detection of narrow [O I] lines in late-time spectra of SN 1937C by Minkowski (1939) and the possible detection of narrow [O I] 8446 emission in a very early spectrum of SN 1991T by Ruiz-Lapuente et al. (1992) are intriguing.

However one model does not exclude the other and there is evidence that both routes may be viable (Howell, 2001).

A third scenario is given by the sub-Chandrasekhar (sub-Ch) model, that is the explosion of a sub-Ch WD. This is a possible outcome of a slow accretion rate ($10^{-9} M_\odot\, yr^{-1} \leq \dot{M} \leq 10^{-8} M_\odot\, yr^{-1}$). In this case, the ignited He shell flash is supposed to be strong enough to initiate an off-center He detonation, which induces a central C detonation and the SN explosion.

With the exception of the sub-Chandrasekhar scenario, the SNe Ia explosions are caused by the same process: a WD reaching the Chandrasekhar limit, no matter if by accretion from a companion or by merging with another WD. This is the reason why Type Ia SNe are a quite homogeneous class of objects.

In a Chandrasekhar mass model, when the WD reaches $\sim 1.4\, M_\odot$ and the central density exceeds $\sim 10^9\ \mathrm{g\, cm^{-3}}$, the high temperature ignites the fusion of carbon nuclei. When C is ignited at the white dwarf center, because of the strong electron degeneracy, its burning is explosive and incinerates the material into iron-peak elements. The details of the explosions are still controversial. Several possibilities have been suggested: a supersonic detonation, in which the shock triggers the burning which in turn drives the shock, or a deflagration, a form of subsonic, but still rapid, combustion in which the flame front is driven by turbolent heat exchange. The former mechanism receives some support from theoretical analysis on the onset of nuclear burning, but the latter mechanism agrees better with observations. There are also delayed-detonation models in which an initially subsonic flame become a supersonic shock. In any case the explosion results in the complete disruption of the star. If the classic deflagration model is assumed, the resulting shock wave is not strong enough to ignite carbon in the adjacent layer producing a detonation wave, instead a slower, subsonic wave propagates outwards and behind its front material undergo explosive nuclear burning of Si, O, Ne and C. The products range from Fe-peak elementes (mainly ^{56}Ni) to intermediate-mass elements (Ca, Ar, S and Si), O-Ne-Mg, and C+O (Nomoto et al., 1997). In the standard deflagration model (W7 model, Nomoto et al. 1984), the amount of ^{56}Ni produced is $M_{Ni} \simeq 0.6 M_{\odot}$ and the explosion energy is E=(nuclear energy release)-(binding energy)=1.3×10^{51}, which is large enough to disrupt the white dwarf completely. This energy goes into kinetic energy of expansion, and without other energy inputs, the SN would not shine as it does. Indeed the observed light curve evolution is powered by the radioactive decay of ^{56}Ni: this decays into ^{56}Co with a half-life of 6.6 days which in turn decays into ^{56}Fe with a half-life of 77 days. These processes produce γ-rays which degrade into X-rays through scattering Compton. The photoelectric absorption of X-rays and the collisional ionization due to energetic electrons eventually heat the expanding material and produce optical radiation. The light curve reaches its peak about 15 days after the explosion and then declines because of the increasing transparency of the ejecta to γ-rays. The light curve shape depends mainly on the explosion energy, on the amount of ^{56}Ni syntesised, on its distribution within the ejecta and on the opacity. For larger M_{Ni}, the brightness is in general higher. The observed variation of the maximum brightness is the result of the variations of ^{56}Ni mass.

- **Core Collapse Supernovae**
  Type II SNe are stellar explosion of stars that have retained their hydrogen envelopes, and whose explosion is triggered by a gravitational collapse. It is currently believed that Type II SN progenitors are massive stars of $8\,M_{\odot}$ or more, mainly red supergiant. Yet, the case of SN 1987A has shown that some fainter CCSNe originate from blue supergiant as well. Stars born with $\sim 8 - 10\,M_{\odot}$ can reach temperatures and densities sufficiently high to produce O, Ne, Mg cores. More massive stars can proceed even further in the nuclear burning and end up with Fe nuclei. Once iron as formed in the center, no further energy can be released by nuclear fusion. When nuclear burning ceases, the gravitational collapse raises the temperature and the pressure but not enough to balance gravity. As the temperature of the iron core grows to 10^{10} °K and more and the density to 10^{10} $\mathrm{g\,cm^{-3}}$, electrons are squeezed into nuclei, leading to heavier neutron rich isotopes. Concurrently, high energy radiation begins to tear nuclei apart into α particles. Both processes subtract energy to the core and the collapse starts. The dynamics of the collapse segregates the imploding core into two regions: an inner core that collapse homologously ($v \propto r$), and an outer core, falling with supersonic velocity ($v \propto r^{-1/2}$). The collapse of the core accelerates up to 70,000 km $\mathrm{s^{-}1}$ and when the central density reaches and exceeds the density of the atomic nucleus (2.7×10^{14} $\mathrm{g\,cm^{-3}}$), the repulsive component of the strong, nuclear, force, stops abruptly the collapse. The inner core halts as a unit, the outer one falls onto the inner core and bounces, originating a shock wave

(Woosley and Weaver, 1986). A rebound of the compressed inner core gives energy to this shock which moves outwards while the central core collapses to a neutron star (or a black hole, according to the entrapped mass). Current calculation shows that the shock loses almost all the kinetic energy in dissipative processes (mainly due to neutrino losses and to the photodissociation of bound nuclei into neutrons and protons) before reaching the edge of the outer core. So it can not sweep away the rest of the star. However the collapsed core, although very dense and neutron rich, is not yet a neutron star. The binding energy of a neutron star ($\sim 3 \times 10^{53}$ erg) is radiated away in the following few seconds as neutrinos. If just a tiny fraction, of the order of one percent ($\sim 10^{51}$ erg), of this energy is deposited at the outer edge of the core (just behind where it has temporarily stalled and material is accreting), a powerful explosion still may develop. The neutrino energy transport is currently believed to explains Type II SNe explosions, but there may well be additional physics that has not yet been modeled and the exact mechanism by which the core implosion triggers the explosion of the outer layers is still a difficult theoretical problem. In any case, if this theory is correct, the shock is revitalized and propagates through the ejecta. The associated high temperature leads to nuclear fusion, producing a number of heavy elements, from silicon to zinc. One of the most important of them is ^{56}Ni. Theory suggest that from a few thousandths (for a $\sim 10\,M_\odot$ SN) to a few tenths (for a $\sim 40\,M_\odot$ SN) of a solar mass of ^{56}Ni are produced in Type II SN explosions. The decay of ^{56}Ni is an important energy source which powers the SN luminosity at late time. Soon after the explosion, as the shock exits the core, the surface of the star is heated to temperatures near one-half million degrees. It is now that the SN becomes visible in the optical range: first in the ultraviolet and then in longer wavelengths. Within one week the temperature declines and the hydrogen of the ejected envelope begins to recombine. The emitted energy is determined by the receding (in mass) of the H recombination front which is responsible for both the release of the stored thermal energy and the recombination energy. At the recombination front the opacity drops providing a self regulating system: if too little energy is released, the opacity drops fast causing an increase in the speed at which the photosphere is receding. This causes a larger energy release and vice-versa (Höflich et al., 2001). During this phase, whose length depend on the mass and radius of the hydrogen envelope, the luminosity stays almost constant. A thick hydrogen envelope leads to the characteristic plateau in the light curve of the Type IIP SNe, which may last from one week to three months. After the recombination the luminosity declines abruptly until a new energy source, the ^{56}Ni decay, emerges. A thin hydrogen envelope is not able to support a constant luminosity phase and leads to a linear decline of the luminosity (Type IIL).

Type Ib/c SNe are probably due to the same explosion mechanism of Type II SNe, but they are supposed to originate from progenitors more massive than $30M_\odot$, which lost, respectively, all or most of the outer layer of H and H/He in violent throbs occurred during their evolution.

Type IIn SNe are Core Collapse SNe are supposed to be embedded in a dense, clumpy CSM, created by very strong mass loss from the progenitor. These SNe are expected to be X and radio sources because of their interaction with the circumstellar material (CSM). The interaction of the shockwave with slower expanding material ejected before the SN explosion can, in principle, trace the mass-loss history of the progenitor in reverse.

During the last few years, a number of exceptional CCSNe have been observed. Although their properties are rather diverse, they have the common feature that some of their basic parameters, as the kinetic energy or the mass of the synthesized ^{56}Ni, are larger, sometimes by more than an order of magnitude, than the typical values found for "normal" CCSNe (e.g. the mass of ^{56}Ni ejected by SN 1999as as been estimated to be greater than $4M_{\odot}$, Hatano et al. 2001). Therefore these objects have been classified as Hypernovae. These new class seems to originate from stars more massive than $20-25M_{\odot}$ on the main sequence, which collapse to a black hole. Some of them are also associated to γ ray bursts (as 1998bw, a Type Ic SN as bright at maximum as a Type Ia SN, likely associated to GRB 980425, Kulkarni et al. 1998, or SN 1997cy, associated with GRB 970514, Turatto et al. 2000).
The variety in the progenitors scenarios of CCSNe is reflected by the variety in the spectra, in the light curve shapes and in the absolute magnitude at maximum.

In the next two sections (§1.3, §1.4) we introduce some basic concepts useful for the following Chapters.

1.3 SNe & Cosmology

As extremely luminous point ($M_{Bmax} \cong -19.5$) sources, SNe Ia are attractive indicators of extragalactic distances.
Even if there are also other secondary distance indicator (Jacoby et al., 1992) as the globular cluster luminosity function (GCLF), the novae, the Tully-Fisher (TF) relation, the planetary-nebula luminosity function (PNLF), the surface brightness fluctuations (SBF), the fundamental-plane relationship for elliptical galaxies ($D_n-\sigma$), to cite the most reliable methods for deriving distances, none of them offer the same possibilities of Type Ia SNe (see Fig. 1.4). Because Type Ia supernovae are so bright, it is possible to see them at very large distances, out to around 3000 Mpc, which is a significant fraction of the size of the known Universe. In order to understand all the cosmological implications of SNe Ia we introduce some basic cosmological concepts.
In the 1930s, the assumption of spatial homogeneity was joined with spatial isotropy to form the Cosmological Principle. The Cosmological Principle asserts that on very large scales there are not preferential points or directions in the Universe. In such a universe, the interval (space-time separation) between events ("points" in space-time) can be described by the Robertson-Walker metric:

$$ds^2 = (cdt)^2 - a(t)^2 \left[\frac{dr^2}{1-Kr^2} + r^2(d\vartheta^2 + sin^2\vartheta d\varphi^2)\right] \tag{1.1}$$

where r, ϑ, φ are polar coordinates (r adimensional variable), t is the proper time, $a(t)$ is the scale factor (or expansion parameter) and K is the curvature parameter. The K value (1, 0, -1) determines the geometry of the Universe (closed, flat, open). The $K=0$ case (flat universe), corresponds to the conventional euclidean geometry.

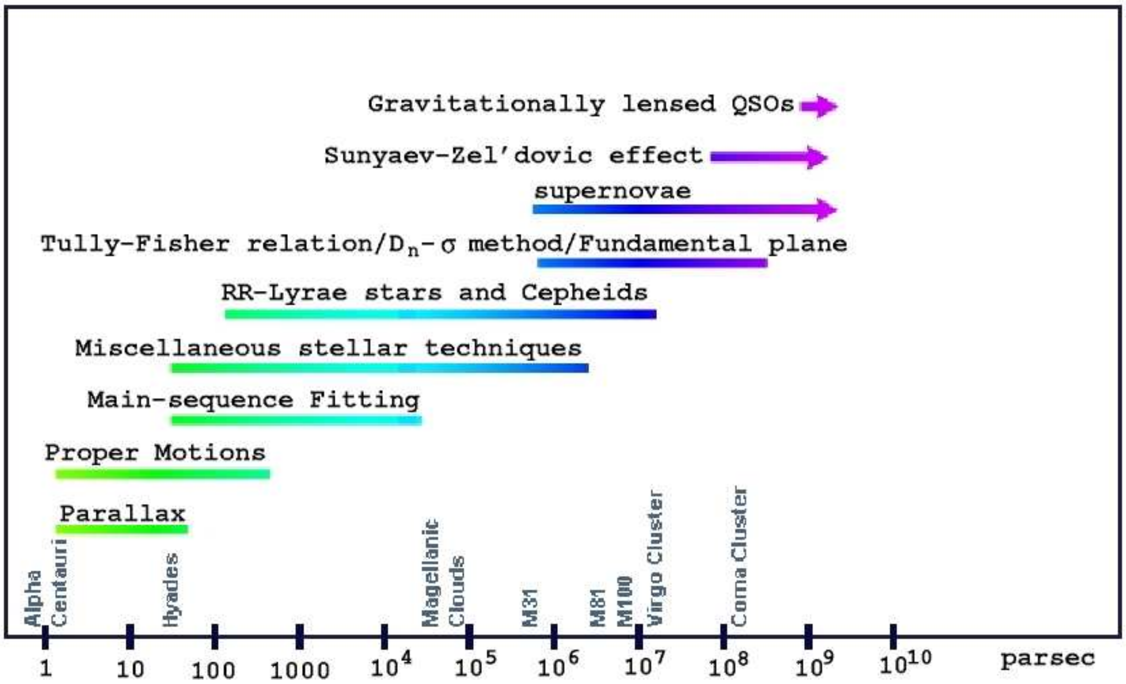

Figure 1.4: The Distance Ladder. Some of the main types of distance estimator and their approximate ranges. Figure adapted from Rowan-Robinson (1985).

The geometric properties of the space-time are linked to the energy-matter by the Friedman cosmological equations 1.2,1.3

$$\ddot{a} = -\frac{4}{3}\pi G\left(\rho + 3\frac{p}{c^2}\right)a \tag{1.2}$$

$$\dot{a}^2 + Kc^2 = \frac{8}{3}\pi G\rho a^2 \tag{1.3}$$

and the space curvature is given by:

$$\frac{K}{a^2} = \frac{1}{c^2}\left(\frac{\dot{a}}{a}\right)^2\left(\frac{\rho}{\rho_c} - 1\right) \tag{1.4}$$

$$\rho_c = \frac{3}{8\pi G}\left(\frac{\dot{a}}{a}\right)^2 \tag{1.5}$$

ρ_c represents the critical density. The space is closed, flat or open according to the density parameter

$$\Omega(t) = \frac{\rho}{\rho_c} \tag{1.6}$$

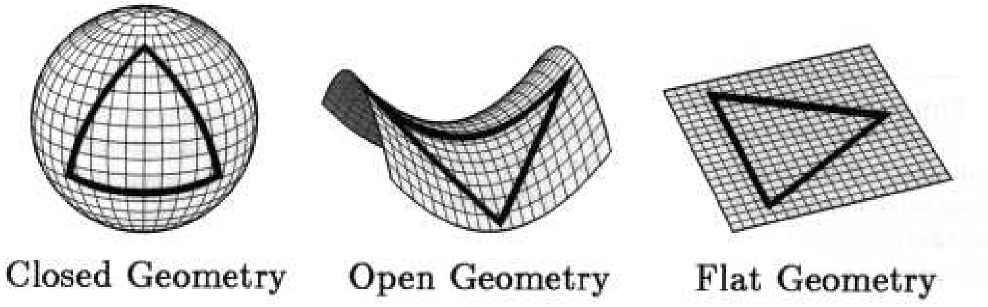

Figure 1.5: Two dimensional representations of possible geometries of the Universe: a flat Universe (Euclidean or zero curvature), a spherical or closed Universe (positive curvature) or a hyperbolic or open Universe (negative curvature). Note that this curvature is similar to spacetime curvature due to stellar masses except that the entire mass of the Universe determines the curvature. So a high mass Universe has positive curvature, a low mass Universe has negative curvature.

as shown in Tab. 1.1 (see also Fig. 1.5). If there is sufficient mass, then the expansion of the Universe will be slowed to the point of stopping and collapsing again. If there is not a sufficient amount of mass, then the Universe will expand forever without stopping. In a flat Universe the amount of mass is sufficient to slow the expansion to zero but it is not enough to produce a collapse (see Fig. 1.6).

$\Omega(t)$	K	Universe
>1	1	closed
1	0	flat
<1	-1	open

Table 1.1: Space properties dependence on the density parameter $\Omega(t)$.

At the beginning of Cosmology, even if the solutions of the Friedmann's equations produced non-static Universe models, it was natural to seek for a static solution, as people had assumed for centuries the universe to be immutable. So in 1917 Einstein, when published his first model of the universe based upon general relativity, introduced the cosmological constant Λ to obtain results consistent with a static Universe, though Slipher's work was by this time giving the first hints of the expansion of the universe (Slipher, 1917). In 1929, after the Hubble's discovery of the Universe expansion, Einstein renounced the idea of the cosmological constant, calling it the greatest blunder of his life. As we will discuss in detail in Chapter 4, the cosmological constant has been recently recovered to explain the results obtained by the high redshift SNe studies. The most distant supernovae are indeed dimmer than they would be if the Universe were slowing under the influence of gravity, as astronomers expected before 1998. This has been attributed to the accelerating expansion rate of the Universe being accelerated. If we take into account this factor the total density can be splitted into two components: the matter density ρ_M and the cosmological constant

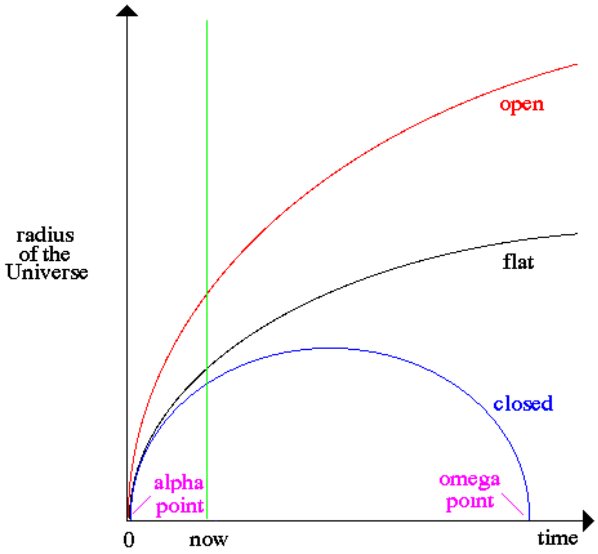

Figure 1.6: Universe evolution for $\Omega > 1$ (open), $\Omega = 1$ (flat), $\Omega < 1$ (closed).

contribution ρ_Λ:

$$\rho = \rho_M + \rho_\Lambda \tag{1.7}$$

Density is related to pressure through the equation of state $p = \omega \rho c^2$ were $\omega = 1/3$ for radiation, $\omega = 0$ for pressureless matter (e.g. cold dark matter), $\omega = -1$ for a cosmological constant.

If we define Ω_M, Ω_Λ as the ratio between ρ_M and ρ_Λ (where $\rho_\Lambda = \Lambda/(8\pi G)$) and the critical density

$$\Omega_M = \frac{8\pi G}{3H_0^2}\rho_M \tag{1.8}$$

$$\Omega_\Lambda = \frac{\Lambda}{3H_0^2} \tag{1.9}$$

eq. 1.4 can be written as:

$$\frac{K}{a^2} = \frac{1}{c^2}\left(\frac{\dot{a}}{a}\right)^2 (\Omega_M + \Omega_\Lambda - 1) \tag{1.10}$$

While Ω_M slows down the Universe expansion, Ω_Λ has the opposite effect, accelerating it. In a flat Universe $\Omega_M + \Omega_\Lambda = 1$.
Two other important cosmological parameters are:
1 - the deceleration parameter q_0

$$q_0 = \frac{1}{2}\sum_i \Omega_i (1 + 3\omega_i) \tag{1.11}$$

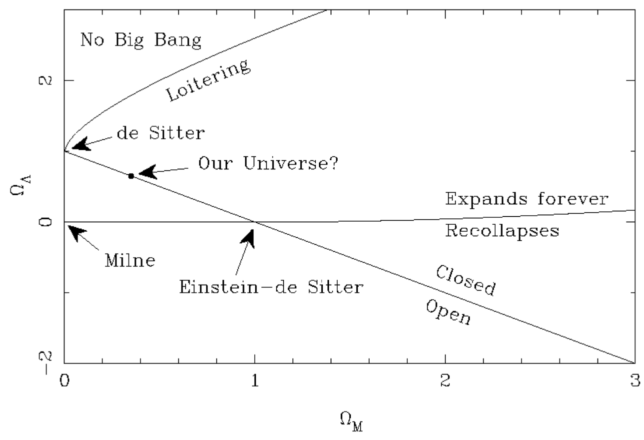

Figure 1.7: Position of some classic cosmological models in the Ω_M–Ω_Λ plane as well as some characteristic properties of different regions.

($\omega = 1/3$: radiation, $\omega = 0$: cold dark matter, $\omega = -1$: cosmological constant)
2 - the expansion rate H (which is called Hubble constant, H_0 at present epoch)

$$H(t) = \dot{a}/a \tag{1.12}$$

In a Universe with cosmological constant and normal matter $q_0 = 1/2\,\Omega_M - \Omega_\Lambda$. If $\Omega_\Lambda < 1/2\,\Omega_M$ then $q_0 > 0$ and the universe is decelerating.
The Hubble constant is a fundamental cosmological parameters, which can be used to estimate (assuming $h \equiv H_0/100$):

- the distance scale:
$$l_{0H} \simeq \frac{c}{H_0} \simeq 3000 h^{-1} Mpc$$
where l_{0H} represent the current cosmological horizon;

- the time scale
$$t_{0H} \simeq \frac{1}{H_0} \simeq 0.98 \times 10^{10} h^{-1} years$$
where t_{0H} is the time interval from the big-bang to present (assuming a constant expansion rate);

- density scale:
$$\rho_{0c} = \frac{3H_0^2}{8\pi G} \simeq 1.9 \times 10^{-29} h^2 gcm^{-3}$$
where ρ_{0c} is the current critical density.

For each combination of the cosmological parameters we have different model for the Universe. A few particular models, which are often used as reference, are reported in Table 1.2 (see also Fig. 1.7).

Model name	Description
Einstein	A steady-state, closed Universe proposed by Einstein in 1917. $\ddot{a} = \dot{a} = H_0 = 0$, $\rho_M = 2\rho_\Lambda$.
Einstein-de Sitter	Matter dominated, flat Universe, expanding forever from a singularity, with zero cosmological constant Λ and pressure P. $\Omega_M = 1$, $\Omega_\Lambda = 0$, $a \propto t^{\frac{2}{3}}$, $t_0 = 2H_0^{-1}/3$
de Sitter	Flat Universe, no matter. Exponential expansion, no singularity. $\Omega_M = 0$, $\Omega_\Lambda = 1$
Milne	No matter or cosmological constant, open Universe. $\Omega_M = \Omega_\Lambda = 0$, $a \propto t$, $t_0 = H_0^{-1}$

Table 1.2: Essential features of classic cosmological models.

In order to understand how the cosmological parameters can be determined by means of SNe, we define the luminosity distance d_L:

$$d_L = \left(\frac{L}{4\pi f}\right)^{\frac{1}{2}} \tag{1.13}$$

where L is the luminosity of the observed source and f the flux measured by the observer. The same relation can be written in terms of magnitudes:

$$m - M \equiv \mu = 5log(d_L) + 25 \tag{1.14}$$

where m and M are the apparent and absolute magnitude respectively and the distance d_L is expressed in Mpc. $m - M$ is also known as the "distance modulus" μ. If both the apparent and absolute magnitude are known, eq. 1.14 give us the distance d_L. In the Robertson-Walker metric d_L can be also expressed as a function of the cosmological parameters as shown in eq. 1.15.

$$d_L(z, \Omega_M, \Omega_\Lambda, H_0) = \frac{c(1+z)}{H_0\sqrt{|k|}} S\left\{\sqrt{|k|}\int_0^z \left[(1+z')^2(1+\Omega_M z') - z'(2+z')\Omega_\Lambda\right]^{-\frac{1}{2}} dz'\right\} \tag{1.15}$$

where

$$S(x) = \begin{cases} sin(x) \\ sinh(x) \\ x \end{cases}, k = \begin{cases} 1 - \Omega_M - \Omega_\Lambda \\ 1 - \Omega_M - \Omega_\Lambda \quad \text{if } \Omega_M + \Omega_\Lambda \\ 1 \end{cases} \begin{cases} < 1 \\ > 1 \\ = 1 \end{cases}$$

For small values of z, eq. 1.15 can be expanded in a Taylor series

$$d_L \frac{H_0}{c} = z + \frac{1}{2}(1 - q_0)z^2 + O(z^3) \tag{1.16}$$

The first order approximation of this relation corresponds to the the empirical relation

$$v_r = H_0 d_L \tag{1.17}$$

proposed in 1929 by E. Hubble, who noticed that the more distant a galaxy, the greater its redshift and hence the greater its recession velocity v_r. The Hubble law is useful in a limited redshift range ($10^{-2} \leq z \leq 10^{-1}$), i.e. for recession velocities greater than the galaxy peculiar motions but not so large to involve relativistic effects. If we join eq. 1.14, 1.17 we obtain the relation $\mu \equiv m - M = 5log(cz) - 5log(H_0) + 25$. In a plot of μ *vs.* $log(cz)$ (the Hubble diagram) we expect a source of a given absolute magnitude to be placed on a line with fixed slope and intercept proportional to the Hubble constant H_0.
At larger redshift the first order approximation of the luminosity distance is not useful any more and the complete expression for the luminosity distance (eq. 1.15) must be computed. Using eq. 1.14 and 1.15 it is possible to predict the apparent magnitude of a standard candle at a given redshift for any pair of values of Ω_M and Ω_Λ. The apparent magnitude difference of a standard candle measured at two different redshifts is sufficient, under the assumption that the absolute luminosity is the same, to determine the Ω_M and Ω_Λ values. For this reason is more useful to plot a diagram of the magnitude differences between various cosmological models (Fig. 1.8).

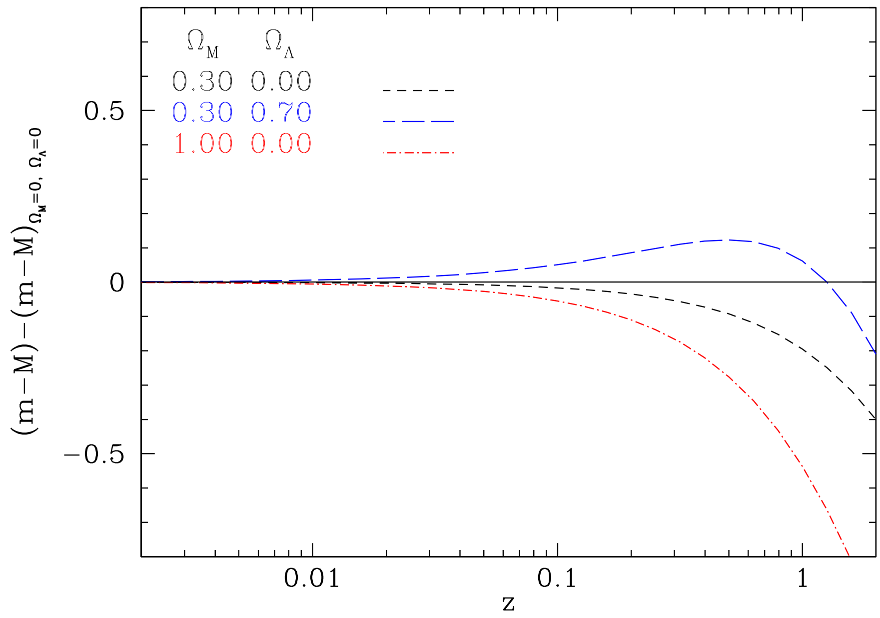

Figure 1.8: Residual of the distances relative to a $\Omega_M = \Omega_\Lambda = 0$ Universe.

Both the Hubble constant and the cosmological parameters can be determined by means of observations of type Ia SNe, at low or high redshift respectively (see Chapter 2 and Chapter 4). To be noticed that, since the determination of the cosmological parameters is based on relative measurements, it does not depend on the particular Hubble constant value used to calibrate Type Ia SNe. The cosmological implications mentioned are based on the assumption of the reliability of the Type Ia SNe as standard candle. But the luminosity of nearby supernovae varies by up to a factor of ten, and it is only by means of empirical relations between luminosity and distance-independent properties, like the the light curve shape, as discussed in §2.1, that supernovae can be turned into good distance indicators. For these reasons it is important not only to look further and further in the Universe but also to collect more and better SN data over a wider redshift range, starting from the local Universe, as aimed by the SN Ia European Research Training Network[1], and passing through intermediate redshift studies.

1.4 SNe & Star Formation Rate

During the history of the Universe, galaxies have evolved, forming stars. As a result, the present Universe is filled with a large number of stars and a significant amount of radiative energy originating from such stars. Tracing the star formation activity over the history in the universe is fundamental to understand its present properties. To quantify the star formation activity, star formation rate (SFR), defined as the stellar mass formed per unit time, is often estimated. The star formation rate depends on the amount of gas converted in stars:

$$\psi(t) = -\frac{df_{gas}}{dt} \tag{1.18}$$

The Schmidt (1959) law assumes that the rate of star formation varies with a power of the density of interstellar gas,

$$\psi(t) = \psi_0 f_{gas}^n [M_\odot/yr] \tag{1.19}$$

with $1 \leq n \leq 2$. Assuming $n = 1$ and a closed-box model (constant total mass) with instantaneous recycling of the gas ejected by the stellar remnants, the Schmidt's law leads to the analytic approximation

$$\psi(t) \propto e^{-\frac{t}{\tau}} \tag{1.20}$$

where $\tau = \psi_0^{-1}$ is a characteristic time-scale of the star formation process.

The SFR can be traced by young (age $\leq 10^7 - 10^8$ years) stars. Since short-lived massive stars are certain to be produced most recently, the SFR is traced with the luminosity of massive stars. One of the well known and commonly used tracer of massive stars is H_α luminosity (e.g., Kennicutt 1983), which originates from the gas ionized by massive-star radiation. Since massive stars are strong Ultra-Violet (UV) sources, UV luminosity is also used as an indicator of SFR. Both this SFR estimators are significantly affected by dust absorption. Another tracer which is widely used is the infrared (IR) emission (Kennicutt, 1998). Contrary to UV and H_α, dust IR luminosity traces the stellar radiation absorbed by dust. Young stars are often embedded in the dust and the absorption cross section of the dust is strongly peaked in the ultraviolet, so in principle the FIR emission can be a sensitive tracer of the young stellar population and hence of the SFR.

[1]http://www.mpa-garching.mpg.de/~rtn/

The history of the cosmic SFR in the Universe has been inferred thanks to the results of ground-based spectroscopic redshift surveys out to $z \sim 1$ and the results of deep photometric surveys like the Hubble Deep Field (HDF). The resulting star formation history has been summarized in the so-called "Madau-plot" (Madau et al., 1998b), which shows a rapid increase up to $z \sim 1$ and then a decrease at higher z, with a peak at $z \sim 1.5 - 2$.

An independent way to constrain the cosmic SFR is to use Supernova Rate measurements (Sadat et al., 1998; Madau et al., 1998a). More specifically, the study of type Ia SNe can allow us to probe the past history of star formation rate, whereas Core Collapse SNe directly probe the instantaneous star formation rate.
If we define $\psi(t)$ the star formation rate per unit volume, $\phi(m)$ a Salpeter (1955) universal initial mass function (IMF) with lower and upper mass cut-off of 0.1 and 125 $M_\odot$ ($\phi \propto m^{-2.35}$), the Core Collapse SN rate and the star formation rate are related by the expression (Madau et al., 1998b):

$$SNR_{CC}(t) = \psi(t) \frac{\int_8^{125} dm\phi(m)}{\int_{0.1}^{125} dmm\phi(m)} \tag{1.21}$$

The results depend on the IMF adopted. Kroupa and Weidner (2003), Kroupa (2003), Weidner and Kroupa (2003), found that the SN rates deduced from the Salpeter IMF would not be correct.
While in CCSNe the clock for the explosion is set by the lifetime of the massive progenitor, for type Ia SNe the time scale is given in the SD model by the time necessary to the companion to evolve and fill its Roche lobe and in the DD model by the time necessary to shorten the separation between the two WD as a result of gravitational wave radiation. This time interval is of course summed to the time necessary to a star to evolve to a WD. Type Ia SN rate can be parametrized in terms of a characteristic explosion time-scale τ, which defines an explosion probability per WD assumed to be independent of time, and an explosion efficiency η. τ accounts for the time it takes in the various models to go from a newly born (primary) WD to a SN explosion itself; η simply accounts for the fraction of stars in binary systems that will never undergo to a SN Ia explosion. Star with initial mass lower than 3 $M_\odot$ or higher than 8 $M_\odot$ are supposed not to explode or to generate a Core Collapse SN (Madau et al., 1998a). Under this assumptions, the rate of Type Ia SNe at any time will be given by:

$$SNR_{Ia}(t) = \frac{\eta \int_0^t \psi(t')dt' \int_{m_c}^{m_{max}} exp\left(-\frac{t-t'-t_m}{\tau}\right) \phi(m)dm}{\tau \int \phi(m)dm} \tag{1.22}$$

where $m_c \equiv max[m_{min}, m(t')]$, $m(t') = (10Gyr/t')^{0.4}$ is the minimum mass of a star that reaches the WD phase at time t', and $t_m = 10Gyr/m^{2.5}$ is the standard lifetime of a star of mass m (all stellar masses are expressed in solar units). For a fixed initial mass m, the Type Ia explosion frequency peaks at an epoch that reflects an "effective" delay $\Delta T = \tau + t_m$ from stellar birth (Madau et al., 1998a). Fig.1.9 shows the predicted Type Ia and CCSN rest frame rates as function of redshift for different scenarios.

As discussed in detail in Chapter 5 SN rates for both Type Ia and Core collapse Supenovae have been estimated, so far, only for the local Universe. At higher redshift only SN Ia rates are available. This is the main motivation of the SN search described in Chapter 3.

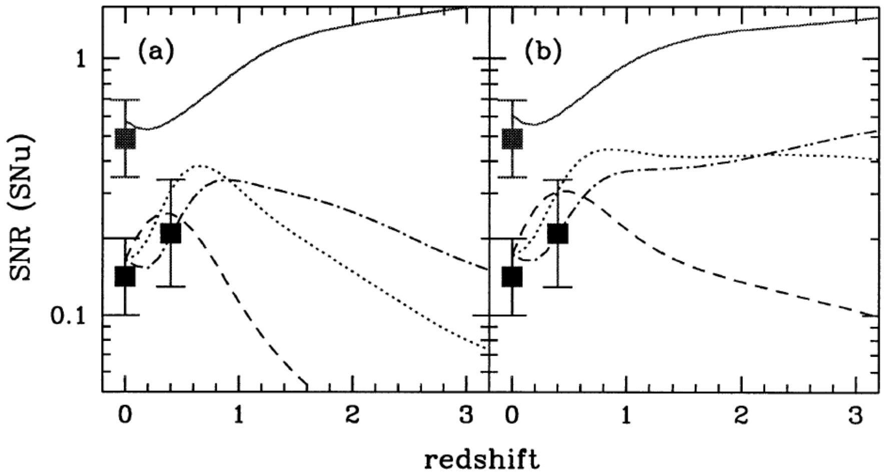

Figure 1.9: Predicted Type Ia and Core Collapse rest frame frequencies as a function of redshift ($H_0 = 50\,\mathrm{km\,s^{-1}Mpc^{-1}}$). Solid line: CCSN rate; dashed-dotted line: Type Ia rate with $\tau = 0.3$ Gyr; dotted line: Type Ia rate with $\tau = 1$ Gyr; dashed line: Type Ia rate with $\tau = 3$ Gyr. Data points have been derived from the measurements of Cappellaro et al. (1997a), Tammann et al. (1994), Evans et al. (1989), Pain et al. (1996). (a) model predictions for the galaxy "merging" scenario,; (b) same for the galaxy "monolithic collapse" scenario. Figure from Madau et al. (1998a)

Chapter 2

SNe Ia as standard candles

To see a world in a grain of sand,
and heaven in a wild flower:
hold infinity in the palm of your hand,
and eternity in an hour.
Blake, *Auguries of Innocence*

Contrary to early claims, the absolute magnitude of SNe Ia at maximum (M_{max}) is not constant, but it ranges over 2–2.5 mag. However a correlation between M_{max} and the shape of the light curve has been suggested which allows to recover SNe Ia as accurate distance indicators. This was first suggested almost thirty years ago (Barbon et al., 1973; Rust, 1974; Pskovskii, 1977), but remained debated until a few years ago (Sandage and Tammann, 1993) because of the large photometric errors of photographic photometry and the contamination of the early sample from other SN types (SNe Ib/c in particular). Eventually, the improved accuracy obtained with CCD photometry definitively proved that M_{max} is brighter in SNe Ia with a slower luminosity decline.By means of 9 well-observed SNe Ia (see Fig.2.1, left panel) Phillips (1993) found that the absolute magnitudes at maximum and decline rate, measured through the B magnitude difference Δm_{15} between the maximum and fifteen days later, were related by the following equations:

$$M_B max = -21.726(\pm 0.498) + 2.698(\pm 0.359)\Delta m_{15}(B)$$

$$M_V max = -20.883(\pm 0.417) + 1.949(\pm 0.292)\Delta m_{15}(B)$$

$$M_I max = -19.591(\pm 0.415) + 1.076(\pm 0.273)\Delta m_{15}(B)$$

These correlations have been confirmed by following studies (Fig. 2.1) but the original coefficients have been revised in the course of the years (Hamuy et al. 1996a, Phillips et al. 1999, see Table 2.1, Table 2.2) and, as described in §2.1.1, other empirical correlations have been proposed. It is still debated what may be the most convenient parameter(s) to describe the light curve shape and discriminate between intrinsically brighter and fainter SNe and, more important, what is the correct absolute calibration.

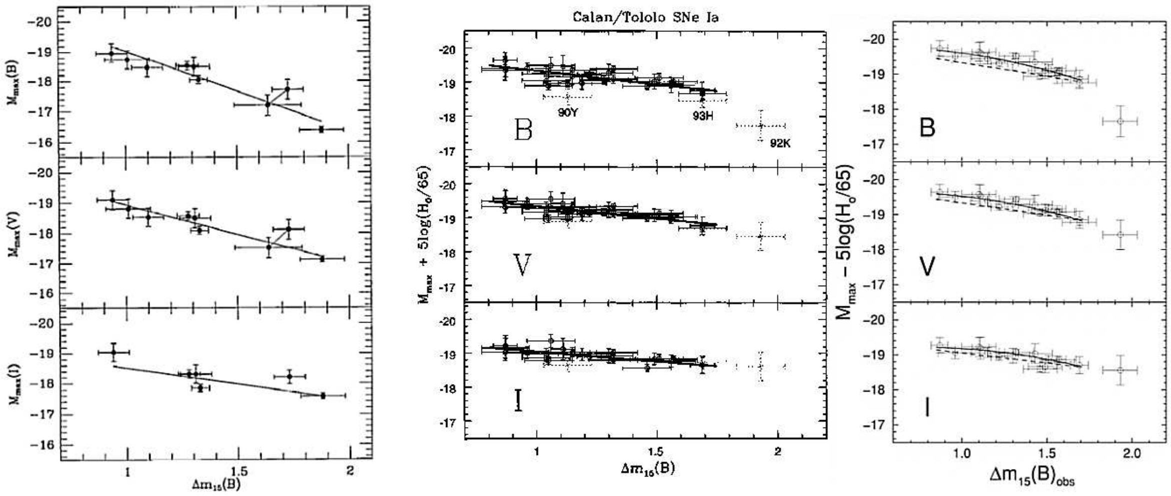

Figure 2.1: Decline rate-peak luminosity relation. Left: Phillips (1993). Center: Hamuy et al. (1996a). Right: Phillips et al. (1999).

Band	a	b	$\sigma(mag)$	n
B	-19.258(0.048)	0.784(0.182)	0.17	26
	-19.256(0.053)	0.860(0.210)	0.20	18
V	-19.267(0.042)	0.707(0.150)	0.14	26
	-19.254(0.046)	0.743(0.173)	0.15	18
I	-18.993(0.044)	0.575(0.178)	0.13	22
	-18.975(0.049)	0.654(0.231)	0.13	14

Table 2.1: $M_{MAX} = a + b[\Delta m_{15}(B) - 1.1]$. Data from Hamuy et al. (1996a).

Band	a	b	$\sigma(mag)$	n
B	0.786(0.398)	0.633(0.742)	0.11	17
V	0.672(0.396)	0.633(0.742)	0.09	17
I	0.422(0.400)	0.633(0.742)	0.13	15

Table 2.2: $\Delta M_{MAX} = a[\Delta m_{15}(B) - 1.1] + b[\Delta m_{15}(B) - 1.1]^2$. Data from Phillips et al. (1999)

The purpose of the work described in this section is to investigate how a new calibration of the Cepheids absolute magnitude, discussed in §2.1.4, propagate through the calibration of SNe Ia on the determination of H_0. In this work we do not rely on published values of SN light curve parameters (in particular maximum magnitudes and decline rates), but we made our own independent estimates. To this aim we exploited the archive of SN Ia light curves which has been collected at the Padova Observatory. Besides all relevant data published in the literature (with a major contribution given by Hamuy et al. 1996c and Riess et al. 1999b), the archive includes also the results of a long standing effort for supernova monitoring at ESO and Asiago Observatories (Turatto, 2000), to which I gave my own contribution with observations and data reduction. The new, unpublished data are reported in Appendix A. After rejecting objects with incomplete photometric coverage we retained a sample of 78 SNe Ia (see Tab. 2.3, Tab. 2.4).

2.1 SNe Ia calibration

Three main issues need to be addressed for a proper calibration of SNe Ia, namely the direct calibration of individual events through primary distance indicators, the determination of the relation between light curve shape and absolute magnitude and the estimate of extinction, in particular that originating the host galaxy dust. The scenario is complicated by the fact that these three items have a deep interplay. This means that it is not easy to predict how the effect of a new finding on one ingredient propagates to the final result. Different assumptions in the calibration chain may explain why different authors, using the same data, obtain different results (Leibundgut, 2000).

Theoretical calculations curves have shown that the absolute magnitude at maximum is proportional to the amount of ^{56}Ni synthesized (Höeflich et al., 1996; Cappellaro et al., 1997a). However it is not yet known how this relates with the progenitor scenarios and explosion mechanism. In particular, a growing number of “outliers” seems to indicate that a one-parameter description of the SNe Ia light curve is not sufficient (for an analysis of the Type Ia luminosity dependence on second parameters see Parodi et al. 2000). In addition, recent observations show an increasing number of “disturbing” objects which merge characteristics of normal, sub-luminous and super-luminous SNe, like SN 2000cx or SN 2002cx. The first one is characterized by a slow decline but a relatively fast pre-maximum brightening, similar to that of the normal SN 1994D. Nevertheless the absolute magnitude at maximum is consistent with a sub-luminous SNe (Candia et al., 2003); besides the $B-V$ colour shows an unusual evolution, bluer than the colour curve of unextinguished normal SNe at late times (Candia et al., 2003); the second one is characterized by a 1991T-like pre-maximum spectrum and a 1991bg-like luminosity, a normal $B-V$ colour evolution, very low expansion velocities and many other peculiarities (Li et al., 2003a).
It should be kept in mind that the correlation between the light curve shape and the absolute magnitude at maximum, is not a universal law. Not only it has an intrinsic dispersion but in addition there are really “anomalous” SNe. However, with this caveat, the luminosity-width relation represents a powerful tool for calibrating type Ia SNe.

2.1.1 Light curve shape

Several different approaches are currently in use to characterize the luminosity evolution of different SN Ia. In principle the Multi-colour Light Curve Shape (MLCS) method of

Table 2.3: (1) the SN name; (2) the apparent B magnitude at maximum; (3) the stretch factor (s^{-1}) and (4) the $\Delta m_{15}(B)_{obs}$ measured as explained in §2.1.1, not corrected for colour excess; (5) the galactic colour excess $E(B-V)_{gal}$ from Schlegel et al. (1998); (6) the colour excess at the blue maximum of the SN light curve: $E(B-V)_{max}$; (7) the colour excess measured in the tail of the SN light curve: $E(B-V)_{tail}$; (8) the weighted mean of $E(B-V)_{max}$ and $E(B-V)_{tail}$: $E(B-V)_{host}$. $E(B-V)_{host}$=$E(B-V)_{tail}$ when $E(B-V)_{max}$ it is not available; (9) distance modulus μ from the Nearby Galaxies Catalogue (Tully and Fisher, 1988); (10) the recession velocity v_{3k} with respect to the microwave background from the NASA/IPAC Extragalactic Database (NED). Continues in the following three tables.

SN (1)	m(B) (2)	s^{-1} (3)	$\Delta m_{15}(B_{obs})$ (4)	$E(B-V)_{gal}$ (5)	$E(B-V)_{max}$ (6)	$E(B-V)_{tail}$ (7)	$E(B-V)_{host}$ (8)	μ_{tully} (9)	v_{3k} (10)
1937C	8.94(0.30)	-	0.85(0.10)	0.014	0.08(0.20)	0.06(0.05)	0.06(0.05)	28.22	543
1972E	8.40(0.04)	0.96(0.06)	1.05(0.05)	0.056	-0.04(0.10)	0.03(0.05)	0.01(0.05)	27.53	671
1972J	14.80(0.20)	1.22(0.09)	1.45(0.20)	0.046	-0.05(0.11)	0.00(0.20)	0.00(0.05)	-	2865
1974G	12.34(0.04)	1.14(0.08)	1.40(0.04)	0.019	0.25(0.20)	0.25(0.20)	0.25(0.05)	29.93	992
1980N	12.49(0.04)	1.06(0.07)	1.30(0.05)	0.021	0.05(0.06)	0.12(0.05)	0.09(0.05)	31.14	1678
1981B	12.04(0.04)	1.10(0.07)	1.13(0.05)	0.018	0.12(0.06)	0.10(0.14)	0.11(0.05)	-	2141
1982B	13.65(0.20)	-	0.94(0.10)	0.064	-	0.14(0.14)	0.14(0.14)	32.68	2203
1983G	13.00(0.10)	1.18(0.08)	1.30(0.20)	0.034	0.19(0.11)	0.42(0.05)	0.35(0.16)	30.89	1566
1986G	12.48(0.04)	1.37(0.11)	1.69(0.05)	0.115	0.95(0.08)	0.67(0.05)	0.78(0.20)	28.45	806
1989B	12.38(0.12)	1.04(0.07)	1.28(0.05)	0.032	0.41(0.06)	0.46(0.14)	0.42(0.05)	29.10	1067
1990N	12.75(0.04)	1.04(0.07)	1.05(0.05)	0.026	0.09(0.06)	0.18(0.05)	0.14(0.06)	31.13	1322
1990O	16.59(0.04)	0.91(0.08)	0.94(0.05)	0.093	0.05(0.10)	0.10(0.05)	0.08(0.05)	-	9175
1990T	17.27(0.20)	-	1.13(0.20)	0.053	0.08(0.30)	0.16(0.05)	0.15(0.06)	-	11893
1990Y	17.69(0.20)	-	1.13(0.20)	0.008	0.26(0.30)	0.34(0.10)	0.32(0.05)	-	11652
1991S	17.78(0.05)	-	1.00(0.10)	0.026	0.06(0.30)	0.13(0.10)	0.11(0.05)	-	16807
1991T	11.69(0.04)	0.93(0.05)	0.94(0.05)	0.022	0.21(0.06)	0.19(0.04)	0.20(0.05)	30.65	2070
1991U	16.67(0.10)	-	1.11(0.10)	0.062	0.07(0.30)	0.15(0.20)	0.12(0.05)	-	9724
1991ag	14.67(0.04)	0.89(0.02)	0.87(0.05)	0.062	0.06(0.30)	0.08(0.05)	0.08(0.05)	-	4521
1991bg	14.75(0.04)	1.47(0.22)	1.94(0.05)	0.041	-0.00(0.07)	0.00(0.09)	0.00(0.05)	31.13	1282

Tab. 2.3 continues...

SN (1)	m(B) (2)	s^{-1} (3)	$\Delta m_{15}(B_{obs})$ (4)	$E(B-V)_{gal}$ (5)	$E(B-V)_{max}$ (6)	$E(B-V)_{tail}$ (7)	$E(B-V)_{host}$ (8)	μ_{tully} (9)	v_{3k} (10)
1992A	12.56(0.04)	1.25(0.09)	1.47(0.05)	0.018	0.05(0.07)	0.02(0.05)	0.04(0.05)	31.14	1737
1992J	17.88(0.20)	-	1.69(0.20)	0.057	-	0.10(0.08)	0.10(0.08)	-	13828
1992K	16.31(0.20)	-	1.94(0.20)	0.101	-	0.00(0.05)	0.00(0.05)	-	3324
1992P	16.14(0.20)	1.00(0.03)	1.05(0.30)	0.021	0.05(0.06)	0.12(0.05)	0.09(0.05)	-	7939
1992ae	18.62(0.04)	-	1.30(0.10)	0.036	0.12(0.11)	0.05(0.10)	0.09(0.05)	-	22442
1992ag	16.64(0.20)	1.07(0.07)	1.20(0.20)	0.097	0.15(0.06)	0.45(0.20)	0.22(0.21)	-	8095
1992al	14.59(0.04)	1.00(0.03)	1.09(0.05)	0.034	-0.01(0.06)	0.07(0.04)	0.04(0.05)	-	4214
1992aq	19.42(0.10)	-	1.69(0.05)	0.012	0.05(0.31)	0.00(0.20)	0.02(0.05)	-	30014
1992au	18.17(0.20)	-	1.69(0.30)	0.017	-	0.00(0.30)	0.00(0.30)	-	18225
1992bc	15.13(0.04)	0.93(0.05)	0.90(0.05)	0.022	0.01(0.06)	-0.03(0.05)	0.00(0.05)	-	5876
1992bg	17.39(0.04)	1.00(0.03)	1.15(0.05)	0.185	-0.04(0.20)	0.04(0.05)	0.02(0.06)	-	10936
1992bh	17.68(0.04)	0.98(0.03)	1.13(0.05)	0.022	0.10(0.10)	0.13(0.10)	0.12(0.05)	-	13519
1992bk	18.07(0.04)	-	1.67(0.05)	0.015	0.04(0.21)	-0.01(0.10)	0.01(0.05)	-	17551
1992bl	17.34(0.04)	1.23(0.05)	1.56(0.05)	0.011	-0.02(0.11)	0.04(0.05)	0.02(0.05)	-	12661
1992bo	15.86(0.04)	1.33(0.11)	1.69(0.05)	0.027	-0.02(0.08)	-0.01(0.12)	0.00(0.05)	-	5164
1992bp	18.53(0.04)	1.12(0.04)	1.52(0.20)	0.069	-0.02(0.11)	0.00(0.20)	0.00(0.05)	-	23557
1992bs	18.33(0.04)	1.01(0.03)	1.15(0.05)	0.011	0.06(0.10)	0.05(0.10)	0.05(0.05)	-	18787
1993B	18.71(0.06)	0.99(0.03)	1.30(0.05)	0.079	-0.02(0.20)	0.24(0.10)	0.15(0.18)	-	21011
1993H	16.99(0.04)	1.18(0.04)	1.69(0.10)	0.060	0.16(0.08)	0.06(0.05)	0.10(0.07)	-	7523
1993L	13.40(0.20)	-	1.47(0.30)	0.014	0.31(0.21)	0.32(0.11)	0.32(0.05)	-	1387
1993O	17.79(0.04)	1.05(0.07)	1.26(0.05)	0.053	-0.07(0.06)	0.04(0.08)	0.00(0.08)	-	15867
1993ac	18.45(0.20)	-	1.25(0.20)	0.163	-	0.04(0.10)	0.04(0.10)	-	14674
1993ae	15.44(0.20)	-	1.47(0.20)	0.038	-0.01(0.30)	0.00(0.05)	0.00(0.05)	-	5405
1993ag	18.30(0.04)	1.06(0.03)	1.30(0.20)	0.112	0.15(0.06)	0.10(0.10)	0.13(0.05)	-	15031

Tab. 2.3 continues...

SN (1)	m(B) (2)	s^{-1} (3)	$\Delta m_{15}(B_{obs})$ (4)	$E(B-V)_{gal}$ (5)	$E(B-V)_{max}$ (6)	$E(B-V)_{tail}$ (7)	$E(B-V)_{host}$ (8)	μ_{tully} (9)	v_{3k} (10)
1993ah	16.32(0.04)	1.19(0.14)	1.45(0.10)	0.020	-	0.15(0.10)	0.15(0.10)	-	8604
1994D	11.86(0.04)	1.27(0.10)	1.31(0.05)	0.022	-0.02(0.06)	0.05(0.08)	0.01(0.05)	31.13	793
1994M	16.35(0.06)	1.18(0.04)	1.45(0.20)	0.023	0.12(0.11)	0.18(0.05)	0.16(0.05)	-	7289
1994Q	16.44(0.10)	-	0.90(0.10)	0.017	-	0.11(0.06)	0.11(0.06)	-	8954
1994T	17.23(0.10)	-	1.45(0.05)	0.029	0.06(0.30)	0.07(0.20)	0.07(0.05)	-	10708
1994ae	13.15(0.06)	1.04(0.07)	0.87(0.10)	0.030	0.17(0.06)	0.16(0.09)	0.16(0.05)	31.85	1609
1995D	13.44(0.04)	0.99(0.06)	1.03(0.05)	0.058	0.07(0.06)	0.13(0.07)	0.10(0.05)	32.43	2289
1995E	16.82(0.04)	0.96(0.03)	1.19(0.05)	0.027	0.77(0.06)	0.72(0.14)	0.76(0.05)	-	3510
1995ac	17.21(0.04)	0.96(0.06)	0.95(0.05)	0.042	0.06(0.06)	-0.01(0.05)	0.02(0.05)	-	14635
1995ak	16.09(0.10)	1.11(0.07)	1.45(0.10)	0.038	-0.04(0.11)	0.28(0.06)	0.16(0.23)	-	6589
1995al	13.36(0.04)	0.93(0.03)	0.89(0.05)	0.014	0.21(0.06)	0.19(0.05)	0.20(0.05)	32.00	1797
1995bd	17.27(0.04)	0.93(0.05)	0.88(0.05)	0.498	0.37(0.06)	0.20(0.05)	0.28(0.12)	-	4326
1996C	16.59(0.08)	0.87(0.02)	0.94(0.10)	0.013	0.11(0.20)	0.07(0.05)	0.08(0.05)	-	8245
1996X	13.26(0.04)	1.09(0.07)	1.32(0.05)	0.069	-0.00(0.06)	0.07(0.07)	0.03(0.05)	32.29	2325
1996ai	16.96(0.20)	0.83(0.02)	0.85(0.08)	0.014	1.76(0.06)	2.07(0.10)	1.88(0.22)	31.64	1177
1996bk	14.84(0.20)	-	1.69(0.20)	0.018	0.38(0.21)	0.33(0.13)	0.35(0.05)	32.55	2147
1996bl	17.08(0.04)	0.99(0.03)	1.11(0.05)	0.092	0.05(0.06)	0.13(0.07)	0.09(0.05)	-	10447
1996bo	16.15(0.04)	1.06(0.07)	1.30(0.05)	0.077	0.35(0.06)	0.30(0.10)	0.33(0.05)	-	4898
1996bv	15.77(0.04)	-	0.84(0.10)	0.105	0.23(0.20)	0.23(0.10)	0.23(0.05)	-	5016
1997bp	14.10(0.20)	0.95(0.09)	0.94(0.20)	0.044	0.09(0.20)	0.45(0.20)	0.27(0.26)	-	2824
1997br	14.06(0.04)	1.04(0.07)	1.04(0.05)	0.113	0.31(0.20)	0.33(0.04)	0.33(0.05)	-	2399
1998bu	12.20(0.04)	1.00(0.06)	1.15(0.05)	0.025	0.39(0.06)	0.36(0.05)	0.37(0.05)	29.54	1238
1998de	17.56(0.02)	1.45(0.13)	1.94(0.05)	0.059	-0.08(0.07)	0.00(0.10)	0.00(0.05)	-	4713
1999aa	14.93(0.05)	0.85(0.07)	0.85(0.05)	0.040	0.11(0.06)	0.07(0.05)	0.09(0.05)	-	4564
1999aw	16.86(0.05)	0.74(0.05)	0.81(0.05)	0.032	0.10(0.09)	0.00(0.10)	0.05(0.07)	-	11362
1999da	16.90(0.10)	-	1.94(0.20)	0.058	-	0.05(0.20)	0.05(0.20)	-	3644

Tab. 2.3

SN (1)	m(B) (2)	s^{-1} (3)	$\Delta m_{15}(B_{obs})$ (4)	$E(B-V)_{gal}$ (5)	$E(B-V)_{max}$ (6)	$E(B-V)_{tail}$ (7)	$E(B-V)_{host}$ (8)	μ_{tully} (9)	v_{3k} (10)
1999dk	15.04(0.05)	0.92(0.08)	1.28(0.10)	0.054	0.13(0.06)	0.17(0.21)	0.14(0.05)	-	4184
1999ee	14.94(0.02)	0.86(0.04)	0.92(0.05)	0.020	0.36(0.06)	0.39(0.06)	0.38(0.05)	-	3153
1999gp	16.25(0.05)	0.83(0.07)	0.94(0.10)	0.056	0.15(0.06)	0.11(0.09)	0.14(0.05)	-	7811
2000E	14.31(0.05)	0.85(0.07)	0.94(0.05)	0.366	0.21(0.10)	0.30(0.10)	0.25(0.07)	31.91	1280
2000bk	16.98(0.10)	1.32(0.17)	1.69(0.10)	0.025	-	0.19(0.05)	0.19(0.05)	-	7976
2000ce	17.24(0.10)	0.86(0.07)	0.94(0.10)	0.057	-	0.65(0.14)	0.65(0.14)	-	4948
2000cx	13.44(0.05)	0.94(0.09)	0.93(0.05)	0.083	0.19(0.06)	-0.20(0.05)	0.00(0.28)	32.53	2115
2001el	12.81(0.02)	1.02(0.06)	1.15(0.05)	0.014	0.13(0.06)	0.33(0.05)	0.24(0.14)	30.55	1091
2002bo	14.01(0.10)	1.02(0.06)	1.17(0.05)	0.025	0.48(0.06)	0.47(0.05)	0.47(0.05)	31.76	1641

Table 2.4: SN data references. Continues...

SN	References
1937C	B.E. Schaefer, 1994, ApJ, 426, 493
	M.J. Pierce & G.H. Jacoby, 1995, AJ, 110, 2885
1972E	A. Ardeberg & M. de Groot, 1973, A&A, 28, 295
	A.M. van Genderen, 1975, A&A, 45, 429
	T.A. Lee et al., 1972, ApJ, 177, L59
	A.W.J. Cousins 1972, IBVS, 700, 1
1972J	F. Ciatti & L. Rosino, 1977, A&A 57, 73 *
	* revised in F. Patat et al. 1997 A&A, 317, 423
1974G	F. Ciatti & L. Rosino, 1977, A&A 57, 73
	B. Patchett & R. Wood, 1976, MNRAS, 175, 595
	I.D. Howarth, 1974, Mitt. Veränderl Sterne, 6, 155
1980N	M. Hamuy et al., 1991, AJ, 102, 208
	P.F. Younger & S. van den Bergh, 1985, A&AS, 61, 365
1981B	R. Barbon; F. Ciatti; L. Rosino, 1982, A&A, 116, 35 *
	* revised in F. Patat et al. 1997 A&A, 317, 423
	R.J. Buta & A. Turner, 1983, PASP, 95, 72
	D.Y. Tsvetkov, 1982, SA, 8, 115
	IAUC 3584
1982B	D.Y. Tsvetkov, 1986, PZ, 22, 279
	F. Ciatti et al., 1988, A&A, 202, 15
	R. Cadanau & C., Trefzger, 1983, IBVS, 2382, 1
1983G	W. E. Harris et al., 1983, PASP, 95, 607
	R.J. Buta et al., 1985, PASP, 97, 229
	S. Benetti et al., 1991, A&A, 247, 410
	D.Y. Tsvetkov, 1985, SA, 29, 211
1986G	M.M. Phillips et al., 1987, PASP, 99, 592
	S. Cristiani et al., 1992, A&A, 259, 63
	B.E. Schaefer 1987, ApJ, 323, 47
1989B	R. Barbon et al., 1990, A&A, 237, 79
	L.A. Wells et al., 1994, AJ, 108, 2233
1990N	P. Lira et al., 1998, AJ, 115, 234
1990O	M. Hamuy et al., 1996, AJ, 112, 2408
1990T	M. Hamuy et al., 1996, AJ, 112, 2408
1990Y	M. Hamuy et al., 1996, AJ, 112, 2408
1991S	M. Hamuy et al., 1996, AJ, 112, 2408
	ESO-Asiago SN Archive
1991T	P. Lira et al., 1998, AJ, 115, 234
	E. Cappellaro et al., 1997, A&A, 328, 203
	B.P. Schmidt et al., 1994, ApJ, 434, 19
	IAUC 5246, 5253, 5256, 5270, 5273, 5309
	W.B. Sparks et al., 1999, ApJ, 523, 585
1991U	M. Hamuy et al., 1996, AJ, 112, 2408
1991ag	M. Hamuy et al., 1996, AJ, 112, 2408

Tab. 2.4 continues...

SN	References
1991bg	B. Leibundgut et al., 1993, AJ, 105, 301
	A.V. Filippenko et al., 1992, AJ, 104, 1543
	M. Turatto et al., 1996, MNRAS, 283, 1
1992A	N.B Suntzeff, 1996, in McCray Z. Wang (eds.), Supernovae and Supernova Remnants, p.41, Cambridge Univ. Press, Cambridge
	E. Cappellaro et al., 1997, A&A, 328, 203
1992J	M. Hamuy et al., 1996, AJ, 112, 2408
1992K	ESO-Asiago SN Archive
	M. Hamuy et al., 1996, AJ, 112, 2408
1992P	M. Hamuy et al., 1996, AJ, 112, 2408
1992ae	M. Hamuy et al., 1996, AJ, 112, 2408
1992ag	M. Hamuy et al., 1996, AJ, 112, 2408
1992al	M. Hamuy et al., 1996, AJ, 112, 2408
1992aq	M. Hamuy et al., 1996, AJ, 112, 2408
1992au	M. Hamuy et al., 1996, AJ, 112, 2408
1992bc	M. Hamuy et al., 1996, AJ, 112, 2408
1992bg	M. Hamuy et al., 1996, AJ, 112, 2408
1992bh	M. Hamuy et al., 1996, AJ, 112, 2408
1992bk	M. Hamuy et al., 1996, AJ, 112, 2408
1992bl	M. Hamuy et al., 1996, AJ, 112, 2408
1992bo	M. Hamuy et al., 1996, AJ, 112, 2408
1992bp	M. Hamuy et al., 1996, AJ, 112, 2408
1992bs	M. Hamuy et al., 1996, AJ, 112, 2408
1993B	M. Hamuy et al., 1996, AJ, 112, 2408
1993H	M. Hamuy et al., 1996, AJ, 112, 2408
	IAUC 5723
	ESO-Asiago SN Archive
1993L	IAUC 5780, 5781
	E. Cappellaro et al., 1997, A&A, 328, 203
1993O	M. Hamuy et al., 1996, AJ, 112, 2408
1993ac	A.G. Riess et al., 1999, AJ, 117, 707
1993ae	A.G. Riess et al., 1999, AJ, 117, 707
	W.C.G. Ho et al., 2001, PASP, 113, 1349
1993ag	M. Hamuy et al., 1996, AJ, 112, 2408
1993ah	M. Hamuy et al., 1996, AJ, 112, 2408
1994D	F. Patat et al., 1996, MNRAS, 278, 111
	E. Cappellaro et al., 1997, A&A, 328, 203
	S. D. Van Dyk et al., 1999, AJ, 118, 2331
	M.W. Richmond et al., 1995, AJ 109, 2121
	W.P.S. Meikle et al., 1996, MNRAS, 281, 263
	D.Y. Tsvetkov & N.N. Pavlyuk, 1995, AstL, 21, 606
	H. Wu, H.J. Yan, Z.L. Zou, 1995, A&A, 294, 9
	M.W. Richmond et al., 1995, AJ, 109, 2121

Tab. 2.4 continues...

SN	References
1994M	A.G. Riess et al., 1999, AJ, 117, 707
	W.C.G. Ho et al., 2001, PASP, 113, 1349
	ESO-Asiago SN Archive
1994Q	A.G. Riess et al., 1999, AJ, 117, 707
	W.C.G. Ho et al., 2001, PASP, 113, 1349
1994T	A.G. Riess et al., 1999, AJ, 117, 707
1994ae	IAUC 6105,6111
	A.G. Riess et al., 1999, AJ, 117, 707
	ESO-Asiago SN Archive
	W.C.G. Ho et al., 2001, PASP, 113, 1349
	D.Y. Tsvetkov et al., 1997, AstL, 23, 26
1995D	IAUC 6134,6149,6156,6166
	K. Sadakane et al., 1996, PASJ, 48, 51
	ESO-Asiago SN Archive
	A.G. Riess et al., 1999, AJ, 117, 707
1995E	A.G. Riess et al., 1999, AJ, 117, 707
1995ac	A.G. Riess et al., 1999, AJ, 117, 707
	ESO-Asiago SN Archive
1995ak	A.G. Riess et al., 1999, AJ, 117, 707
1995al	IAUC 6255,6256
	A.G. Riess et al., 1999, AJ, 117, 707
	D. Yu. Tsevtkov et al. 2001 Astr. Rep. 45, 527
1995bd	A.G. Riess et al., 1999, AJ, 117, 707
	ESO-Asiago SN Archive
1996C	A.G. Riess et al., 1999, AJ, 117, 707
1996X	IAUC 6380,6381
	M.E. Salvo et al. 2001, MNRAS 321, 254
	A.G. Riess et al., 1999, AJ, 117, 707
1996ai	A.G. Riess et al., 1999, AJ, 117, 707
1996bk	A.G. Riess et al., 1999, AJ, 117, 707
1996bl	A.G. Riess et al., 1999, AJ, 117, 707
1996bo	A.G. Riess et al., 1999, AJ, 117, 707
	D. Yu. Tsevtkov et al. 2001 Astr. Rep. 45, 527
	ESO-Asiago SN Archive
1996bv	A.G. Riess et al., 1999, AJ, 117, 707
1997bp	ESO-Asiago SN Archive
	A.G. Riess et al., 1998, ApJ, 504, 935
1997br	W.D. Li et al., 1999, AJ, 117, 2709
	ESO-Asiago SN Archive
1998bu	N.B. Suntzeff et al., 1999, AJ, 117, 1175
	S. Jha et al. 1999, ApJS, 125, 73
	E. Cappellaro et al., 2001, ApJ, 549, 215
	M. Hernandez et al., 2000, MNRAS, 319, 223

Tab. 2.4

SN	References
1998de	M. Modjaz et al., 2001, PASP, 113, 308
1999aa	ESO-Asiago SN Archive
	K. Krisciunas et al., 2000, ApJ, 539 ,658
1999aw	L.G. Strolger et al., 2002, AJ, 124, 2905
1999da	K. Krisciunas et al., 2001, AJ, 122, 1616
1999dk	K. Krisciunas et al., 2001, AJ, 122, 1616
	ESO-Asiago SN Archive
1999ee	M.D. Stritzinger et al., 2002, AJ, 124, 2100
1999gp	K. Krisciunas et al., 2001, AJ, 122, 1616
2000E	G. Valentini et al. astro-ph/0306391
	J. Vinkó et al., 2001, A&A, 372, 824
2000bk	K. Krisciunas et al., 2001, AJ, 122, 1616
2000ce	K. Krisciunas et al., 2001, AJ, 122, 1616
2000cx	P. Candia et al., 2003, PASP, 115, 277
	ESO-Asiago SN Archive
2001el	K. Krisciunas et al., 2003, AJ, 125, 166
2002bo	IAUC 7863
	S. Benetti et al., 2003, MNRAS accepted
	Gy.M. Szabo et al., astro-ph/0306606

Riess et al. (1996a), which make use of the entire early light curve (from discovery to 80-100 days) in different colours, is expected to be the most robust from a statistically point of view. This method has also the great advantage of giving at the same time the absolute calibration and the extinction. However the MLCS method heavily relies on the accurate calibration of a few template light curves especially for what concerns the extinction correction. This explains the difference in the template colour curves in Riess et al. 1996a and Riess et al. 1998 (see also Salvo et al. 2001).
Very recently Wang et al. (2003) introduced a new method called the Colour-Magnitude Intercept Calibration (CMAGIC) which makes use of multi-colour post-maximum light curves. It is based on the empirical linear relation found between the B magnitude and the B-V (or B-R or B-I) colour during the first month past maximum. A complete analysis of this method, discussing also the B-R and B-I colours will be presented by the same authors in a later paper.
Two straightforward measurements of the luminosity evolution are the Δm_{15} (the magnitude decline between the maximum and fifteen days later) (Phillips, 1993), and the "stretch factor" s (Perlmutter et al., 1997), a coefficient used to expand or contract linearly the time-scale of a particular light curve in order to match a template.

To measure $\Delta m_{15}(B)$ and s for the SNe of our sample (Tab. 2.3, Tab. 2.4) we proceeded as follows:

1. B and V light curves of all SNe were corrected for the effect of redshift on the photo-

metry (K-correction) and of the temporal evolution (time dilatation). In particular for the former one we applied the K corrections given by Hamuy et al. (1993b);

2. among the SNe of our sample we selected 28 events for which the most complete temporal coverage was available. For each individual object we measured the epoch and magnitude of maximum and the $\Delta m_{15}(B)$. The SNe light curves were then grouped in seven bins of similar $\Delta m_{15}(B)$ (in order to have a good $\Delta m_{15}(B)$ sampling and enough statistics per bin). The individual observations were merged together to derive seven template light curves characterized by the average $\Delta m_{15}(B)$ (see Table 2.5). Due to the paucity of light curves with coverage during the rise phase, the light curve trend before maximum is quite uncertain. The template light curves are shown in Fig. 2.2 where it can be seen that with the increasing of $\Delta m_{15}(B)$ the light curve shape varies with continuity. That is, the magnitude differences which originates from the different early decline rates are more or less maintained after the inflection point when the light curve turn on a more gentle decline. The exception are the SNe with high early decline ($\Delta m_{15}(B) = 1.94$) that, because of an earlier occurrence of the inflection point, 1-2 months after maximum appear brighter (relatively to maximum) than other SNe Ia.

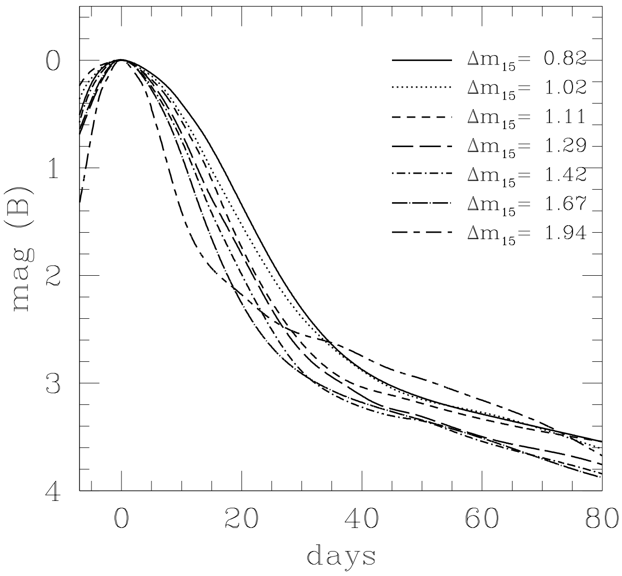

Figure 2.2: B band templates for seven different decline rates.

3. for SNe with incomplete temporal coverage we have selected, by means of a χ^2 test, the best matching template and attributed to the object the corresponding $\Delta m_{15}(B)$. For practical reasons, the section of the light curve which goes from maximum to the inflection point is that for which detailed monitoring for the largest sample of events is available. Therefore, in the light curve fit, we gave more weight to the points in this phase range. Eventually, the shifts in phase and magnitude adopted to get the best match were used to refine the initial guess for the epoch and magnitude at maximum.

To measure the stretch factor s, we have adopted as reference the template light curve with $\Delta m_{15}(B) = 1.11$, i.e. our template closer to the "standard light curve", arbitrary chosen to be characterized by $\Delta m_{15}(B) = 1.1$ (Perlmutter et al., 1997). In practice, for each SN the time scale of the light curve was compressed or expanded by a factor s, chosen to get the best χ^2 fit with the reference template light curve. Due to the uncertainties on the rising branch of the light curve templates and on the paucity of observations before maximum, the comparison has been performed mainly taking into account the light curve evolution from maximum to 80 days at most.

Following this procedure, we could measure $\Delta m_{15}(B)$ and s for 58 SNe Ia (columns 3 and 4 in Tab. 2.3). Fig. 2.3 shows that $\Delta m_{15}(B)$ and s^{-1} are indeed well correlated. We notice

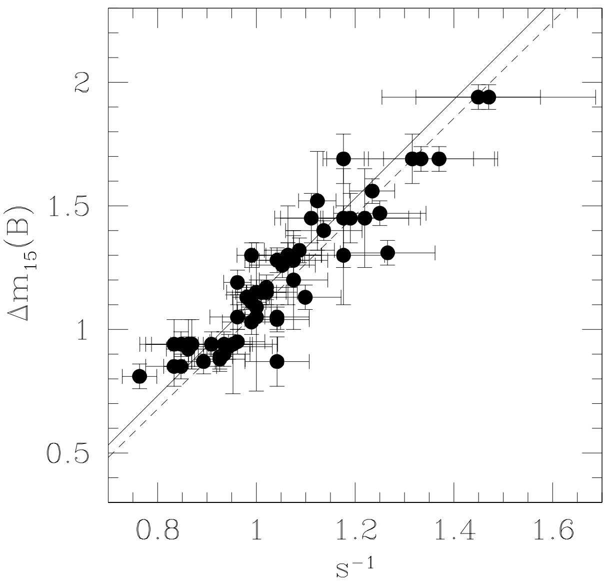

Figure 2.3: $\Delta m_{15}(B)$ versus stretch factor s for the 58 SNe of our sample whose stretch factor s has been measured. The inferred relation (solid line) is in good agreement with that obtained by Perlmutter et al. (1997) (dashed line).

that, as expected from Fig. 2.2, the stretched template light curve gives a very poor fit of the observed light curve for fast declining objects (like SN 1991bg), which can not be well fitted simultaneously in the early and late phases. This is the reason of the large error-bars for such objects. A least-squares fit accounting for the errors on both variables gives $\Delta m_{15}(B) = (1.98 \pm 0.16)(s^{-1} - 1) + (1.13 \pm 0.02)$; the slope of this relation is very close to that obtained by Perlmutter et al. (1997) ($\Delta m_{15}(B) = (1.96 \pm 0.17)(s^{-1} - 1) + 1.07$) from 18 low redshift SNe. The slightly different zero point reflects the different reference template used to measure the stretch factor. We note that the dispersion along the fitting line is consistent with the error estimates and, even in this large sample, there are no obvious outliers. Hence, the systematic differences in the SN magnitudes calibrated using either Δm_{15} or the stretch factor (Drell et al., 2000; Leibundgut, 2000) are not due to a misalignment of the different methods of measuring the light curve shapes and instead must originate in some other steps of the calibration chain. As we will see the reddening correction is a most critical issue.

Because of the good correlation between Δm_{15} and stretch factor and because Δm_{15} is available for a larger number of objects, for the SNe Ia calibration hereafter we will use the Δm_{15} light curve parameterization (see §2.1.3).

Table 2.5: Light curve templates for different decline rates. Continues...

Δm_{15}	0.82	1.02	1.11	1.29	1.42	1.67	1.94
phase				$m(B)$			
-7	0.510	0.361	0.238	0.689	0.578	0.641	1.322
-6	0.347	0.246	0.155	0.546	0.396	0.500	1.002
-5	0.217	0.168	0.098	0.405	0.264	0.363	0.683
-4	0.125	0.107	0.062	0.274	0.166	0.238	0.400
-3	0.064	0.057	0.038	0.161	0.090	0.134	0.229
-2	0.025	0.021	0.019	0.073	0.038	0.059	0.125
-1	0.005	0.002	0.005	0.019	0.008	0.015	0.028
0	0.000	0.000	0.000	0.000	0.000	0.000	0.000
1	0.008	0.015	0.011	0.010	0.014	0.014	0.036
2	0.027	0.041	0.042	0.040	0.048	0.053	0.106
3	0.054	0.073	0.085	0.084	0.101	0.114	0.186
4	0.087	0.107	0.132	0.140	0.168	0.191	0.296
5	0.124	0.148	0.181	0.207	0.246	0.280	0.465
6	0.166	0.199	0.236	0.285	0.331	0.377	0.647
7	0.213	0.262	0.300	0.371	0.421	0.485	0.844
8	0.268	0.337	0.378	0.466	0.518	0.605	1.046
9	0.332	0.421	0.468	0.569	0.627	0.741	1.240
10	0.402	0.509	0.565	0.680	0.745	0.891	1.417
11	0.477	0.601	0.666	0.798	0.873	1.049	1.565
12	0.554	0.698	0.766	0.924	1.010	1.211	1.687
13	0.634	0.802	0.871	1.051	1.150	1.369	1.787
14	0.721	0.910	0.985	1.173	1.288	1.521	1.868
15	0.815	1.018	1.109	1.285	1.418	1.664	1.935
16	0.915	1.122	1.239	1.390	1.539	1.799	1.992
17	1.019	1.225	1.371	1.491	1.656	1.926	2.042
18	1.126	1.327	1.499	1.593	1.769	2.046	2.088
19	1.235	1.428	1.622	1.697	1.880	2.158	2.133
20	1.344	1.529	1.739	1.802	1.990	2.262	2.181
21	1.453	1.629	1.851	1.908	2.099	2.359	2.231
22	1.560	1.727	1.958	2.013	2.205	2.447	2.280
23	1.665	1.822	2.059	2.116	2.308	2.529	2.328
24	1.769	1.915	2.156	2.217	2.408	2.602	2.372
25	1.869	2.005	2.247	2.314	2.504	2.668	2.413
26	1.966	2.091	2.333	2.406	2.595	2.729	2.449
27	2.059	2.172	2.414	2.493	2.680	2.782	2.480
28	2.147	2.248	2.491	2.572	2.758	2.831	2.507
29	2.230	2.321	2.562	2.644	2.828	2.874	2.531
30	2.310	2.387	2.629	2.709	2.889	2.914	2.550
31	2.385	2.450	2.691	2.767	2.944	2.951	2.567

Table 2.5

Δm_{15}	0.82	1.02	1.11	1.29	1.42	1.67	1.94
phase				$m(B)$			
32	2.455	2.509	2.749	2.819	2.990	2.984	2.582
33	2.521	2.565	2.801	2.864	3.031	3.016	2.597
34	2.584	2.617	2.849	2.905	3.067	3.044	2.612
35	2.641	2.667	2.892	2.942	3.099	3.071	2.628
36	2.695	2.714	2.930	2.977	3.128	3.096	2.648
37	2.745	2.759	2.963	3.012	3.155	3.120	2.670
38	2.791	2.802	2.991	3.048	3.180	3.141	2.695
39	2.833	2.843	3.016	3.083	3.202	3.162	2.722
40	2.873	2.883	3.036	3.118	3.223	3.181	2.750
41	2.909	2.920	3.055	3.150	3.243	3.200	2.778
42	2.942	2.956	3.071	3.180	3.261	3.217	2.806
43	2.973	2.989	3.086	3.205	3.277	3.234	2.832
44	3.001	3.019	3.099	3.225	3.291	3.251	2.856
45	3.027	3.047	3.113	3.240	3.304	3.267	2.877
46	3.052	3.073	3.127	3.254	3.315	3.283	2.896
47	3.075	3.096	3.142	3.266	3.324	3.299	2.914
48	3.095	3.116	3.157	3.279	3.331	3.315	2.930
49	3.116	3.135	3.173	3.294	3.339	3.330	2.946
50	3.135	3.151	3.189	3.311	3.351	3.346	2.963
51	3.154	3.166	3.204	3.329	3.364	3.361	2.982
52	3.172	3.180	3.220	3.349	3.382	3.377	3.001
53	3.188	3.193	3.235	3.369	3.402	3.393	3.021
54	3.203	3.205	3.250	3.388	3.423	3.409	3.042
55	3.219	3.216	3.265	3.408	3.444	3.426	3.062
56	3.233	3.227	3.279	3.427	3.465	3.443	3.082
57	3.247	3.238	3.294	3.445	3.485	3.460	3.102
58	3.261	3.249	3.307	3.463	3.504	3.477	3.122
59	3.274	3.260	3.321	3.481	3.523	3.495	3.142
60	3.288	3.272	3.334	3.497	3.540	3.513	3.161
61	3.301	3.284	3.346	3.513	3.557	3.531	3.181
62	3.314	3.298	3.359	3.528	3.574	3.550	3.201
63	3.327	3.312	3.371	3.542	3.590	3.569	3.221
64	3.340	3.327	3.383	3.555	3.605	3.588	3.242
65	3.353	3.342	3.395	3.567	3.620	3.607	3.263
66	3.366	3.358	3.406	3.578	3.636	3.627	3.284
67	3.379	3.374	3.417	3.589	3.650	3.646	3.306
68	3.391	3.391	3.428	3.600	3.664	3.666	3.329
69	3.404	3.409	3.439	3.611	3.679	3.685	3.353
70	3.417	3.427	3.449	3.621	3.693	3.705	3.378
71	3.430	3.445	3.459	3.632	3.707	3.724	3.404
72	3.442	3.463	3.469	3.643	3.720	3.743	3.430
73	3.455	3.481	3.479	3.655	3.734	3.762	3.458
74	3.468	3.500	3.489	3.667	3.749	3.780	3.488
75	3.481	3.519	3.498	3.680	3.763	3.798	3.518
76	3.493	3.537	3.507	3.694	3.778	3.816	3.549
77	3.506	3.556	3.516	3.708	3.794	3.833	3.581
78	3.519	3.574	3.525	3.723	3.809	3.849	3.613
79	3.532	3.593	3.534	3.739	3.825	3.865	3.644
80	3.545	3.611	3.542	3.756	3.842	3.880	3.676

2.1.2 Reddening correction

SN light extinction occurs both in our own Galaxy and in the host galaxy. For the Galactic extinction we have independent estimates either from HI maps and galaxy counts (Burstein and Heiles, 1982) or from the COBE/DIRBE and IRAS/ISSA maps (Schlegel et al., 1998). The latter has been adopted in the present work.

Instead, to estimate the extinction in the host galaxy, following the usual approach we make use of the observed SN colour. In practice, we derive two different estimates as follows:

1. a plot of the $B-V$ colour at maximum (corrected for galactic extinction) versus the light curve decline rate $\Delta m_{15}(B)$ for the SNe of our sample is shown in Fig. 2.4. The $B-V$ colour at maximum has been measured on the $B-V$ colour curve

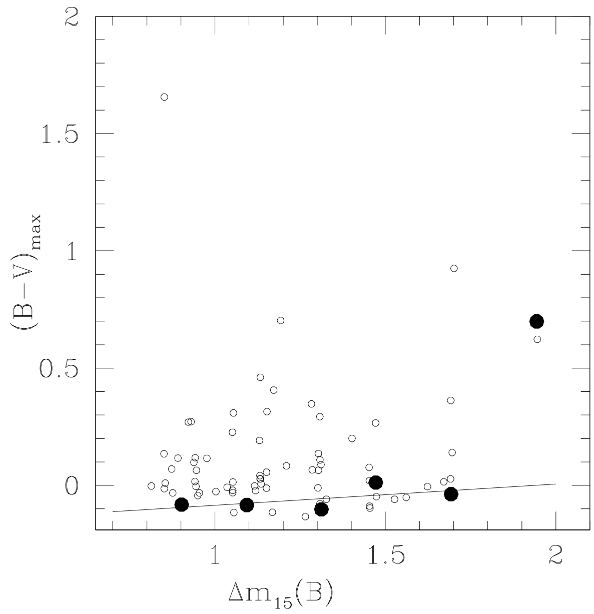

Figure 2.4: $(B-V)_{max}$ vs Δm_{15}. Correction for Galactic extinction has been applied. Black dots are SNe not affected by host galaxy reddening and spanning a wide range of decline rates (SN 1999bc, 1992al, 1994D, 1992A, 1992bo, 1991bg). The extremely fast declining SN 1991bg has a completely different behaviour. The solid line is the linear fit of these unreddened SNe (excluding SN 1991bg). The three SNe with "normal" decline rate ($\Delta m_{15} < 1.8$) and highest $(B-V)_{max}$ are (from left to right) SN 1996ai, 1995E and 1986G. The scatter of the empty circles is due to the host galaxy reddening.

either by means of a polynomial fit of the points around the maximum or by a template colour curve fit when the sampling was poor. We used different templates corresponding to SNe Ia with different Δm_{15}. Most of the observed dispersion is due to host galaxy extinction, but there are also intrinsic differences. In particular it is now known that SN Ia with $\Delta m_{15}(B) > 1.8$ are intrinsically red at maximum, with $(B-V)_0 \simeq 0.7$. For all other SNe Ia and assuming that the lower rim of the distribution corresponds to SNe with negligible extinction, the differences in the intrinsic colours are certainly small but still there is an indication that the intrinsic colour correlates with the luminosity decline rate: SNe with a faster decline rate are redder (Riess et al., 1998; Phillips et al., 1999; Nobili et al., 2003). This is shown in Fig. 2.4: by fitting the data of 5 SNe (SN 1999bc, 1992al, 1994D, 1992A, 1992bo) spanning a wide range of decline rates and for which there are indications that the host galaxy reddening was very low (Phillips et al., 1999), we found $(B-V)_{max} = 0.09(\pm 0.08) \times (\Delta m_{15} - 1.1) - 0.08(\pm 0.03)$. This relation was adopted to derive the colour excess for all Type Ia SNe but the very fast declining objects ($\Delta m_{15}(B) > 1.8$). For the latter we assumed that they have all the same intrinsic colour $(B-V)_0 = 0.70$. $E(B-V)_{max}$, corrected for the galactic component, are reported in column 6 of Table 2.3.

2. As shown by Lira (1996), the colour evolution of SN Ia between 30 and 90 days can be well approximated by the following linear relation: $(B-V)_0 = 0.725 - 0.0118 \times (t_V - 60)$, where t_V is the time (in days) from the V maximum. This is independent on the SN decline rates, including extreme objects like SN 1991bg. There is however at least one important exception, SN 2000cx (Candia et al., 2003) which should not be overlooked.

   The shift of observed colour of SN Ia required to fit this relation gives an alternative estimate of the host galaxy extinction $E(B-V)_{tail}$ reported in column 7 of Table 2.3.

Finally, as estimate of the host galaxy extinction, $E(B-V)_{host}$, was adopted the weighted mean of $E(B-V)_{max}$ and $E(B-V)_{tail}$ (cf. Phillips et al. 1999). In the few cases, when the formal mean turns out to be negative, the $E(B-V)_{host}$ were set equal to zero. This is equivalent to adopt a Bayesian filter with a flat a priori distribution for positive $E(B-V)$ and zero for $E(B-V) < 0$. Our adopted $E(B-V)_{host}$ are reported in column 8 of Table 2.3.

Some authors applied a different Bayesian filter to the measured values of $E(B-V)$. In particular, Phillips et al. 1999 assumed a one-sided Gaussian "a priori distribution" (Riess et al., 1996a). It turns out that their choice of a relatively small value of σ corresponds to an arbitrary reduction of $E(B-V)_{host}$, especially for objects with high colour excess. In turn, this results in smaller absorption corrections for the SN magnitudes. This choice, while not well justified, has the positive effect to reduce the dispersion of the corrected SN absolute magnitudes. We will come back to this point in the next section.

Phillips et al. (1999) have shown that because of the rapid spectral evolution of SN Ia and of the (small) dependence of the reddening on the colour of the source the observed $\Delta m_{15}(B)$ must be corrected as follows: $\Delta m_{15}(B) \simeq \Delta m_{15}(B)_{obs} + 0.1 \times E(B-V)$. The $\Delta m_{15}(B)$ reported in column 4 of the Table 2.3 are the observed values but we have taken into account this correction in our computation.

A comparison of our estimates of $\Delta m_{15}(B)$ and colour excess with those reported by Phillips et al. (1999) (Fig. 2.5) for the objects in common shows that, except for a few

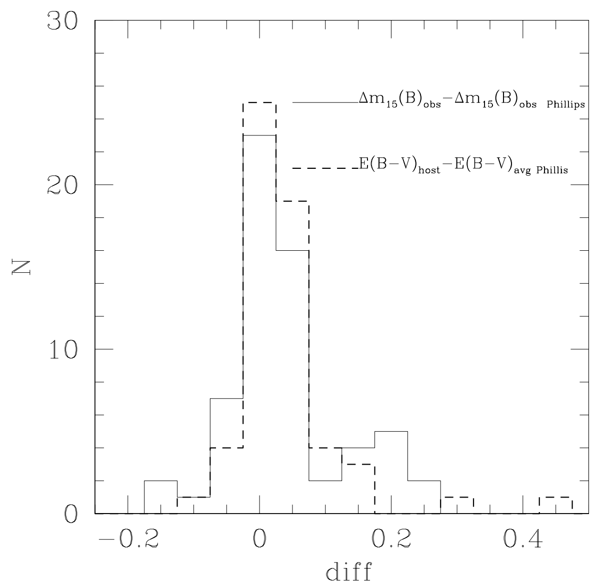

Figure 2.5: Comparison of the $\Delta m_{15}(B)$ and $E(B-V)$ between this work and Phillips et al. 1999.

cases, the values agree within the errors. The differences are due to slightly different choices for the epoch and magnitude at maximum.

2.1.3 Absolute magnitude vs. $\Delta m_{15}(B)$

In order to use SNe Ia as distance indicators, their absolute magnitude M_B needs to be calibrated. This requires that at least for a sub-sample of objects, the distance modulus of the host galaxies is measured by means of some independent distance indicators. As we will argue in the next section, this is best done with Cepheids. If SNe Ia were real standard candles, the calibrated absolute magnitude could be directly used to measure the distance of all other SN host galaxies.
As we mentioned before, this is not the case but, thanks to the relation between absolute magnitude at maximum and luminosity decline (Phillips, 1993), the role of SNe Ia as distance indicators can be recovered. Therefore is this relation which needs to be calibrated. Unfortunately this cannot be done using the Cepheid calibrated SNe Ia alone for two reasons:

1. the number of SN Ia host galaxies with Cepheid measured distances is too small (only 9 objects, as shown in Tab. 2.6);

2. as shown in Fig. 2.6, SNe Ia with different absolute magnitudes are not uniformly distributed versus galaxy types. In particular faint, rapidly declining SNe Ia occur preferentially in early type galaxies (Fig. 2.6) (see also Filippenko 1989, Hamuy

et al. 1996a, Cappellaro and Turatto 2001). As discussed by Ivanov et al. (2000) this effect can be due to the age of the progenitors (the older the progenitor system, the fainter the corresponding SN), but also to metallicity (Umeda et al. 1999) (lower metallicity systems produce fainter SNe). Another possible explanation has been recently proposed by Uenishi et al. (2003), who show a possible correlation between the initial mass of a WD in a close binary system, the rotational speed and the peak brightness of the SN (see also Piersanti et al. 2003). They found that, taking into account the effect of rotation, accreting WDs with small initial mass grow to larger mass and angular momentum at explosion with respect to WDs with large initial mass. Although the difference in the final mass is probably too small ($\sim 0.02M_{\odot}$) to contribute to the observed brightness diversity of SNe Ia, the difference of angular momentum can be sufficiently large to affect the speed of the flame nucleosynthesis in the explosion. In elliptical galaxies, where star formation ceased long time ago, massive stars have already evolved, therefore WDs with small initial mass cannot accrete enough mass to explode as a SN because no companion star can supply enough matter to it. On the other hand, in spiral galaxies, where star formation is still active, WDs with small initial mass can get enough mass to explode from massive companion stars. In this scenario the effect of rotation might qualitatively explain the dependence of the SN Ia peak brightness on their parent galaxy.

Since Cepheids are found in spirals only, it is not possible to properly sample the $M_B - \Delta m_{15}(B)$ relation by means of Cepheid calibrated SNe Ia.

To overcome these difficulties we adopted a two-step procedure. We first determine the slope of the relation using some widely available, though less accurate, distance indicators (Fig. 2.7); then, since the linear fit depends on the assumed value of H_0 (75 $\mathrm{km\,s^{-1}Mpc^{-1}}$), we determine the zero point by minimizing the deviation of the Cepheids calibrated SNe Ia on this fixed slope (see next section).

For the first step, absolute magnitudes have been calculated using distances obtained from two different sources. Distance moduli for 24 host galaxies in our sample were retrieved from the *"Nearby Galaxies Catalog"* (Tully and Fisher 1988). For the galaxies not listed there and with recession velocity larger than 3000 $\mathrm{km\,s^{-1}}$ (49 objects), we have determined the distance from the recession velocity, adopting $H_0 = 75\ \mathrm{km\,s^{-1}Mpc^{-1}}$ to be consistent with the Tully's catalogue scale. In order to avoid contamination from peculiar motions, we rejected 5 of the 78 SNe of the sample which are not listed in Tully's catalogue and have low recession velocity. Recession velocities in the reference frame of the 3K background microwave radiation were retrieved from the NASA/IPAC Extragalactic Database[1]

[1]NED, http://nedwww.ipac.caltech.edu/

Table 2.6: Cepheid calibrated SNe. (1) SN name; (2) host galaxy; (3) apparent B magnitude at maximum; (4) $B-V$ colour at maximum; (5) $\Delta m_{15}(B)_{obs}$ (not corrected for colour excess); (6) $E(B-V)_{gal}$ from Schlegel et al. 1998; (7) $E(B-V)_{host}$: weighted mean between $E(B-V)_{max}$ and $E(B-V)_{tail}$; (8) μ_0(KP), (9) $\mu_0(\Delta Y/\Delta Z) = 2.5$, (10) $\mu_0(\Delta Y/\Delta Z) = 3.5$ are the distance moduli given by the HST Key Project (Freedman et al., 2001) and the distance moduli obtained for two different metallicity (see §2.1.4).

SN	galaxy	m(B)$_{max}$	$B-V$	$\Delta m_{15}(B)_{obs}$	$E(B-V)_{gal}$	$E(B-V)_{host}$	μ_0(KP)	$\mu_0(\frac{\Delta Y}{\Delta Z} = 2.5)$	$\mu_0(\frac{\Delta Y}{\Delta Z} = 3.5)$
(1)	(2)	(3)	(4)	(5)	(6)	(7)	(8)	(9)	(10)
1990N	NGC4639	12.75(0.04)	0.04(0.05)	1.05(0.05)	0.026(0.003)	0.14(0.06)	31.61(0.08)	31.47(0.26)	31.55(0.31)
1981B	NGC4536	12.04(0.04)	0.06(0.05)	1.13(0.05)	0.018(0.002)	0.11(0.05)	30.80(0.04)	30.66(0.20)	30.71(0.23)
1989B	NGC3627	12.38(0.12)	0.38(0.05)	1.28(0.05)	0.032(0.003)	0.42(0.05)	29.86(0.08)	29.88(0.42)	30.11(0.54)
1998bu	NGC3368	12.20(0.04)	0.34(0.05)	1.15(0.05)	0.025(0.003)	0.37(0.05)	29.97(0.06)	29.94(0.50)	30.12(0.63)
1972E	NGC5253	8.40(0.04)	-0.06(0.10)	1.05(0.05)	0.056(0.006)	0.01(0.05)	27.56(0.14)	27.65(0.15)	27.65(0.14)
1937C	IC4182	8.94(0.30)	0.00(0.20)	0.85(0.20)	0.014(0.001)	0.06(0.05)	28.28(0.06)	28.31(0.08)	28.31(0.08)
1960F	NGC4496	11.65(0.20)	...	1.10(0.20)	0.025(0.005)	...	30.81(0.03)	30.70(0.18)	30.72(0.20)
1974G	NGC4414	12.34(0.04)	0.22(0.20)	1.40(0.04)	0.019(0.005)	0.25(0.05)	31.10(0.05)	31.07(0.38)	31.25(0.48)
1991T	NGC4527	11.69(0.04)	0.14(0.05)	0.94(0.05)	0.022(0.002)	0.20(0.05)	30.74(0.12)	30.60(0.57)	30.65(0.66)

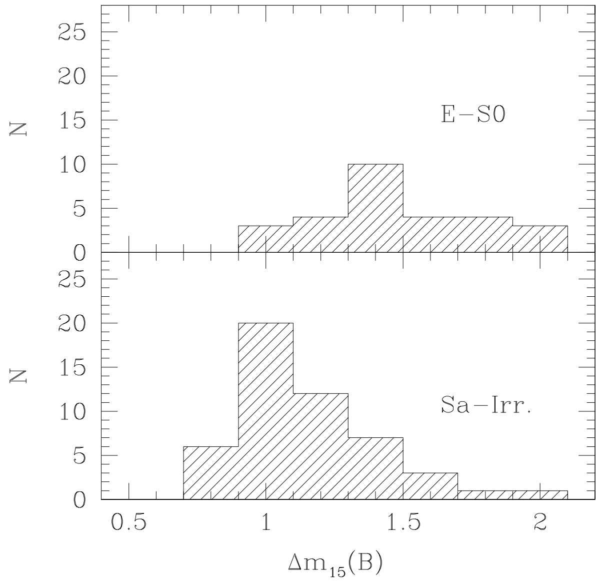

Figure 2.6: Histogram of $\Delta m_{15}(B)$ for SNe Ia in early type galaxies (upper panel) and in late galaxies (lower panel). The $\Delta m_{15}(B)$ values have been corrected for extinction, as explained in §2.1.2. A Kolmogorof–Smirnov test shows that the probability that the two distributions derive from the same population is very small ($P = 0.003\%$). Out of the 78 SNe of our sample 50 occurred in spiral-irregular galaxies and 28 in ellipticals-S0.

To show the importance of the host galaxy extinction correction, in Fig. 2.7**a** we have plotted the data of 73 SNe, corrected for Galactic extinction only. As it can be seen, the the points show a large dispersion and the correlation between M_B and $\Delta m_{15}(B)$ remains hidden.

The scatter appears greatly reduced in Fig. 2.7**b** where the SN magnitudes have been corrected for extinction in the host galaxy. The latter has been derived from the colour excess estimated in §2.1.2 and assuming a standard reddening law, that is $A_B = 4.315 \times E(B-V)$ (Schlegel et al. 1998, see also Cardelli et al. 1989). The only evident outliers are now four fast declining SNe (the sub-luminous SNe 1992K, 1999da, 1998de, 1991bg), SN 1996ai, whose colour excess is very high but not well defined (Phillips et al., 1999), and 1986G, another highly reddened SN.

Actually, we found that the dispersion in the M_B – $\Delta m_{15}(B)$ relation can be further reduced assuming, for the host galaxy extinction correction, a different value for R_B in the conversion between colour excess and extinction. As shown in Fig. 2.8, a minimum dispersion is obtained for $R_B = 3.5$, somewhat smaller than the canonical values $R_B = 4.315$. A qualitatively similar result was obtained, again using SN Ia, by Capaccioli et al. (1990), who favoured $R_B = 1.7$. However, previous measurements of low values for R_B from SNe were plagued by an inadequate understanding of the relation between intrinsic color and luminosity at maximum (Riess et al., 1996b). Other measurements of absorption in nearby galaxies provided values for R_B ranging from the canonical value ($R_B \sim 4.3$) to

much smaller values ($R_B \sim 3.6$: Bouchet et al. 1985, Brosch 1988, Brosch and Loinger 1991; $R_B \sim 2.4$: Rifatto 1990). However a lower estimate for the host galaxy reddening correction R_B has been suggested also by more recent studies ($R_B \sim 3.5$ Phillips et al. 1999; Knop et al. 2003).
Actually, even in our own Galaxy the ratio of the total to selective absorption has been found to vary significantly from place to place (e.g. R_V varies from 2.6 to 5.5 in the measurements of Clayton and Cardelli 1988). Therefore, in principle, it would be interesting to study the dependence of R_B on other observables, such as the distance from the host galaxy centre or the integrated galaxy properties. This would require the possibility to derive estimate of R_B for individual objects which, unfortunately, cannot be done with the present data. We note that, from a practical point of view, reducing R_B has the same effect of the adoption of a relatively narrow a-priori distribution of the reddening for a Bayesian estimate of the individual SN extinction (cf. §2.1.2). In §2.2 we will check what is the effect on the Hubble diagram of this different choice for R_B.

The issue is important (see also Fischer 2003; Combes 2003) because it turns out that, on average, the more distant SNe of our sample are less affected by the extinction than nearby ones. This is shown in Fig. 2.9: it turns out that for SNe in galaxies with recession velocity smaller than 3000 $km\,s^{-1}$ the average colour excess is ~ 0.27, whereas the same number for more distant galaxies is ~ 0.13.

This is likely due to selection effects, since distant obscured objects are more difficult to detect and SNe are likely to be discovered far from their host nucleus in distant galaxies.

As a final test we plot the $M_B - \Delta m_{15}(B)$ for the subsample of 26 SNe with $E(B-V)_{host} < 0.1$ and well measured Δm_{15} (Δm_{15} uncertainties < 0.2) (see also Phillips et al. 1999, Freedman et al. 2001). This has two advantages, it gives a more homogeneous sample and the uncertainties related to the host galaxy extinction correction are reduced. The result, shown in Fig.2.7**c**, is a very tight relation with dispersion $\sigma = 0.20$.

The comparison of our results, reported in Table 2.7, with those obtained from 26 SNe of the Calán - Tololo survey (Hamuy et al., 1996a), indicates that we find a slightly steeper slope, in the range 1.061 ± 0.154 to 1.102 ± 0.147 depending on the sample vs 0.784 ± 0.182 of Hamuy et al. (1996a). It is interesting to note that the difference disappears if, as in Hamuy et al. (1996a), we neglect the host galaxy extinction correction ($a = 0.855 \pm 0.182$).

The next step is determine the zero point of the M_B – $\Delta m_{15}(B)$ relation by means of Cepheids calibrated SNe.

2.1.4 Effect of the metal content on the Cepheids-distance scale

Classical Cepheids are fundamental primary distance indicators thanks to their characteristic Period-Luminosity (PL) and Period-Luminosity-Colour (PLC) relations. Such relations, once calibrated, allow one to evaluate distances of the order of 3 Mpc from ground-based observations and about 30 Mpc from space observations (HST, Freedman et al. 2001 and references therein). Moreover, the Cepheid distance scale constrains the evaluation of the Hubble constant H_0 through the calibration of secondary distance indicators. This implies that any systematic error on the Cepheids as standard candles may affect the inferred extragalactic distance scale and, in turn, the value of H_0.

In the recent years, one of the most debated issues concerning the extragalactic distance scale is the possible dependence of Cepheid properties on the chemical composition of the host stellar population. Indeed, Cepheid PL relations are traditionally considered to be "universal" (Iben and Renzini 1984, Freedman and Madore 1990), with the slope derived from Cepheids in the Large Magellanic Cloud (LMC), (Madore and Freedman 1991, Udalski 2000) and the zero point corresponding to some assumption on the LMC distance modulus or on Galactic Cepheids with independent distance estimates. Empirical tests of the metallicity effect on the Cepheid distance scale suggest that either the effect is very small (Freedman and Madore 1990) or it goes in the direction of predicting brighter Cepheids for higher metallicities (Kennicutt et al. 1998).
On the basis of the latter test, the HST Key Project (KP) distance moduli are corrected for the metallicity effect by adopting the correction $\Delta\mu_0/\Delta[O/H] = 0.2 \pm 0.2$ (see Freedman et al. 2001).
From the theoretical point of view, nonlinear convective pulsation models (Bono et al. 1999b), which are able to predict all the relevant pulsation observables, suggest that in the range $0.004 < Z < 0.02$ metal poor Cepheids are brighter than the metal-rich ones at fixed pulsation period (see Bono et al. 1999a, Caputo et al. 2000a). As a consequence, at least in this range of Z values, the adoption of "universal" LMC-based PL relations provides distance values that are systematically overestimated (underestimated) for galaxies more metal-rich (metal-poor) than LMC (see Caputo et al. 2000b).
On the other hand, when the pulsation analysis is extended to metallicities higher than the solar value (up to Z=0.04) in order to cover the whole range of metal abundances of the HST Key Project galaxies (see Ferrarese et al. 2000), and the simultaneous effect of the increase in the helium abundance is taken into account, the predicted metallicity correction turns out to change its sign around the solar value and to depend significantly on the adopted helium to metallicity enrichment ratio $\Delta Y/\Delta Z$ (see Fiorentino et al. 2002 for details). In particular Fiorentino et al. (2002) find that for $\Delta Y/\Delta Z$=3.5, the theoretical metallicity correction is in agreement with the result of the empirical test by Kennicutt et al. (1998).

In order to calibrate the $M_B - \Delta m_{15}(B)$ relation, we have considered three different estimates for the Cepheid distance to the SN host galaxies: μ_0(KP), computed without metallicity correction, and $\mu_0(\Delta Y/\Delta Z = 2.5)$, $\mu_0(\Delta Y/\Delta Z = 3.5)$ with the metallicity corrections corresponding to two different choices of the adopted helium to metallicity enrichment ratio $\Delta Y/\Delta Z$ (Table 2.6). The zero point of the $M_B - \Delta m_{15}(B)$ relation was determined by minimizing the deviation of the linear fit for the Cepheids calibrated SN, maintaining a fixed slope (Fig. 2.10). The inferred parameters of the correlation are reported in Table 2.7. The zero point obtained with different assumptions in the calibration lies in the range $-19.613 < b < -19.399$, to be compared with $b = -19.258 \pm 0.048$ in Hamuy et al. 1996a.

Table 2.7: Parameters of the M_B=a$(\Delta m_{15}(B) - 1.1) + b$ relation. From top to bottom: values obtained for case **b** (using two different values for R_B) and case **c** (as in §2.1.3). From left to right: number of objects used for the correlation; R_B adopted; slope (error); zero point derived from three different assumptions on the metallicity PL relation (error); dispersion.

n	R_B	a	b				σ
			KP	$\Delta Y/\Delta Z = 2.5$	$\Delta Y/\Delta Z = 3.5$		
67	4.315	1.102 (0.147)	-19.613	-19.523	-19.582	(0.037)	0.31
67	3.5	1.092 (0.124)	-19.460	-19.399	-19.472	(0.031)	0.28
26	3.5	1.061 (0.154)	-19.455	-19.403	-19.476	(0.044)	0.20

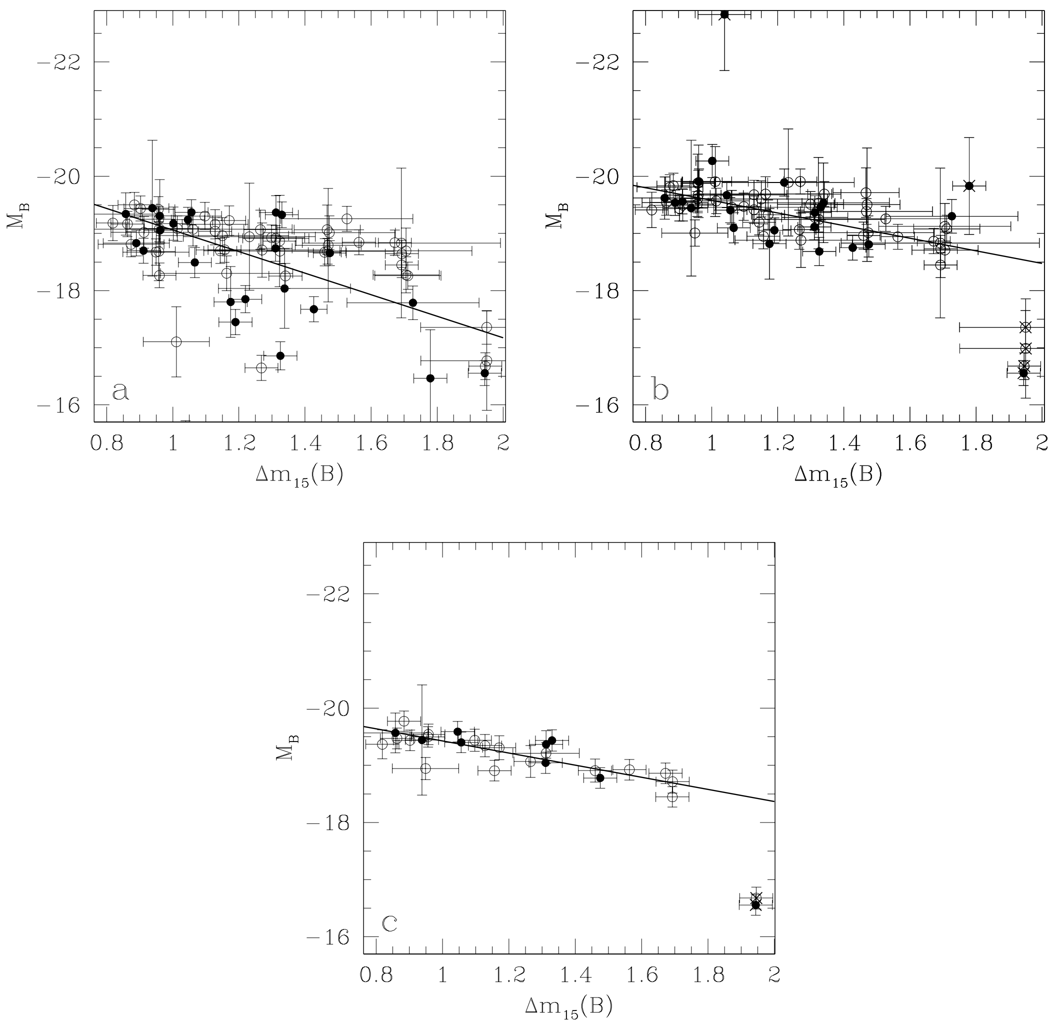

Figure 2.7: M_B versus $\Delta m_{15}(B)$ relation; filled circles indicate objects whose distances are given by Tully's catalogue, open symbols are objects whose distances are calculated from their recession velocity. The linear fit is weighted in both axes (Press et al. 1992). **a**: Only galactic reddening correction applied. Number of objects used for the linear fit n=73, dispersion $\sigma = 0.83$. **b**: Both Galactic and host galaxy reddening corrections applied. The outliers, marked with a cross, are (from left to right, from top to bottom): SN 1996ai, which is characterized by high and not well known reddening; SN 1986G, another highly reddened event; SN 1992K, 1999da, 1998de, 1991bg, which are peculiar sub-luminous events. The latters seem to form a separate class and do not fit the linear relation defined by all others. n=67, $\sigma = 0.31$. **c**: as the previous case but selecting only SNe with $E(B-V) < 0.1$ and small errors (< 0.2) in $\Delta m_{15}(B)$. n=26, $\sigma = 0.20$, $R_B = 3.5$.

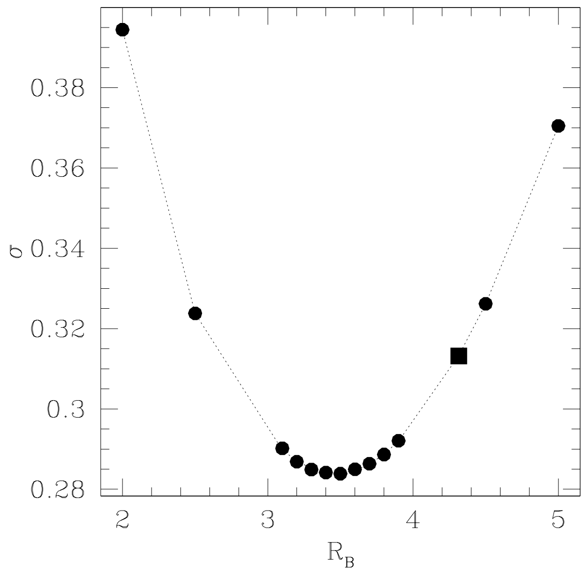

Figure 2.8: Dispersion of the $M_B - \Delta m_{15}$ relation for different values of R_B. The assumption are the same as in figure 2.7 **b**. The minimum of the σ fit corresponds to $R_B = 3.5$.

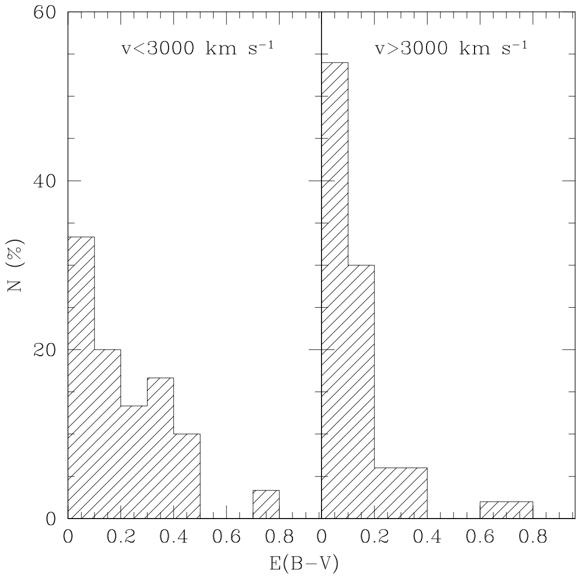

Figure 2.9: Distribution of the host galaxy extinction $E(B-V)_{host}$. Left: SNe with recession velocity smaller than 3000 $\mathrm{km\,s^{-1}}$; Right: SNe with recession velocity bigger than 3000 $\mathrm{km\,s^{-1}}$.

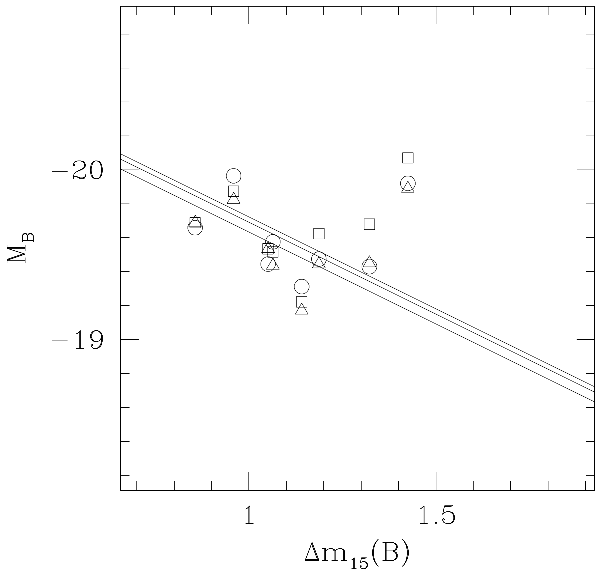

Figure 2.10: M_B versus $\Delta m_{15}(B)$ for 8 of the 9 SNe calibrated by Cepheids (SN 1960F has been excluded because colour excess for reddening correction is not available). Circles: Distance modulus μ from Freedman et al. 2001; triangles: μ corrected assuming $\Delta Y/\Delta Z = 2.5$; square: μ corrected assuming $\Delta Y/\Delta Z = 3.5$. All the values agree within the error-bars. Solid lines are the best fits obtained with a fixed slope minimizing the deviation of the three sets of Cepheids calibrated SNe. The slope is given by Fig. 2.7**c**.

2.2 The Hubble Constant

After completion of the calibration path, we can now use SNe Ia to measure the Hubble constant.

In Fig. 2.11 we show three examples aimed to show how different corrections and sample selection affect the scatter of the Hubble diagram. For this purpose, we adopted the PL relation corrected for $\Delta Y/\Delta Z$=2.5 (see Table 2.7) and we excluded from the fit all SNe Ia with recession velocity $v < 3000$ km s^{-1}. The latter is intended to avoid contamination by peculiar motions, which, on average, amount to ~200–300 km s^{-1} (Tonry et al., 2000; Giovanelli et al., 1999). We have also excluded SNe with $\Delta m_{15}(B) > 1.8$ because they do not fit the linear relation M_B – $\Delta m_{15}(B)$, as seen in Fig. 2.7**b**.
In panel *a* of Fig. 2.11 is the Hubble diagram obtained using the complete sample and a standard reddening law, in panel *b* is the plot obtained adopting $R_B = 3.5$ for the ratio of total to selective extinction (cfr. §2.1.3) and finally, in panel *c* is shown the Hubble diagram for the sample of SN Ia with the best photometric coverage $\Delta m_{15}(B) < 0.2$ and low reddening $E(B-V)_{host} > 0.1$ ($R_B = 3.5$).
The fact that the dispersion of the points in panel *b* ($\sigma = 0.24$) is significantly reduced compared with panel *a* ($\sigma = 0.29$) is consistent with the finding of §2.1.3. Again, it appears that the host galaxy absorption correction deduced from the measured colour excess and adopting a standard reddening law is an overestimate of the true absorption. On the other side, this turns out to have a small effect on the value of the Hubble constant itself ($H_0 = 74^{+9}_{-8}$ in panel *b* compared with $H_0 = 74^{+11}_{-9}$ in panel *a*) provided that in all steps the calibration of the SN magnitudes is done consistently (see also Table 2.8).
The dispersion of the Hubble diagram is further reduced by selecting the subsample of SN Ia with good photometry and low reddening SNe ($\sigma = 0.20$). This time the Hubble constant is slightly reduced $H_0 = 71^{+7}_{-6}$. Although this is our preferred result and that with the smallest statistical uncertainty, we stress that the selection criteria were not applied to the SN calibrated with Cepheids of Table 2.6, which otherwise would be reduced to only two cases. One should keep in mind that this asymmetry introduces some bias.
The different results are summarized in Table 2.8 where in particular it can be seen the sensitivity of the estimate of the Hubble constant on the different corrections of the PL relation. As it can be seen the effect is, in all cases, quite small.

H_0 ranges between 68 and 74 km s^{-1} Mpc^{-1}, with uncertainties of the order of ~ 7 km s^{-1} Mpc^{-1} ($\sim 10\%$)[2]

[2]The fact that the distance scale turned out to be very close to that of the Nearby Galaxies Catalogue by Tully and Fisher (1988) which was used to derive the slope of the M_B – $\Delta m_{15}(B)$ relation assure on the negligible impact of possible second order effects.

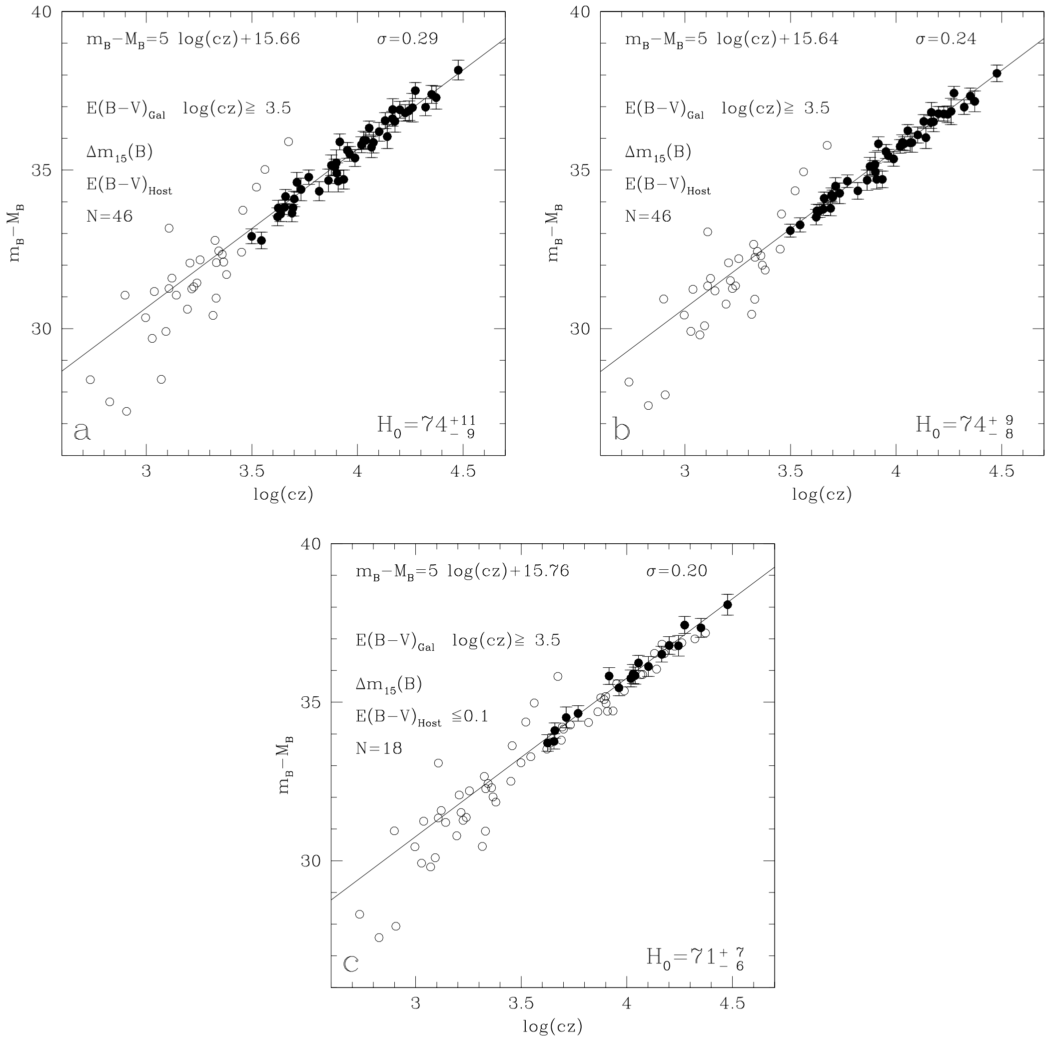

Figure 2.11: **a**: Hubble diagram of the whole sample assuming $R_B = 4.315$ in the estimate of the host galaxy absorption. **b**: as the previous plot but with $R_B = 3.5$. **c**: Hubble diagram for the good photometry, low extinction sample ($R_B = 3.5$). In all plots, we have used for the fit only those SN with recession velocity > 3000 km s^{-1} and we have adopted the Cepheids P-L correction for $\Delta Y/\Delta Z$=2.5. The fast declining SNe 1991bg, 1992K, 1999da and 1998de have been excluded from the fit. Points which do not contribute to the fit are indicated as open circles.

Table 2.8: Values of H_0 (in km s−1 Mpc^{-1}) for different assumptions on the Cepheid calibration and R_B. a and b are the values for the complete sample, whereas in c are the values for the good photometry, low reddening sample.

	a	b	c
N(SN)	46	46	18
R_B	4.315	3.5	3.5
μ_0(KP)	71^{+10}_{-9}	72^{+8}_{-7}	69^{+7}_{-6}
$\mu_0(\frac{\Delta Y}{\Delta Z} = 2.5)$	74^{+11}_{-9}	74^{+9}_{-8}	71^{+7}_{-6}
$\mu_0(\frac{\Delta Y}{\Delta Z} = 3.5)$	72^{+10}_{-9}	72^{+8}_{-7}	68^{+6}_{-6}

These values are in agreement with the result of the Hubble Space Telescope Key Project (Freedman et al. 2001) which gives $H_0 = 72 \pm 8$ km s^{-1} Mpc^{-1}. They are also in agreement with the recent results of *WMAP*, namely $H_0 = 72 \pm 5$ km s^{-1} Mpc^{-1} (Spergel et al., 2003), obtained for a spatially flat cosmological model dominated by cold dark matter and non-zero cosmological constant (ΛCDM model). Note that the same *WMAP* data give smaller value for H_0 if fitted by different cosmological models.

2.3 Conclusions

Using a large sample of SNe Ia light curves, both from the literature or unpublished data from the Padova-Asiago archive, we have revisited the different steps required to calibrate the SN absolute magnitude and to derive the Hubble constant.

In particular, we have re-calibrated the relation between the SN absolute magnitudes and the rate of decline soon after maximum. The latter can be measured either by the $\Delta m_{15}(B)$ or by the "stretch factor"

SN Ia with Cepheids calibrated distances are crucial because they are used to calibrate the zero point of the M_B vs. $\Delta m_{15}(B)$ relation. We have considered the effect of a new metallicity correction of the Cepheids PL relation, how this reflects on the calibration of SN Ia and finally on the estimate of the Hubble constant. Fortunately, the latter turned out to be not very important.

Instead we found that a major uncertainty is related to the correction of the extinction in the host galaxy. In particular, we found that the scatter of the M_B – Δm_{15} relation and of the Hubble diagram itself can be reduced assuming a (slightly) smaller value for the ratio of the total to selective absorption, R_B. Indeed, the scatter is minimum for $R_B = 3.5$. The difference with the standard value, $R_B = 4.315$, is well within the variance of the measurements of this parameter even within our own Galaxy. Therefore it does not require different properties for the dust in other galaxies. Still this is an important issue for the use of SN as distance indicators.

The Hubble constant, obtained with different assumptions on the metallicity dependence of the Cepheid PL relation, different cuts in the sample and varying the value of R_B, lies in the range 68–74 $\mathrm{km\,s^{-1}Mpc}$, with uncertainties of the order of 10%.

Chapter 3

The Southern inTermediate Redshift ESO SN Search

The fires that arch this dusty dot
Yon myriad-worlded ways
The vast sun-clusters' gathered blaze,
World-isles in lonely skies,
Whole heavens within themselves amaze
Our brief humanities.
Tennyson, *Epilogue*

3.1 SNe searches

Supernova Searches are important both because single SN discoveries are intrinsically valuable, providing information on astrophysics of stars and galaxies, and because the collection of large samples are useful for determining the explosion rates and for cosmology. As discussed in §2, the use of SNe as distance indicators requires detailed light curve measurements. This means that SNe need to be discovered near maximum or, even better, before. SNe discovered by random searches are typically too old to perform a good photometric follow-up and to produce a well sampled light curve. On the contrary in systematic searches, where each field is observed regularly, the ages of the SN at detection is constrained to be less than the time since the field was last observed. Tuning the interval between the observation it is possible to identify SNe in the rising branch of the light curve, that is soon after the explosion. This enables more accurate light curve shape measurements, and thus more accurate absolute magnitude and distance determinations.

In 1934 F. Zwicky started the first systematic supernova search using a modest 3-1/4 inch lens camera. In 1936 he continued the search using photographic plates obtained with the 18 inch Schmidt telescope at Palomar Observatory (Baade and Zwicky, 1938). This program was followed by the Palomar Supernova Search (Humason and Gates, 1960), per-

formed with the 18 and 48 inch Schmidt telescopes, which lasted from 1959 till 1974 and discovered, on average, ~ 10 SNe/year.
A few years later (1979) another photographic search started at the University of Chile in Santiago, using the 0.7m Maksutov telescope locate at Cerro El Roble (Maza et al., 1981). This program ended in 1984 but in 1990 it was followed by the Calán - Tololo Supernova Search (Hamuy et al., 1993a), a collaboration between The University of Chile and the Cerro Tololo Inter-American Observatory (CTIO), aimed to the collection of moderately distant ($0.01 < z < 0.10$) SNe of type Ia and type II, suitable for cosmological studies. Even if the search was performed using photographic plates obtained with the CTIO Curtis Schmidt Camera (60/90cm) the follow-up was performed with more accurate CCDs. The search produced 47 SNe between 1990 and 1993 (29 SNe Ia, 2 type Ic, 15 type II) (Maza et al., 1993).
Two important european photographic searches are the Asiago SN search and the Sternberg-Crimean SN search. The first one was started in 1959 by L. Rosino using the 40/50/100 cm Schmidt telescope located at the Astrophysical Observatory of Asiago (Italy). After 1967 a larger Schmidt telescope (67/92/200cm) has also been used. In the course of the search, which lasted till 1990, 31 SNe were discovered (mostly by L. Rosino) and about 20 more, first discovered by others, were recorded in the survey plates (Cappellaro et al., 1993a). The Sternberg-Crimean SN search started in 1961 with a 40 cm (f = 160 cm) astrograph located at the Crimean Station of the Sternberg Institute of Moscow (Russia). Because of the similarity of these two searches and in order to improve the statistics, the two independent groups co-operated in 1993 to release combined supernova rates from the two searches (Cappellaro et al., 1993a,b). Some year later, this sample was enlarged with the inclusion of Calán - Tololo and OCA (Observatoire de la Côte d'Azur) photographic surveys and of the visual search by Evans (Cappellaro et al., 1997b, 1999). During the almost two decades of the latter search (1981-2001), Evans collected over 200,000 individual observations, surveying a sample of more than 3000 nearby galaxies. The search resulted in the discovery of 38 SNe. These numbers qualify Evans' search as the most successful amateur SN search and make it very competitive even to professional searches. Rev. Robert Evans is still a prolific observer (Evans and Quirk, 2003; Evans and McNaught, 2003; Evans and Hazelbrook, 2003) and amateur astronomers in general plays an important role in SN discovery, e.g. the UK nova/SN patrol (Hurst et al., 2000; Boles, 2002), the Puckett Observatory[1] (Puckett and Newton, 2000), and the Tenagra Observatory (Puckett and Newton, 2000) to cite just a few names.
In recent years a large number of low-z searches (often performed by small dedicated telescopes, covering a wide field in completely automated way) and a few intermediate-z searches have been undertaken. Some of them are are listed in Table 3.1.

Leaps in technological capabilities, especially the accelerated progress in CCD development over the past two decades, which led to the production of more sensitive, more reliable and larger formats detectors (Wittman et al., 1998), as well as the improvements in computer processing and in data storage capabilities, boosted the SN detection rates enormously and made feasible to conduct high redshift SN searches.
The first distant SN search was undertaken by the Danish team of Norgaard-Nielsen et al. (1989), using the 1.5m Danish telescope at La Silla. With significant effort and large amounts of telescope time spread over more than two years, they discovered a type Ia SN

[1] http://www.cometwatch.com/

Table 3.1: Recent Low and Intermediate redshift SN searches.

the Lick Observatory and the Tenagra Observatory Supernova Searches (LOTOSS, http://astron.berkeley.edu/~bait/lotoss.html), a collaboration between the Lick Observatory Supernova Search (LOSS, http://astron.berkeley.edu/~bait/kait_lwd.html), (Filippenko, 2003; Li et al., 2003b; Treffers et al., 1997), and Michael Schwartz of the Tenagra Observatories (Schwartz et al., 2000) (http://www.tenagraobservatories.com/index.html),
the Beijing Astronomical Observatory SN Survey (BAOSS; Li et al. 1996, 2001);
the EROS Nearby SN Search (EROSNSS; Hardin et al. 2000)
the Nearby Galaxies SN Search (NGSS; Strolger et al. 2000);
the QUEST (Schaefer et al., 1999; Schaefer, 2000);
the British Astronomical association UK Nove/Supernova Patrol;
the European SN Cosmology Consortium (ESCC; Hardin et al. 1999);
the Super Livermore Optical Transient Imaging System (Super-LOTIS);
the Nearby Supernova Factory (http://snfactory.lbl.gov/), part of the SCP, using NEAT (http://neat.jpl.nasa.gov/) images to look for SN;
the Perth Automated SN Search (Williams et al., 1998).
the Mount Stromlo Abell Cluster SN Search (MSACSS; Reiss et al. 1998);
the Wise Observatory Optical Transients Search (WOOTS; Gal-Yam et al. 1998);
the Seoul National University SN Search (SNUSS; Lee et al. 1999);
the All-sky Southern Supernova Search (http://msowww.anu.edu.au/~salvo/snsearch.html, Marilena Salvo, Brian Schmidt, Michael Ashley, Andre Phillips);

in a cluster of galaxies at z = 0.3, and a Type II SN at z = 0.2 (Norgaard-Nielsen et al., 1989; Hansen et al., 1989).
More or less at the same time, the Lawrence Berkeley National Laboratory (LBNL) and the Center for Particle Astrophysics, at Berkeley, started a search for high redshift type Ia SNe using a novel wide field camera on a 4m telescope. This search, now known as the Supernova Cosmological Project[2] (SCP), was inspired by the impressive studies of the late 1980s indicating that extremely similar type Ia SN events could be recognized by their spectra and light curves, and by the success of the LBNL, a fully robotic low-redshift SN search that, with automatic image analysis, discovered 20 SNe (Muller et al., 1992; Perlmutter et al., 1992). The SCP targeted high redshift range, $z > 0.3$, in order to measure

[2]http://panisse.lbl.gov/public/

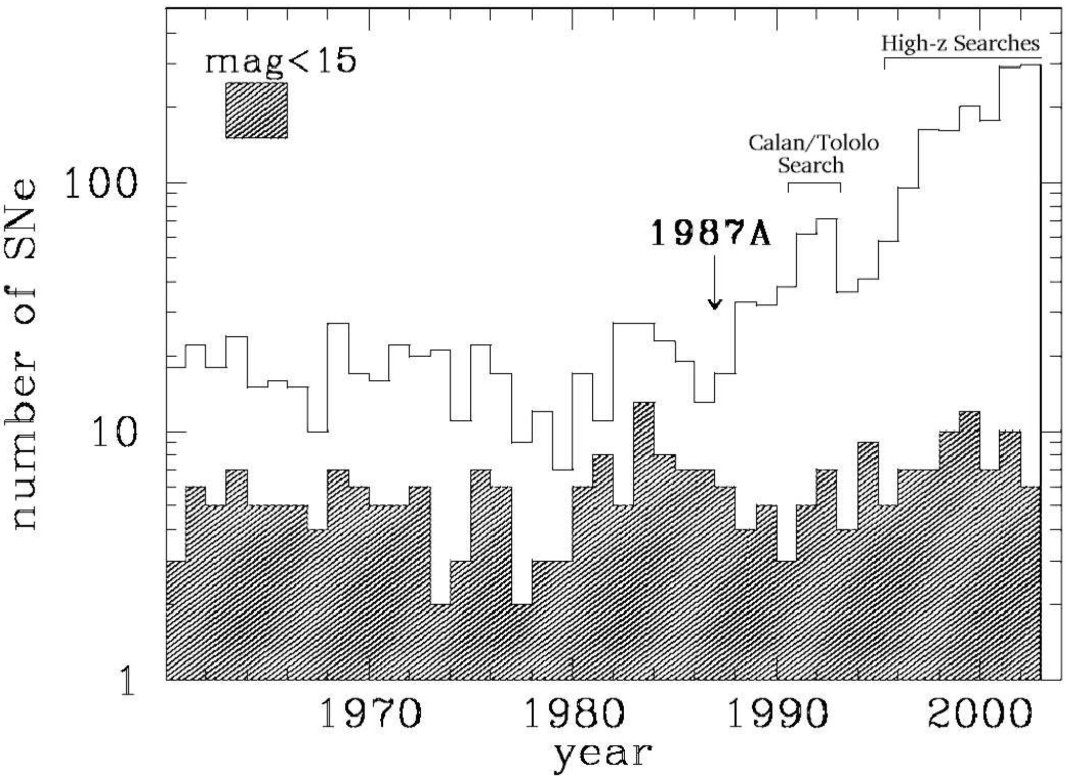

Figure 3.1: SN discovery rate in last decades. Figure based on the data collected in the Padova-Asiago SN archive.

the (presumed) deceleration of the Universe
In 1994, a group of astronomers from all over the world joined in the High-Z SN Search Team[3], with the aim of tracing the expansion of the Universe. With general surprise, in 1998 the two groups provided evidences that actually the Universe expansion is accelerating (Schmidt et al., 1998; Perlmutter et al., 1999).
More recently the advent of wide-field CCD mosaics on large telescopes has boosted the hight redshift SN searches (Schmidt et al., 1998; Perlmutter et al., 1999; Hardin et al., 1999). Nowadays we count a few hundreds SNe per year, at ever increasing distances. Fig. 3.1 shows the increasing number of SNe discovered in the last decades. It is interesting to note that the bright objects (mag<15) discovery rate has not increased with time. This fact suggests that in the last decades all relatively bright supernovae are discovered.

[3]http://cfa-www.harvard.edu/cfa/oir/Research/supernova/HighZ.html

3.2 STRESS

In spite of the large number of SN searches performed in recent years, so far there are few and uncertain observational constraints on the frequencies of SNe at high redshifts (see §5). Moreover observations have been focussed on type Ia SNe only. Because of this situation, some years ago we decided to start a SN search, the *S*outhern in*T*ermediate *R*edshift *E*SO *S*N *S*earch (STRESS[4]), especially designed to estimate the rate of SNe of all types at intermediate redshift ($0.1 < z < 0.6$). The procedure adopted to calculate the SNR follows as close as possible that used to estimate the local SN rates (Cappellaro et al., 1997b, 1999) and allow us to make a direct and sound comparison of our intermediate redshift measurements with the local ones (cf. §5). This search represents a long term project and it is the result of the combined efforts of several researchers from different institutions as the Astronomical Observatory of Padova, the Astronomical Observatory of Capodimonte, the University of Padova, the University of Napoli, the European Southern Observatory, the Departamento de Astronomía y Astrofísica, PUC, Chile. Each of the people involved in the search gave a specific contribution and all of them contributed to the success of the project.
In particular, I worked on the software developed for the SN search (see §3.4), I carried out and/or organized large part of the observations performed from november 2000 onwards and I reduced all the resulting data. Besides, since the data collected before this date had not been homogeneously analyzed, I devoted a significant effort to the uniform and systematic analysis of the whole SN search image archive, starting from the very first observation. This implied the standard image reduction (described in §3.3) and the SN detection (see §3.4) and produced a bulk of data useful for the following observing runs and fundamental for the further analysis (see §3.4.4, §3.5, §3.6).
In the following sections the instrumentation adopted, the observing strategy, the data reduction as well the software package built for the SN detection are presented. The supernovae spectroscopically confirmed are presented in a final section.

3.2.1 Telescopes & instrumentation

One of the difficulties of SN searches is to reconcile width and depth of the surveyed area. This is true in particular for intermediate z searches. In fact in this redshift range ($0.1 \leq z \leq 0.6$) is not useful to target individual galaxies with small telescopes and short exposure times, as in nearby searches (the KAIT robotic telescope can take 70 images/hour, 30 seconds each, with limiting magnitude of about 19.5 mag, scanning thousands of galaxies per night) and the volumes (and galaxies numbers) surveyed are much more smaller than those in the deep high-z searches, performed in smaller fields with larger telescopes (with modern 4 meter-class telescopes, which reach R = 24 mag in less than 10 minutes, it is possible to scan a million galaxies in a single night) (Perlmutter and Schmidt, 2003).
A compromise between width and depth has been offered by the advent of wide field cameras mounted at the focus of medium size telescopes. This is a fast developing technological branch and the list of wide field imagers reported in Tab. 3.2 shows clearly the

[4]http://web.pd.astro.it/supern/esosearch/

Table 3.2: Examples of wide field imagers, either already operational or at different development stages

Instrument	telescope Ø	Field of view
VISTA the UK's Visible and Infrared Survey Telescope for Astronomy, a new 4m wide field survey telescope currently under development. It will be equipped with an IR camera. http://www.vista.ac.uk/	4m	$\sim 1^\circ \times 1^\circ$
NEWFIRM the NOAO Extremely Wide-Field Infrared Imager. http://www.noao.edu/ets/newfirm/	4m	$30' \times 30'$
WFC a Wide Field Camera mounted at the 2.5m Isaac Newton Telescope (INT) on La Palma. WFC is made up by 4 thinned EEV 2k×4k CCDs. http://www.ast.cam.ac.uk/ING/WFS/WFCsur_home.html	2.5m	$34' \times 34'$
CFH12K a mosaic of twelve 2048x4096 pixel CCDs mounted at the 3.6m Canada France Hawaii Telescope; http://www.cfht.hawaii.edu/Instruments/Imaging/CFH12k/	3.6m	$28' \times 42'$
MegaPrime the new prime focus environment for the 3.6m Canada France Hawaii Telescope, which will be equipped with MegaCam, a mosaic of 40 CCDs. http://www.cfht.hawaii.edu/Instruments/Imaging/Megacam/	3.6m	$1^\circ \times 1^\circ$
Suprime-Cam a wide field CCD camera (a mosaic of 2x5 CCDs) for the prime focus of the 8.2m SUBARU Telescope. http://indus.astron.s.u-tokyo.ac.jp/works/suprime/index.html	8.2m	$30' \times 30'$
Megacam a wide field CCD imager made up of 36 CCDs, 2048x4608 pixels each, for the 6.5m MMT telescope. http://cfa-www.harvard.edu/cfa/oir/MMT/MMTI/megacam.html	6.5m	$24' \times 24'$
OmegaCAM a wide field, 16k X 16k, camera for the VLT Survey Telescope, a 2.6m telescope which is expected to become operational at Paranal during the year 2004 (VST, http://twg.na.astro.it/vst/vst_homepage_twg.html). http://www.astro.rug.nl/~omegacam/	2.6m	$1^\circ \times 1^\circ$
WFI a wide field camera mounted at the Cassegrain focus of the 2.2m MPG/ESO telescope at La Silla. http://www.ls.eso.org/lasilla/sciops/wfi/	2.2m	$34' \times 33'$

more and more important role played by wide field observations in modern astronomy.

The availability the *Wide Field Imager* (WFI), a wide-field CCD mosaic, at the Max-Planck-Gesellschaft (MPG) 2.2m telescope at ESO-La Silla (first light in december 1998), gave us the opportunity to start a search for intermediate-distance SNe. Thanks to the wide field of view ($\sim 1/4$ square degree), and the excellent spatial resolution (0.238 arcsec/pix.), the deep monitoring of a wide field area became feasible.
This camera, a joint project between the European Southern Observatory (ESO), the Max-Plank-Institut für Astronomie (MPI-A) in Heidelberg (Germany) and the Osservatorio Astronomico di Capodimonte (OAC) in Naples (Italy), opened the wide field imaging era in the ESO community.
The WFI is a focal reducer-type camera mounted at the Cassegrain focus of the MPG/ESO 2.2m telescope at La Silla, Chile. The telescope field of view has a diameter of ~ 0.8 degree, while the detector coverage is 34'x33' (in this respect it exceeds any other current La Silla or VLT ESO instrument by at least a factor of 2). The detector system for scientific exposures consists of an array of 2x4 CCD44 chips by EEV, 2046x4098 pixels each. The pixel size is 15 μm, corresponding to 0.238 arcseconds on the sky. Narrow inter-chip gaps ($\sim 98 \pm 2$ pixels along the long and $\sim 58 \pm 2$ pixels along the short side of the chips) yield a filling factor of 95.9%. To reduce the noise the detectors are cooled with liquid nitrogen at the temperature of ~ 167.0 K.
The physical layout of the WFI camera is shown in Fig. 3.2, together with the numbering scheme and the orientation in the sky. The position of the auxiliary CCD which is used for tracking is visible in Fig. 3.3. The technical details of each chip are reported in Tab. 3.3.

Table 3.3: WFI chips basic features.

	CCD #50	CCD #51	CCD #52	CCD #53
Read Out Noise [e^-]	4.5	4.6	4.6	4.4
Gain [e^-/ADU]	1.9	2.0	2.2	1.9
	CCD #57	CCD #56	CCD #55	CCD #54
Read Out Noise [e^-]	4.5	4.6	4.7	4.5
Gain [e^-/ADU]	2.1	2.1	1.9	1.9

Read out noise and gain however are periodically checked by the 2p2 Team (http://www.ls.eso.org/lasilla/sciops/2p2/CCDs/WFI/DailyHealthCheck.html).

The filter storage and change mechanism can accommodate up to 50 filters. The default filter set includes a large number of medium- and narrow-band filters. For our SN search we used the broad bands B, V, R [5].
The WFI and filters technical details are reported in Tab. 3.4, 3.5 and Fig. 3.4.

[5]The B filter (#842) initially available was characterized by a large deviation from the standard Johnson B filter, with the mean wavelength ($\sim$ 4590 Å) significantly shifted to the red if compared to a typical Johnson B filter (mean wavelength $\sim$ 4300 Å).The "B new" filter (#878) shows shows a better match with the Johnson B and it is currently used in the standard calibration plan:
The V filter (#843) shows a good match with the Johnson V filter while the R filter (#844) shows a relatively good match with the Cousins R filter.

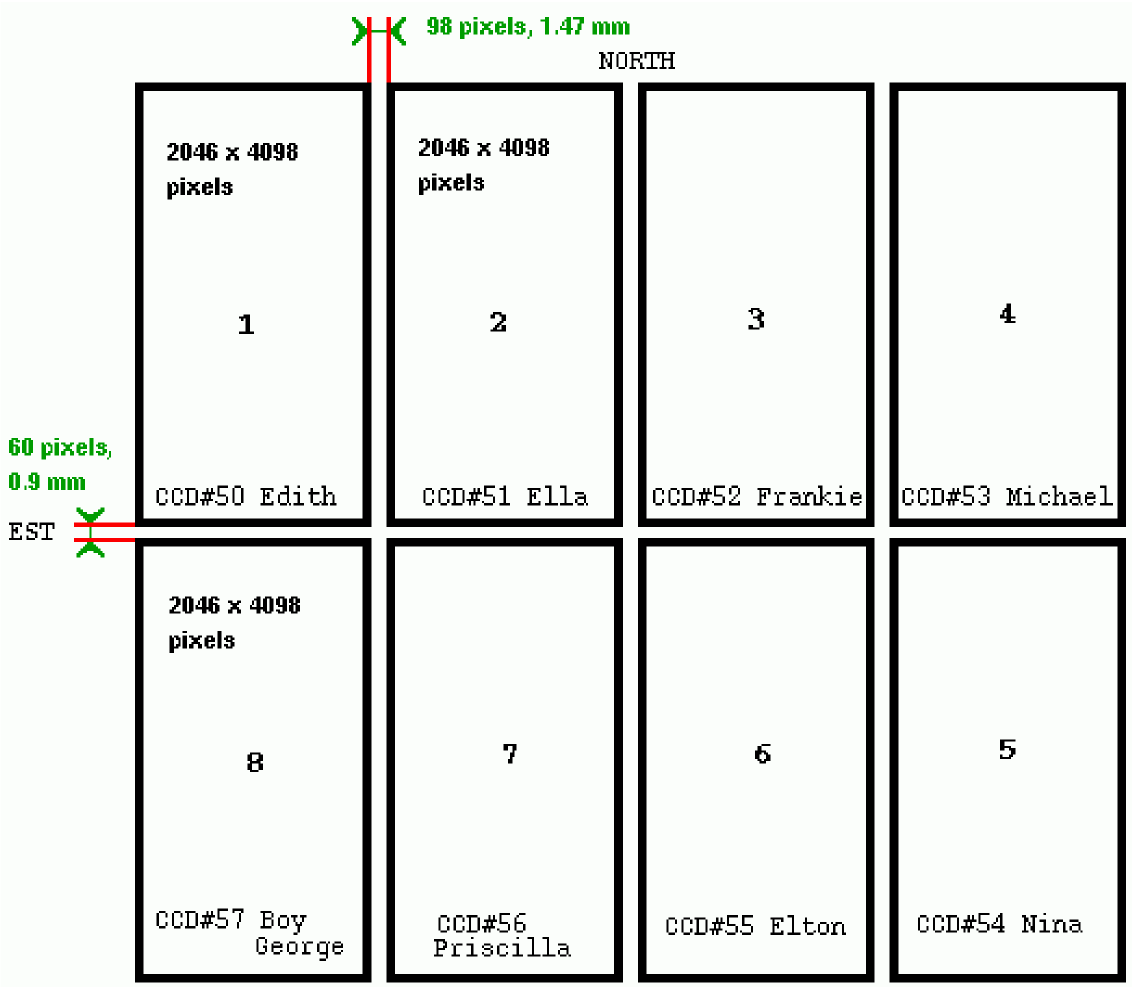

Figure 3.2: WFI physical layout. The numbering scheme and the orientation in the sky are shown. All the 8 CCDs have also nicknames.

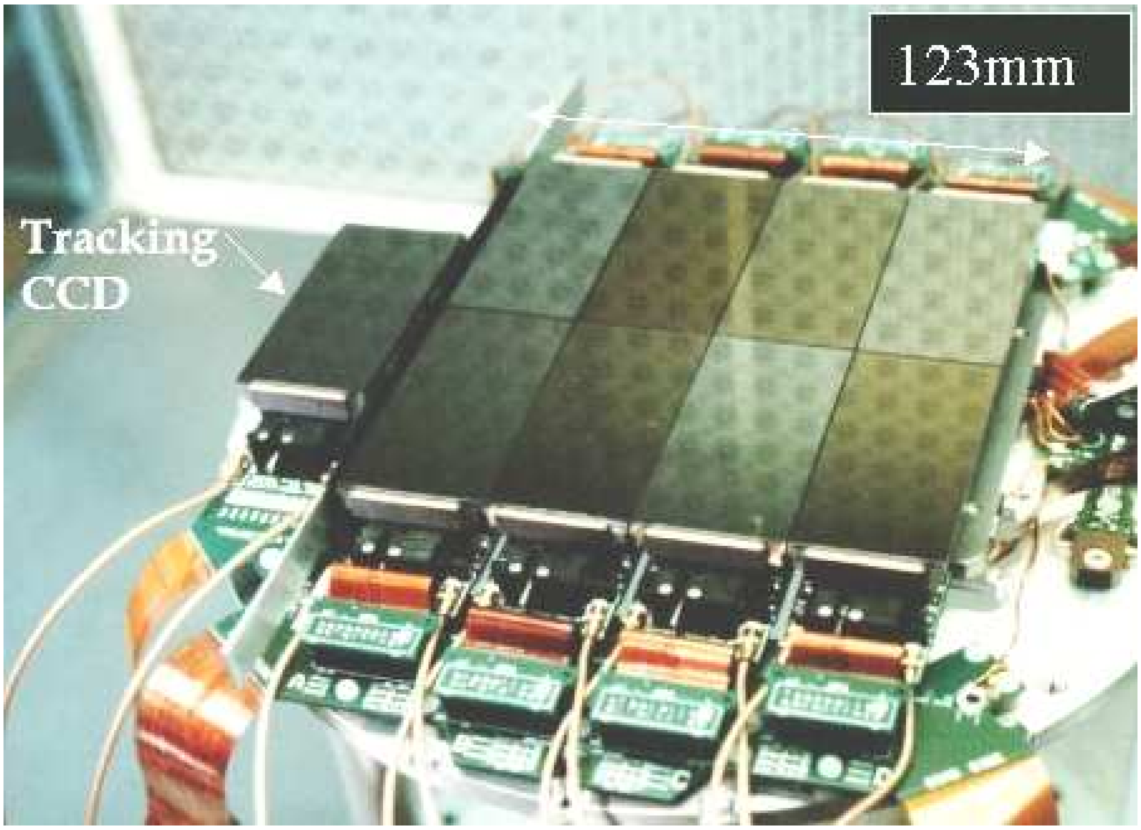

Figure 3.3: WFI with all 8 + 1 CCDs. The additional CCD on the left is the tracker chip used for autoguiding.

Table 3.4: WFI and MPG/ESO 2.2m telescope basic features.

Field of view	34'x33'
Pixel scale	0.238 arcsec/pixel
Detector	4x2 mosaic of 2kx4k CCDs
Filling factor	95.9%
Read-out time	27 seconds
Read-out noise	4.5 e^-/pixel
(Inverse) gain	2.0 e^-/ADU
Dynamical range	16 bit
Full-well capacity	>200,000e^-
Telescope aperture	2.2 m
Telescope focus	Cassegrain (f/8)
Instrument F ratio	5.9
Wavelength range	Atmospheric cutoff to 1 μm
Intrinsic image quality	0.4 arcsec
Geometrical distortions	$\leq$ 0.08%
Slitless spectroscopy	4.5 (5.7) nm resolution at 400-640 (650-850) nm
Raw data format	FITS (with extensions), 142 Mbyte/file

Table 3.5: WFI filters basic features.

Filter (ESO#)	CWL [nm]	FWHM [nm]	PWL [nm]	PT (%)
B/99 (#842)	456.252	99.014	475.0	91.2
B new (#878)	451.100	133.500	502.5	88.5
V/89 (#843)	539.562	89.386	523.0	87.0
Rc/162 (#844)	651.725	162.184	668.5	93.9

CWL: Central WaveLength; FWHM: Full-Width at Half-Maximum; PWL: Peak WaveLength (i.e. Wavelength with highest transmittance); PT: the percentage transmission at the PWL.

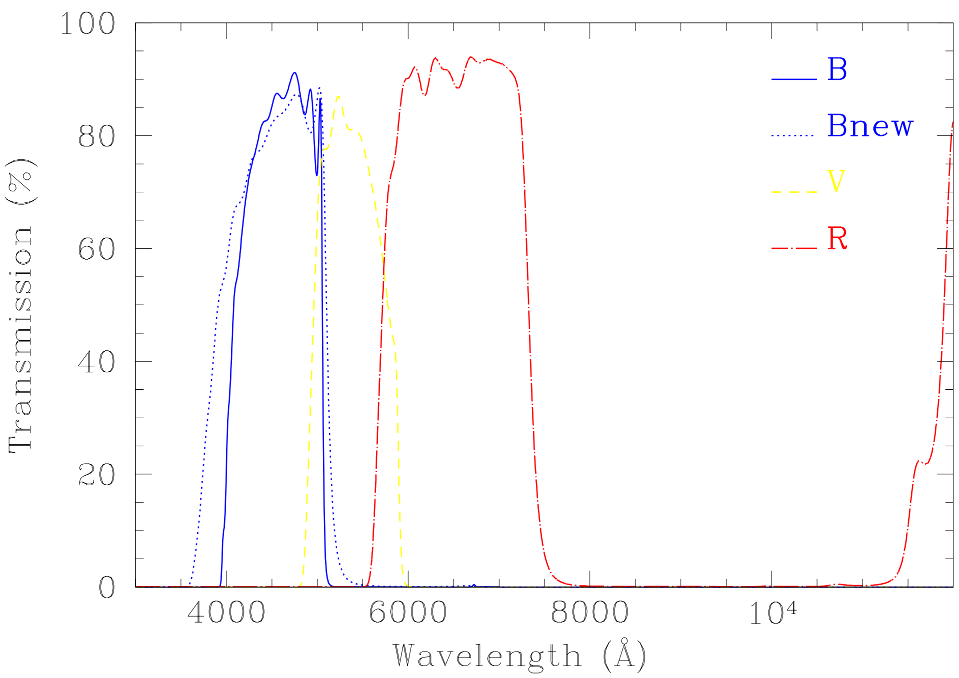

Figure 3.4: WFI filters efficiency (B, V, R bands).

3.2.2 Observing strategy

As for all SN searches, the building block is the search of variable sources through the comparison of images of selected sky areas obtained at different epochs. To this aim we developed a package, described in detail in §3.4, to perform the SN detection in a semi-automatic way.
Many of the sky fields we selected were chosen specifically to target known galaxy clusters, in order to monitor a large number of galaxies and to have additional information from other works (e.g. the fields from the ESO Imaging Survey program (EIS[6]), Renzini and da Costa 1997; Scodeggio et al. 1999). The fields were chosen properly spaced in right ascension, in order to perform the search during all the year (Fig. 3.5), at high galactic latitude (to reduce the contamination by Galactic dust and stars) and with very few bright stars (which could reduce the effective surveyed area and generate tiresome ghosts and reflections). The selected 21 fields and their coordinates are listed in Tab. 3.6.

The temporal spacing of the images is tuned to the specific goal one wants to achieve. For the use of type Ia as distance indicators it is important to catch SNe early on and the time span between the images to be compared has to be of the order of the rise time to maximum light, that is 2–3 weeks. Instead in our search, with the aim to maximize the events statistics, the time span has been chosen to be equal (or longer) than the time a typical event remains brighter than the detection limit of the search.

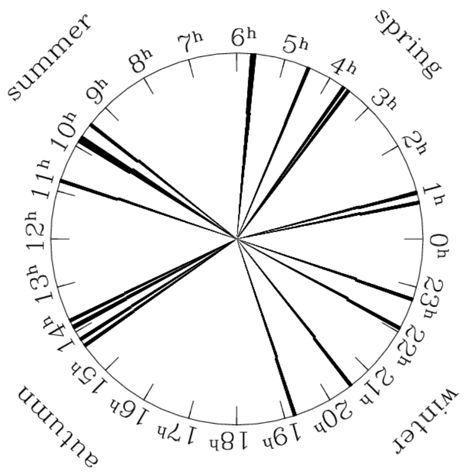

Figure 3.5: RA. distribution of the selected fields.
Seasons are referred to the southern hemisphere.

The observing strategy evolved with time because of the late delivery of some filters: at the beginning the fields were observed in B and V bands and the detection for SN candidates was performed in the B band frames. We tested also the U, R and I filters, but U band was rejected because not useful to look for SNe at intermediate redshift while I band was rejected because affected by a strong fringing. After this first testing phase -

[6] http://www.eso.org/science/eis/

Table 3.6: List of the observed fields.

Name	α *hh mm ss*	δ $^{\circ}$ ' "
EisB	00:45:25.5	-29:36:47
J1888	00:57:35.4	-27:39:16
AXAF	03:32:23.7	-27:55:52
03Z3	03:39:31.1	-00:07:13
EF0427	04:29:10.7	-36:18:11
EisC	05:38:19.8	-23:50:11
F0540	05:41:10.3	-23:16:12
SN33	09:27:48.1	-04:49:05
F0946	09:47:11.6	-21:07:07
EisD	09:51:31.4	-20:59:25
F0952	09:52:34.4	-20:32:29
10Z2	10:46:45.8	-00:10:03
13Z3	13:44:28.3	-00:07:47
white23	13:52:56.4	-11:37:03
whitehz2	13:54:06.1	-12:30:03
white27	14:10:59.7	-11:47:35
white31	14:20:15.3	-12:35:43
Field2	19:12:51.9	-64:16:31
RXCJ	20:31:30.0	-40:42:41
22Z3	22:05:05.8	-18:34:33
EisA1	22:43:25.6	-40:09:11

Equinox 2000.0

from 2001 onwards - in order to detect candidates at higher redshift, we observed mainly in V and R (the rest-frame B band shift into the observer-frame V and R at $z \sim 0.2$ and $z \sim 0.5$ respectively), searching for candidates mainly in the V band frames.
Also the software tools available for wide field astronomy evolved with time. At the very beginning of our SN search, started in 1999 soon after the WFI first light, it was not clear how to handle the *multiextension FITS* format images generated by the new camera and the mosaic reduction packages were at very early stages. Even the simple display of the whole mosaic was a problem and just the fast reading of one image was a challenge for the most powerful PC available at that time.
This fact, together with the early stage of our software for the SN candidates detection and the need of collecting template images for the surveyed fields are the reasons why the number of SNe confirmed during the first nine observing runs is $\sim 1/3$ of the SNe announced in the the following six observing runs. Moreover the spectroscopic follow-up, required to confirm the SN candidates detected with the WFI, has been performed with different instruments. During the first "experimental" phase of the search the spectroscopic classification of the candidates (SN type and redshift) was attempted with the ESO Multi-Mode Instrument (EMMI), mounted at the 3.6m New Technology Telescope (NTT), and with the ESO Faint Object Spectrograph and Camera (EFOSC2) at the ESO 3.6m

telescope. From 2001 onwards, after refining the observational strategies and our search software (which allowed us the detection of fainter SN candidates), the spectroscopic classification was performed with the FOcal Reducer/low dispersion Spectrograph (FORS) at VLT. Actually there are two version of this instrument, FORS1 and FORS2, operating at Paranal Observatory. The main features of these multi mode instruments are listed in Tab. 3.7.

Table 3.7: FORS1/2 basic features.

Pixel scale (pixel size)	Field of view	Spect. mode*	Grism	λ_{range} $[nm]$	Dispersion [Å/mm]/[Å/pix]	Filter	Slit ["]
			FORS1				
0.2"/pix.	6.8'x6.8'	LSS	300V+10	445 – 865	112/2.69	GG435	0.7-1.0
($24\mu n$)			300I+11	600 – 1100	108/2.59	OG590	
			FORS2				
0.125"/pix.	6.8'x6.8'	LSS/MOS	300V+20	445 – 870	112/1.68	GG435	0.7-1.0
($15\mu n$)			300I+21	600 – 1100	108/1.62	OG590	

* Spectroscopy mode: LSS - longslit spectroscopy; MOS - multi-object spectroscopy (movable slits)

After the first testing phase the SN search was organized as follows.
The single observing run is divided into two parts:

1. **Search Run** : two subsequent nights at the WFI for the candidate detection. The images for the candidate detection were obtained in the V band over one of the two nights while, in the other night, the same fields were re-observed in another filter (B, R or I) in order to have the color information. For each epoch we obtained three 900s dithered exposures (limiting V magnitude ~ 24) in order to get rid of the cosmic rays, satellite tracks, minor planets and the detector cosmetic defects. In order to speed up the search, frames pre-reduction (bias subtraction and flat fielding) was performed in real time during the observing nights.

2. **Follow-up Run**: one night at the VLT+FORS1/2 for the spectroscopic classification of the candidates. The 8-m class telescope is needed as most of the SN candidates that were selected for the follow-up phase spanned a magnitude range of $V \simeq 22.5$–23.5. We note also that FORS1/2 with GRISM300I+21 provided both an appropriate resolution (~ 10Å) and wavelength coverage (6000 – 11000Å). Depending on the candidate magnitude, one or more spectra were obtained. The classification was eventually achieved looking for the characteristic features of different SN types. This task was made easier and more robust by comparing the high-z spectra with those of well observed local SN which are stored in the Padova SN archive. The spectroscopic follow-up was allocated usually ~ 10 days after the search run. This time interval is a compromise between the need to check the candidates as soon as possible, before they fade away, and the time needed for the image reduction and candidate selection.

The schedule of the observations is reported in Tab. 3.8.

Table 3.8: List of the approved ESO proposals upon which the results of this thesis are based and future allocated observing runs.

Proposal ID.	Date	Nights	Instrument@Telescope	Observer(s)
62.H-0833(A)	Feb. 23, 1999	1	WFI@MPG/ESO2.2m	F. Patat
62.H-0833(A)	Mar. 10, 1999	1	WFI@MPG/ESO2.2m	E. Cappellaro
62.H-0833(A)	Mar. 19, 1999	1	WFI@MPG/ESO2.2m	E. Cappellaro
62.H-0833(B)	Mar. 22, 1999	0.5	EMMI@NTT	F. Patat
63.H-0322(A)	May 08, 1999	1	WFI@MPG/ESO2.2m	L. Rizzi
63.H-0322(A)	May 17, 1999	1	WFI@MPG/ESO2.2m	F. Patat, L. Rizzi
63.H-0322(B)	May 20, 1999	0.5	EFOSC2@3.6m	F. Patat, L. Rizzi
63.H-0322(A)	Aug. 03, 1999	1	WFI@MPG/ESO2.2m	L. Rizzi
63.H-0322(A)	Aug. 14, 1999	1	WFI@MPG/ESO2.2m	L. Rizzi
63.H-0322(B)	Aug. 18, 1999	0.5	EFOSC2@3.6m	L. Rizzi
63.H-0322(A)	Aug. 31, 1999	1	WFI@MPG/ESO2.2m	L. Rizzi
63.H-0322(A)	Sep. 13, 1999	1	WFI@MPG/ESO2.2m	L. Rizzi
63.H-0322(B)	Sep. 16, 1999	0.5	EFOSC2@3.6m	L. Rizzi
64.H-0390(A)	Oct. 30, 1999	1	WFI@MPG/ESO2.2m	E. Cappellaro
64.H-0390(A)	Nov. 09, 1999	1	WFI@MPG/ESO2.2m	S. Benetti
64.H-0390(B)	Nov. 13, 1999	0.5	EFOSC2@3.6m	S. Benetti
64.H-0390(A)	Dec. 02, 1999	1	WFI@MPG/ESO2.2m	A. Pastorello
64.H-0390(A)	Dec. 10, 1999	1	WFI@MPG/ESO2.2m	A. Pastorello
64.H-0390(B)	Dec. 12, 1999	0.5	EFOSC2@3.6m	A. Pastorello
64.H-0390(A)	Dec. 28, 1999	1	WFI@MPG/ESO2.2m	M. Salvo
64.H-0390(A)	Jan. 08, 2000	0.7	WFI@MPG/ESO2.2m	A. Piemonte, E. Pompei
64.H-0390(B)	Jan. 10, 2000	0.5	EFOSC2@3.6m	P. Leisy, E. Pompei
66.A-0413(B)*	Nov. 16, 2000	1	WFI@MPG/ESO2.2m	A. Clocchiatti, G. Altavilla
66.A-0413(C)*	Nov. 25, 2000	1	EFOSC2@3.6m	Clocchiatti
66.A-0413(D)*	Dec. 16, 2000	1	WFI@MPG/ESO2.2m	A. Clocchiatti
66.A-0413(E)*	Dec. 21, 2000	1	EFOSC2@3.6m	Clocchiatti
67.D-0422(A)	Apr. 18, 2001	2	WFI@MPG/ESO2.2m	E. Cappellaro, G. Altavilla
67.D-0422(B)	Apr. 28, 2001	1	FORS1@VLT	E. Cappellaro
67.D-0422(A)[⊘]	Jul. 16, 2001	2	WFI@MPG/ESO2.2m	M. Turatto, A. Pastorello
67.D-0422(B)	Jul. 26, 2001	1	FORS1@VLT	M. Turatto
68.D-0273(A)	Nov. 11, 2001	2	WFI@MPG/ESO2.2m	G. Altavilla
68.D-0273(B)	Nov. 21, 2001	1	FORS1@VLT	S. Benetti
68.D-0273(A)	Dec. 08, 2001	2	WFI@MPG/ESO2.2m	G. Altavilla, M. Riello
68.D-0273(B)	Dec 19, 2001	1	FORS1@VLT	G. Altavilla
69.D-0453(A)	Apr. 07, 2002	2	WFI@MPG/ESO2.2m	G. Altavilla, F. Patat
69.D-0453(B)	Apr. 20, 2002	1	FORS2@VLT	F. Patat
69.D-0453(A)[⊘]	Jun. 04, 2002	2	WFI@MPG/ESO2.2m	M. Riello
69.D-0453(B)	Jun. 15, 2002	1	FORS2@VLT	M. Turatto
72.D-0745(A)	Feb. 18, 2004	2	WFI@MPG/ESO2.2m	...
72.D-0745(B)	Feb. 26, 2004	2	FORS2@VLT	...

* observations made in collaboration with A. Clocchiatti, Departamento de Astronomía y Astrofísica, PUC, Chile. [⊘] run completely lost because of bad weather.

3.3 Data reduction

The primary aim of CCD data reduction is to remove any peculiar effect due to the detector and the telescope: the so called "instrumental signature".
The pre-reduction was performed using the Image Reduction and Analysis Facility (IRAF[7]) and `MSCRED` (Valdes, 1997, 1998), a package specifically designed to handle mosaic images in multiextension FITS format (MEF).
The `MSCRED` package was used to perform all the usual frames pre-reduction steps as follows:

- **Translation of the ESO WFI raw headers for use with `MSCRED`.** First of all the `esosetinst` task is run to fix automatically the default instrument parameters, then all the ESO HIERARCHICAL raw header keywords have to be translated into IRAF standard keywords by means of the `esohdr` package. This includes renaming all HIERARCH keywords, renaming the extension names, setting the observation type, the geometry keywords, and a first order astrometric solution. The RA and DEC keywords are used to define the tangent point of the world coordinate system (wcs) for the mosaic exposure. Because of different pointing set-up required by the observer, not always the pointed coordinates corresponds to the center of the image, as assumed by the astrometric solution. In this case the astrometric solution could be significantly offset with respect to the real pointing. We will come back to this point in §3.4.
  The tasks described above are both contained in the `esowfi` package of `mscred`.
  After these preliminary steps the images are ready for the standard reduction.

- **Overscan correction and bias subtraction.** The `mscred` task `ccdproc` is used to remove the bias level from the images too. The bias level is an electronic offset added to the signal from the CCD that makes sure that the Analogue-to-Digital Converter (ADC) always receives a positive value.

  The ADC samples the charge accumulated in a CCD pixel and returns a digital value (a 16 bit value for WFI). This value is proportional to the actual number of electrons detected in the pixel and is measured in Analogue-to-Digital Units (ADUs). The relation between ADU and the number of photons (charge) is a scale factor known as the gain (2.0 e^-/ADU for WFI).
  In principle the bias level is constant, but it can slightly change during the night because of external factors (like temperature variations). To monitor this effect, the bias level of each image is measured in the "overscan" region (a stripe of a few columns/rows at the edge of the CCDs, which is not exposed to the light, see Fig. 3.6) and removed from the whole frame. To take into account the possible dependence of the bias on the pixel position and remove the residual dishomogeneities from pixel to pixel, a "master bias" image is subtracted from all images. The master bias (Fig. 3.7, left panel) is the average of several ($\sim$ 10) bias images (frames obtained

[7] http://iraf.noao.edu/
IRAF is distributed by the National Optical Astronomy Observatories (NOAO), which are operated by the Association of Universities for Research in Astronomy (AURA), Inc., under cooperative agreement with the National Science Foundation.

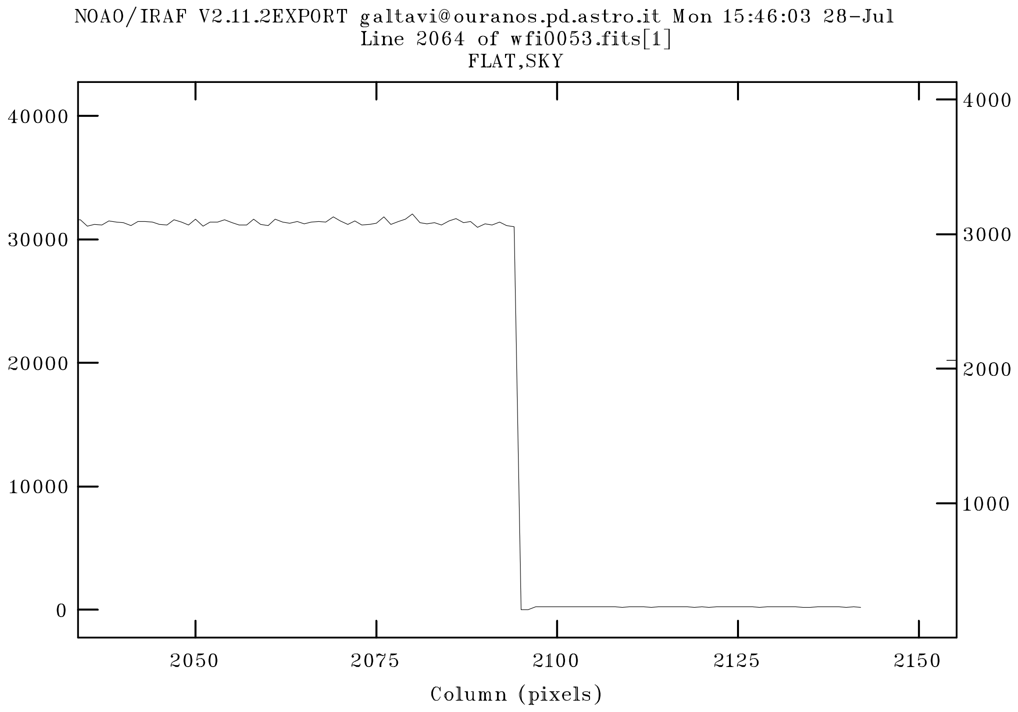

Figure 3.6: For chip #1 of the WFI mosaic the overscan section is [2095:2142,*], that is from column 2095 to 2142, from the first to the last line of the image.

with exposure time of 0 seconds and closed shutter), and is obtained with the `mscred` task `zerocombine`. Several images are combined in order to gain a better statistics, to reduce the read-out noise (RON$\simeq 5e^-$/pixel for the WFI) and to get rid of cosmic rays.

- **Dark correction** is the subtraction of the electron count which accumulates in each pixel due to thermal noise. The reduction of dark current is the main reason why all astronomical CCDs are cooled to liquid nitrogen temperatures. Most modern CCDs only produce a few ADU counts per pixel per hour. In particular the WFI dark signal is hardly measurable and typically of the order of 3×10^{-4} – 6×10^{-4} ADU/sec/pix, so this correction can be ignored.

  After bias subtraction (and dark correction) the data values are now directly related to the number of photons detected in each CCD pixel.

- **Trimming.** The `mscred` task `ccdproc` is used for trimming the images, reading the information embedded in the header by the `esowfi` package (each CCD of the mosaic has a different trim section). The trimming is necessary to cut off the edge of the images, often affected by irregular response and degraded, and to cut off the overscan region after use.

- **Flat fielding.** The final stage in the correction of CCD data for instrument signature is the "flat fielding". The CCD response to the incident light is not uniform

(i.e. the recorded signal per unit of incident flux - photons - is not uniform) and can shows variations on the large scale (from one side of the frame to the other) and pixel-to-pixel. The basic idea of flat-field correction is to divide the data by a "sensitivity map" (flat-field) created from calibration exposures.
The effect of dust on the filters or on the detector and the vignetting are also corrected by flat fielding. When imaging, an evenly illuminated scene is used as the flat field. It can be a uniformly illuminated screen inside the telescope dome (dome-flats) or, better, the sky at twilight/dawn (sky-flat), which secure a more uniform illuminated field of view and preserves the natural path of light, coming from "infinite" distance. Since the detector efficiency changes with the wavelength, flats are needed in all the bands used for the scientific frames. Also in this case "master-flats" (see Fig. 3.7, right panel) are built averaging a number of flats in order to have a better statistics, to reduce the read-out noise and to get rid of cosmics. The `mscred` tasks used are `flatcombine` (for dome flat exposures) and `sflatcombine` (for sky flat exposures).

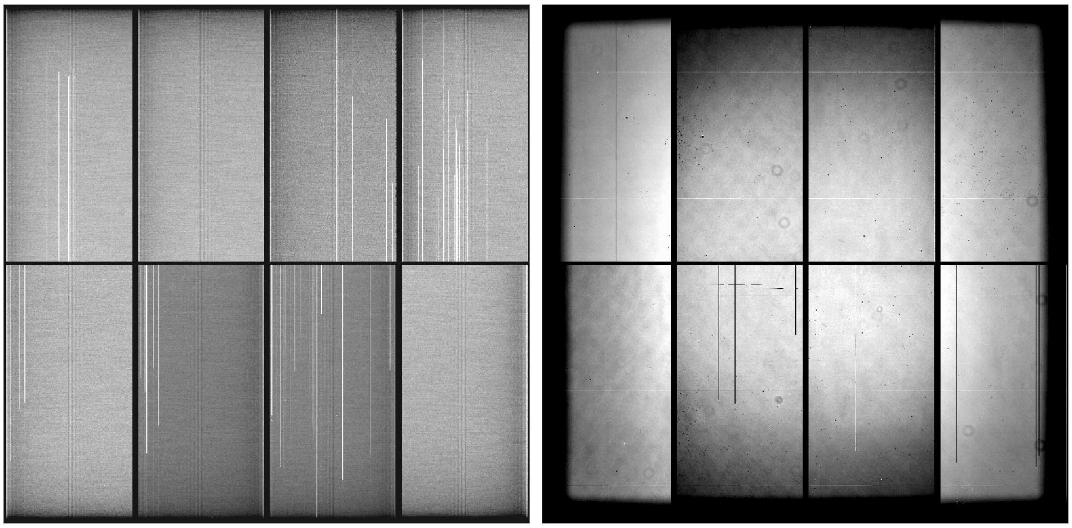

Figure 3.7: Left: Master bias. This image is the average of 10 frames. Right: Master Flat. This image is the median of 4 sky-flats in the V band.

It is common experience that sky flats do a better job of flattening the data. But also sky flats are not perfect, since they can not reproduce exactly the sky condition during the observations. A simple example is given by the illumination pattern due to a bright moon. Clearly, sky flats couldn't work in this case. For these reasons, to remove remaining large scale features, it is usually necessary to combine all the scientific images, already flat fielded, in order to build a "super-flat" (see Fig. 3.8), one for each band. An outlier rejection is necessary to get rid of stars and galaxies. The selection of the images to be used (with no or just a few bright stars), the number of frames available to combine and the rejection algorithm adopted are critical to obtain good results. For this reason the "super-flat" correction has not always been applied.

Fig. 3.9, 3.10 shows a typical raw image and how it appears after debiassing, trimming and flat fielding; Fig. 3.11 show the improvement obtained with a super-flat

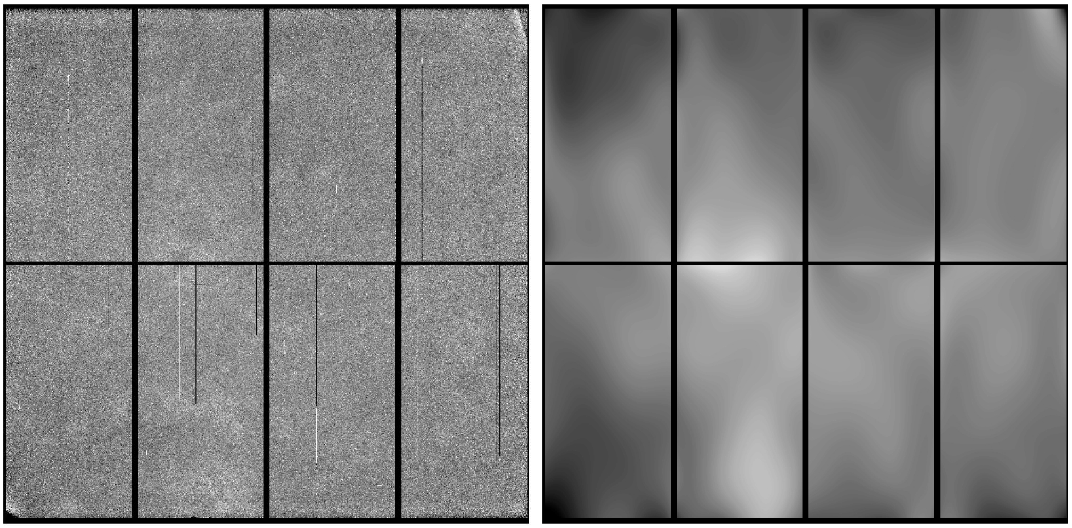

Figure 3.8: Left: Super-Flat. This image is the median of 8 scientific images in the V band. Right: Since there are still residual haloes of bright stars and we are not interested any more in small scale sensitivity variations but only in large scale gradients, we use the task `mscskysub` to smooth the original super-flat.

correction. Again the adopted `mscred` task is `ccdproc`.

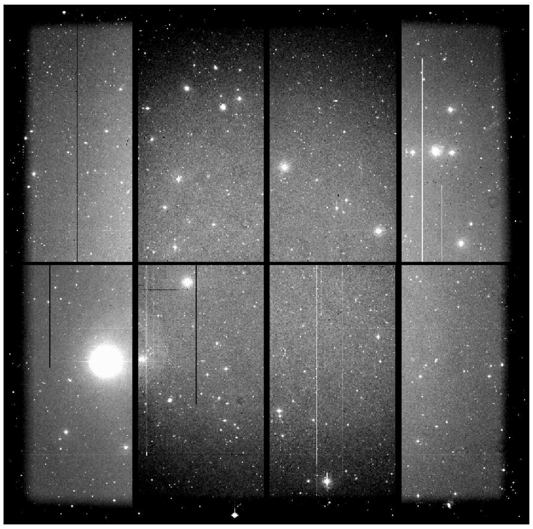

Figure 3.9: Typical raw image. Field name: 22Z3, V band, exposure time: 900s, observing date Nov. 11, 2001 (size: $\sim$ 142 Mbytes).

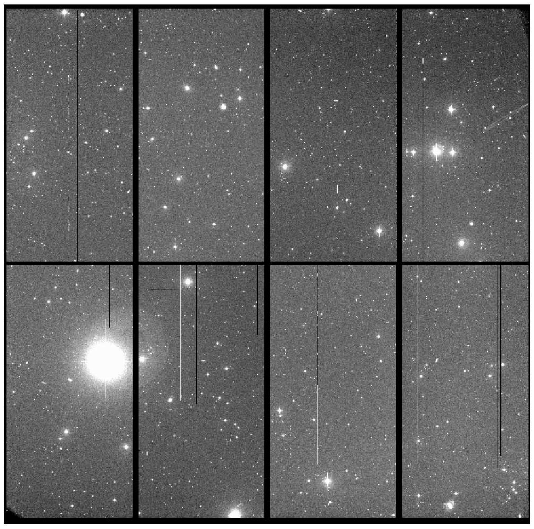

Figure 3.10: Image debiassed, flat-fielded and trimmed. (size: $\sim$ 268 Mbytes)

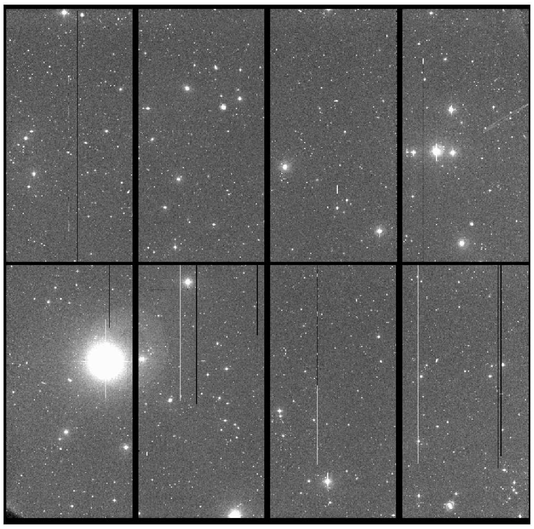

Figure 3.11: Image debiassed, flat-fielded , trimmed and corrected with a super-flat field.

3.4 The STRESS package

In order to minimize the amount of the observer interaction required to perform the SN search on the pre-reduced frames, we developed a specific package, dubbed `stress` as the SN search project.
Our reduction strategy was based on a full integration in the IRAF environment. The `stress` package has been written using the IRAF command language. Two external packages widely used, ISIS[8] (Alard and Lupton, 1998; Alard, 2000) and SExtractor[9] (Bertin and Arnouts, 1996), have been implemented to perform specific operations, as described in the following sections.

The development of this software as well as the artificial star experiments performed to check and improve its efficiency represent one of my major contribution to the SN search programme.

Besides providing a set of well tested facilities (*tasks*) for wide field image manipulation, the IRAF context allowed us a great flexibility and portability of the specific reduction tools we developed.
This is an important point because the SN search need to be performed during the observing run, far from the home institution, and it was often necessary to install the package on the machines available on site.
The SN search is performed in three steps:

1. **image coaddition** of the dithered pre-reduced images;
2. **image subtraction** of a template frame properly chosen;
3. **SN candidates detection** on the subtracted images.

The image coaddition is necessary to get rid of cosmic rays, satellite tracks, minor planets, detector defects (bad column, hot or dark pixels...) and of any other spurious detection which appears in only one of the dithered images and can produce false supernova detection. For this reason during observations of the same field, multiple exposures are taken, with pointing shifted by ~ 7 arcsec (that corresponds to ~ 30 pixels) both in right ascension and declination. This shift is large enough to avoid the larger batches of bad columns (~ 10 pixels wide) to overlap and multiple exposure,together with an outlier rejection, allow us to reject the spurious detection.

In order to identify supernova events, the combined images are compared to a reference image, taken in a different epoch. After the subtraction of the template image, all variable sources (SN events included) in the image to be searched stand alone and can be easily identified.

Of course not all the residuals left in image obtained after the subtraction represent

[8] http://www2.iap.fr/users/alard/package.html

[9] http://terapix.iap.fr/cplt/oldSite/soft/sextractor/

Table 3.9: List of the tasks of the `stress` package along with a short description of their function.

Task	Description
`combina`	Coaddition of the mosaic dithered images and splitting
`castro`	Astrometrical calibration of the combined splitted images
`isisdiff`	Image subtraction (by *ISIS2.1*)
`candidate`	Search for SN candidates, scoring and display of the detected sources
`variability`	For comparing photometry and verify variable sources
`cara`	For stellar and galaxy counts
`look`	For comparison and analysis of the SN candidates
`checkhist`	For checking the "variability history" of the SN candidates
`swarpcom`	Coaddition of the mosaic dithered images by the SWARP package
`map`	Print a gif image of a field, marking the coordinates of a reference star

supernovae, there are also other sources such as variable stars or active galactic nuclei (AGN). There are also spurious residuals due to bad subtractions and image defects. In order to reduce the false detections we developed a scoring algorithm which automatically evaluate the reliability of a residual detection and gives an higher score to the events which, on the base of artificial stars experiment previously performed, could be a SN event.
These three steps will be described in details in sections §3.4.1, §3.4.3, §3.4.4. The tasks developed to perform these steps and additional auxiliary tools are listed in Tab. 3.9.

After this the image analysis proceeds as follows.
As explained in §3.3, the original astrometric solution, associated to each mosaic image by the `mscred.esohdr` task, is often significantly offset with respect to the real pointing. Since a correct astrometric calibration speeds up the reduction (e.g. the `isisdiff` task can read the shift between the images to be subtracted by the corresponding headers instead of waiting for an input from the observer), the first step is to correct the WCS zeropoint. This is done with the `mscred.msczero` task using the coordinates of a reference star (see Fig. 3.12). Maps of the fields and reference stars are made available in web[10]. As we will see later, the centering of the astrometric solution is be refined in a second phase with `stress.castro`, in order to get accurate coordinates for the SN candidates.

3.4.1 Combining images: `combina.cl`

The `stress` task for the image coaddition is `combina`. The input frames are mosaic MEF images, but they are soon splitted into singles chips and all the following analysis will be performed chip by chip.

First, the dithered images of each field are trimmed to the overlapping region. The small fraction of area lost ($\sim 6\%$) is compensated by the better quality of the combined smaller

[10] http://web.pd.astro.it/supern/esosearch/public/fieldlist.php?action=list

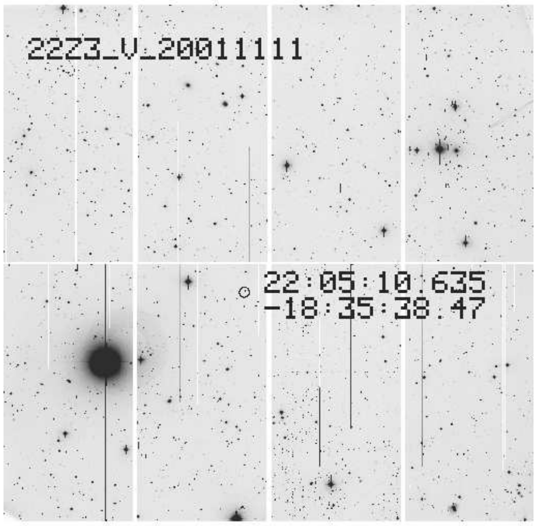

Figure 3.12: Map for the 22Z3 field. Filter, observing date and reference star coordinates are shown.

image.
The shift between dithered images is automatically computed exploiting the first order astrometric solution previously centered with `msczero`. The computed shifts are then used to trim the frames to the common area. If the dimension of each image is dim_x, dim_y, and if the shifts are $x_1, x_2, ..., x_n$ with $x_1 = 0$, and $y_1, y_2, ..., y_n$ with $y_1 = 0$, then the overlapping region bottom-left corner and top-right corner are given respectively by $(max(x_1, x_2, ..., x_n), max(y_1, y_2, ..., y_n))$ and $(min(x_1, x_2, ..., x_n)+dim_x, min(y_1, y_2, ..., y_n)+dim_y)$. After this step the images are roughly coincident. There are actually small differences due to the geometrical distortions (smaller than 0.08%, see Tab. 3.4, which corresponds to ~ 3.5 pixels from one end to the other of a single CCD).

The background of the dithered images can be different because of variable sky condition (Moon, humidity and sky transparency), because of the shifts (bright star falling at the edge or out of the CCDs) and because of technical factors (e.g. detector temperature variation). For the same reasons also the counts associated to each source (star or galaxy) can be slightly different.
The `combina` task correct for these effects before combining the dithered images.

The geometric alignment is performed through the standard IRAF tasks **`xyxymatch`**, **`geomap`** and **`gregister`**. The accuracy of the first order astrometric solution does not affect the quality of the stacked image because the dithered exposures are aligned geometrically matching the common stars in the frames. To perform this step is necessary to create, for each image to be combined, a catalogue of stars, which are used as references to compute the spatial distortions. For a good result is important to have enough and well distributed stars to compute the geometrical transformations.
The catalogues we need are created with *SExtractor* (software for source extraction), a programme which extracts and classifies objects in a FITS image (Bertin and Arnouts,

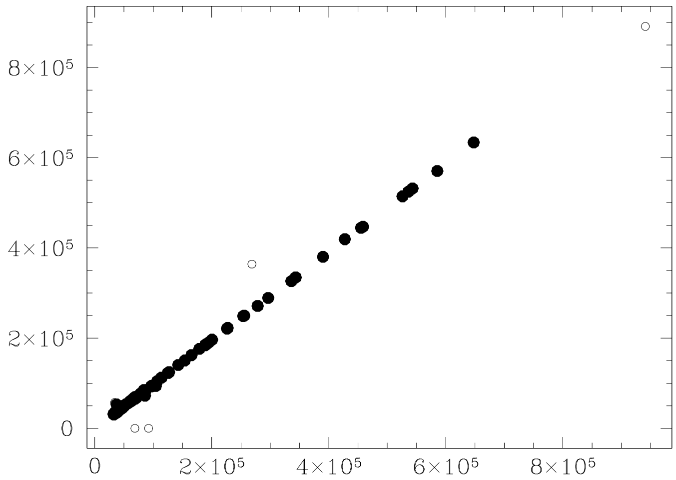

Figure 3.13: Photometric comparison of two images. y axis: flux of the reference stars; x axis flux of the stars to be matched. The slope represents the multiplicative factor to be used to match photometrically the images. Filled dot: points used for the linear regression, empty dots: points rejected after iteration.

1996). This is a very powerful and flexible tool, extensively tested and widely used by the astronomical community, capable of detecting objects above a fixed threshold and performing both deblending and star/galaxy classification in an automatic way. SExtractor uses a neural network to compute whether an object is stellar or a galaxy, returning the so called "stellarity index". This parameter varies between 0 (for galaxies) and 1 (for stars).

Trimmed images are not yet perfectly matching and, in order to measure x and y residual shifts, different magnifications factors and rotation angles, the stars in the common area are selected and matched. This is done by `xyxymatch`.
The `geomap` task reads the lists of common stars and by comparing their pixel coordinates computes spatial transformation functions to be applied in order to match the images (usually the first image of each dithered set is taken as reference).
Then the `gregister` task is used to apply the coordinate transformation functions correcting for the images geometric distortions.

After geometrical alignment and before combination, photometric registration is necessary. The photometric differences between the images can be splitted into two components, the sky background and the stars, with different behaviour, additive or multiplicative respectively. These two components are treated separately.
Using the IRAF task `imsurfit`, the sky background is modelled with a low order polynomial and subtracted.
Next, the flux of a number of common stars is measured on each image and compared to flux of the same stars in the first image of each set, which is taken as reference. From the average ratio of the corresponding fluxes one derive the multiplicative factor to be used to match photometrically the images. Since individual stars can be affected by bad pixels or cosmic rays, the procedure is iterated to reject all stars deviating more than 1 rms from

the average (see Fig. 3.13).
Images are now ready to be combined. This step is performed with the IRAF task `combine`. In order to obtain a better result, the images are combined using a median algorithm and a bad-pixel mask (already trimmed and registered as the corresponding images) built on purpose (see Fig. 3.14). A bad-pixel mask is a frame of the same dimension of CCD to which it is associated, with pixel value zero but in the hot/dark pixel and in the bad columns. Masked pixels are rejected while combining. Since the images are dithered, the same anomalous pixel is projected in different sky positions and it can be replaced by the corresponding area, free from defects, in one of the dithered images.

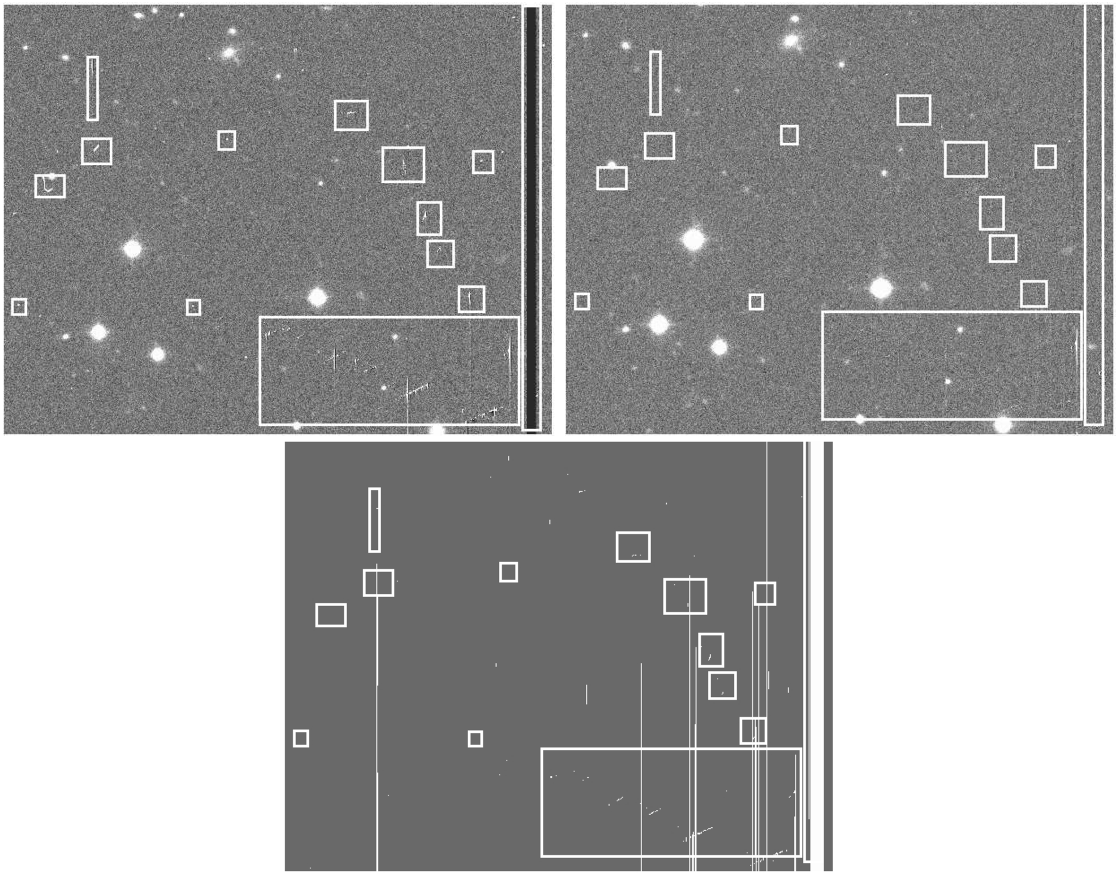

Figure 3.14: Comparison between a pre-reduced image (top-left panel) and the sum of three dithered exposures of the same region (top right panel). The CCD defects and spurious detections (the white boxes marks some of them) are strongly reduced. The bottom-center image shows the bad-pixel mask of the same CCD area.

Finally an average background level is added to the combined image. This is useful to maintain the statistics for further step of the analysis.
The `input/output` of the `combina` task is shown in Fig. 3.15. This is one of the most time consuming step of the procedure: on a Linux PC (RAM = 1 Gbyte, processor clock = 1.2 MHz) the coaddition of three mosaic images takes $\sim$ 18 min.

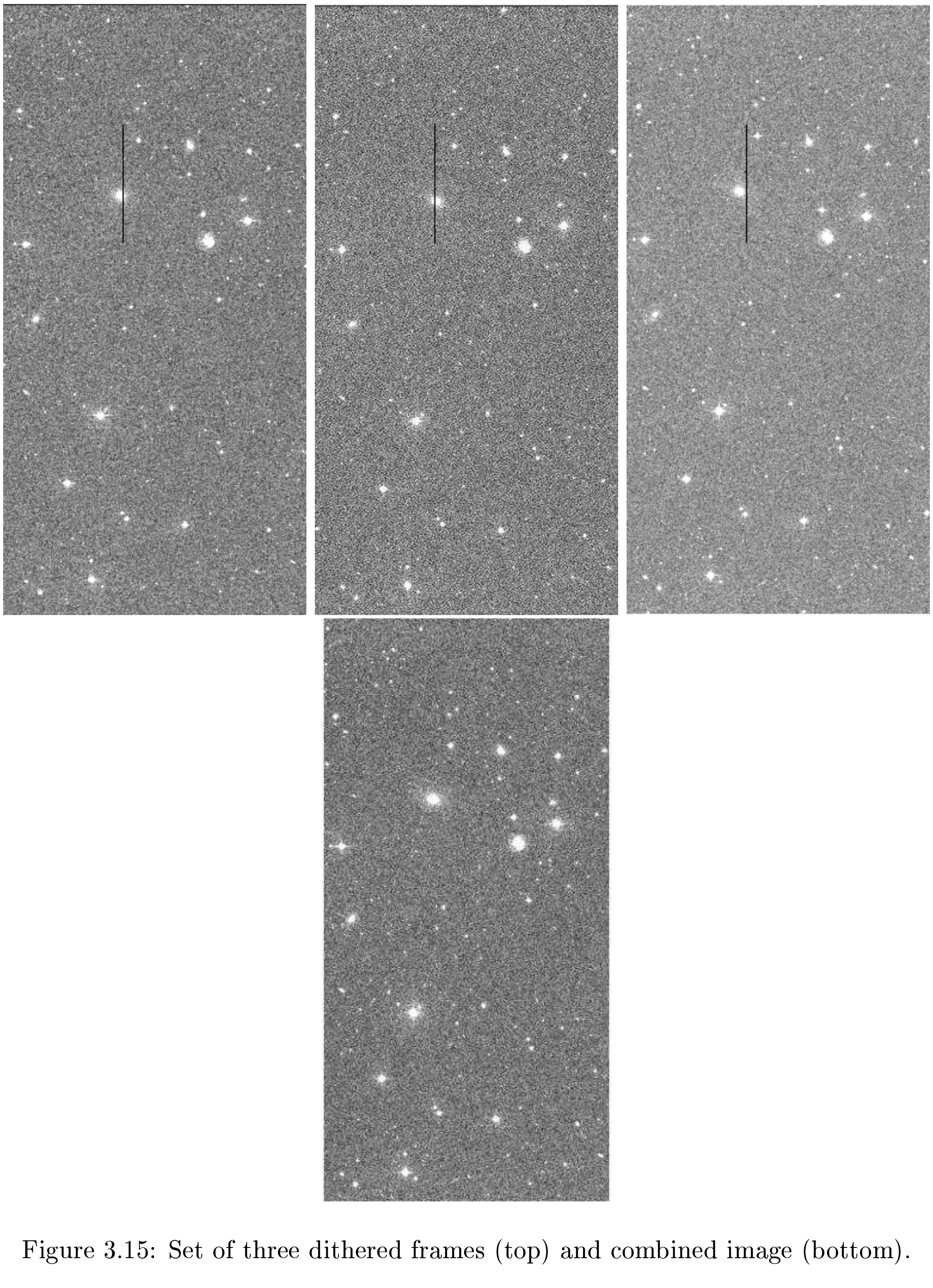

Figure 3.15: Set of three dithered frames (top) and combined image (bottom).

3.4.2 Refining astrometry: `castro.cl`

The combined images astrometry is refined with the `stress` task `castro`. Independent solutions are computed for each of the eight CCDs. First the `mscred.mscgetcat` task is used to download from the web a star catalogue (in our case the USNO-A2 catalogue by Monet et al. 1998), centered on the field (the coordinates are read from the image header). Then only the stars falling in the processed chip are selected. `ccfind` locates the objects of the input catalogue in the input images using the first order astrometric solution already provided by the task `esowfi`, and writes the located objects to the output matched coordinates files. The `ccmap` task is used to compute the plate solutions using the `ccfind` output. This procedure is iterated twice because in case of large correction to the original astrometry, a single run is not enough to obtain good results.
To estimate the precision of the astrometric calibration, the positions (α, δ) (world coordinate) of more than 1500 objects were extracted from the USNO-A2 catalogue, converted into (x, y) (logical coordinates) by means of the astrometric solution and compared to the (x, y) coordinates of the corresponding objects. The offsets between the positions measured on the image and those retrieved from the USNO catalogue are shown in Fig. 3.16 (left panel). The average offset is $\bar{r} \sim 0.37 \pm 0.43$ arcsec (1.55 ± 1.8 pixels), but, as shown in Fig. 3.16 (right panel), most of the objects differ from the catalogue position $\sim 0.2''$ (i.e. less than 1 pixel) and $\sim 70\%$ of the objects falls within $\sim 0.35''$ (~ 1.5 pixel) from the catalogue position (see Fig. 3.17).
Of course this experiment is related to the precision of the catalogue used as reference and not to the astrometric absolute accuracy. However the fact that our results reflects the precision of the catalogue (the USNO-A2 typical astrometric errors are 0.25 arcsec) shows that astrometry can not be significantly improved but using more precise star catalaogue (e.g. the star positions given by Stone et al. 1999 are typically accurate to ± 26 mas, ± 12 mas precision, but data are limited to 16 fields located around the celestial equator). In any case high precision astrometry is not required by our purposes.

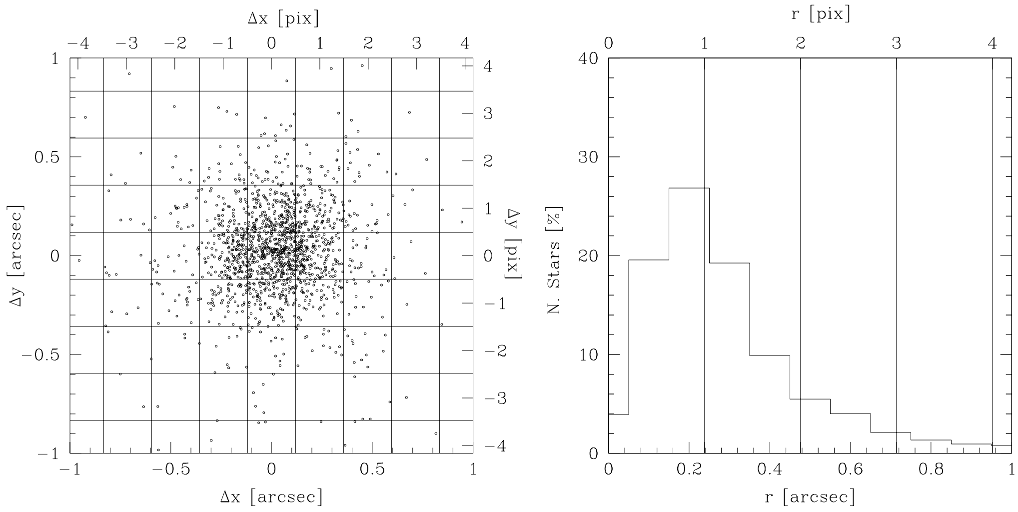

Figure 3.16: Left: Distribution of the differences Δx, Δy between the absolute position of the USNO-A2 stars and the computed position using a V frame astrometrically calibrated. The grid shows the physical dimensions of the pixels. 1568 stars from the field 22Z3 are shown. Right: Histogram of the distances r derived from the left panel. Mode of the distribution: 0.2 arcsec. The vertical grid shows the physical dimensions of the pixels.

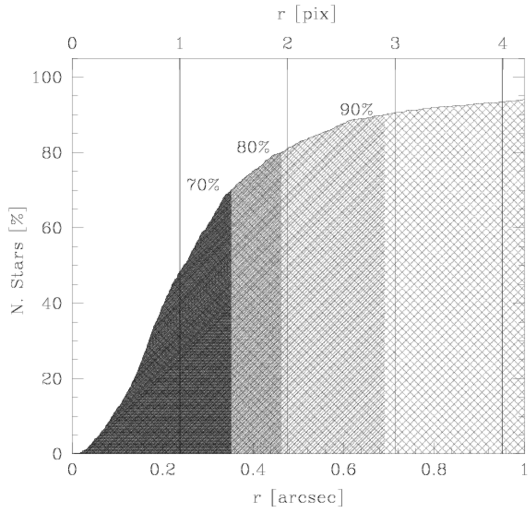

Figure 3.17: Cumulative distribution of the residuals between the absolute position of the USNO-A2 stars and the computed position using a V frame astrometrically calibrated. The vertical grid shows the physical dimensions of the pixels. The 70, 80, 90% levels are shown.

3.4.3 Image subtraction: `isisdiff.cl`

The first steps of the **stress** task **isisdiff** are similar to those of the task **combina** (already described in §3.4.1): first the images to be searched and the template ones are trimmed to the overlapping area and geometrically registered.
Then the template frame for each field is subtracted from the image to be searched using the *ISIS2.1* package by Alard and Lupton 1998 (see also Alard 2000), which takes care of matching the PSF of the two images using a space-varying kernel.
Even if *ISIS* always tries to match the seeing of the two images by degrading the best image to the worst, our experience is that the best results can be achieved when the seeing of the images to be subtracted is similar (the difference is less than 50%).
The reference image (in the *ISIS* convention that with the best seeing) is convoluted with a space-varying kernel in order to match as close as possible the other frame. The *ISIS* software takes care of the photometric matching and of the geometrical alignment, correcting for small shift or rotation, due to a not perfect image registration of the two frames. Finally, the image obtained after the subtraction is photometrically scaled to the reference image.
There are a number of important parameters for image subtraction, which can affect strongly the result. The most important parameters are the kernel size, the degree of spatial variations of the kernel coefficients as a function of the position in the image, the degree of the differential background variations and the number n and size of the "stamps" taken by the program around each object. Basically, the program looks for a number n of bright objects (not necessary stars) and defines small windows ("stamps") around each of them. The stamp size must be somewhat larger than the size of the kernel to be derived. Other relevant inputs are the saturation limit of the image and the minimum value for the pixels to fit.
The **input/output** of the **isisdiff** task is shown in Fig. 3.18.
This is the most time consuming task of the pipeline: on a Linux PC (RAM = 1 Gbyte, processor clock = 1.2 MHz) the subtraction procedure takes on average $\sim$ 25 min (for 8 chips).

3.4.4 Searching for SNe: `candidate.cl`

The point sources in the difference image are detected using the *SExtractor* program (Bertin and Arnouts, 1996).
The output catalogue contains true variable sources, including SN events, but also many false detections due to the presence of bad subtraction residuals produced by bright saturated object or cosmic rays.
The detection list is then sorted according to a custom made ranking program designed to remove false detections thus reducing the sources list from about one thousand to about one hundred. The program check position, shape and flux of the detected sources and assign each source a score proportional to the reliability as SN candidate. This scoring algorithm has been tuned through extensive artificial star experiments.
In order to cross-check the detection, both the new image and the template one are also searched with *SExtractor*. The corresponding three catalogues are used by the scoring

Figure 3.18: From left to right: image to be searched, template image, subtracted image. To be noticed that the images can have different size. The resulting difference image is trimmed to the common area. The subtraction is performed after geometric and photometric alignment. The best PSF image is convolved to the other.

algorithm as explained below:

- Remove saturation residual: the capability of pixels to hold charge has a limit[11] and, after this limit is exceeded, the pixel stops accumulating charge. The excess from it "bleeds" along the readout columns and sometimes even across them (see Fig. 3.19,3.20). This features, due to bright saturated stars, are not constant. For this reason and because of the anomalous shape, saturated stars can not be perfectly subtracted and leave residuals. So first of all, detections near saturated stars are removed from the detection list.
- Faint objects near bright stars or bright galaxy nuclei are penalized (but not removed) because they are most often residual due to a poor subtraction.
- Detections with no counterpart on new image are also penalized (but not removed because the source could be under the adopted detection threshold).
- Detections with Full Width Half Maximum (FWHM) outside the average range, are reduced in rank by assigning them a negative score proportional to the difference from the expected value;

[11]The WFI Full-well capacity is more than 200000e$^-$/pixel, but the 16 bit gain amplifier saturates at ~ 130000 e$^-$/pixel (at the fixed inverse gain factor of ~ 2e$^-$/ADU it provides a dynamical range up to ~ 65000 ADU).

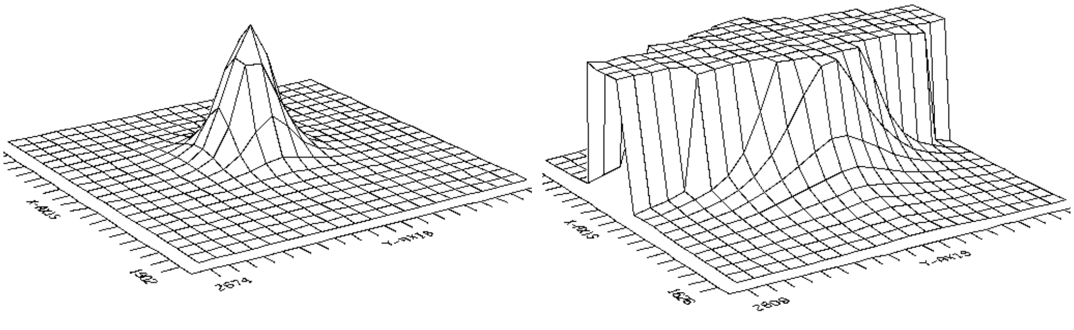

Figure 3.19: Left panel: normal star shape; Right panel: bright saturated star shape.

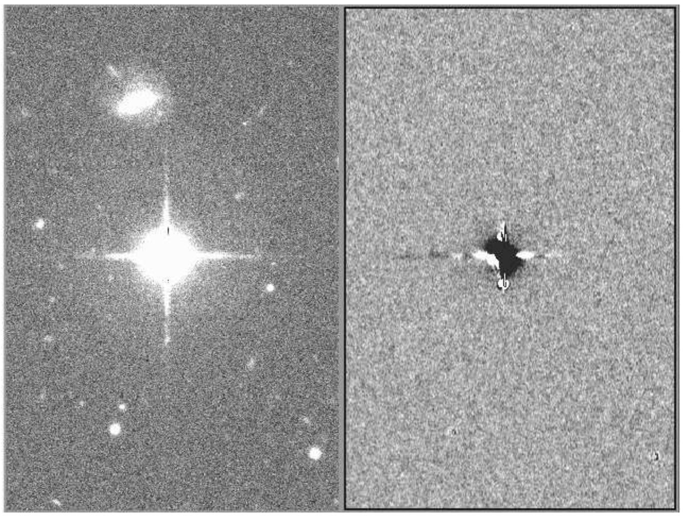

Figure 3.20: Residuals left by saturated star. Left panel: image to be searched. Right panel: subtracted image.

- Candidates whose fixed aperture magnitudes and aperture magnitudes scaled to the FWHM differ more than fixed values (0.5 or 1.0 mag.) are penalized (bad subtracted sources which appear in the subtracted image as bright and dark spots (see Fig. 3.21) shows different magnitudes if measured in different ways).
- Finally, detection close to galaxies and with appropriate FWHM for stellar sources are assigned a positive score.

All these operations are very fast. Usually a complete mosaic (8 chips) with about one thousand residuals detected by *SExtractor*, is searched and the detection analyzed by the scoring algorithm in a few minutes (~ 3), and a list of ≤ 100 candidates is obtained. The procedure was calibrated through artificial stars experiments in order to give a positive score to real variable sources.
The SN candidates with score ≥ 0 are visually inspected for the final selection, starting

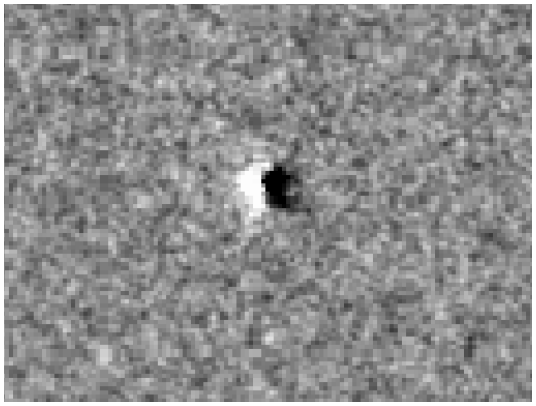

Figure 3.21: Example of bad subtraction.

from the ones with the higher score. The visual output of the `candidate` task is shown in Fig. 3.22. The SN candidate and its main characteristics (coordinates, position on the frame, magnitude, *SExtractor* stellarity index, FWHM, distance from the host galaxy) are also shown. Magnitudes have been measured with aperture photometry. The photometric calibration of the images has been done using the Landolt (1992) standard fields observed the same night of the images to be calibrated. In the case that the night was not photometric, we computed the photometric zero points for each field in a relative way, by comparison with an image obtained in photometric conditions. The photometric calibration was needed only to have a rough estimate of the candidate magnitudes for the follow-up selection.

At this stage most of the SN candidates are rejected. Most of them turn out to be bad subtractions (Fig. 3.23) and only a small fraction turn out to be real variable sources like variable stars or AGNs. A few detections turn out to be minor planets[12]. At the end we are left with one or two promising SN candidates per field.
During the last runs of the SN Search we took advantage of the data accumulated in the past runs in order to check the "variability history" of the detected candidates. This was done with queries to our archive[13] (see Fig. 3.24) which contains the data of the past runs. Thus it is possible to check, and reject, the objects that already occurred in the past and are not compatible with a SN light curve (periodically variable sources). The archive is a MySQL database built by Riello (2002), with a web interface, designed to be useful both during the observation and the reduction-analysis phases, giving fast access to all the information about the monitored fields and past candidates.

A typical observing run, with $\sim$ 10 observed fields, provides from 5 to 15 reliable SN candidates, depending on the seeing and the sky transparency.

[12]Slow moving objects are detected by chance when the tracks left in the dithered exposure partially overlap. In fact the search technique is not optimized for their detection, indeed when the tracks are well separated, these objects are removed from the combined image of the dithered frames.

[13]http://web.pd.astro.it/supern/esosearch/

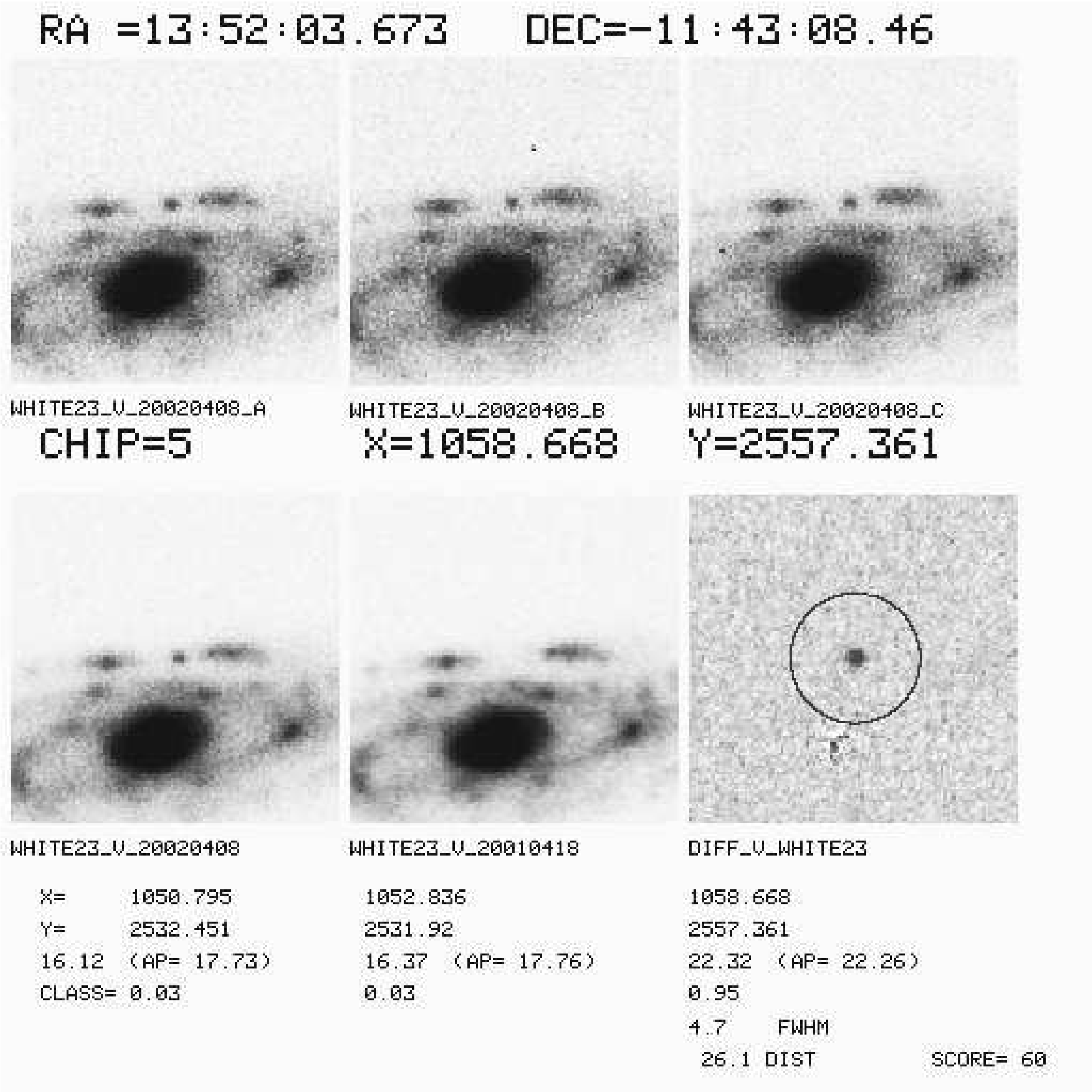

Figure 3.22: Example of the `candidate` output used for the visual inspection of the SN candidates. The three images in the upper line are the dithered frames, in the second line, from left to right, the combined, the template and the subtracted image are shown. This SN candidate turned out to be a type II SN at $z \sim 0.09$ after spectroscopic check (SN 2002cm, cf. IAUC 7885). The principal information about the object are also shown: coordinates α, δ; (x, y) position in the chip and chip number, magnitudes, stellarity index (given by *SExtractor*), FWHM, distance from the host galaxy, score obtained by the ranking program.

The selected SN candidates are spectroscopically observed 1–2 weeks after the search run, in order to determine their nature and redshift. For the observing runs previous to april 2001 the spectroscopic follow-up was performed with the 3.6m telescope and NTT at ESO-La Silla. After this date the follow-up was performed with the 8.2m VLT telescope, equipped with FORS1/2. The need for VLT is due to the faintness of the

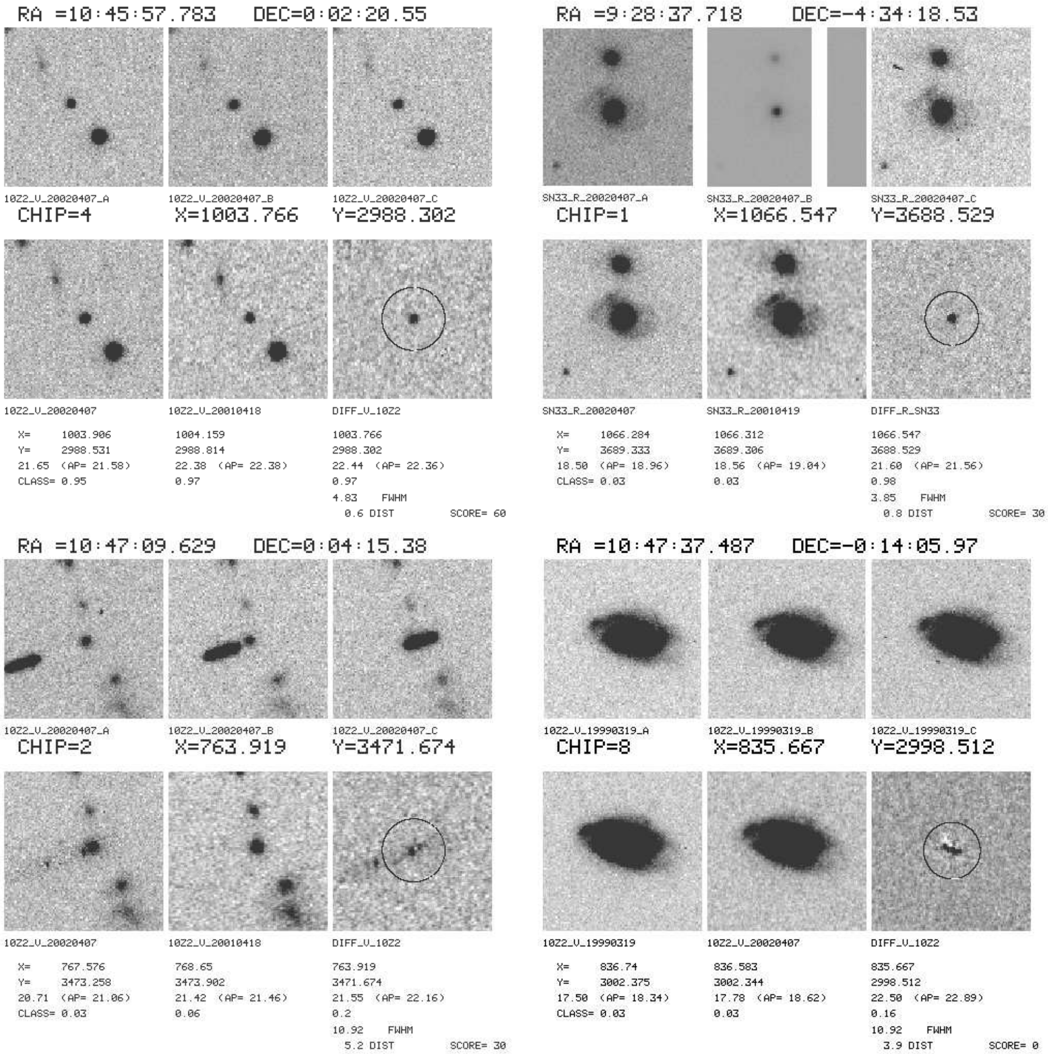

Figure 3.23: Example of SN candidates. In clockwise order: a possible variable star, a spectroscopically confirmed AGN, a slow moving objects and a bad subtraction.

selected candidates (typical mag. $\sim 22.5 - 23.8$), which require long exposure times (1–3h) in order to reach a useful signal to noise ratio ($3 < S/N < 15$).

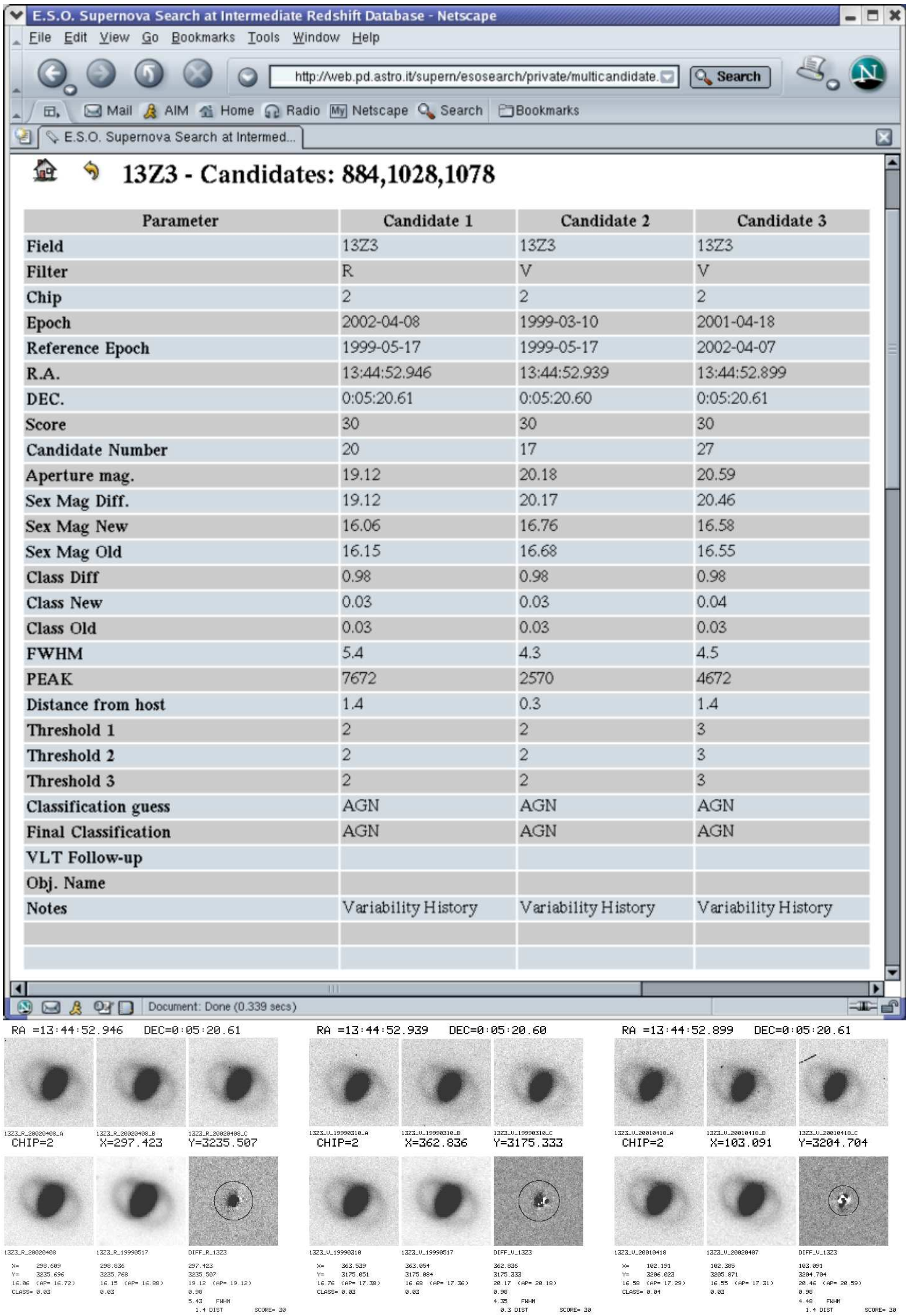

Parameter	Candidate 1	Candidate 2	Candidate 3
Field	13Z3	13Z3	13Z3
Filter	R	V	V
Chip	2	2	2
Epoch	2002-04-08	1999-03-10	2001-04-18
Reference Epoch	1999-05-17	1999-05-17	2002-04-07
R.A.	13:44:52.946	13:44:52.939	13:44:52.899
DEC.	0:05:20.61	0:05:20.60	0:05:20.61
Score	30	30	30
Candidate Number	20	17	27
Aperture mag.	19.12	20.18	20.59
Sex Mag Diff.	19.12	20.17	20.46
Sex Mag New	16.06	16.76	16.58
Sex Mag Old	16.15	16.68	16.55
Class Diff	0.98	0.98	0.98
Class New	0.03	0.03	0.04
Class Old	0.03	0.03	0.03
FWHM	5.4	4.3	4.5
PEAK	7672	2570	4672
Distance from host	1.4	0.3	1.4
Threshold 1	2	2	3
Threshold 2	2	2	3
Threshold 3	2	2	3
Classification guess	AGN	AGN	AGN
Final Classification	AGN	AGN	AGN
VLT Follow-up			
Obj. Name			
Notes	Variability History	Variability History	Variability History

Figure 3.24: The top panel shows the output generated by the database query which retrieves the information for variable sources detected in different epochs. For each detection the page summarizes the parameters of interest (magnitudes, *SExtratctor* stellarity index, celestial coordinates etc.) The page also show the `candidate` output of each detection (bottom panels). In this example a recurring variable source has been detected in march 1999, april 2001, april 2002. The stellar residual at the center of the galaxy and the 3 years baseline variability allows us to classify with high confidence this sources as an AGN.

3.5 Spectroscopically confirmed SNe

In Fig. 3.25, 3.26 we show examples of confirmed supernovae. The first one, SN 2002cm, is easily detected, while the second one, SN 2002cn, is a more difficult object, well visible only after the galaxy subtraction.

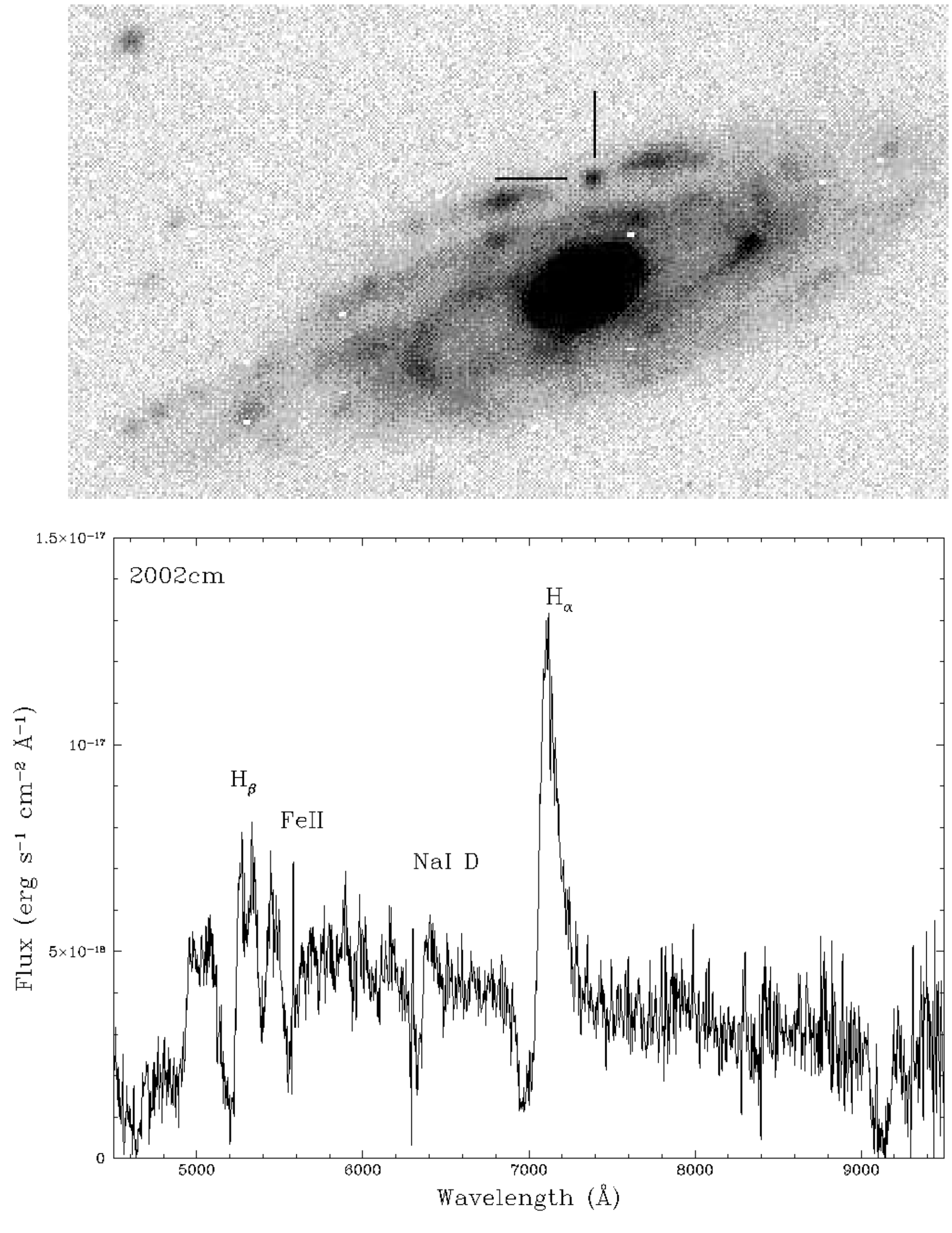

Figure 3.25: Upper figure: SN 2002cm, type II, V=22.3, z=0.09, IAUC 7885. The host galaxy LCRS B134923.7-112828 is classified as irregular in the NASA/IPAC Extragalactic Database (NED), but in the FORS2 image shown here this galaxy seems to be a spiral with extensive arms. Lower figure: SN 2002cm spectrum.

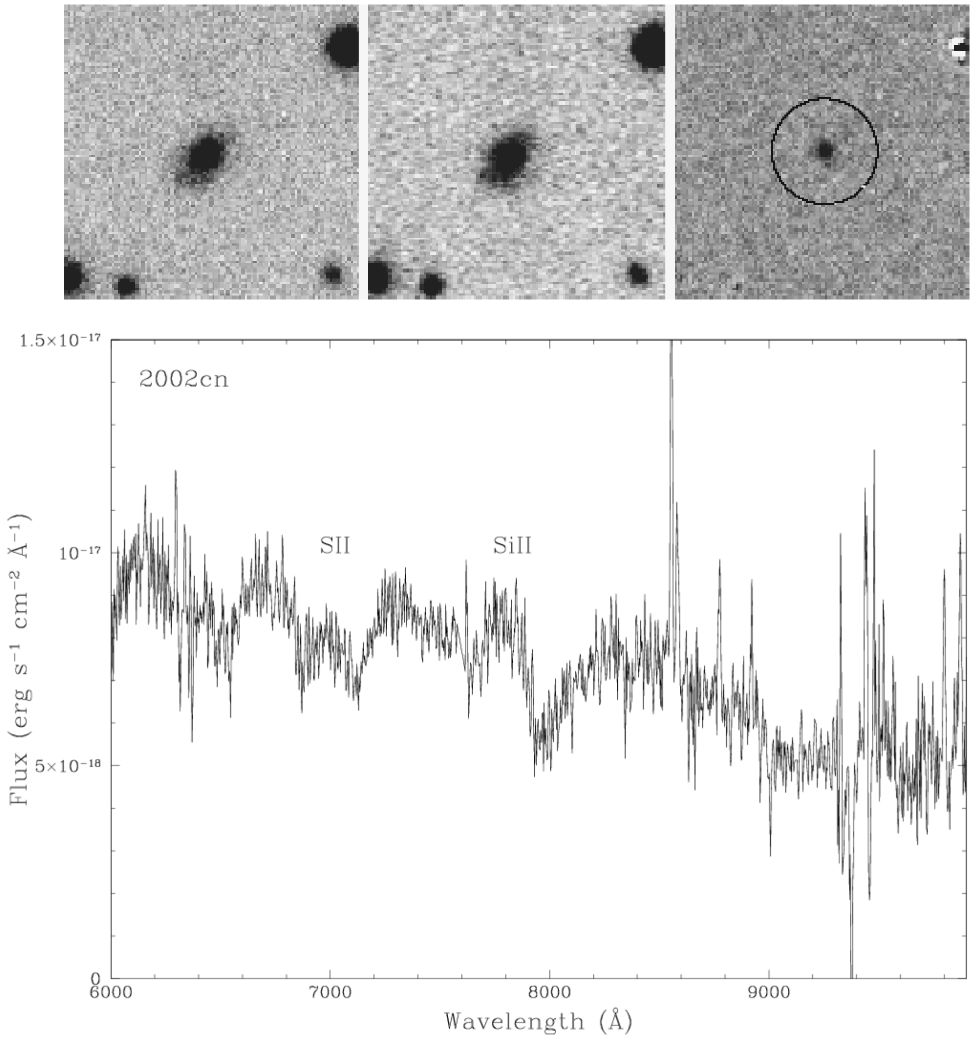

Figure 3.26: Upper figure: SN 2002cn, type Ia, V=22.3, z=0.30, IAUC 7885. From left to right: image to be searched, reference image, subtracted image. Only after the subtraction the SN, close to the host galaxy nucleus, is well visible. Lower figure: SN 2002n spectrum.

In the course of our search we surveyed 21 fields. The effective searched area is $\sim$ 5.1 square degrees. We detected $\sim$ 200 SN candidates and we confirmed spectroscopically 22 supernovae, distributed as follows: 10 type Ia, 10 type II, 1 type IIn and 1 type Ic (Tab. 3.10). The SN redshifts range in the interval $0.07 \leq z \leq 0.61$ with a peak at $z \sim 0.2$. The apparent V magnitude at discovery is in the interval 20–24, with a peak at magnitude $\sim$ 22.5 (Fig. 3.27a). We found CCSNe and SNe Ia in almost equal proportion but, as expected, due to the brighter absolute magnitude the latter are on average at higher redshift than the former ones (Fig. 3.27b).
As a rule, during the visual inspection of the candidates selected by the software, we gave higher priority to the brightest candidates, which require short exposures for the spectroscopic follow-up, and thus allow us to observe a large number of candidates. We also favoured the candidates far from the host galaxy nucleus in order to observe the largest number of real SNe. However these prescriptions were not strictly applied. Indeed most

of our candidates were faint and centrally located. We can compare the distribution of the distance from the host galaxy center of the spectroscopically observed SNe (Fig. 3.28) with the distribution obtained from nearby photographic SN searches and from nearby and high-z CCD SNe searches (Fig. 3.29, 3.30, Howell et al. 2000). It is interesting to note that, because of saturated galaxy cores, the projected distance from the host galaxy center of SN phographically discovered, do not show a decreasing trend from the center outwards, but have a peak at $4 - 7$ kpc. Our data present an higher concentration of nuclear SNe. This shows that our bias is not as severe as typical SN searches.
Due to the fainter absolute magnitude of CCSNe, the equal proportion of type Ia and core collapse events detected already suggests that the CCSNe explosion rate should be significantly higher than type Ia rate.
Images and spectra of all the SNe are shown in Appendix B and a more detailed description is provided by Valenti (2003), who performed an accurate spectrophotometric analysis of each object.

Table 3.10: SNe spectroscopically confirmed

SN	type	$z(v_{3k})$	IAUC	SN	type	$z(v_{3k})$	IAUC	SN	type	$z(v_{3k})$	IAUC
J1888_A	Ia	0.42	⋆	2001be	Ia	0.24	7615	2001ip	Ia	0.54	7780
1999ey	IIn	0.09	7310	2001ge	Ia	0.22	7762	2002cl	Ic	0.07	7885
1999gt	Ia	0.27	7346	2001gf	Ia	$0.13^{\diamond}$	7762	2002cm	II	0.09	7885
1999gu	II	0.15	7346	2001gg	II	0.61	7762	2002cn	Ia	0.30	7885
2000fc	Ia	0.43	7537	2001gh	II	0.16	7762	2002co	II	0.32	7885
2000fp	II	0.30	7549	2001gi	Ia	0.20	7762	2002du	II	0.21	7929
2001bc	II	0.20	7615	2001gj	II	0.27	7762				
2001bd	II	0.10	7615	2001io	Ia	0.19	7780				

Type	Ia	Ib/c–II
N.	10	12
z_{min}	0.10	0.07
z_{max}	0.54	0.61

⋆ J1888_A was not formally announced because of the uncertain preliminary classification;
its spectrum was consistent with a type Ia SN or, less probably, with a very bright SN Ic. The following photometric follow-up showed a light curve consistent with that of a type Ia SN.
$^{\diamond}$ SN 2001gf original redshift value ($z = 0.20$ in IAUC 7762) revised.

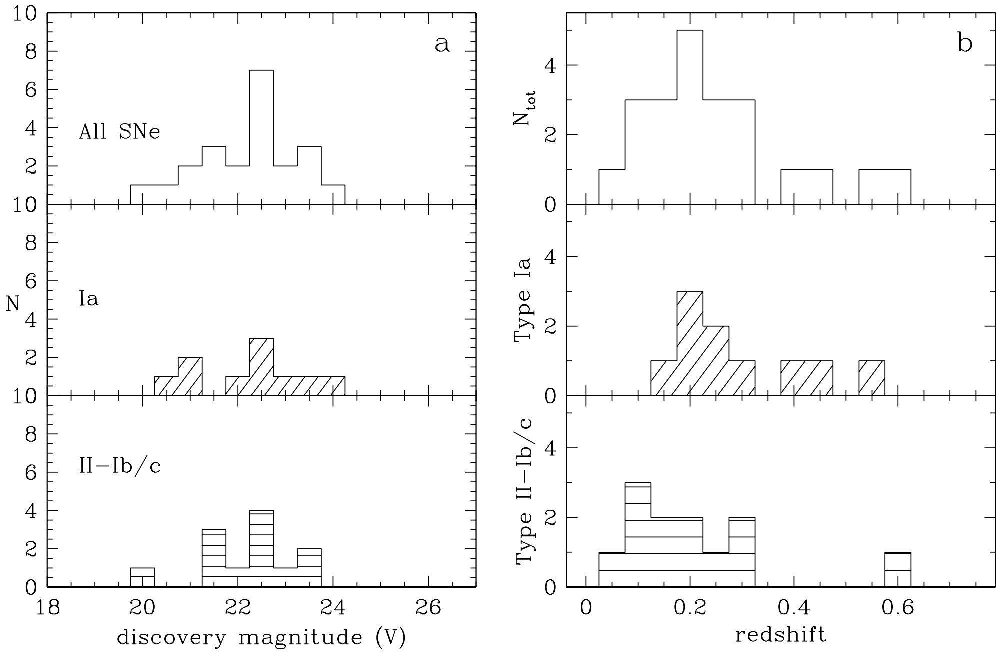

Figure 3.27: (**a**) V magnitude distribution and (**b**) redshift distribution of the 22 SNe spectroscopically confirmed. Upper panels: SNe Ia+CCSNe; middle panels: SNe Ia; lower panels: CCSNe

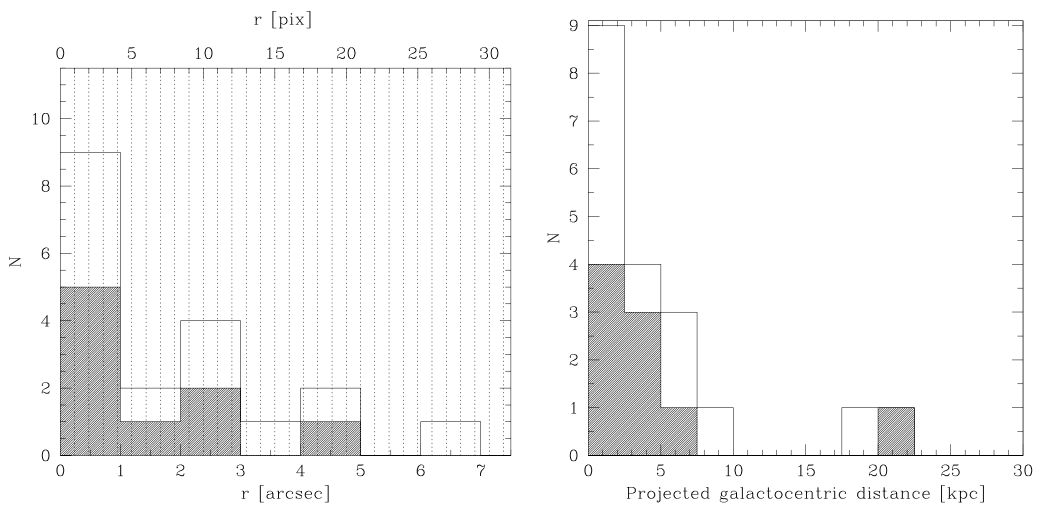

Figure 3.28: Left: histogram of the angular distance from the host galaxy center of the SN spectroscopically observed. The vertical grid shows the physical dimensions of the pixels. Right: histogram of the projected galactocentric distance. SN 2002co host galaxy is too faint, if any, to measure the distance. Shading marks the type Ia contribution to each bin.

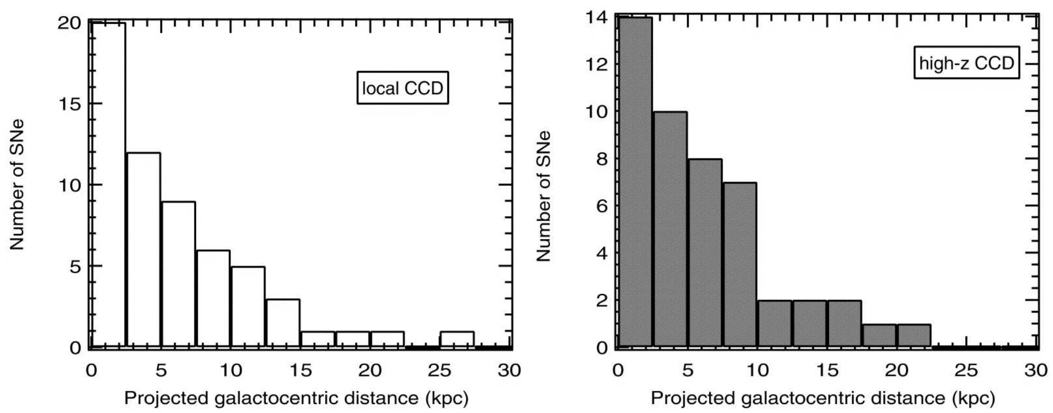

Figure 3.29: Projected distances from the host centers of nearby SNe Ia (left) and high-z SNe discovered (right). Both samples have been collected with CCD observations. Figures from Howell et al. (2000).

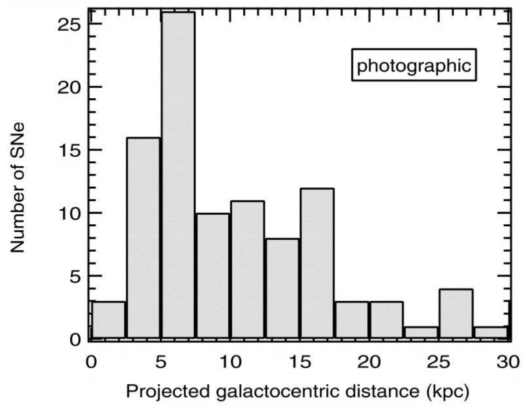

Figure 3.30: Projected distances from the host centers of nearby SNe Ia discovered photographically. Figure from Howell et al. (2000).

3.6 Search byproducts

Not all selected candidates turned out to be supernovae after spectroscopic observation, but the effectiveness of the candidate selection criteria is demonstrated by the fact that after spectroscopic observation of 28 selected candidates, 22 ($\sim 79\%$) of them turned out to be SNe, while 6 ($\sim 21\%$) turned out to be AGNs-QSOs, with redshift in the range $0.3 < z < 2.3$ (Fig. 3.31, 3.32, 3.33). A significant contamination of AGNs is unavoidable because we tried to minimize the selection biases.

In addition to these sources spectroscopically confirmed, there is a plethora of detection of probable variable stars. Besides, even if the search technique is not optimized for moving sources detections, a small number of minor planets has been detected too (Fig. 3.34)

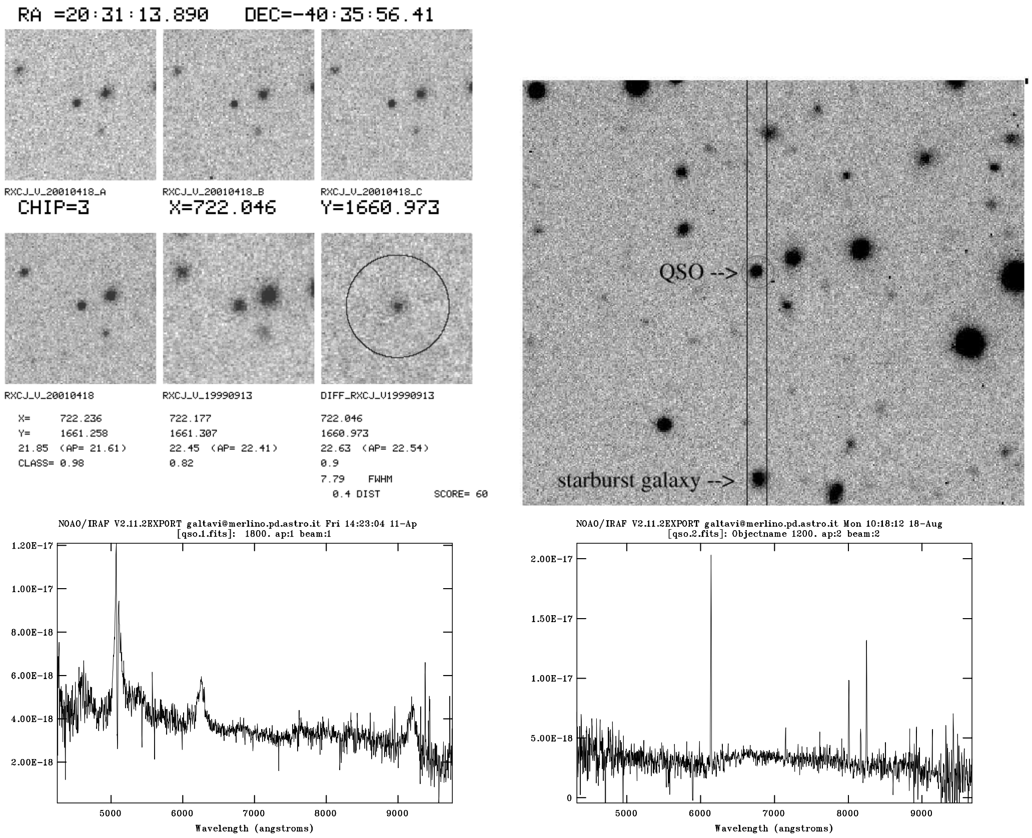

Figure 3.31: Top-left: QSO at $z \sim 2.28$. Top-right: By chance another source falling inside the slit for spectroscopy resulted to be a starburst galaxy. Bottom-left: QSO spectrum. Bottom-right: Starburst galaxy spectrum.

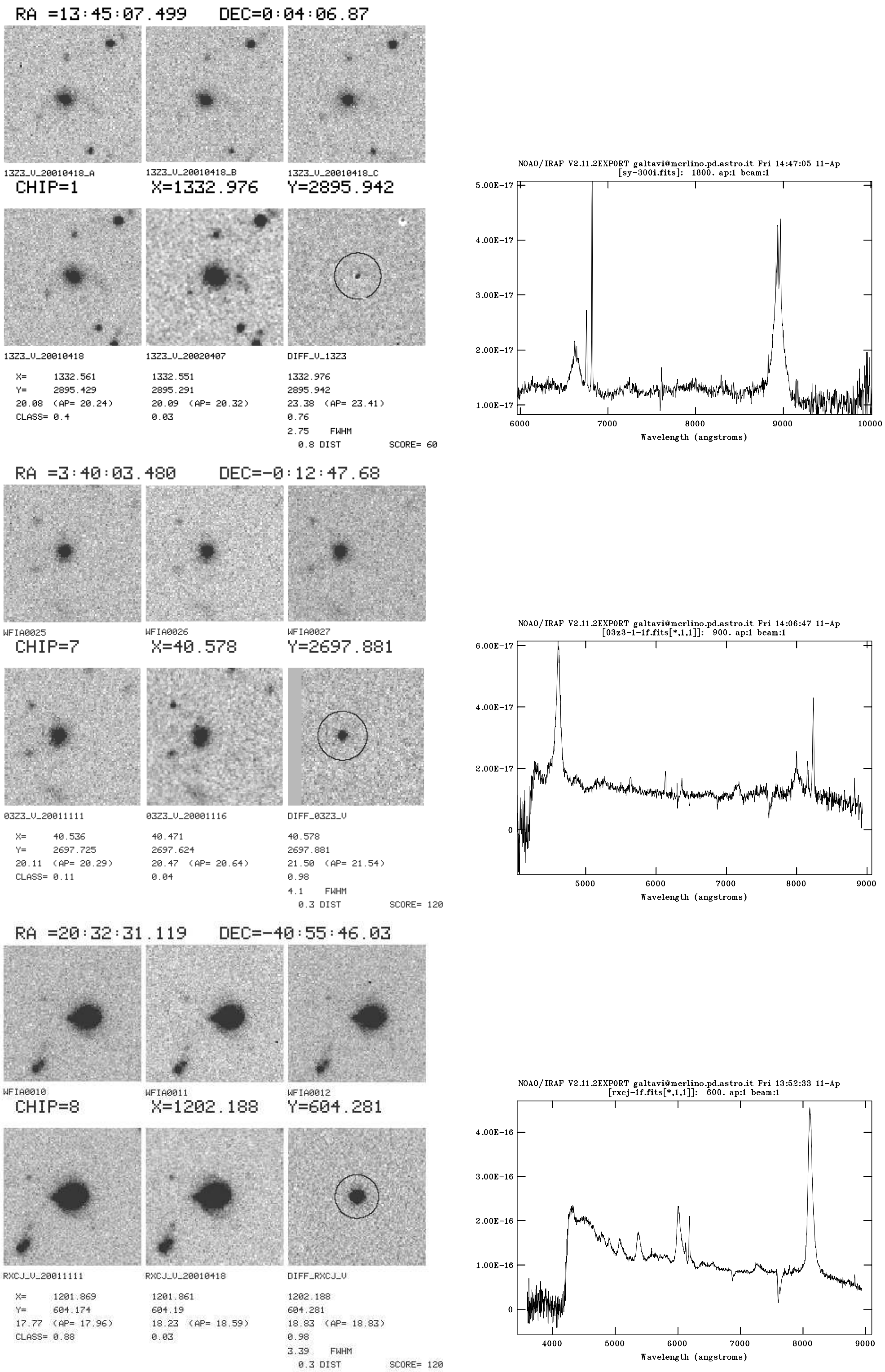

Figure 3.32: Seyfert galaxy at $z = 0.36$, AGN in 03Z3, AGN in RXCJ.

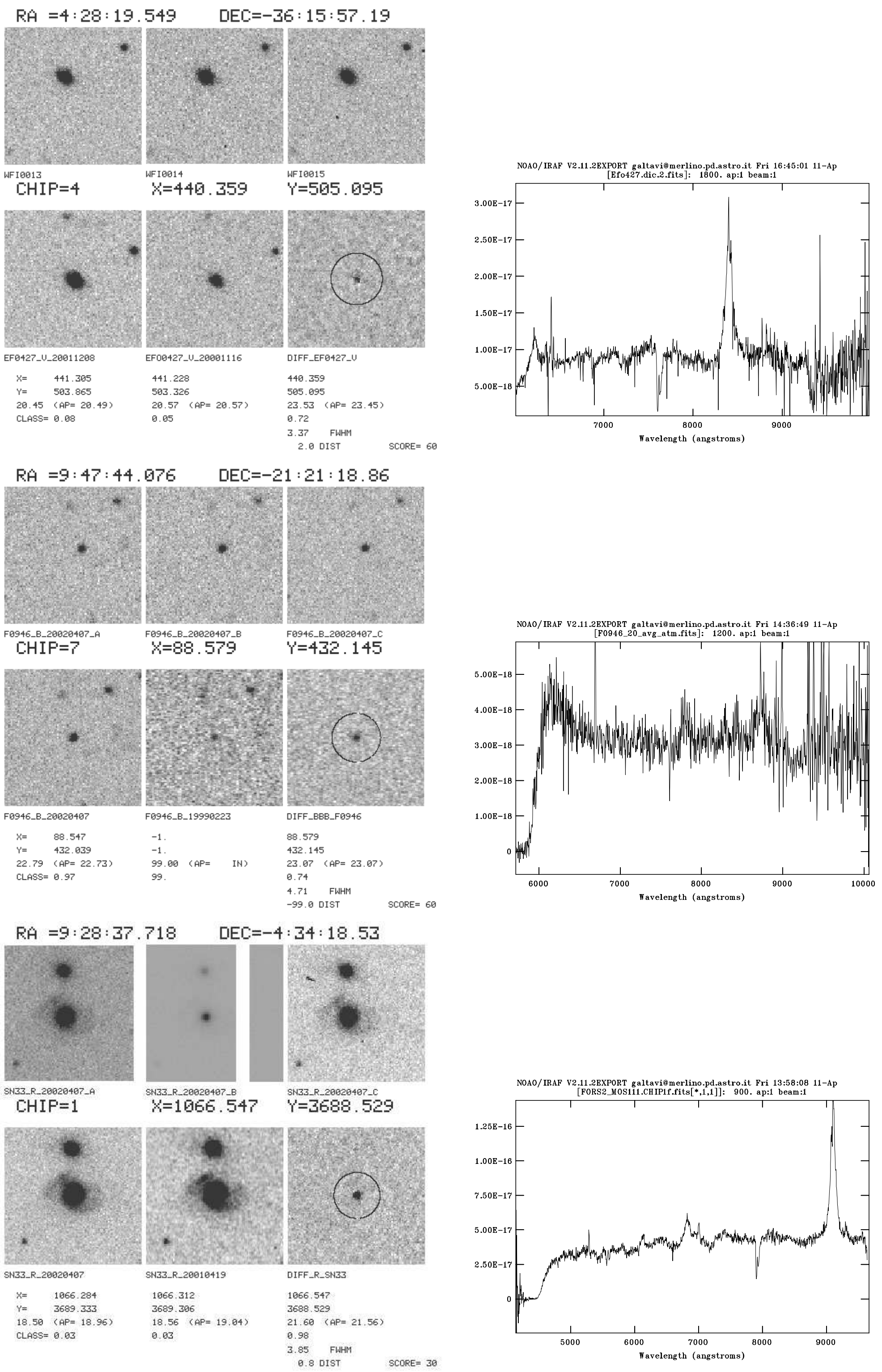

Figure 3.33: AGN in EF0427 at $z = 0.28$, AGN in F0946, AGN in SN33 at $z = 0.40$.

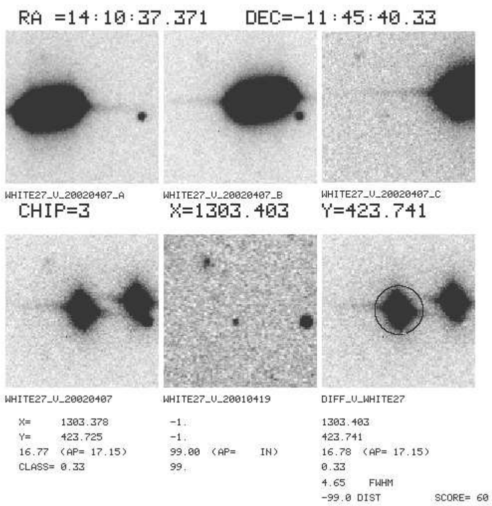

Figure 3.34: Laurentia minor planet. The bright spots in the combined (and subtracted) image are due to the overlapping tracks of the dithered images.

Chapter 4

SNe Ia and the destiny of the Universe

While to deny the existence of an unseen kingdom is bad,
to pretend that we know more about it than its bare existence is not better.
Samuel Butler, *Erewhon*

4.1 Nearby and distant SNe

In this section we will join the data of the SNe Ia spectroscopically observed during our SN search program, reported in Tab. 4.1, to the ones shown in Tab. 2.3. Our search was not specifically designed for detection of type Ia SNe at early stages and the results based on our data can not provide but a rough estimate of cosmological parameters.
We will exploit the $M_B - \Delta m_{15}(B)$ relation discussed in §2 to calibrate our "intermediate-z" SN sample and extend the Hubble diagram to higher redshift.
In §2 we defined the relation

$$M_B = a[\Delta m_{15(B)} - 1.1] + b \tag{4.1}$$

M_B is related, through b, to a given value of the Hubble constant H_0 and, if a different constant H_0' is adopted, M_B must be scaled according to the formula

$$M_B'(H_0') = M_B(H_0) + 5log(H_0'/H_0) \tag{4.2}$$

In order to get rid of the Hubble constant dependence and compute the cosmological parameters Ω_M, Ω_Λ, we will build the Hubble diagram following a procedure different from the one used in §2. Instead of computing the absolute magnitude for each SNe, the effective magnitude m_{eff} is used. We proceed as follows:

in eq. 1.15 the luminosity distance depends on H_0, Ω_M, Ω_Λ and z. We define a new luminosity distance (Perlmutter et al., 1997), H_0 free, as:

$$D_{Lfree}(z, \Omega_M, \Omega_\Lambda) = H_0 d_L(z, \Omega_M, \Omega_\Lambda, H_0) \tag{4.3}$$

Using eq. 4.1, eq. 4.2 can be written as

$$M'_B(H'_0) = \Delta_{corr} + b + 5log(H'_0) - 5log(H_0) \tag{4.4}$$

where

$$\Delta_{corr} = -a[\Delta m_{15(B)} - 1.1] \tag{4.5}$$

We define now the effective magnitude as

$$m_{eff}(B) = m_B - ABi - ABg - K_{BB} + \Delta_{corr} \tag{4.6}$$

Using eq. 4.3, 4.4, 4.6, 1.14, we obtain the relation:

$$m_{eff}(B) = 5log(D_{Lfree}) + b - 5log(H_0) + 25 \tag{4.7}$$

It is now clear that by means of eq. 4.7 it is possible to estimate Ω_M, Ω_Λ without any dependence on the adopted value of the Hubble constant. Tab. 4.1 summarizes the data of our 10 intermediate z type Ia SNe (based on measurements by Valenti 2003).
We can now plot m_{eff} vs. z. As in §2.2 we excluded from the sample very nearby SNe, i.e. the SNe with velocity recession smaller than 3000 km s^{-1}. We obtain a subsample of 56 SNe with z ranging in the interval 0.01–0.54 (SN 2001io, a 1991bg-like, has been excluded because can not be calibrated through the $M_B - \Delta m_{15}(B)$ relation). We also took into account the results obtained in §2.1.3 and we assumed $R_B = 3.5$. The resulting Hubble diagram is shown in Fig. 4.1. As shown in Fig. 4.1, bottom panel, the Hubble diagrams expected from different cosmological model can be better descriminated around $z \sim 0.5$. It is thus important to fill this redshift range with accurate measurements. Our intermediate redshift SN sample is not large enough to give tight constraints on the cosmological parameters, as shown in Fig. 4.2. Anyway our measurements are consistent with a universe dominated by the cosmological constant. In order to obtain tigher constraints and to check how our intermediate z SNe compare with other SN measurements, we merged our intermediate z SNe to the sample collected by Tonry et al. (2003) (230 SNe with $0.002 < z < 1.75$) and that by Barris et al. (2003) (23 SNe with $0.34 < z < 1.03$). The results is shown in Fig. 4.3. Our sample magnitudes agree well with the general trend within the errorbars. The Ω_M, Ω_Λ confidence region, obtained considering all objects with recession velocities larger than 3000 km s^{-1} (i.e. 228 SNe) are shown in Fig. 4.4. The confidence regions determined with the extended sample of 228 SNe are narrower than the previous case and they suggest a Universe dominated by the cosmological constant. It is evident that, also using a large SN sample, the Ω_M, Ω_Λ values are not well defined. Better constraints can be obtained merging the results obtained means of SNe with those obtained by other methods. In particular it is crucial the indication of measurements of the cosmic microwave background that the Universe is flat, that is $\Omega_M + \Omega_\Lambda = 1$.

SN	Type	Host galaxy type	$\Delta m_{15}(B)$	$m_{eff}(B)^*$	redshift (v_{3K})	ABi	ABg
$J1888\_A$	Ia	(Sb)	1.5(0.5)	23.1(0.9)	0.42(0.05)	0	0.074
SN 1999gt	Ia	late spiral	1.05(0.6)	22.6(0.7)	0.275(0.005)	...	0.033
SN 2000fc	Ia	...	0.87(0.10)	22.7(0.2)	0.430(0.005)	...	0.082
SN 2001be	Ia	Sc	1.3(0.3)	20.7(0.9)	0.242(0.001)	1.2(0.8)	0.208
SN 2001ge	Ia	(Sb)	1.45(0.09)	21.0(0.3)	0.218(0.001)	0	0.181
SN 2001gf	Ia	Sb	1.47(0.15)	19.9(0.4)	0.132(0.001)	0	0.127
SN 2001gi	Ia	...	0.94(0.15)	20.8(0.5)	0.200(0.005)	0	0.094
SN 2001io	Ia	Sb	1.94(1)	23.8(0.2)	0.187(0.001)	0	0.106
SN 2001ip	Ia	E3/S0	1.1(0.4)	23.4(0.7)	0.536(0.001)	0	0.034
SN 2002cn	Ia	Sc	0.94(0.15)	22.2(0.3)	0.303(0.001)	0	0.319

Table 4.1: Summary of the SNe Ia spectroscopically observed during the SN Search program.

* $-a(\Delta m_{15} - 1.1)$ correction not applied.
$\Delta m_{15} - M(B)$ relation it is not linear for high decline rate and thus can not be applied to the SN 2001io. According to the data reported in Chapter 2, 1991bg-like SNe can be roughly corrected assuming them to be ~ 2.7 mag fainter than the standard SN with $\Delta m_{15} = 1.1$.

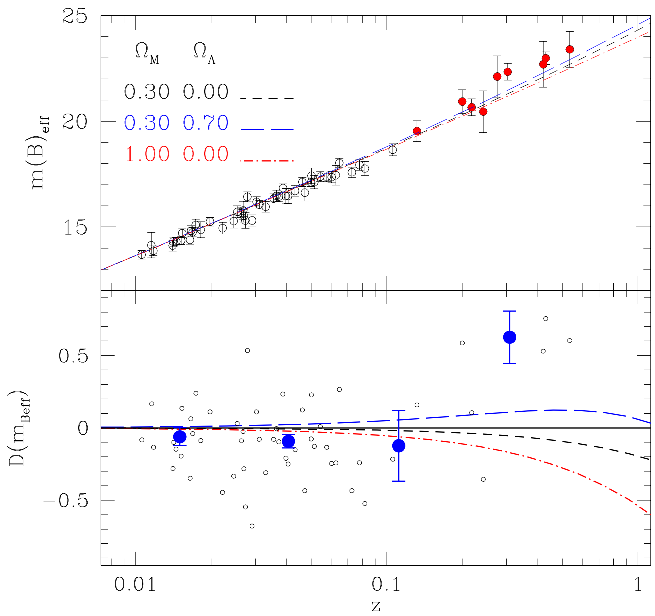

Figure 4.1: Upper panel: the extended Hubble diagram obtained adding our intermediate redshift SNe (filled circles) to the diagram shown in Fig. 2.11**b**, under the same assumptions (see §2.2, $\Delta_{corr} = -1.092(\Delta m_{15} - 1.1)$). Lower panel: the residual of the distance relative to $\Omega_M = \Omega_\Lambda = 0$. Filled dots marks the the average residual of the observed objects per redshift bin. Theoretical residual of the luminosity distances relative to three different cosmological models are also shown.

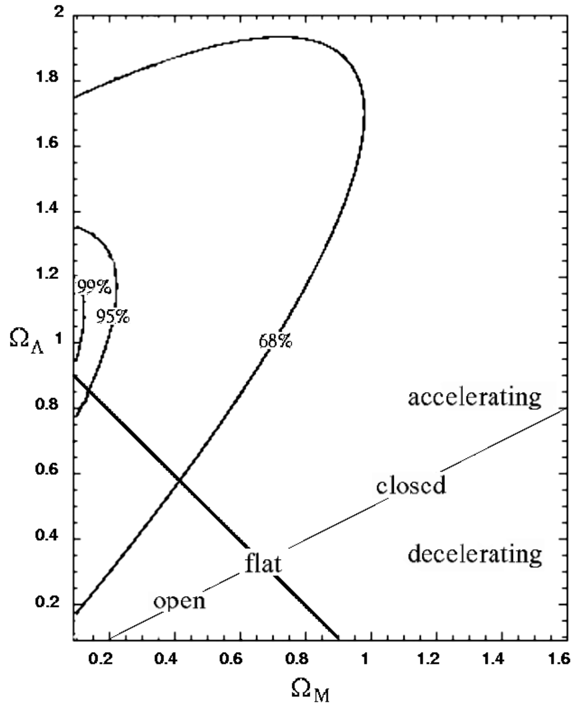

Figure 4.2: $\Omega_M - \Omega_\Lambda$ plane, confidence regions obtained from our SN sample. The 68%, 95%, 99% confidence level are shown.

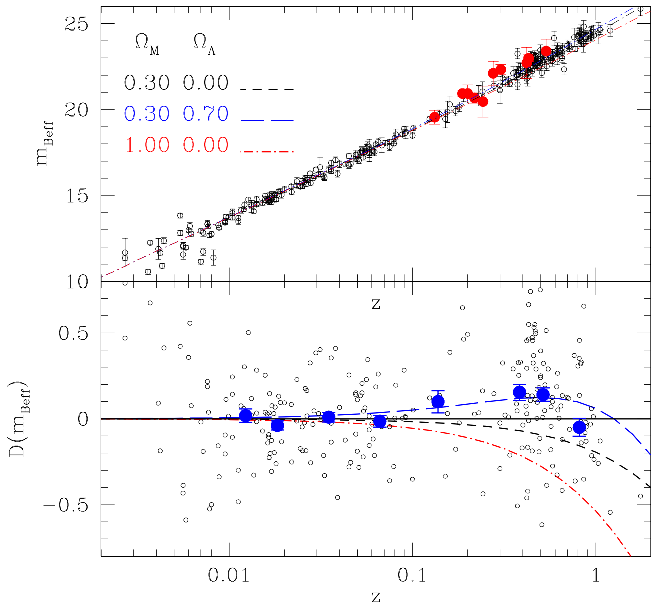

Figure 4.3: Upper panel: the extended Hubble diagram obtained adding our intermediate redshift SNe (filled circles) to the sample collected by Tonry et al. 2003 and Barris et al. 2003. Lower panel: the residual of the distance relative to $\Omega_M = \Omega_\Lambda = 0$. Filled dots marks the the average residual of the observed objects per redshift bin. Theoretical residual of the luminosity distances relative to three different cosmological models are also shown.

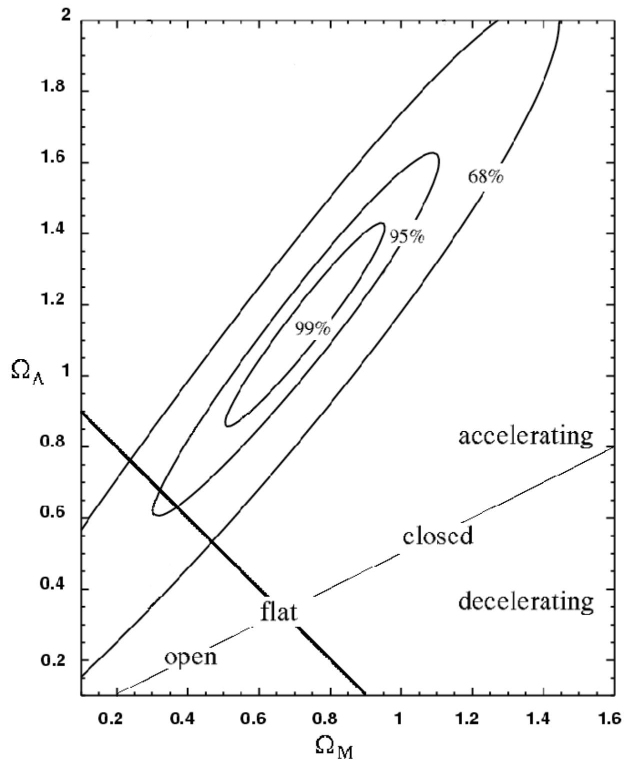

Figure 4.4: $\Omega_M - \Omega_\Lambda$ plane, confidence regions obtained from our intermediate z SN sample + 195 SNe from Tonry et al. (2003) + 23 from Barris et al. (2003). The 68%, 95%, 99% confidence level are shown.

4.2 The accelerating Universe

Searches especially designed for high redshift SN detection produce, nowadays, type Ia SN samples extended up $z \sim 1$. The farthest SN ever observed so far is SN 1997ff, at redshift $z \simeq 1.7$, found in the HST deep field (Gilliland and Phillips, 1998), but it is an extreme case, whose magnitude has been probably magnified by gravitational lensing (Lewis and Ibata, 2001; Mörtsell et al., 2001; Vishwakarma, 2002; Benítez et al., 2002). These high-z SNe have been successfully used to probe the universal expansion rate with time and to estimate the cosmological parameters Ω_M, Ω_Λ. In particular, the measurements obtained at the end of 1990's by two collaborations ("The Supernova Cosmology Project", SCP, led by S.Perlmutter, and "The High-Z SN Search", HZSNS, led by B. Schmidt) suggested an accelerated expansion of the Universe. In fact, high redshift SNe are on average fainter than expected and the most likely explanations, in the framework of a standard Friedman-Robertson-Walker cosmology, is an acceleration of the cosmic expansion. In particular the implication of the SN data is that $\sim 70\%$ of the energy density of the Universe is in some form of "dark energy" such as vacuum energy or quintessence, an exotic kind of energy that pushes particles away from each other (Perlmutter et al., 1999; Schmidt et al., 1998). The confidence region for Ω_Λ, Ω_M obtained by both the SCP and the HZSNS is shown in Fig. 4.5.

The results recently obtained by Tonry et al. (2003) and Barris et al. (2003) are in agreement with those of The Supernova Cosmology Project and of The High-Z SN Search Team. A recent work by Knop et al. (2003) confirmed the previous results by means of eleven high redshift SNe ($0.36 \leq z \leq 0.86$) observed using the WFPC2 on the Hubble Space Telescope. Combined with the earlier SCP data, they yield a measurement of the mass density $\Omega_M = 0.25^{+0.07}_{-0.07}$ (statistical) ± 0.04 (systematics), or equivalently, a cosmological constant of $\Omega_\Lambda = 0.75^{+0.06}_{-0.07}$ (statistical) ± 0.04 (systematics), under the assumption of a flat Universe with vacuum energy ($\omega = -1$).

Confidence that the Universe is dominated by dark energy has been boosted by recent observations of the power spectrum of fluctuations in the cosmic microwave background (CMB). Since the SN data probe the Universe at "moderate" redshift ($z < 2$) and the CMB data come from higher redshift ($z \sim 1100$), the two data sets are complementary. Because of the different orientation of the corresponding confidence region in the Ω_Λ *vs.* Ω_M parameter space, the two data set strongly constrain the allowed pairs of Ω_Λ, Ω_M values (see Fig. 4.6).

A significant example is given by the results obtained by de Bernardis et al. (2002) and, more recently, by the Wilkinson Microwave Anisotropy Probe (WMAP[1], Spergel et al. 2003), whose data, merged with other astronomical data sets (ACBAR[2], Kuo et al. 2002; CBI[3], Contaldi and CBI/BOOMERanG Collaboration 2002, Pearson et al. 2003; 2dF-GRS[4], Percival et al. 2001, Colless et al. 2001, Efstathiou et al. 2002; Lyman α forest data, Croft et al. 2002, Gnedin and Hamilton 2002; SN data, Garnavich et al. 1998, Riess et al. 2001, Freedman et al. 2001) tight constrain the cosmological parameters: $\Omega_{tot} = 1.02 \pm 0.2$, $P(\omega < -0.78) > 95\%$, $h = 0.71^{+0.04}_{-0.03}\,\mathrm{km\,s^{-1}Mpc^{-1}}$, age: 13.7 ± 0.2 Gyr.

[1]http://map.gsfc.nasa.gov/

[2]http://cosmology.berkeley.edu/group/swlh/acbar/

[3]http://www.astro.caltech.edu/ tjp/CBI/

[4]http://msowww.anu.edu.au/2dFGRS/

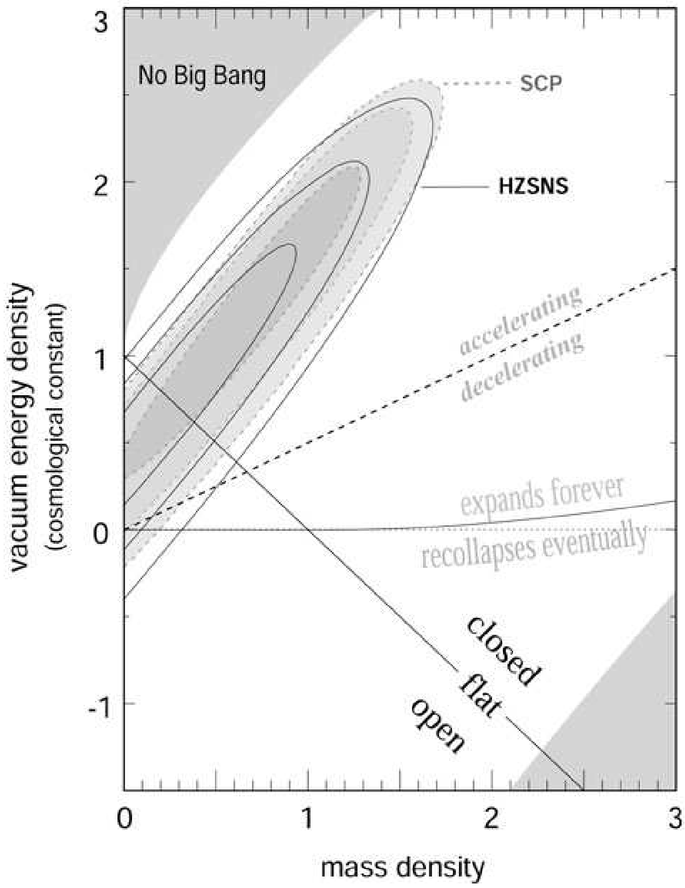

Figure 4.5: The confidence regions for both the SCP and HZSNS for Ω_Λ, Ω_M. The two experiments show, with remarkable consistency, that $\Omega_\Lambda > 0$ is required to reconcile observations and theory.

The results obtained in all these works, based both on SNe and on CMB, show a clear convergence toward a cosmological "Standard Model" in which the accelerating expansion is driven by dark energy and the role of ordinary matter is secondary. The main conclusion are that we live in a geometrically flat Universe with $\Omega_{total} \simeq 1$, $\Omega_M \simeq 0.3$ and $\Omega_\Lambda \simeq 0.7$. However these measurements are not easy and the interpretation of this result rests on some critical assumptions. Adopting a cosmological model with $\Omega_M = 0.3$, $\Omega_\Lambda = 0.7$, a standard candle at $z = 0.1$ would appear 0.05 mag fainter than in an empty Universe ($\Omega_M = \Omega_\Lambda = 0$). This difference increases to 0.12 mag at $z = 0.5$ and decreases again at 0.06 mag at $z = 1$. These are small values, considering how difficult is to observe objects at these redshifts and that important corrections have to be applied to them (e.g. phase dependent and cross-filter K-correction, Galactic and host galaxy absorption correction, absolute magnitude calibration, cosmological time dilatation). Besides, if some of them are well known (e.g. time dilatation, which is a firm prediction of cosmological expansion models, Wilson 1939; Colgate 1979), other are more uncertain (e.g. reddening corrections) or relies on assumptions, as the K-correction, which assume that the spectral characteristic (and colours) of nearby and distant SNe are not significantly different.

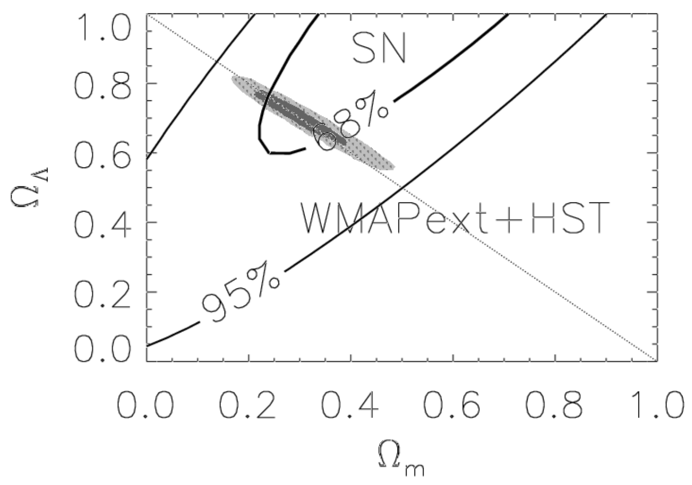

Figure 4.6: $\Omega_\Lambda - \Omega_M$ plane. This figure shows how the two dimensional likelihood surface for SN data (by Riess et al. 1998, 2001) and CMB data (by Spergel et al. 2003) constrain the geometry of the Universe.

4.2.1 Alternative hypotheses

For completeness we mention a few alternative hypotheses, which do not invoke cosmic acceleration to explain the observed dimming of the distant SNe, have been proposed too (see Riess 2000 and Leibundgut 2001 for reviews):

- **Grey Dust**
  SN Ia colors, together with a reddening law, can be used to correct for the effect of ordinary intergalactic and host galaxy dust. Dust extinction in our own galaxy has been extensively studied (Galactic extinction maps are available to correct individual SNe Ia for Milky Way extinction, Burstein and Heiles 1982; Schlegel et al. 1998) and it is of less concern in Supernova distance measurements. As discussed in §2, a full understanding of the reddening of nearby SNe Ia (or galaxies in general) has not been achieved yet and the small-magnitude offset observed for the distant SNe Ia could easily be explained by a small change in the reddening law (i.e. in the dust properties).
  Even more troublesome than ordinary dust is the "grey" intergalactic dust, with properties that do not change the color of the objects significantly. Grey dust can explain the observed dimming of light from distant supernovae (Fischer, 2003) without telltale reddening. The wavelength dependence of silicates and graphites is a strong function of the minimal grain sizes, and grey dust can be produced by graphite grains greater than $0.1\mu m$. Such dust could make the SN data consistent with an

open universe (Aguirre, 1999). However an important consequence of such grey dust would be a strong far-infrared background, as the radiation is thermalized (Aguirre and Haiman, 2000), easily detected with infrared observations. The recent detection of a diffuse but faint, far-infrared background limits the amount of dust that could be responsible for this emission (Fixsen et al., 1998). With an increased wavelength base, the effects of grey dust will become detectable by means of SN observations too. In addition grey dust would cause SNe Ia to be systematically fainter at higher redshift and thus show a shape on the Hubble diagram different from the one expected assuming a standard cosmological model. In this case, in fact, SNe are expected to appear fainter than expected from a non accelerating Universe up to $z \sim 1$ but brighter at higher redshift.

- **Evolution**
The observed dimming of type Ia SNe might be attributed to evolutionary effects. In fact it is not yet certain that the most distant SNe show the same observable outcome as the closer ones (Riess et al., 1999a, 2000). The favored model consists in the thermonuclear explosion of a Chandrasekhar-mass white dwarf. Then, unless we invoke changes in the physics law driving the nuclear burning, small differences might be attributed to different composition of the exploding WD. This could potentially change the energy of the explosion and, hence, the SN brightness. These differences could be caused by the different age of the progenitor systems or an altogether different progenitor evolution. Since little is known about the progenitors, theoretical investigations are difficult. However, it could be argued that, since the nearby SNe explode both in elliptical and spiral galaxies, originating from progenitors of all ages, the observed range should encompass all possible explosion configurations, with the normalization applied through the luminosity-width corrections being universal. Although this is a largely untested assumption, so far the comparisons of high signal-to-noise ratio spectra of nearby and high-z SNe Ia have not revealed significant differences (Riess et al., 1998; Perlmutter et al., 1998, 1999) and also the distributions of light-curve shapes at high and low redshift are statistically consistent (Riess et al., 1998; Perlmutter et al., 1999). A recent claim that the rise times to maximum for distant objects is different than for the nearby ones (Riess et al., 1999a) has been contested on statistical grounds (Aldering et al., 2000). Another discrepancy emerging is the colours of the distant objects. As pointed out by Falco et al. (1999), the distant SNe Ia appear bluer than the nearby objects. But the significance of this change is not yet obvious. So, though some discrepancies have been noted, the distant SNe Ia seem to resemble the nearby objects in most measured aspects.

- **Gravitational lensing**
As the SN light propagates through the universe to the observer, it can be deflected by massive objects. Modelling suggest that inhomogeneous distribution of matter in the universe typically deamplifies and very rarely amplifies the observed brightness of distant SNe Ia (Kantowski et al., 1995; Wambsganss et al., 1997). Any object at a considerable distance will suffer to some degree from gravitational lensing. For the SNe, any brightness bias that is introduced by lensing could change the cosmological conclusions. Note that this effect should also increase the observed scatter in peak luminosity, if significant. In a standard cosmological scenario (i.e., $\Omega_M = 0.3$ and mostly diffuse dark matter) the typical deamplification for SNe Ia at $z = 0.5$ is 2%,

much smaller than the cosmological effect. An extreme case (i.e., $\Omega_M = 0.5$ and all matter in point masses) could deamplify a SN Ia at $z = 0.5$ by 5% (Holz, 1998), but this model is unlikely to be correct and the effect is still not large enough to rule out the cosmological interpretation of high-redshift SNe Ia.

- **Measurement biases**
  Measuring the distance to high-redshift SNe Ia, which are 6-7 mag. fainter and have lower signal-to-noise ratio than those which delineate the Hubble flow, is an observational challenge. Differences in the way low- and high-redshift SNe Ia are observed could introduce biases in their measurements. For example many CCDs, including the well studied detectors of the Wide Field Planetary Camera 2 (WFPC2) aboard the Hubble Space Telescope (Stetson, 1998), show a "charge transfer efficiency" problem which leads to flux underestimation for faint objects. However it is only a problem at the few-percent level in the HST/WFPC2 and it is even smaller, typically, in high-background ground based observations. In addition, only a subset of the high-redshift SNe Ia have been measured with HST, and the cosmological conclusions do not depend on the inclusion of these objects.
  High-precision, flux-conserving algorithms have been developed to properly subtract images of the host galaxy from images with SN light (Alard and Lupton, 1998).
  Hogg and Turner (1998) discuss a bias toward higher observed fluxes which occurs when measuring the brightness at discovery of low signal-to-noise sources. This bias is due to the preferential selection of faint sources on the bright side of the Poisson distribution of photon statistics. Follow-up observations of the source would not incur this effect. This bias would have little impact on the supernova distances because the light curves are usually dominated by observations made after discovery. Moreover this effect is opposite to the signal of an accelerating universe. However, this effect may become more important for SNe Ia found at $z > 1$ for which the discovery observation may provide one of the most significant measurements.

- **Selection biases**
  Many nearby SNe were found in the photographic survey in which saturated galaxy cores masked SNe near their hosts' centers. The result is that distant SNe are more centrally located, with respect to their host galaxy, than those in the nearby sample. This is in principle a selection bias, but Riess et al. (1999b) found no dependence of the luminosity on the projected distance from the host center.
  Malmquist bias plays an important role while observing faint objects, but the preferential sampling of bright sources would lead to under-estimated distances, in contrast with the observed cosmological dimming. However, if the nearby sample were more afflicted by Malmquist bias than the distant sample, this bias could mimic an accelerating universe. Perlmutter et al. (1999) and Riess et al. (1998) estimated the net bias between the low and high-z samples, reporting a net bias smaller than 0.03 or 0.01 mag. respectively and hence a negligible impact on the cosmological conclusions.

All these effects can mimic the dimming of high redshift SNe due to dark energy and, a priori, are equally likely. But these effects should also leave clues that can be detected, and current indications are that none of these alternatives alone can explain the dimness of the distant SNe.

The previous alternative hypotheses are all consistent with the cosmological and physical laws currently accepted to describe the Universe, but, a priori, “exotic” explanations can not be ruled out:

- **Alternative cosmological models**
  The interpretation of the high-z SNe results are based on our current understanding of astrophysics and are based on Friedmann-Robertson-Walker cosmology, with two free parameters, Ω_M and Ω_Λ. But the conclusions drawn from high-z SNe Ia can also be interpreted in world models that are based on assumptions deviating from the Friedmann models. The main motivation for these approaches is to explain the faintness of the distant SNe without a cosmological constant. The observed SN dimming can be successfully explained rejecting the homogeneity and isotropy hypotheses (Célérier, 2000), which is the base of the Cosmological Principle and a fundamental assumptions of the Friedmann models.
  In steady state cosmologies, SN redshifts do not come from expansion, but rather through "tired-light" processes (however, the SN Ia data exhibit the time dilatation effect expected in an expanding universe, implying that the tired-light hypothesis is incorrect, Leibundgut et al. 1996)
  In a quasi-steady state cosmology, a combination of acceleration due to the formation of matter and the particular, grey dust proposed by Aguirre (1999) can reproduce the SN observations Banerjee et al. (2000).
  Alternative theories of gravity such as modified Newtonian dynamics models (MOND) (Milgrom, 1983, 1988) could also modify the interpretation of the observations of high-redshift SNe Ia.
  Finally, changing the values of physical constants, such as the gravitational constant, the fine-structure constant, the speed of light, or the value of Planck's constant, can of course have dramatic effects on the results.

4.3 Conclusion

Our results, based both on our SN sample and to the extended sample including 230 SNe from Tonry et al. (2003) and 23 SNe from Barris et al. (2003), confirm the current claims of an accelerating Universe dominated by the cosmological constant. Both samples in fact, show that SNe are, on average, fainter than what would be expected, even for an empty Universe ($\Omega_M = \Omega_\Lambda = 0$). This result is in agreement with that obtained at the end of 1990's by the Supernova Cosmology Project and the High-Z SN Search Team, which provided strong evidence, based on distant type Ia SNe, for an accelerating expansion of the Universe, and hence for a non-zero cosmological constant, or dark energy density (§1.3).
All recent results show a convergence toward an $\Omega_M \sim 0.3$, $\Omega_\Lambda \sim 0.7$ Universe, with $P(\Omega_\Lambda > 0) > 99\%$.

4.4 The future

High redshift SNe, together with other current cosmological observations of the CMB, are providing a consistent picture of a low-mass, flat Universe, filled with a not well defined dark energy, whose nature and properties will be a challenging issue for cosmologists in the next years. We do not know, in fact, what kind of the dark energy is leading to the acceleration, and it is worthwhile investigating.
Improving the current constraints on the cosmological parameters and determining the nature of the dark energy requires improving the control of the systematic uncertainties dramatically. A much better knowledge of SNe Ia, both theoretical and observational, is strongly required, as well as a significant increase of the number of well observed SNe, both at low and high redshift.
Several ground-based programs, designed to observe hundreds of SNe, are already running or have been planned for the next future. For example, the Nearby Supernova Factory (Aldering et al., 2002; Wood-Vasey et al., 2002) aims at the discovery of $\sim$ 300 SNe Ia at redshifts $0.03 < z < 0.08$. The search will be performed on images taken by the two 1.2m telescopes operated by the Near Earth Asteroid Tracking (NEAT). To observe these events, a dedicated SuperNova Integral Field Spectrometer (SNIFS) is being built in France and will be mounted on the UH 2.2m telescope, in Hawaii. This program will provide an exceptional data set of well studied supernovae in the nearby smooth Hubble flow which can be used as calibration for the programs designed to use supernovae to measure the cosmological parameters, like the CFHT Legacy Survey[5] or the High-Z Team project ESSENCE[6]. The CFHT Legacy Survey is aimed mainly at the detection and monitoring of $\sim$ 2000 type I SNe with the CFHT 3.6m telescope equipped with the wide field camera MegaCam. Several hundreds high-z supernovae will be observed with 8m class telescopes too. This survey will allow a better understanding of the early universe as well as a determination of the dark energy parameter with an unprecedented accuracy.
The HZT project ESSENCE (Equation of State: SupErNovae trace Cosmic Expansion, Garnavich et al. 2002; Kirshner et al. 2003) aim to the discovery of $\sim$ 200 SNe Ia evenly distributed over the redshift range $0.15 < z < 0.75$, with the Mosaic Imager on the Blanco 4m telescope, over a five-year period. This project will eventually provide an estimate for ω to an accuracy of 10% and a better understanding of the systematic uncertainties inherent to type Ia SNe. This a crucial step, since large samples and homogeneous measurements allow us to reduce dramatically the statistical errors, but systematic effect will always limit the precision of the distance measurements based on SNe. Farther in the future, space-based projects like the SuperNova Acceleration Probe (SNAP[7], Linder 2003), besides a larger numbers of objects and an extended redshift range (over a thousand SNe Ia per year out to $z = 1.7$), will also provide the opportunity to control many systematic effects better than from the ground (Frieman et al., 2003; Linder and Huterer, 2003). The instrumentation includes a half billion pixel wide field optical and near infrared imager and an optical and near infrared integral field low resolution spectrograph coupled to a 2 meter telescope. This project is expected to obtain measurement of the cosmological parameters with a precision of a few percent. Besides SNAP should be able to test a wide

[5]http://www.cfht.hawaii.edu/Science/CFHLS/overview.html

[6]http://www.ctio.noao.edu/wproject

[7]http://snap.lbl.gov/

range of dark energy models and detect a possible dependence of ω on time.
The Large Synoptic Survey Telescope, an 8m class telescope also referred to as the Dark Matter Telescope (LSST[8], Tyson and LSST Collaboration 2002), should reveal whether the value of ω depends on redshift, while high redshift surveys of galaxies such as DEEP2[9] (Davis et al., 2001), performed using the Keck telescopes, as well as space based mission to map the CMB (Plank[10]), should provide additional information about the cosmological constant.
The CMB measurements are relatively insensitive to the dark energy and the epoch of cosmic acceleration. Therefore, SNe Ia are currently the only cosmological tool which allow us to directly study the acceleration epoch with precision high enough to reveal the properties of the dark energy and its time dependence, if any. However other complementary and supporting measurements are extremely important for constraining the cosmological parameters and to control the systematic uncertainties of each method.

Moving forward simultaneously on these experimental fronts offers the stimulating opportunity of achieving a comprehensive measurement of the fundamental properties of our Universe. For these reasons observational cosmology promises to remain exciting for quite some time and we can expect that, within a few years, SNe Ia will produce measurements of energy densities with a precision of $\sim$ 10% and, more importantly, a first characterization of the dark energy.

[8] http://www.lsst.org/Project/lsst_project.html

[9] http://deep.berkeley.edu/

[10] http://astro.estec.esa.nl/SA-general/Projects/Planck/

Chapter 5

Supernova rates

The Sun is lost, and the earth, and no man's wit
Can well direct him where to look for it.
And freely men confess that this world's spent,
When in the Planets, and the Firmament
They seek so many new; then see that this
Is crumbled out again to his Atomies.
'Tis all in pieces, all coherence gone;
All just supply, and all Relation.
John Donne, *The Anatomy of the World*

Modeling the evolution of individual stars and binary systems after a burst of star formation is possible, in principle, to predict the number of expected SN events. On the contrary estimates of the SN Rate can be used to constrain the models.
In recent years, many authors have published predictions of the expected SN rate as a function of redshift based on SN progenitor scenarios and modeling of the cosmic star formation evolution (Madau et al., 1998a; Sadat et al., 1998; Dahlén and Fransson, 1999; Yungelson and Livio, 2000; Kobayashi et al., 2000; Sullivan et al., 2000a).

Whereas the local SNR for different SN classes and morphological galaxy types is reasonably well known (Cappellaro et al., 1999), at present there are few observational constraints on the frequencies of SNe at higher redshifts, and their estimates are still rather uncertain. Two pioneering works estimated type Ia SN rate at $z = 0.1$ (Hardin et al., 2000) and $z = 0.4$ (Pain et al., 1996) but they were based on only four and three SNe respectively; in a more recent study, Pain et al. (2002) have presented the results based on a larger sample, including 38 SNe, again of type Ia only.
This is because to date observational estimates of the SN rate at high redshift have been based on the SN searches aimed to use SN Ia as cosmological probes (Pain et al., 1996,

2002). This has two disadvantages: only type Ia SNRs are provided and the SN candidates selection is strongly biased. Indeed in most cases SN candidates are selected for spectroscopic confirmations only if they are not coincident with the host galaxy nucleus (to avoid contamination by variable AGN), if the host galaxy is not two bright (to make accurate photometry easier) and if they have blue color (to avoid uncertain reddening correction). Besides, only in Pain et al. (2002) the statistical error is small enough to make the measurement significant. They derived a type Ia supernova rate at a mean redshift $z \sim 0.55$ of $\nu(\mathrm{SNIa}) = 0.58^{+0.10+10}_{-0.9-0.9} h^2$ supernova units ($1SNu = 1SN(100yr)^{-1}(10^{10}L_{B\odot})^{-1}$), that is a factor ~ 1.6 higher than the local rate (Cappellaro et al., 1999). Although this is a suggestive results, we stress that it is not conclusive given both the caveats mentioned above and the fact that the rate was first calculated per unit comoving volume and then converted in SNu through galaxy counts. This step introduce further uncertainties in the comparison between local and high-z rates.

5.1 The SN rate recipe

For this analysis we have considered a subsample of the collected data (Tab. 5.1), consisting in 5 of the 21 fields monitored in our campaign (corresponding to ~ 1.2 square degree[1]). For these fields we have obtained several observations, at different epochs, in V, B, R bands. The 9 SNe spectroscopically confirmed in these fields are listed in Tab. 5.1 together with the number of SN candidates non spectroscopically confirmed.

Field	SNe spect. confirmed	type	$z(v_{3k})$	SNe candidates
J1888	1999ey	IIn	0.09	12(7)
	2000fc	Ia	0.43	
	2001gh	II	0.16	
	J1888_A	Ia	0.42	
AXAF	1999gt	Ia	0.27	11(8)
	1999gu	II	0.15	
	2001ip	Ia	0.54	
10Z2	-	-		4(1)
13Z3	2002cl	Ic	0.07	9(6)
Field2	2001bd	II	0.10	5(4)

Table 5.1: Subsample of the data used to compute the SN rate.
The number of candidates located in the nuclear region of the host galaxy is indicated in brackets.

[1]Each WFI field cover an area of 0.31 square degree, but the combined image of the dithered frames is slightly smaller ($\sim 90\%$ of the original frames). The effective searched area is given by the overlapping region with a reference frame. Because of slightly different pointings, the resulting effective area is on average $\sim 80\%$ of the WFI original field ($\sim 90\%$ of the combined dithered images). A single field on average correspond to an effective monitored area of ~ 0.24 square degree. Thus the whole monitored area (21 fields) corresponds to ~ 5 square degree.

In order to make a sound and direct comparison of our SN rate estimates at intermediate redshift with the values for the local universe (Cappellaro et al., 1999), we compute the SNR in SNu[2] following the same method used to estimate the local SN rates. The rest-frame SNR at a given redshift z is thus defined in the following way:

$$r_{SN}(z) = \frac{N_{SN}(z)}{\sum_{i=1}^{N_{gal}(z)} L_{B\odot_i} \Delta t(z)} (1+z) \tag{5.1}$$

where $N_{SN}(z)$ is the observed number of SNe occurred per redshift interval, $N_{gal}(z)$ is the number of galaxies with rest-frame $L_{B\odot_i}$ blue luminosity per redshift interval (in unit of solar B luminosity) and $\Delta t(z)$ is the time interval (control time) during which a supernova of a given type at redshift z is brighter than the detection limiting magnitude. The detection limiting magnitude m_{detect} of a given observation can be roughly defined as the magnitude of the faintest SN candidate that can be detected by the data analysis software.
As shown by eq. 5.1, to estimate the SNR we need to:

- define a distance limited sample of galaxies with known integrated luminosity;
- calculate, for each galaxy of the sample, the control time;
- determine the number of all the SNe exploded in the given sample.

5.1.1 The galaxy sample

According to eq. 5.1, to calculate the rates we need to know the intrinsic rest-frame B luminosity and redshift of each galaxy in our sample. We exploited our multi-color and multi-epoch observations to create very deep images, for each field and filter, by stacking the images with good seeing (≤ 1"). The limiting V magnitude in a typical search image is ~ 24.5 while in the deep stacked image is $V \sim 25$ (see Fig. 5.1). The deeper images are useful to detect the faintest galaxies in our fields, to discriminate better between stars and galaxies and to measure galaxy magnitudes and colours with higher accuracy.
Galaxy counts and photometric redshifts have been provided by Botticella (2003), who built the objects catalogs for each deep field with *SExtractor* and, using the *Hyper-z* software[3] (Bolzonella et al., 2000), derived the B luminosity and the photometric redshift of each galaxy by means of a standard Spectral Energy Distributions (SED) fitting procedure (i.e. comparing the observed magnitudes with the expected ones, computed from template SED).
The galaxy sample has been limited in magnitude in order to obtain more reliable colours and so redshifts. All the galaxies fainter than $R = 21.8$ have been excluded from the sample. Only the SN candidates occurred in this sample will be taken into account in our computation.
Fig. 5.2 shows a comparison between the *Hyper-z* photometric redshift of a subsample of galaxies whose spectroscopic redshift is available in the NASA/IPAC Extragalactic

[2] $1SNu = 1SN(100yr)^{-1}(10^{10}L_{B\odot})^{-1}$

[3] http://webast.ast.obs-mip.fr/hyperz/

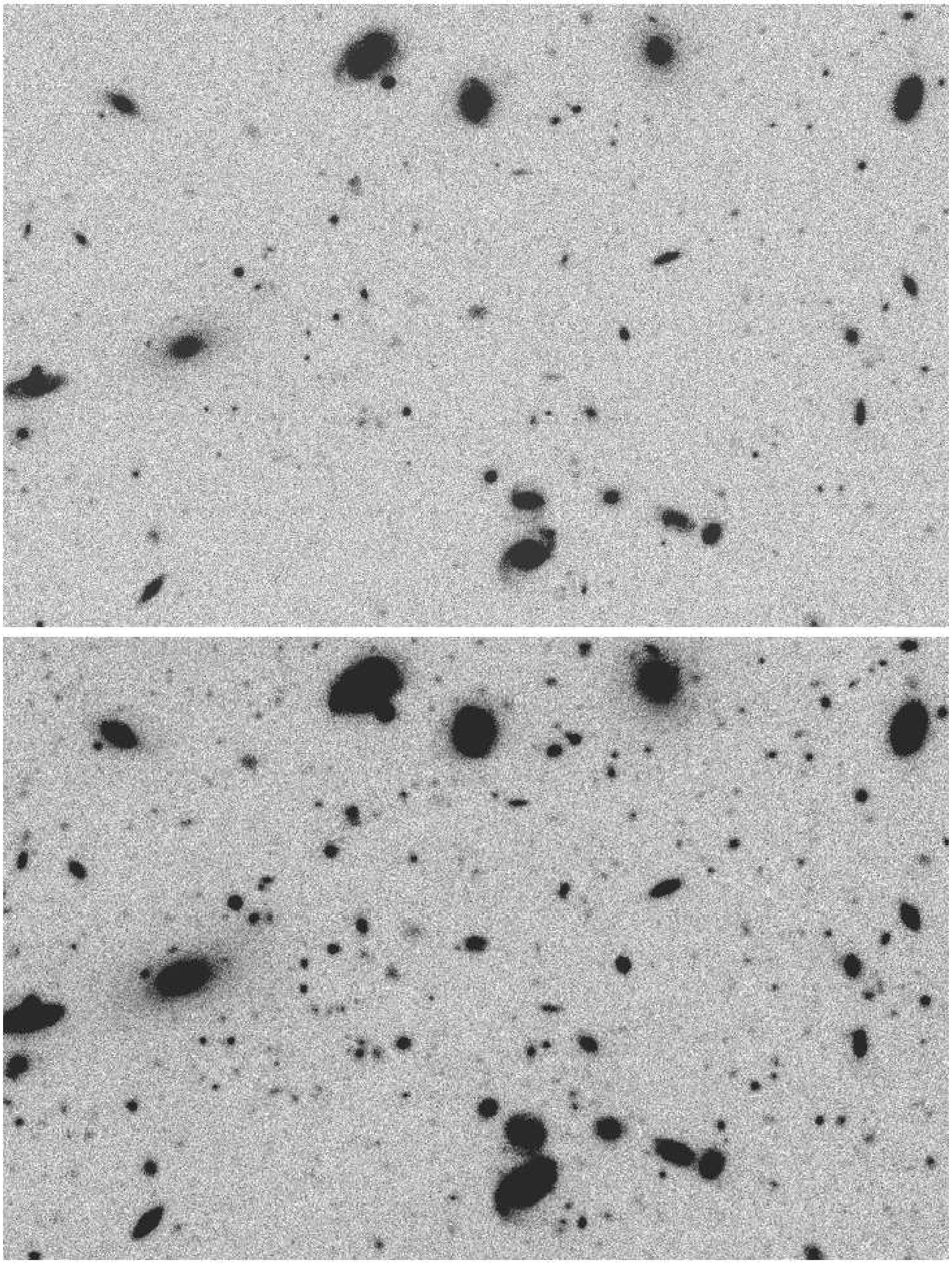

Figure 5.1: Top-panel: The image, sum of 3 dithered V band frames (1 epoch) show a detail of the Field J1888. Exposure time: 2700 sec, magnitude limit $\simeq 24.5$. Bottom-panel: as the previous image but coadding 21 frames (7 epochs), exposure time 18900 sec, magnitude limit $\simeq 25$.

Database (NED) and a comparison between the spectroscopic and the photometric redshift of the 9 SNe of the subsample.

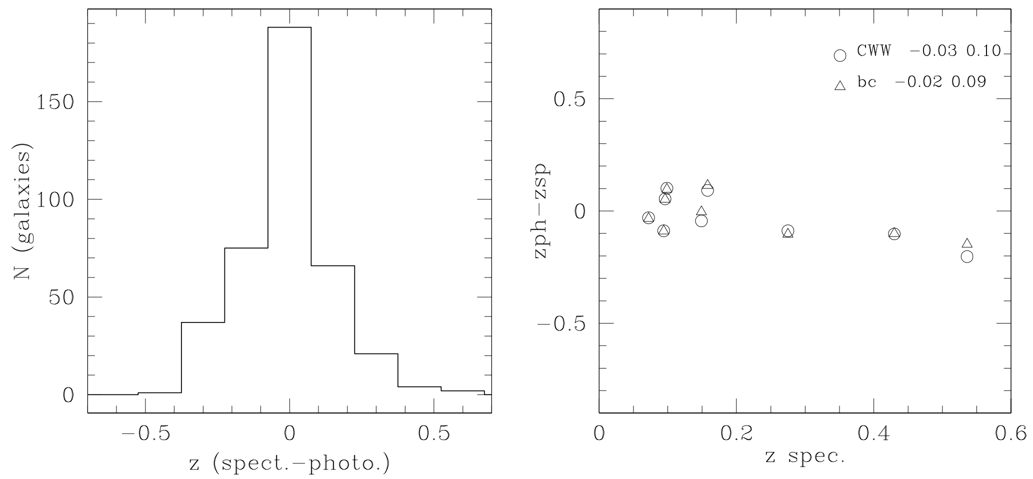

Figure 5.2: Left: Distribution of the galaxies in our sample as a function of the difference between the spectroscopic and photometric redshift. Right: Comparison between the spectroscopic and photometric redshift of the 9 SNe of the analyzed subsample. Two different sets of galaxy spectra have been used for the photometric redshift technique: the synthetic spectra by Bruzual A. and Charlot 1993 (triangles) and the observed ones by Coleman et al. 1980 (circle). $z_{spec} - z_{phot}$ is close to zero and $rms \simeq 0.10$ in both cases.

We stress that in our estimate of the SN rate we do not calculate the total luminosity of galaxies surveyed by theoretical galaxies counts but we measure it directly on our images.

5.1.2 Detection efficiencies and control time

A more precise definition of the control time can be given taking into account an "efficiency curve", which provide the percentage of SN candidates detected by the software as a function of the candidate magnitude. The limiting magnitude m_{detect} can be defined as the magnitude corresponding to a fixed detection efficiency value (for example 90%). There are several concurrent factors determining the detection efficiency:

- the seeing: the better the seeing, the fainter the SN candidates that can be detected;
- the sky transparency: given a fixed exposure time, the clearer the sky, the deeper the images obtained. The sky transparency is quantified by the photometric zero point obtained from the standard stars calibration.
- the field characteristics: each field has a different fraction of galaxies, saturated objects and stars, thus it is very likely that the S/N of the residual objects in the subtracted image as well as the smoothness of the background depend on these

fractions. The completeness curve should thus be determined for each field and each epoch in order to be reliably used for the control time estimation.

We performed a number of artificial star experiments which gave us the detection efficiency for each field and for different seeing conditions.
Artificial stars with proper PSF were added to each galaxy of the field. The position (x, y) from the host galaxy nucleus was computed randomly assuming a gaussian distribution (σ=FWHM$_{galaxy}$/2, see also Pain et al. 1996). For each galaxy, 1000 positions (r, θ) are computed. Then one of them was chosen by means of gaussian random numbers are generated with the Box-Müller method (from "Numerical Recipes: The Art of Scientific Computing", Press et al. 1992). Fig. 5.3 shows an example of the Gaussian radial distribution (computed for a given FWHM) with respect to the host galaxy center, from which the position of an artificial star is randomly extracted.

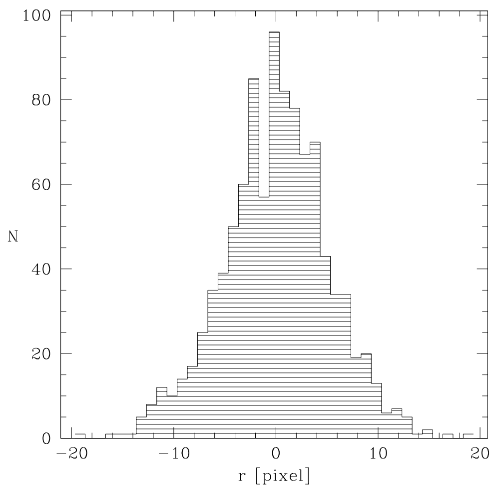

Figure 5.3: Example of Gaussian random radial distribution (σ = 5.4) from which the position of an artificial star is randomly extracted.

The images with the artificial stars included are searched for candidates with our standard pipeline and the number of artificial stars recovered is compared to the total number of artificial stars. The stars are considered successfully recovered if they are detected by the software and the score assigned by `candidate` (described in §3.4.4) is ≥ 0 (these, in fact, are the objects visually inspected by the observer during a real search). This procedure has been repeated for the same field but different artificial star magnitudes and seeing in order to check the efficiency dependence on these parameters.
Typical artificial star experiment performed to compute the search efficiency generate $\sim$ 11.5 GBytes of data. This gives an idea of the bulk of data to be handled.
Fig. 5.5 shows the dependence of the efficiency curve on the seeing conditions for one of our fields. Efficiency is not 100% even at bright magnitudes because a fraction of the added artificial stars statistically lies close to saturated objects and thus rejected by the software (as already described in §3.4.4). The important role played by the seeing conditions stands out clearly: the SN detection limiting magnitude with a good seeing (0.65 arcsec) is $\sim$ 1.2 mag. fainter than the limiting magnitude corresponding to a poor seeing

(1.32 arcsec).
The crucial role of the seeing in the SN search is also shown by Fig. 5.4: the number of sources detected in a given field with a very good seeing ($0.65''$) is almost three times the number of sources detected with poor seeing ($1.32''$). It is interesting to note that galaxies, already characterized by an intrinsic diffuse appearance, are more affected by poor seeing than stars and they are lost or not well classified in greater proportion than stars. It is also significant the difference between the faintest sources detected (adopting the same *SExtractor* threshold), which is about 2 magnitudes. Besides, as obvious, stars and galaxies are better discriminated by the *SExtractor* stellarity index up to fainter magnitudes in the image with better seeing.
For this reason when the seeing conditions during the observing run were worse than $\sim 1.5''$, or when the sky transparency was not good, we performed a "backup program" for bright SNe monitoring.

We also checked the dependence of the detection efficiency on the threshold adopted during the search. As an example we show four artificial stars experiment on one field observed with seeing $=0.90''$ and using different thresholds (expressed in units of the background *rms*) for `SExtractor`. As shown in Fig. 5.6, adopting a threshold equal to 1.5σ, the limiting magnitude is ~ 1 mag. fainter than the one measured adopting a threshold equal to 4σ. However, using a lower threshold has the important drawback of increasing significantly the number of spurious detections. We found that a 2.0–3.0σ threshold is usually a good compromise.

In the artificial stars experiment performed to evaluate the software efficiency, every star added is considered "detected" if the assigned score is ≥ 0. But the "SNe" really recovered are those selected by the observer as reliable candidates (score ≥ 0 is not sufficient now to consider a star successfully recovered, even if it is always a necessary condition). After checking the detection efficiency of our software, we also evaluated the efficiency of the observer. We performed artificial stars experiment using the same strategy as before, but checking the artificial SN candidates by eye, as in a real supernova search. In order to compare the new efficiency tests to the software efficiency we performed the new experiments on the same fields, using the same reference images as for the software efficiency tests.
To perform a more realistic experiment we added only a few artificial stars per chip. Galaxy and position of the artificial star inside the galaxy are always chosen at random and are not known to the observer. We tested the observer efficiency for two very different seeing values (chosen at the ends of the seeing range), to test the dependence on this parameters, as already done for the software efficiency.
In Tab. 5.1.2 we show the results of the artificial star experiments: the efficiency in recovering the stars is very high also at faint magnitudes. We always identify as real variable sources all the stars recovered by the software and only in a few cases we do not classify them as "SN" either because they are very close to the center of the host galaxy (they can be AGN as well as SNe), or because the host galaxy has a stellar appearance (in this case the classification is "variable star"). Mixed definitions like "AGN-variable star" or "SN-VAR" are due to the uncertain classification (star or galaxy) of the sources detected.

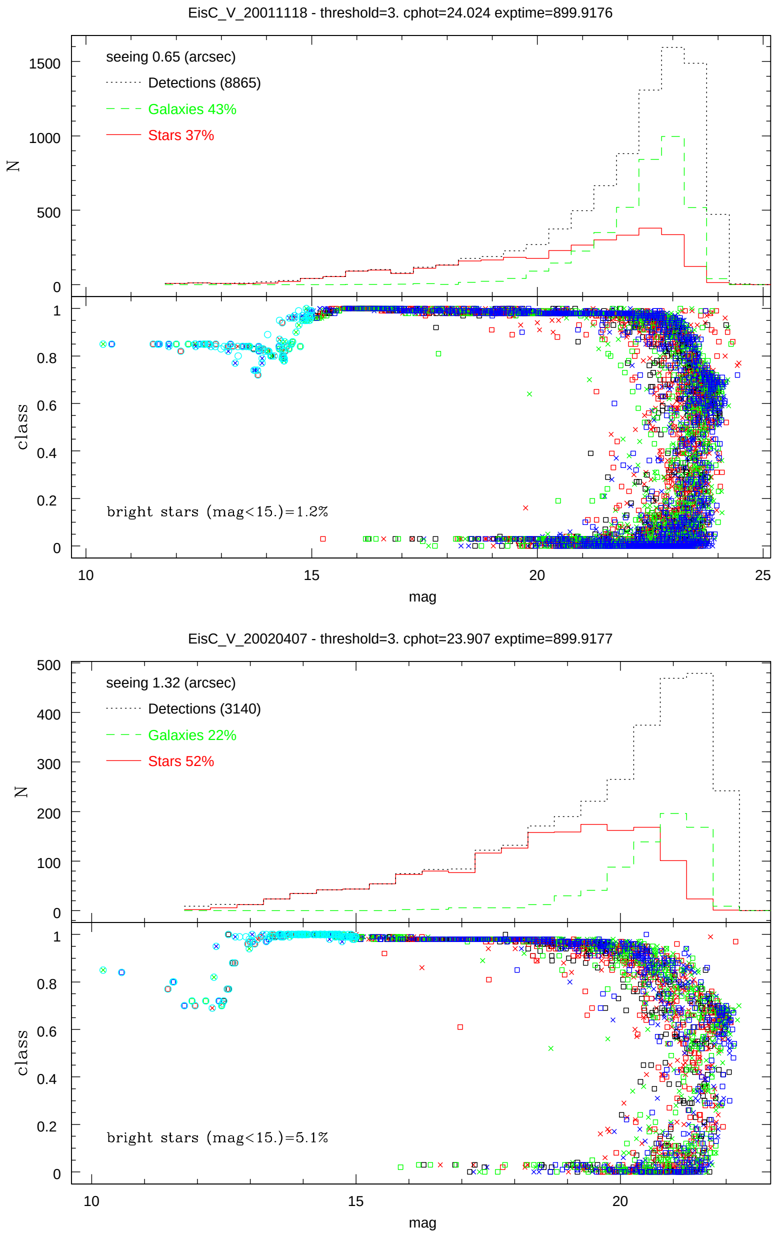

Figure 5.4: Galaxy-star distribution for two different seeing valus (0.65″, 0.32″). *CLASS* is the *SExtractor* stellarity index (0 ⇔ galaxy, 1 ⇔ stars). Note the decrease in "stellarity" for bright, saturated stars (In a typical 900 sec. exposure time WFI image, in V band, saturation starts for objects brighter than $V \sim 15$). At faint magnitudes the galaxy-star separation degrades and most of the objects have an intermediate stellarity index.

The results obtained show that an experienced observer accept $\sim 100\%$ of the artificial stars and that the result doesn't depend on seeing. So, in the following analysis, we will account for the software efficiency curves only.

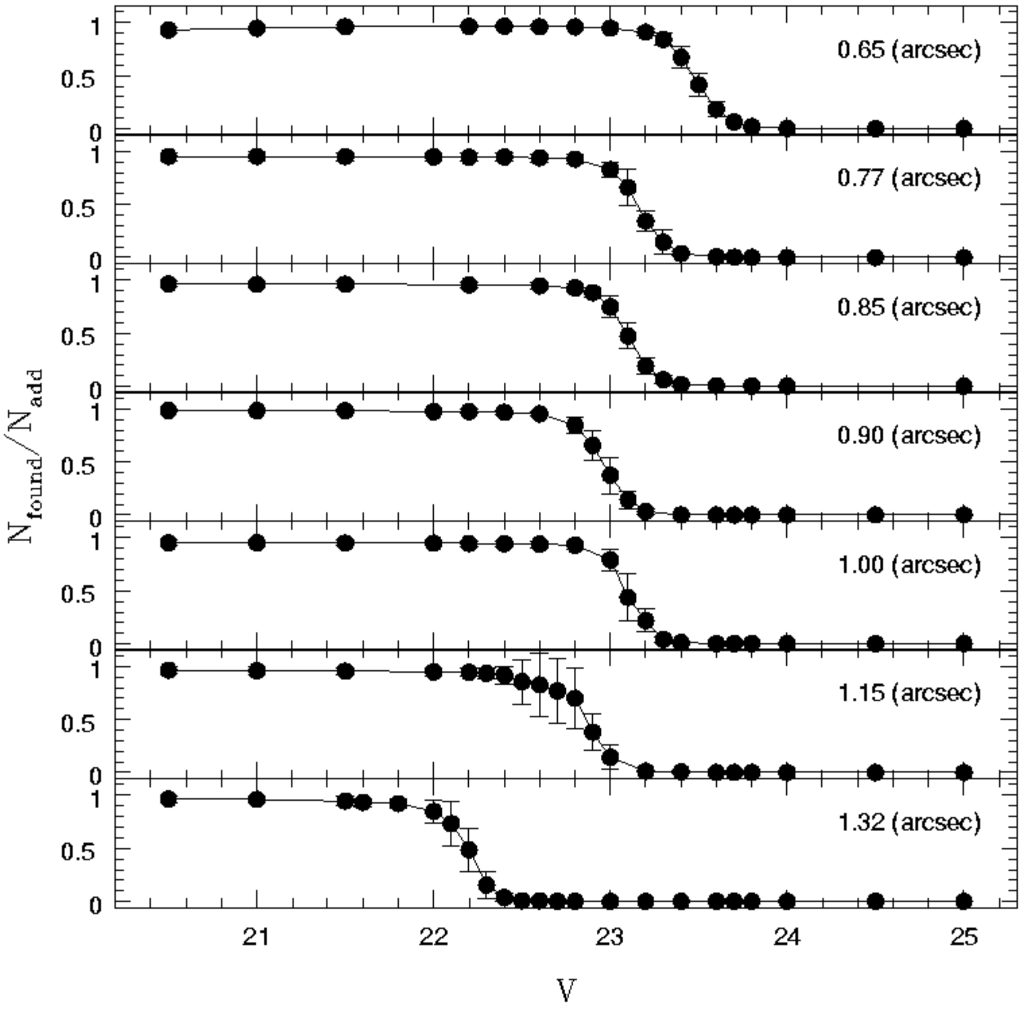

Figure 5.5: SN candidates detection efficiencies curves for one of the search field observed with different seeing conditions. Each curve is the average of the efficiency curves computed for the 8 chips of the WFI mosaic. Errorbars are given by the dispersion of the efficiency at a given magnitude between the 8 CCDs.

We computed the control time as a function of redshift and SN magnitude equal to the weighted sum of the number of days during which the SN could be detected. The weighting was done according to the corresponding SN detection efficiency $\epsilon(m(t))$, which is function of the SN magnitude m and, in turn, of time t relative to maximum. Control times were computed for each value of z as in eq. 5.2.

$$\Delta t(z) = \int \epsilon(m_z(t))dt \tag{5.2}$$

If the time interval between the search and reference frames is shorter than the computed control time, the effective control time, for a single epoch, is given by the time interval

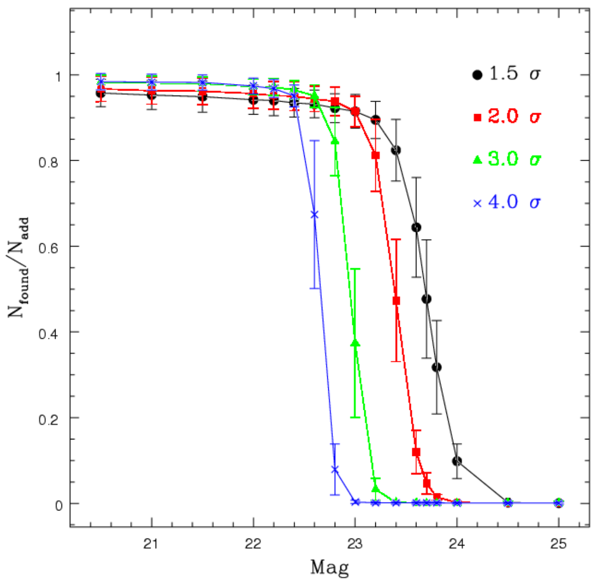

Figure 5.6: Dependence of the efficiency curve on the *SExtractor* adopted threshold for the sources detection.

between the new and reference epoch, according to eq. 5.3.

$$\Delta\hat{t}(z) = \begin{cases} \Delta t(z) \\ t_i - t_{i-1} \end{cases} \text{if } t_i - t_{i-1} = \begin{cases} > \Delta t \\ \leq \Delta t \end{cases} \tag{5.3}$$

The total control time for an individual galaxy at redshift z in a field observed in N epochs is given by

$$\Delta\tilde{t}(z) = \sum_{n=i}^{N} \Delta\hat{t}(z) \tag{5.4}$$

For each field we estimated the overall control time for four SN types (Ia, IIP, IIL, Ib/c) and different redshift bins using the same template SN light curves by Cappellaro et al. 1993a and references therein (see Fig. 5.7, Tab. 5.3). SN absolute magnitudes were not corrected for extinction since we are interested in the observed absolute magnitudes rather than in the extinction corrected ones (this implies the assumption that high redshift SNe suffer, on average, the same extinction as nearby ones). It is important to note that the adopted value $H_0 = 75\,\mathrm{km\,s^{-1}Mpc^{-1}}$ does not affect the control time because, appearing both in the determination af the absolute magnitude of SNe and in the galaxy distance estimate, disappears in the computation.

The template SN light curves are redshifted and corrected for the cosmological time dilatation $(1 + z)$, due to the recession velocity, and the K-correction, which accounts for the doppler shift between the observer frame and the SN rest frame photometric bandpass (see Fig. 5.9). The K-correction, which is necessary to calculate the apparent magnitude

NEW: EisC, V band, 2001-11-18, seeing 0.65, phot. cost=24.024 REF: EisC, V band, 1999-12-28, seeing 0.77, phot. cost=24.053						
mag (1)	N_{tot} (2)	N_{comm} (3)	$N_{score\geq 0}$ (4)	$threshold$ (5)	$N_{recovered}$ (6)	$efficiency_{obs}$ (7)
21.0	8	6	6	3-3-3	5 SN +1 VAR-SN	83-100%
21.5	8	3	3	3-3-3	3	100%
22.4	8	7	6	3-3-3	5 SN +1 SN-VAR	83-100%
22.8	8	7	7	3-3-3	5 SN +1 SN-VAR +(1 AGN-VAR)	71-85-(100)%
23.0	8	8	8	3-3-3	8	100%
23.2	8	8	7	3-3-3	5 SN +(2 AGN)	71-(100)%
23.3	8	8	7	3-3-3	7 SN	100%
23.4	8	7	7	3-3-3	7 SN	100%
23.5	8	7	4	3-3-3	4 SN	100%
23.6	8	8	0	3-3-3	0 SNe with score ≥ 0	-
NEW: EisC, V band, 2002-04-07, seeing 1.32, phot. cost=23.907 REF: EisC, V band, 1999-12-02, seeing 1.15, phot. cost=24.040						
(1)	(2)	(3)	(4)	(5)	(6)	(7)
21.0	32	30	27	3-3-3	21 SN +2 AGN-SN +(4 AGN)	78-85-(100)%
21.5	32	29	27	3-3-3	24 SN +2 SN-AGN +(1 AGN)	89-96-(100)%
21.6	32	30	28	3-3-3	19 SN +2 SN-AGN +(6 AGN)	68-75-(96)%
21.8	32	30	28	3-3-3	20 SN +3 SN-AGN +(5 AGN)	71-82-(100)%
22.0	32	31	27	3-3-3	20 SN +1 SN-AGN +(6 AGN)	74-78-(100)%
22.1	32	30	22	3-3-3	17 SN +3 SN-AGN +(2 AGN)	77-91-(100)%
22.2	32	31	17	3-3-3	14 SN +2 AGN-SN +(1 AGN)	82-94-(100)%
22.3	32	31	7	3-3-3	7 SN	100%
22.4	32	30	2	3-3-3	1 SN +(1 AGN)	50-(100)%
22.5	32	31	0	3-3-3	0 SNe with score ≥ 0	-

Table 5.2: Observer detection efficiency.

(1): artificial stars magnitude; (2): stars added; (3) stars in the overlapping region of the new and reference images; (4) stars recovered by our software (we assume a star to be recovered if the corresponding score is ≥ 0; (5) *SExtractor* threshold in the new-reference-difference image; (6) stars recovered by the observer; (7) observer efficiency (calculated as $N_{recovered}/N_{score\geq 0}$). N_{comm} can be smaller than N_{tot} because one ore more objects can fall out of the overlapping region of the new and reference images; $N_{score\geq 0}$ can be smaller than N_{comm} when one or more objects are not recovered by the software (for example if an object falls very close to a saturated, masked star or if the S/N of the object in the subtracted image is too low). If we assume to confirm spectroscopically the variable sources labeled as "SN", the efficiency is the first value in column (7); if we check also uncertain objects like "SN-AGN" or SN-VAR", the efficiency is the second value; if we assume to observe spectroscopically all the variable sources labeled "SN", "SN-...", "AGN", the corresponding efficiency is the third value, in brackets. In this context "AGN" simply means that the candidate fall close to the center of the host galaxy.

in a y filter band of a source observed in a x filter band at redshift z, is given by:

$$K_{xy} = 2.5log(1+z) + 2.5log\left(\frac{\int F(\lambda)S_x(\lambda)d\lambda}{\int F(\lambda/(1+z))S_y(\lambda)d\lambda}\right) + Z_y - Z_x \tag{5.5}$$

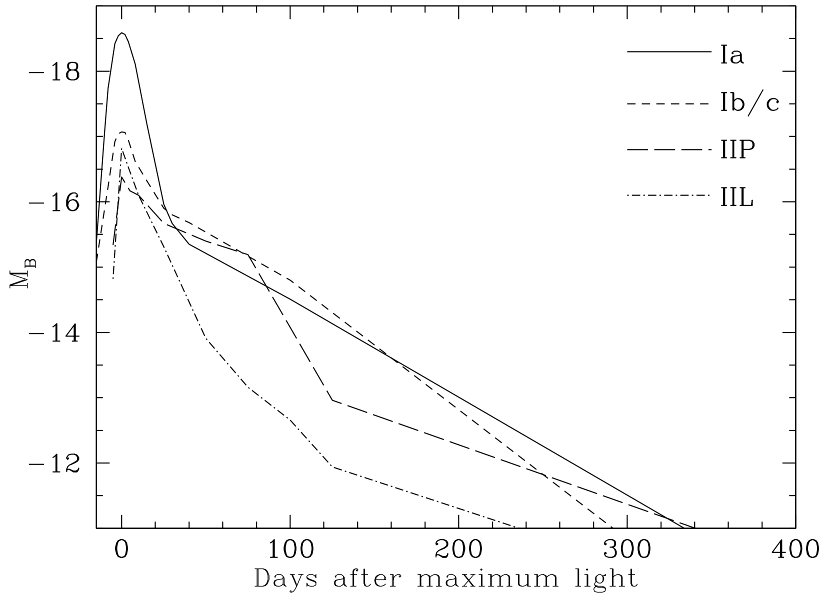

Figure 5.7: Comparison between light curve templates for different SN types.

where $F(\lambda)$ is the source spectral energy distribution (a SN in this case), and $S_x(\lambda)$ is the transmission of the filter x. The $Z_y - Z_x$ term accounts for the difference in zeropoints of the filters (see Kim et al. 1996). K-corrections have been computed following eq. 5.5 and exploiting a sample of good signal-to-noise SN spectra available in the archive of the Padova Observatory. For each SN type (Ia and Core Collapse), spectra of local supernovae, taken at different phases, have been redshifted at different z and the difference K_{xy} between the x magnitude at redshift z and the y magnitude at $z = 0$ have been computed. Fig. 5.8 shows the K_{BV} and K_{BR} for type Ia SNe at $z = 0.25$ and $z = 0.5$ respectively. We stress that at $z \sim 0.25$, which is close to the mean redshift of our SN sample, the SN rest frame B band is redshifted and almost coincident to the observer V band. This means that the K_{BV} correction is independent from the source spectrum and the related uncertainties are minimized. This is our case, since we performed the search in V and we used B band templates, K corrected, to compute the control time.

Finally, the apparent V magnitude has been computed as

$$m_V(z, t_{obs}) = M_B(t_{rest}) + \mu(z) + K_{BV}(z, t_{rest}) + A_V \tag{5.6}$$

SN type	Ia	Ib/c	IIP	IIL
M_B	-18.59	-17.07	-16.38	-16.82
σ_B	0.71	0.39	1.49	1.10

Table 5.3: Observed absolute magnitude at maximum for different SN types.

Data from Cappellaro et al. 1993a.

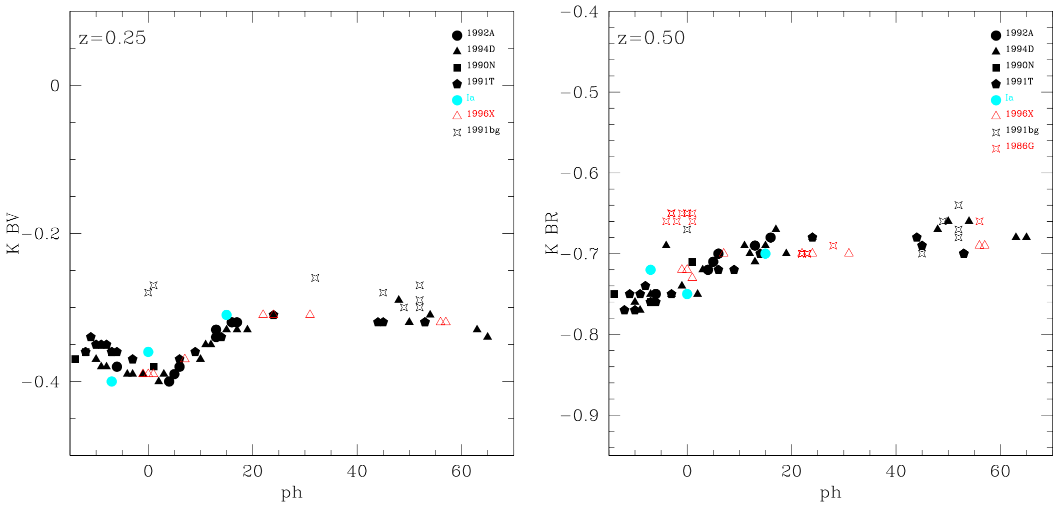

Figure 5.8: K_{BV}-correction at $z = 0.25$ and K_{BR}-correction at $z = 0.0.5$ for type Ia SNe.

where $\mu = 5logd_L(z) - 5$ is the distance modulus (based on luminosity distance), M_B is the absolute B magnitude, t_{rest} is the SN rest frame time, $t_{obs} = (1+z)t_{rest}$ is the time in the observer frame and A_V the Galactic absorption. For each field we adopted the galactic extinction A_V by Schlegel et al. (1998), relative to the coordinates of the field centre. Luminosity distance has been determined, for a given z, following Schmidt et al. (1998) (we assumed a flat Universe with $\Omega_M = 1 - \Omega_\Lambda = 0.3$, $H_0 = 75\,\mathrm{km\,s^{-1}Mpc^{-1}}$, see eq. 1.15).

The control time calculation takes into account the luminosity distance of the SN and the dispersion of the magnitude at maximum for each SN type (Cappellaro et al., 1993a). In fact, for each SN type, we assumed the absolute magnitude at maximum to be characterized by a gaussian distribution, z independent, with peak value and width given by M_B and σ_B (see Tab. 5.3). For each redshift bin, several light curves, corresponding to an absolute magnitude at maximum ranging in the interval $M_{max} \pm \sigma$, have been computed and the control time corresponding to the given z has been computed as the weighted mean of the different values obtained.

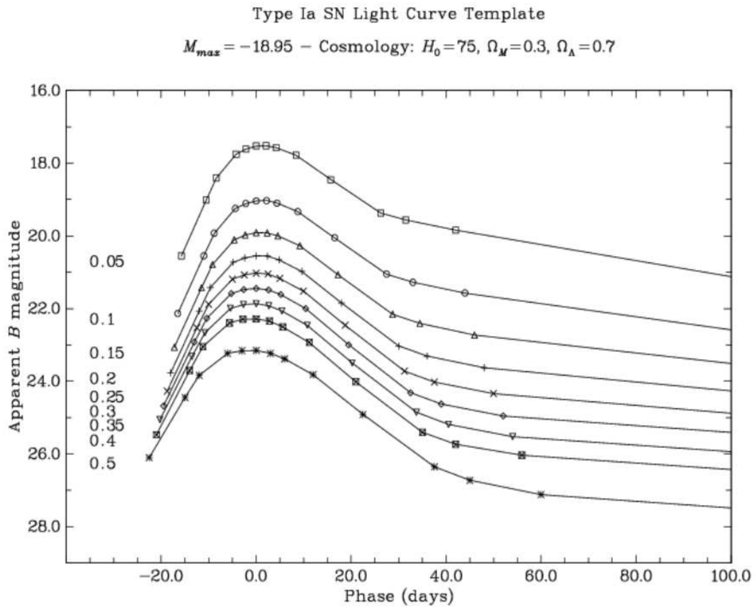

Figure 5.9: SN Ia light curve at different redshifts.

5.1.3 SN Candidates

Because of the limited VLT time available, we could not observe spectroscopically all our candidates. So, to determine the number of SNe occurred in observed fields, we must take into account this fact and correct the SNe spectroscopically confirmed for completeness. In the 5 fields analyzed in this work (see Tab. 5.1) we confirmed spectroscopically 9 SNe out of 50 selected SN candidates. To determine the reliability of the candidates we exploited the multi-band, multi-epoch information collected in our database, checking the variability history, as well as the candidate colour (when available). Following this procedure we were able to reject those candidates with light curves not consistent with those of SNe.
We proceeded as follows: in addition to the spectroscopically confirmed SNe, we assumed to be true SNe all the candidates far from the host galaxy nuclei. For what concerns the other candidates (65% of all the candidates are located in the nuclear region of the host galaxy) there is a significant chance that they are AGN. Actually, from the follow-up observations, we found that $\sim 40\%$ of the candidates located in the nuclear region were eventually confirmed to be SNe, so they were weighted accordingly to estimate the total number of SNe exploded.
The candidates associated to galaxies not included in the selected galaxy sample (see §5.1.1) have been rejected.
We thus estimated the "true" global number of SNe occurred in our sample ($n_{SNe} \simeq 30$).

5.2 SN Rates

We do not have enough data to discriminate between different SN types, so, in order to compute the SNR, we compared the redshift distribution of all the SNe candidates, obtained through the host galaxy using the photometric redshift technique by Botticella (2003), with the expected global SN distribution, given by

$$N_{exp}^{tot}(z) = N_{exp}^{Ia}(z) + N_{exp}^{Ib/c}(z) + N_{exp}^{II}(z) \tag{5.7}$$

Eq. 5.7 can be written by means of the SN rates r:

$$N_{exp}^{tot}(z) = \frac{r_{Ia}}{1+z} \sum_{i=1}^{N_{gal}(z)} L_{B\odot_i} \Delta\tilde{t}_{Ia}(z) + \frac{r_{CC}}{1+z} \sum_{i=1}^{N_{gal}(z)} L_{B\odot_i} \Delta\tilde{t}_{CC}(z) \tag{5.8}$$

where, for simplicity sake and because the explosion mechanism is the same, we have joined the CCSNe rates and control times in r_{CC} and $\Delta\tilde{t}_{CC}$ (in the computation the contribution of type Ia, Ib/c and type II SNe has been treated separately).

Fig. 5.10 shows the comparison between the observed and the expected distribution obtained assuming the SN rates to be constant and equal to the values found for the local universe (without reddening correction[4]): $r_{I_a} = 0.14 \pm 0.06$ SNu, $r_{CC} = 0.30 \pm 0.10$ SNu

[4]The extinction correction was not applied because of the difficulties in determining the effects of absorption at high z. Thus reference has been made to the local SN rate values and the light curve templates non corrected for absorption.

($r_{CC} = r_{Ib/c} + r_{II}$, $r_{Ib/c} = 0.05 \pm 0.04$, $r_{II} = 0.25 \pm 0.09$) ($H_0 = 75\,\mathrm{km\,s^{-1}Mpc^{-1}}$, Cappellaro et al. 1999). The comparison shows a deficit of the expected distribution suggesting that, if we assume the SN rates to be constant with redshift, they are higher than the local values, or that the SN rate values change with redshift. Indeed, theoretical expectations

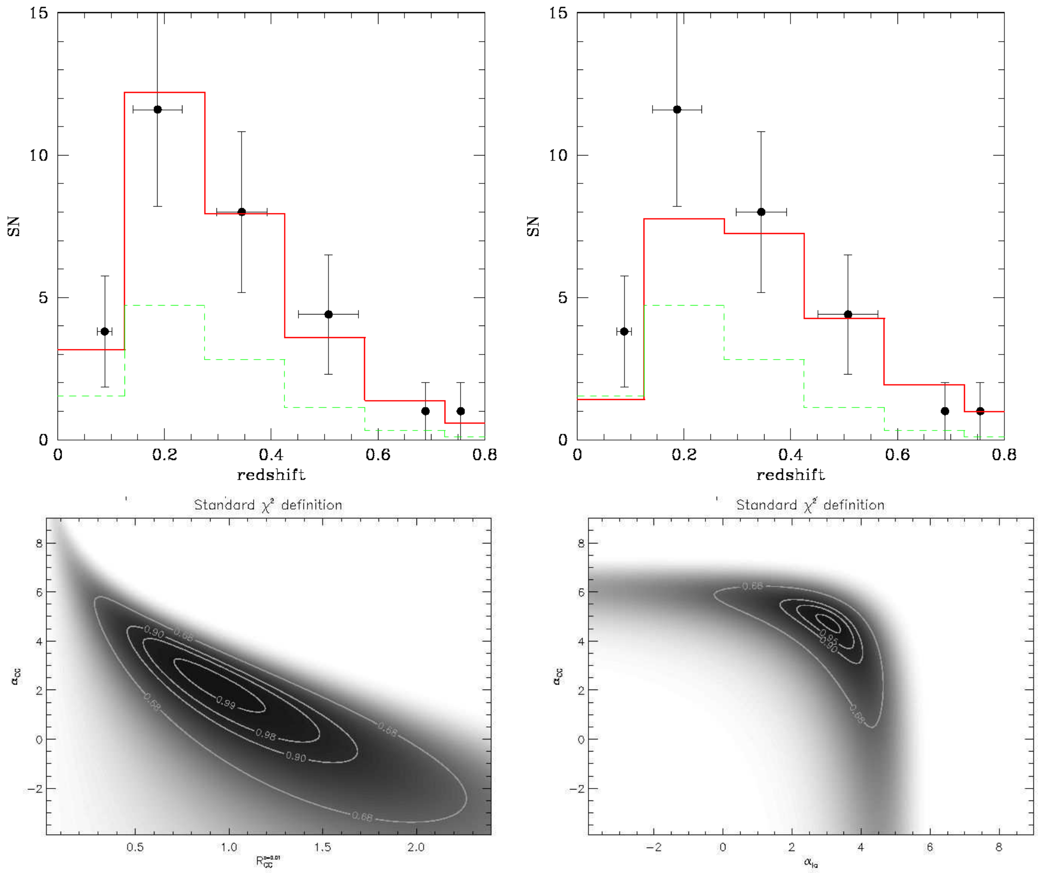

Figure 5.10: Upper panels: Comparison between the observed distribution (filled dots) and the expected distribution (short dashed histogram) obtained assuming the SN rate to be constant and equal to the values found for the local universe. Solid line histogram shows the best match between expected and observed SN distribution, obtained assuming the type Ia and CCSNe rates varying with redshift according to the law: $r_{SN}(z) = \bar{r}_{\bar{z}}^{SN}[(1+z)/(1+\bar{z})]^{\alpha_{SN}}$. Left panel: r_{Ia}, α_{Ia} fixed (case 1, see text); Right panel: r_{Ia}, r_{CC} fixed (case 2, see text). Lower panels: Two-parameters maximum likelihood fit of the observed SN distribution and the SN distribution expected in case 1 and 2. Left panel: $r_{CC} - \alpha_{CC}$ plane. Right panel: $\alpha_{Ia} - \alpha_{CC}$ plane. The 68%, 90%, 95% levels are shown (probabilities have been normalized at $P(\chi^2)_{bestfit} = 100\%$ and only statistics errors have been considered).

(Madau et al., 1998a; Ruiz-Lapuente and Canal, 1998; Sadat et al., 1998) seems to favour a possible evolution in the rate. For this reason we try to derive constraints on possible SN rate evolution and we choose to approximate any potential evolution with a power law:

$$r_{SN}(z) = \bar{r}_{\bar{z}}^{SN}[(1+z)/(1+\bar{z})]^{\alpha_{SN}} \tag{5.9}$$

where α_{SN} is an index of evolution ($\alpha_{SN} = 0$ indicates no evolution) and $\bar{r}_{\bar{z}}$ is the SN rate at $z = \bar{z}$ (see also Pain et al. 2002). In this case eq. 5.8 becomes:

$$N_{exp}^{tot}(z) = \frac{r_{\bar{z}}^{Ia}(1+z)^{\alpha_{Ia}-1}}{(1+\bar{z})^{\alpha_{Ia}}} \sum_{i=1}^{N_{gal}(z)} L_{B\odot_i} \Delta\tilde{t}_{Ia}(z) + \frac{r_{\bar{z}}^{CC}(1+z)^{\alpha_{CC}-1}}{(1+\bar{z})^{\alpha_{CC}}} \sum_{i=1}^{N_{gal}(z)} L_{B\odot_i} \Delta\tilde{t}_{CC}(z) \tag{5.10}$$

Our data are not enough to constrain all the unknown parameters ($r_{\bar{z}}^{Ia}$, α_{Ia}, $r_{\bar{z}}^{CC}$, α_{CC}), therefore we need to use additional information, either on the rates or the evolutionary coefficients. We can perform a two-parameters fit of the expected and the observed distribution, fixing two of the four parameters and varying the remaining parameters in order to get the best match between observed and expected SN distribution.
We studied two cases:

1. type Ia SN rate at $\bar{z} = 0.55$ is fixed according the results obtained by Pain et al. (2002): $r_{0.55}^{Ia} = 0.58_{-0.18}^{+0.20} h^2$ SNu, $\alpha_{Ia} = 0.8$ ($h = H_0/100$);
2. the SN rates at $\bar{z} = 0.01$ for type Ia and CCSNe are fixed according to Cappellaro et al. (1999): $r_{0.01}^{Ia} = 0.14 \pm 0.06$ SNu, $r_{0.01}^{CC} = 0.30 \pm 0.10$ SNu, ($H_0 = 75\,\mathrm{km\,s^{-1}Mpc^{-1}}$).

In the first case we look for the values of the pair r_{CC}, α_{CC} that give the best fit of the expected and observed SN distribution. We point out that, since the evolutionary index is given by Pain et al. (2002) for the SN rate in unit of comoving volume, to assume the same evolutionary index for the rate in SNu implies the assumption of a constant B luminosity density with redshift. This issue will be discussed more in detail in §5.3.
In the second case we look for the most probable pair of values for α_{Ia}, α_{CC}.
For each pair of free parameter values we performed a χ^2 test of the observed and expected SN distribution and we converted the results in probability through the Γ function. The parameter pair associated with the higher probability give us the most reliable values. The results obtained in the two cases (see Fig. 5.10) are listed below ($H_0 = 75$):

1. $r_{0.01}^{CC} = 0.90_{-0.6}^{+0.9}$ SNu, $\alpha_{CC} = 2.4_{-2.4}^{+3.4}$ (1σ), $P(\chi^2)_{bestfit} = 99\%$;
2. $\alpha_{Ia} = 2.9_{-2.9}^{+1.8}$, $\alpha_{CC} = 5.1_{-4.7}^{+0.9}$ (1σ), $P(\chi^2)_{bestfit} = 60\%$.

The expected SN distribution corresponding to case 1 is shown in Fig. 5.10 (Left), while the expected SN distribution corresponding to case 2 is shown in Fig. 5.10 (Right). The better agreement between the observed and expected distributions obtained in case 1 seems to favour a shallower evolution of SN rates with redshift but, on the other hand, the corresponding local SN rates are too large if compared to the values given by Cappellaro et al. 1999.

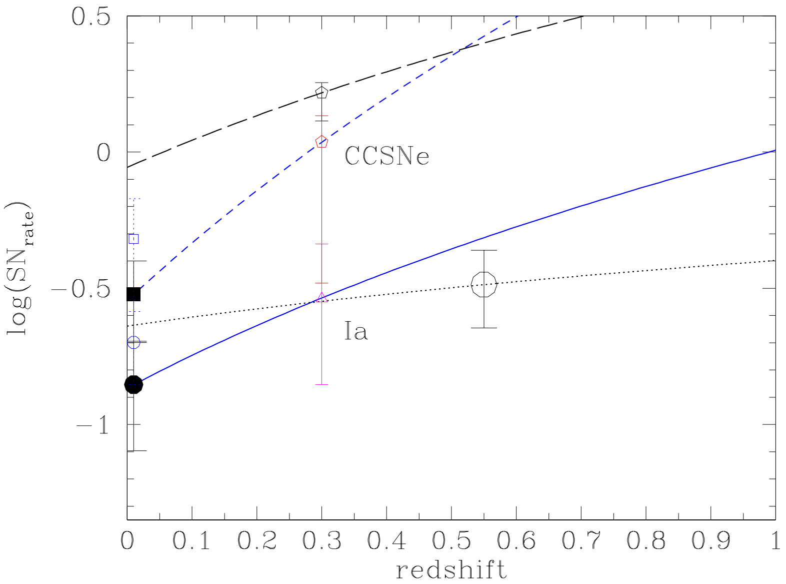

Figure 5.11: SN rate evolution with z. The circles and squares at $z = 0.01$ mark respectively the local SN rate for type Ia and CCSNe given by Cappellaro et al. 1999, the filled symbols marks the local SN rates not corrected for extinction. The empty circle at $z = 0.55$ marks the SN rate estimate given by Pain et al. 2002. Dotted and long dashed lines: SN Ia and CCSN rates obtained in case 1 (see text). Solid and short dashed lines: SN Ia and CCSN rates obtained in case 2 (see text). Our estimates for type Ia and Core Collapse SN rates at $z = 0.30$, obtained in the two cases, are shown. SN rates are expressed in SNu and scaled to H=75 km s^{-1}Mpc^{-1}.

Although the current data set does not allow us to derive tight constraints, the results suggests an evolution in the SN rates. In particular CCSN rate increase with redshift is steeper than type Ia evolution. If we compute the rates at $z = 0.3$ in the two cases we obtain:

1. $r^{CC}_{0.3} = 1.65^{+0.15}_{-0.35}$ SNu (1σ), $r^{Ia}_{0.3} = 0.28$ SNu
2. $r^{CC}_{0.3} = 1.09^{+0.27}_{-0.76}$ SNu, $r^{Ia}_{0.30} = 0.29^{+0.17}_{-0.15}$ SNu (1σ)

The CCSN rate at $z = 0.3$ results a factor ~ 1.8 and ~ 3.6 larger than the local one, in the case 1 and 2 respectively. The comparison with the ratio between CCSNe and type Ia SNe found for the local universe

1. $r^{CC}_{0.01}/r^{Ia}_{0.01} \simeq 3.9$
2. $r^{CC}_{0.01}/r^{Ia}_{0.01} \simeq 2.14$

shows a significant increase of CCSNe with redshift in both cases:

1. $r_{0.3}^{CC}/r_{0.3}^{Ia} \simeq 5.9$
2. $r_{0.3}^{CC}/r_{0.3}^{Ia} \simeq 3.8$

The results are summarized in Fig. 5.11 and suggest an evolution for both type Ia and Core Collapse SNe.

5.3 SN Rates and luminosity density

SN rate in supernova unit $[events \times h^2(100yr)^{-1}(10^{10}L_{B\odot})^{-1}]$ and in unit of comoving volume $[events \times h^3 Mpc^{-3}yr^{-1}]$ are linked each other by the B luminosity density $\rho_{L(B)}$ (usually expressed in $[\times hL_{B\odot}Mpc^{-3}]$). The luminosity density at a given z is crucial to compare SN rates determined in different units of measurement. If we approximate any potential evolution with a power low: $\rho_{L(B)}(z) = \rho_{L(B)}(local)(1+z)^{\beta}$ and if α represents the evolutionary index for the SN rate in unit comoving volume (see eq. 5.9), then the evolutionary index for the SN rate in SNu is simply given by the difference $\alpha - \beta$. If the luminosity density is constant with redshift (i.e. $\beta = 0$), SN rates in SNu and events/volume are characterized by the same evolutionary index. We also point out that before comparing SN rate values, one must convert them in the same reference cosmological model. We summarized in Tab. 5.4 the SN rates at different redshifts obtained by several authors, all scaled to h_{100} and with the corresponding adopted cosmological model and luminosity density $\rho_{L(B)}$.

Lilly et al. (1996) found that, for a $q_0 = 0.5$, $\Omega = 1$ cosmological model (i.e. $\Omega_M = 1$, $\Omega_\Lambda = 0$), the comoving luminosity density increases as $(1+z)^{2.72\pm0.5}$ at 4400Å (the Loveday et al. 1992 local luminosity density $1.9770 \times 10^{19} h_{50}\, W\, Hz^{-1}\, Mpc^{-3}$ was adopted, corresponding to a $\rho_{L(B)}(local) = 1.16 \times 10^8 hL_{B\odot}Mpc^{-3}$).
If we adopt the favoured cosmological model ($\Omega_M = 0.3$, $\Omega_\Lambda = 0.7$) the evolutionary index must be reduced by 0.85 ($\rho_{L(B)}(z) = \rho_{L(B)}(local)(1+z)^{1.85}$).
Unfortunately there is still a significant uncertainty in the luminosity density and its evolution with z. However, even if the uncertainties and the scatter between different measurements is still high (see Fig. 5.12), more recent studies suggest higher values for $\rho_{L(B)}(local)$: Marzke et al. (1998) obtained 1.7×10^8, Folkes et al. (1999) found 2.7×10^8 and Cross et al. (2001), exploiting the 2dF Galaxy Redshift Survey data, derived $2.49 \times 10^8 hL_{B\odot}Mpc^{-3}$.
If we compute the luminosity density evolutionary index as in Lilly et al. (1996) but assuming $\rho_{L(B)}(local) = 2.2 \times 10^8 hL_{B\odot}Mpc^{-3}$ (which is a reasonable average value of the luminosity density estimates in literature, see Fig. 5.12) and we adopt $\Omega_M = 0.3$, $\Omega_\Lambda = 0.7$, we find $\beta = 0.45^{+0.45}_{-0.45}$ which is consistent with a very small evolution, if any. This result is confirmed also by Wolf et al. (2003), who found that the B luminosity density remains virtually unchanged from $z = 1.1$ to $z = 0.5$ and show a decrease to the present epoch, most strongly at shorter wavelenghts and dependent on the adopted local value, as shown in Fig. 5.13. In B band, if we exclude an old estimated by Loveday et al. (1992), data are consistent with an almost flat trend also at low redshit. Therefore our previous assumption of a constant luminosity density wit redshift results well justified. Under this

z	r_{Ia}	α_{Ia}	r_{CC}	α_{CC}	SNu*	events/vol.$^\diamond$	Cosmology		ref.
							Ω_M	Ω_Λ	
0.01	$0.4^{+0.2}_{-0.2}$	-			$\surd$				0
0.01	$0.25^{+0.11}_{-0.11}$	-	$0.53^{+0.18}_{-0.18}$	-	$\surd$				1
0.01	$^\dagger 0.36^{+0.11}_{-0.11}$	-	$^\dagger 0.85^{+0.34}_{-0.34}$	-	$\surd$				1
0.06	$^c 0.44^{+0.24}_{-0.28}$	-			$\surd$				2
0.10	$0.44^{+0.48}_{-0.29}$	-			$\surd$				3
0.10	$^\ddagger 0.62^{+0.68}_{-0.40}$	-				$\surd$			3
0.11	$0.40^{+0.28}_{-0.28}$	-			$\surd$				2
0.25	$^c 0.80^{3.36}_{0.76}$	-			$\surd$		0.30	0.70	4
0.30			$2.93^{+0.27}_{-0.62}$	$2.4^{+3.4}_{-2.4}$	$\surd$		0.30	0.70	case 1
0.30	$0.51^{+0.30}_{-0.27}$	$2.9^{+1.8}_{-2.9}$	$1.94^{+0.48}_{-1.35}$	$5.1^{+0.9}_{-4.7}$	$\surd$		0.30	0.70	case 2
0.50	$1.4^{+0.50}_{-0.50}$	-				$\surd$	0.30	0.70	5
0.50	$^\triangleleft 0.64^{+0.23}_{-0.23}$	-			$\surd$		0.30	0.70	5
0.55	$^\Lambda \underline{1.53}^{+0.28}_{-0.25}$	-				$\surd$	0.28	0.72	6
0.55	$^O 2.42^{+0.44}_{-0.40}$	-				$\surd$	0.30	0.00	6
0.55	$^E 3.25^{+0.58}_{-0.53}$	-				$\surd$	0.30	0.00	6
0.55	$^\Lambda 1.55^{+0.29}_{-0.30}$	$0.8^{+1.6}_{-1.6}$				$\surd$	0.28	0.72	6
0.55	$^O 2.48^{+0.48}_{-0.48}$	$1.3^{+1.6}_{-1.6}$				$\surd$	0.30	0.00	6
0.55	$^E 3.36^{+0.64}_{-0.64}$	$1.7^{+1.5}_{-1.6}$				$\surd$	1.00	0.00	6
0.55	$^\Lambda 0.63^{+0.11\triangle}_{-0.10}$	-			$\surd$		0.28	0.72	6
0.55	$^\Lambda \underline{0.58}^{+0.10\triangledown}_{-0.09}$	-			$\surd$		0.28	0.72	4
0.55	$^O 0.78^{+0.14}_{-0.13}$	-			$\surd$		0.30	0.00	6
0.55	$^E 0.91^{+0.16}_{-0.14}$	-			$\surd$		1.00	0.00	6
0.90	$^c 1.64^{+4.92}_{-1.56}$	-			$\surd$		0.30	0.70	4

Table 5.4: SN rates estimates at different redshifts

case 1, case 2 - this Thesis,

0 -Madgwick et al. (2003),

1 - Cappellaro et al. (1999), † values corrected for host galaxy extinction;

2 - Reiss (2000), ^{c} cluster;

3 - Hardin et al. (2000), ‡ obtained from the SN rate in SNu through $\rho_L = 1.4 \pm 0.1\, 10^8 h L_\odot Mpc^{-3}$ by Lin et al. (1996);

4 - Gal-Yam et al. (2002), ^{c} cluster;

5 - Tonry et al. (2003), $^\triangleleft$ obtained from the SN rate in events/volume through $\rho_L = 2.2{\pm}0.1\, 10^8 h L_\odot Mpc^{-3}$, average between the results obtained by Marzke et al. (1998) (1.7×10^8) and Folkes et al. (1999) (2.7×10^8);

6 - Pain et al. (2002), $^\Lambda$ (flat Λ dominated model consistent with the latest SCP results), ^{O} ($\Lambda = 0$, $\Omega_M = 0.3$ Universe) and ^{E} (Einstein-de Sitter Universe) with statistical uncertainty only (total systematic uncertainties computed in a flat Λ dominated Universe using $\Omega_M = 0.28$ are: $^{+0.32}_{-0.31}$ per unit comoving volume and $^{+0.10}_{-0.09}$ per unit luminosity). $^\triangle$ from CFRS galaxy counts, $^\triangledown$ from luminosity function. Underlined values are the most reliable estimates.

$h = H_0/100$; $^\star \times h^2 (100yr)^{-1} (10^{10} L_{B\odot})^{-1}$; $^\diamond \times 10^{-4} h^3 Mpc^{-3} yr^{-1}$.

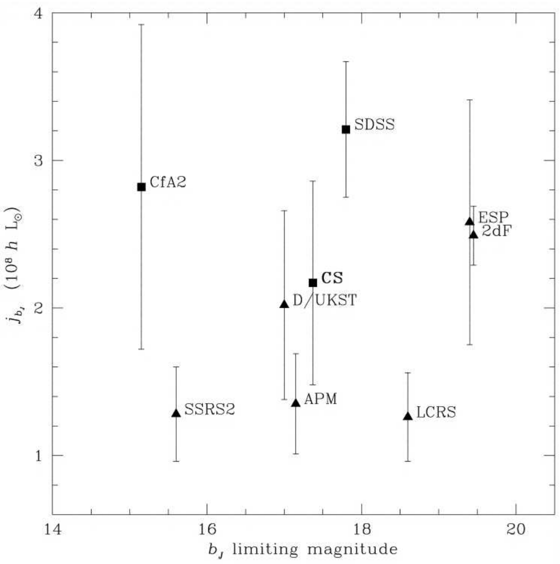

Figure 5.12: Luminosity density, j_b, and the b_J limiting magnitude of various redshift surveys.
Squares mark the northern surveys, while triangles mark the southern surveys. CDM cosmology ($\Omega_M = 1$, $\Omega_\Lambda = 0$) adopted. Figure from Brown et al. (2001).
CFA2: the Center for Astrophysics Redshift Survey (Marzke et al., 1994); SSRS2: the Southern Sky Redshift Survey (Marzke et al., 1998); APM: the Stromlo-APM Redshift Survey (Loveday et al., 1992); D/UKST: the Durham/UKST Galaxy Redshift Survey (Ratcliffe et al., 1998); ESP: the ESO Slice Project redshift survey (Zucca et al., 1997); 2dF: the 2 Degree Field Galaxy Redshift Survey (Cross et al., 2001); LCRS: the Las Campanas Redshift Survey (Lin et al., 1996); SDSS: the Sloan Digital Sky Survey (Blanton et al., 2001) CS: the Century Survey (Geller et al., 1997)

assumption the comparison of the type Ia supernova rate estimates, shown in Fig. 5.14, suggest an increasing rate with redshift. Unfortunately errorbars are still large and the luminosity density uncertain, and the same data can be marginally consistent with a flat evolution. The CCSN rate estimates at $z = 0.3$ reported in this thesis are the only one available so far for $z > 0.1$. The results obtained under different assumptions (case 1, case 2, cf. §5.2) suggest, if compared to the local value, a significative increase with redshift.

5.4 Conclusion

The main achievement of the present work is the first estimate of CCSNe rate beyond the local universe. As already mentioned in §3.2, Core Collapse SNe (CCSNe) are correlated with the instantaneous SFR while type Ia SNe, originating in evolved binary system, are expected to depend on the star formation rate history.
The increased CCSNe rate, which is a factor 1.8–3.6 greater than the local one, is in agreement with the SFR evolution with redshift derived by Fujita et al. (2003) (Fig. 5.15) who found the SFR at $z = 0.24$ about a factor 3 greater than the local one, and with the results obtained by Rosa-González et al. (2002), who found that the general behaviour of the star formation history of the Universe can be represented with a steep rise in the SFR

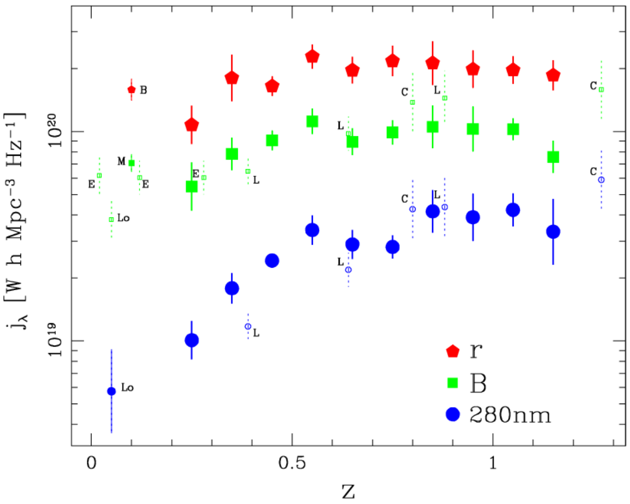

Figure 5.13: Overall redshift evolution of the luminosity density.
The data points represent the total luminosity density (integrated to faintest luminosities) for 2800 Å (circles), B (squares) and r (pentagons). The large solid symbols are the values from Wolf et al. (2003), from which this figure is taken. The small solid symbols at the low redshifts represent the local comparison surveys (the the Sloan Digital Sky Survey, Blanton et al. 2001; the 2dF Galaxy Redshift Survey, Madgwick et al. 2002) and small open symbols represent the results from previous redshift surveys (Madau et al. 1998b listed values for Ellis et al. 1996; Lilly et al. 1996 listed values for Loveday et al. 1992).

rate from $z = 0$ to $z = 1$ with SFR $\propto (1+z)^{4.5}$.

As far as type Ia SN rate is concerned, if we do not assume the rate and the evolutionary index by Pain et al. (2002) we find a steeper evolution with redshift which better agrees with some theoretical models (e.g. Madau et al. 1998a) which predict a strong evolution in the SN Ia rate in the redshift range $0 < z < 1$, in contrast with the shallower trends seen by Pain et al. (2002) and Tonry et al. (2003).

The detailed form of the star formation history is still debated. Initial studies based on the UV and IR luminosity density of star-forming galaxies (e.g. Lilly et al. 1996; Madau et al. 1996; Connolly et al. 1997; Madau et al. 1998b) suggested a sharp increase of the SFR up to $z \sim 1$–2, followed by a decrease at higher redshift. On the other hand different scenarios have been proposed by Steidel et al. (1999), who favour an almost constant SFR in the range $1 < z < 4$, and by Lanzetta et al. (2002) who suggest a monotonic increase of the SFH out to $z \sim 10$. At lower redshift Cowie et al. (1999) and Sullivan et al. (2000b) have found a shallow dependence of the SFR, Ψ, on redshift ($\Psi(z) \sim (1+z)$), while a recent work by Hippelein et al. (2003) confirm a the sharp rise initially reported by Lilly et al. (1996) ($\Psi(z) \sim (1+z)^4$). Our results favour a significative evolution for both type Ia and CCSNe, and thus a significative evolution in the star formation rate too.

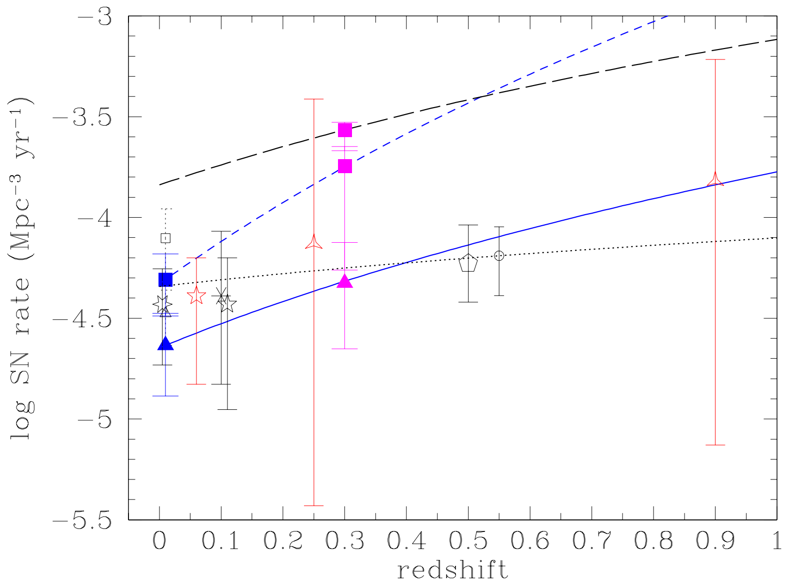

Figure 5.14: SN rates comparison.

The six points stars a $z = 0.005$ represents the local SN Ia rate found by Madgwick et al. (2003). The triangles and squares at $z = 0.01$ mark respectively the local SN rate for type Ia and CCSNe given by Cappellaro et al. 1999, the filled symbols marks the local SN rates not corrected for extinction. Local values have been plotted at $z = 0.005$ and $z = 0.01$ in order not to overlap. Other type Ia SN estimates from literature (see Tab. 5.4): stars at $z = 0.06$ and $z = 0.11$: Reiss (2000); asterisk at $z = 0.10$: Hardin et al. (2000); three points stars at $z = 0.25$, $z = 0.90$: Gal-Yam et al. (2002); triangle at $z = 0.3$: type Ia rate, this Thesis (case 2, see §5.2) squares at $z = 0.3$: CCSN rate, this Thesis (case 2 lower value, case 1 upper value, see §5.2); pentagon at $z = 0.50$: Tonry et al. (2003); circle at $z = 0.55$: Pain et al. (2002).
Dotted and long dashed lines: SN Ia and CCSN rates obtained in case 1; Solid and short dashed lines: SN Ia and CCSN rates obtained in case 2 (see §5.2).
SN rates are scaled to H=75 km s^{-1}Mpc^{-1} and luminosity density has been assume to be constant with z and equal to $\rho_{L(B)}(local) = 2.2 \times 10^8 h L_{B\odot} Mpc^{-3}$.

5.5 The future

The use of the SN rate for probing the star formation rate with cosmic age is a long term project. With the instrumentation used in the search presented in this work, we reached $z \sim 0.6$. Collecting a larger number of SNe in this range will allows us to search for possible evolution of the SN progenitor population. A more efficient search at intermediate redshift can be performed with a larger telescope and field of view. In this respect the 1 square degree field of view of OmegaCAM at the VLT Survey Telescope (VST) (Kuijken et al., 2002) can give an invaluable contribution.
Thanks to the larger collecting area (a factor 1.4 larger than the MPG/ESO 2.2m telescope) and the larger field of view (4 times the area covered by WFI), a single, deep exposure with OmegaCAM at the VST is expected to records ~ 15 SNe (Fig. 5.16).
Due to the large number of candidates, most of them very faint ($R > 23$), a classical spectroscopic follow-up will be very heavy because of the huge amount of time required for the spectroscopic confirmation of all the condidates may not be feasible, also with 8m class telescopes. Alternative methods like photometric classification may be required

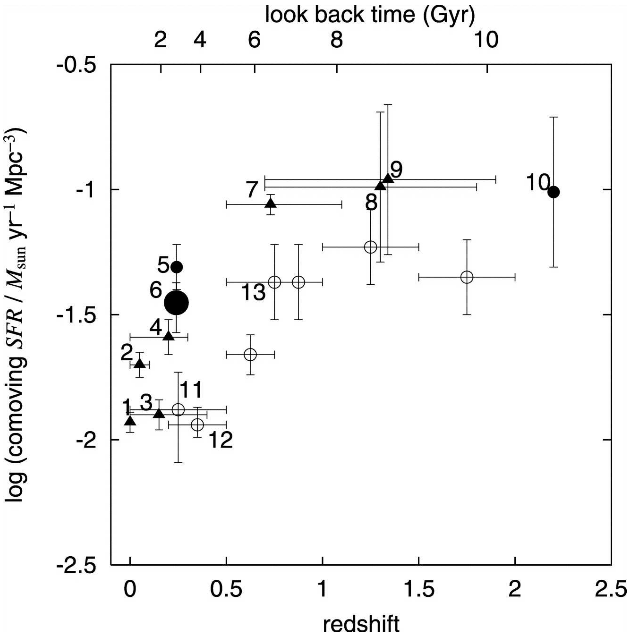

Figure 5.15: SFR density at $z = 0.24$ derived from Fujita et al. (2003) (filled circle; reference 6) shown together with previous investigations. Figure from Fujita et al. (2003).

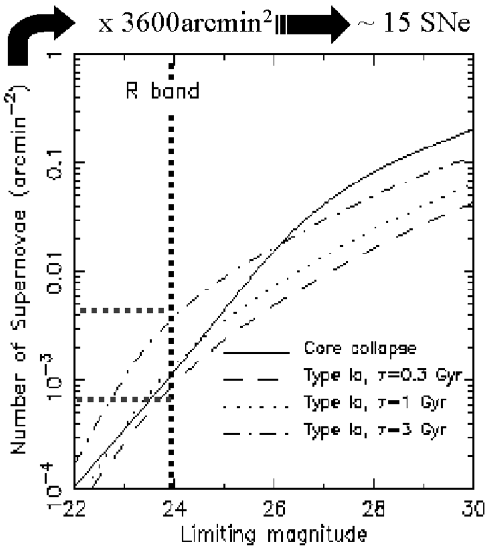

Figure 5.16: Number of SNe per square arcmin that can be detected down to different limiting magnitudes in the R band. Solid lines represent core collapse SNe. Dashed, dotted and dash-dotted lines represent Type Ia SNe with time delays =0.3, 1 and 3 Gyr, respectively. Assuming a detection limit $R \sim 24$, we expect about a dozen of SNe per field. Figure adapted from Dahlén and Fransson 1999.

(Poznanski et al., 2002). This approach, after proper calibration at intermediate redshift,

can become a powerful tool for high redshift surveyes.
This will be expecially interesting considering that by using the Wide Field Camera (WFC) at the 2x8m LBT telescope (Ragazzoni et al., 2000) we will be able to measure the SN rates up to z=1–1.5.

CHAPTER 6

Conclusions

With equal passion I have sought knowledge.
I have wished to understand the hearths of men,
I have wished to know why the stars shine.
And I have tried to apprehend the Pythagorean power
by which numbers holds sway above the flux.
A little of this, but not much, I have achieved.
Bertrand Russel, *Autobiography*, Prologue

In this Thesis we presented the analysis of low and intermediate redshift samples of Supernovae and their use as distance indicators, useful for determining the cosmological parameters, and as tracer of the star formation rate.
Both samples have been built combining unpublished data and data from literature. The local sample has been enriched thanks to a long standing effort for SN monitoring at ESO and Asiago Observatories while the intermediate redshift sample is the result of a long term SN Search program (the Southern inTermediate Redshift ESO SN Search, STRESS) performed at the ESO observatories of La Silla and Paranal (Chile), specifically designed for the detection of both Thermonuclear and Core Collapse SNe at redshift $0.1 < z < 0.6$.

In particular, nearby SNe have been used to re-calibrate the relation between the SN absolute magnitudes and their decline rate soon after maximum and to examine how different metallicity-dependent calibration of Cepheids affect the SN Ia calibration and, in turn, the Hubble constant. The $M_B - \Delta m_{15}(B)$ relation has been determined under different assumptions for the Cepheid PL metallicity correction and different cuts in the sample. The coefficient obtained in the different cases varies at the level of $\sim 1\%$ for the slope and $\sim 4\%$ for the zero point, without significant repercussions on the resulting Hubble constant, that lies in the range 68–74 $\mathrm{km\,s^{-1}Mpc}$, with uncertainties of the order of 10%. The data analysis highlighted the crucial role of reddening, whose correction is still uncertain. In particular we found that the use of a relative narrow Bayesian filter, adopted by several authors to estimate the colour eccess, is essentially equivalent to adopting a smaller value of R_B in the standard reddening law $A_B = R_B \times E(B-V)$. Actually we found that $R_B = 3.5$, which is somewhat smaller than the canonical value for dust in the Galaxy ($R_B = 4 - 4.3$), reduce the scatter in the $M_B - \Delta m_{15}(B)$ relation and seems appropriate to correct for the host galaxy extinction.

Our intermediate redshift sample (made up of 22 SNe, with redshift in the range $0.07 \leq z \leq 0.61$) is the result of a SN search based on observations collected at the ESO/MPG 2.2m telescope equipped with the WFI wide field imager (a mosaic of eight $2k \times 4k$ pixel CCDs). The detection of possible supernovae on such a wide images, covering a field of view of $\sim 1/4$ square degree, as been performed by means of a reduction package, named STRESS, specifically developed to this aim, as a part of this Thesis.

The intermediate redshift SNe, calibrated through the $M_B - \Delta m_{15}(B)$ relation previously determined have been used to extend the local SN sample to higher redshift. The resulting Hubble diagram has been used to determine the cosmological parameters Ω_M, Ω_Λ. Due to the small number of high redshift SNe, the confidence region in the Ω_M, Ω_Λ plane are quite large, but indicative of a Universe dominated by the cosmological constant. The same result, but with narrower constraints, is obtained after merging our 10 intermediate redshift type Ia SNe with 253 SNe from literature, with redshift in the range $0.02 \leq z \leq 1.75$.

Finally, our the intermediate redshift sample, has been used to estimate the SN rates for both Thermonuclear and Core Collapse Supernovae. In particular we have presented the first estimate of CCSN rate beyond the local Universe. Under different assumption we found that the CCSN rate at $z = 0.3$ is a factor $\sim 1.8 - 3.6$ larger then the local value. The results obtained in this Thesis are reported in Tab. 6.1. In "case 1" the type Ia rate

z	r_{Ia} [SNu]	α_{Ia}	r_{CC} [SNu]	α_{CC}	Cosmology Ω_M	Ω_Λ	case
0.30			$2.93^{+0.27}_{-0.62}$	$2.4^{+3.4}_{-2.4}$	0.30	0.70	1
0.30	$0.51^{+0.30}_{-0.27}$	$2.9^{+1.8}_{-2.9}$	$1.94^{+0.48}_{-1.35}$	$5.1^{+0.9}_{-4.7}$	0.30	0.70	2

Table 6.1: SN rates estimates at different redshifts
$1SNu = 1SN \times (100yr)^{-1}(10^{10}L_{B\odot})^{-1}h^2$; $h = H_0/100$

and evolutionary index by Pain et al. (2002) have been adopted to compute the rate and evolutionary index for CCSNe. In "case 2" the local SN rates for type Ia and CCSNe by Cappellaro et al. (1999) have beed assumed to compute the evolutionary index for both CCSNe and Thermonuclear SNe.

Our results favour a significative evolution with redshift,especially for CCSNe, in agreement with the star formation rate evolution in the same redshift range. As far as type Ia SNe are concerned, other modern syudies report a shallower evolution with redshift, but the uncertainties that afflict the rate estimates are still too large to rule one of the two hypotheses.

6.1 Future perspectives

Improved techniques for imaging supernovae as well as a better understanding of how their luminosity varies has allowed for great advances in supernova studies over the last decade. Nevetheless our understanding of the supernova physics is still incomplete and only after a full comprehension of the physics of the explosions will we be able to assess whether they can be used as distance indicators reliably. This is one of the aim of the SN Ia European Research Training Network. This goal should be achived in the next years by a combined efforts of all major groups working in this field in Europe, collecting high quality and homogeneous sets of lightcurves and spectra for a large sample of Type Ia supernovae and developing new theoretical models to interprete them. A better knowledge of SN Ia, both theoretical and observational, is necessary to constrain the cosmological implications of type Ia SNe. Indeed, among all areas of current research in modern cosmology and astrophysics, perhaps no area is more exciting and mysterious than the study of the nebulous component of our universe known as "dark energy". While theorists conjecture about possible candidates for dark energy, its exact nature continues to elude us. Nevertheless the observation of distant supernovae are, together with observation of the CMB, a primary pieces of evidence that point to the existence of dark energy and the accelerated expansion of the Universe. Several ground-based programs, specifically designed to observe hundreds of SNe, are already running or will be operating in the coming years. We just mention again the Nearby Supernova Factory, aiming at the discovery of ~ 300 SNe Ia at redshifts $0.03 < z < 0.08$ in the nearby smooth Hubble flow, which can be used as calibration; the CFHT Legacy Survey aimed mainly at the detection and monitoring of ~ 2000 type I SNe and the High-Z Team project ESSENCE aimed to the discovery of ~ 200 SNe Ia evenly distributed over the redshift range $0.15 < z < 0.75$. The goal of this pojects is an estimate of the comological parameters with unprecedented accuracy. Farther in the future, space-based projects like the SuperNova Acceleration Probe, besides a larger numbers of objects and an extended redshift range (over a thousand SNe Ia per year out to $z = 1.7$), will also provide the opportunity to control many systematic effects better than from the ground, testing a wide range of dark energy models and detecting a possible dependence of the equation of state parameter ω on time. Also the Large Synoptic Survey Telescope should reveal whether the value of ω depends on redshift, while high redshift surveys of galaxies such as DEEP2 as well as space based mission to map the CMB (Plank) should provide additional information about the cosmological constant.

The evolution of the SN rate with redshift is still poorly known and a better knowledge should provide us unique information on the star formation history of the Universe, the initial mass function (IMF) of stars and the nature of the binary companion in type Ia events. With the instrumentation described in this Thesis it is feasible to improve the statistics at redshift smaller than ~ 0.6 and to obtain better constrains on the evolution of SN rates with time. But a more efficient search at these redshifts could be performed with the advent of new wide field cameras, as OmegaCAM, which is expected to record a dozen of SNe in a single exposure.

The observations performed with the WFI@ESO/MPG2.2m, the software developed for the search described in this thesis and the experience in wide field imaging can also be seen as a starting point for the observational strategies and the reduction packages for

OmegaCAM@VST because, except for the number of CCDs of the mosaic, the two instrument are very similar. In principle the software developed for the SN search could be easily adapted to the larger mosaic of OmegaCAM, simply changing the number of CCDs to be analyzed from 8 to 32. But, because of the enormous size of each image (~ 600 Mbyte for the raw, about 1 Gbyte for the reduced ones) the classical approach will be very heavy. Also the technical resources for data analysis and storage must be adapted to the the very large data flow expected by this camera. This is why Beowulf architecture for parallel processing, multi terabyte disks and automatic pipeline are strongly needed.
Wide field cameras mounted at 8m class telescope, already operational, as the Suprime-CAM, or available in the next years, as the WFC at the Large Binocular Telescope, can extend SN rates measurments at higher redshifts ($z = 1 - 1.5$).
Farther in the future, through a combination of deep wide field imaging and near IR spectroscopy the Next Generation Space Telescope (NGST) will be able to map the evolution of cosmic structures up to $z \sim 5$. In particular, accurate measurments in this wide and deep redshift range of the type Ia and Core Collapse Supernova will trace the star formation and the heavy elements enrichment history of the Universe, improving our knowledge of the nature and age of the populations involved in SN explosions.

Appendix A

ESO-Asiago photometric data

Table A1 reports the unpublished photometry based on observations collected mainly at ESO - La Silla (Chile) and Asiago (Italy), plus some data from TNG (La Palma, Canary Islands, Spain) and from the HST WFPC2 Archive.
Data reduction has been performed using IRAF[1] standard recipes for trimming, bias and overscan correction and flat fielding. These steps are the same as the ones described in §3.3, except for the different number of CCDs adopted by different instruments.
SN magnitudes have been measured mainly using a Point Spread Function (PSF) fitting technique, which ensures a good removal of bad pixels and cosmic rays (Turatto et al., 1993). The PSF is modeled measuring the PSF of stars with a large spread in luminosities and lying in the same field of the SN. The PSF model is then used to fit the SN profile simultaneously to another function representing the background contribution. From the residual map, i.e the image obtained subtracting the fitted SN to the original frame, one can judge the fit goodness and, if necessary, refine the magnitude measurement, for example adopting a different analytical function to fit the background or masking features that does not have to be fitted.
Photometric calibration was obtained from observation of Landolt standard stars (Landolt, 1992) in photometric nights. This was also used to establish a local sequence which was used to calibrate the other observations.
In brackets are indicative estimates of the errors, obtained from the values measured on several reference nights through artificial stars experiments, i.e. adding a fake star, as bright as the SN, in several different positions around the SN location, and measuring the spread of the resulting magnitudes with the same procedure used for the SN.
The codes for the telescope/instrument used are as follows:
1= Danish 1.54m + DFOSC, 2= MPG/ESO 2.2m + EFOSC2, 3= ESO 3.6m + EFOSC1, 4= NTT + SUSI, 5= Dutch 0.91m, 6= NTT + EMMI, 7= Asiago 1.82m + AFOSC, 8= ESO 3.6m + EFOSC2, 9= TNG + OIG, 10= ESO 1.0m, 11= HST WFPC2 Archive.

[1]Image Reduction and Analysis Facility, http://iraf.noao.edu/

Table A1

Date	Julian Day +2,400,000	U	B	V	R	I	tel.
				SN 1991S			
13/04/91	48359.67	-	-	18.15(0.03)	-	-	1
18/04/91	48364.51	-	18.94(0.02)	18.42(0.03)	18.31(0.02)	-	2
20/04/91	48366.64	-	19.34(0.03)	18.51(0.02)	18.25(0.03)	-	3
				SN 1991T continues			
16/04/91	48362.85	12.26(0.02)	12.98(0.02)	12.84(0.02)	12.67(0.02)	12.87(0.02)	10
17/04/91	48363.80	12.04(0.02)	12.80(0.02)	12.74(0.02)	-	-	10
17/04/91	48363.65	-	12.73(0.01)	12.61(0.01)	-	-	2
18/04/91	48364.64	-	12.46(0.01)	12.34(0.01)	12.32(0.01)	-	2
20/04/91	48366.67	-	12.06(0.01)	12.00(0.01)	11.97(0.01)	-	3
21/04/91	48367.65	-	-	11.89(0.01)	-	-	3
22/04/91	48368.70	-	11.78(0.01)	11.80(0.01)	11.70(0.01)	-	3
20/05/91	48396.56	-	13.39(0.01)	12.32(0.01)	12.32(0.01)	-	3
20/05/91	48396.56	-	13.48(0.01)	12.29(0.01)	-	-	3
20/05/91	48396.56	-	-	12.45(0.01)	-	-	3
20/06/91	48427.67	-	14.77(0.01)	13.60(0.01)	13.51(0.01)	-	3
20/06/91	48427.67	-	-	13.66(0.01)	13.45(0.01)	-	3
20/06/91	48427.67	-	-	13.59(0.01)	-	-	3
01/08/91	48469.51	-	15.42(0.02)	-	14.78(0.02)	-	2
12/08/91	48480.49	-	-	15.29(0.02)	-	-	2
02/12/91	48593.46	-	16.98(0.06)	17.01(0.05)	17.62(0.06)	-	7
02/12/91	48593.46	-	16.95(0.06)	17.01(0.05)	17.59(0.06)	-	7
03/12/91	48594.46	-	17.06(0.06)	17.10(0.06)	17.65(0.06)	-	7
12/12/91	48603.46	-	17.04(0.06)	17.07(0.06)	17.68(0.06)	-	7
01/02/92	48653.90	-	17.66(0.05)	17.95(0.05)	18.54(0.05)	-	2
05/02/92	48657.82	-	17.74(0.04)	17.96(0.03)	18.56(0.04)	-	3
05/02/92	48657.60	-	-	17.88(0.07)	-	-	7
06/02/92	48658.66	-	17.75(0.07)	17.94(0.08)	18.52(0.06)	-	7
29/02/92	48681.78	-	18.02(0.06)	18.34(0.05)	18.97(0.05)	-	2
04/03/92	48686.46	-	18.25(0.10)	18.27(0.06)	19.00(0.08)	-	7
06/03/92	48688.46	-	18.25(0.10)	18.35(0.06)	19.05(0.08)	-	7
11/03/92	48692.67	-	18.42(0.07)	18.42(0.07)	19.07(0.06)	-	6
04/05/92	48746.69	-	18.99(0.05)	19.12(0.05)	19.58(0.05)	19.00(0.08)	3
26/07/92	48829.67	-	19.97(0.10)	20.27(0.05)	20.57(0.05)	-	2
23/12/92	48979.67	-	21.04(0.10)	20.95(0.08)	-	-	3
22/01/93	49010.67	-	21.02(0.10)	21.00(0.08)	21.28(0.09)	-	3
17/02/93	49035.67	-	-	20.97(0.09)	21.25(0.07)	-	6
27/02/93	49045.79	-	21.08(0.10)	20.99(0.09)	-	-	2
28/02/93	49046.79	-	21.21(0.10)	21.02(0.10)	21.36(0.10)	-	2
15/03/93	49061.67	-	21.03(0.10)	21.08(0.07)	21.17(0.07)	-	3

Table A1

Date	Julian Day +2,400,000	U	B	V	R	I	tel.
				SN 1991T			
26/04/93	49103.60	-	21.06(0.10)	-	21.22(0.07)	-	3
27/04/93	49104.60	-	21.06(0.10)	21.21(0.08)	-	-	3
17/03/94	49428.78	-	21.43(0.11)	21.45(0.10)	-	-	6
10/05/94	49482.62	-	21.13(0.11)	-	-	-	3
15/05/94	49487.65	-	21.30(0.11)	-	-	-	2
17/03/96	50159.77	-	21.49(0.12)	21.48(0.10)	-	-	3
				SN 1992A			
14/01/92	48635.06	-	12.84(0.01)	12.81(0.01)	12.76(0.01)	-	6
15/01/92	48636.06	-	12.86(0.01)	12.79(0.01)	12.75(0.01)	-	6
16/01/92	48637.03	-	12.75(0.01)	12.73(0.01)	-	-	6
17/01/92	48638.03	-	12.68(0.01)	12.69(0.01)	-	-	6
18/01/92	48639.03	-	12.62(0.01)	12.66(0.01)	12.70(0.01)	-	6
04/02/92	48656.57	-	14.17(0.01)	13.43(0.01)	13.32(0.01)	-	3
11/03/92	48692.03	-	16.03(0.03)	15.19(0.02)	15.10(0.02)	-	3
26/07/92	48829.92	-	17.94(0.03)	18.24(0.03)	18.53(0.03)	-	2
01/09/92	48867.80	-	18.43(0.03)	18.61(0.03)	19.15(0.04)	18.90(0.05)	3
30/09/92	48895.40	-	-	-	20.00(0.07)	-	5
23/10/92	48918.74	-	18.94(0.05)	19.60(0.05)	20.18(0.05)	19.69(0.08)	2
29/11/92	48956.70	-	19.69(0.08)	19.98(0.05)	20.66(0.05)	20.09(0.08)	3
02/12/92	48958.63	-	-	20.08(0.07)	-	-	6
22/12/92	48979.64	-	19.99(0.08)	20.29(0.07)	20.76(0.06)	20.16(0.07)	3
24/01/93	49011.55	-	20.43(0.08)	20.68(0.09)	21.28(0.08)	20.54(0.10)	3
24/01/93	49011.55	-	-	20.76(0.09)	21.15(0.07)	-	3
27/02/93	49045.54	-	20.74(0.10)	21.23(0.12)	-	21.10(0.15)	2
28/02/93	49046.50	-	-	21.22(0.11)	-	-	2
27/03/93	49073.54	-	21.41(0.07)	21.49(0.07)	21.82(0.07)	-	6
07/07/93	49176.20	-	>22.5	-	-	-	1
02/08/94	49566.50	-	-	25.9 (0.30)	-	-	11
04/09/96	50331.12	-	-	>27.0	-	-	11
				SN 1992K			
07/04/92	48719.80	-	19.23(0.03)	18.18(0.02)	17.90(0.02)	17.51(0.02)	2
				SN 1993H			
26/04/1993	49103.67	-	20.12(0.04)	19.02(0.03)	18.51(0.03)	-	3
05/05/1993	49112.90	-	-	-	18.85(0.05)	-	1
16/05/1993	49123.67	-	20.53(0.13)	19.58(0.07)	19.32(0.06)	-	1
17/05/1993	49124.63	-	20.49(0.04)	19.70(0.05)	19.46(0.04)	-	3
08/07/1993	49176.67	-	21.73(0.20)	21.04(0.10)	21.18(0.15)	-	1

Table A1

Date	Julian Day +2,400,000	U	B	V	R	I	tel.
				SN 1993L			
05/05/93	49112.90	-	14.84(0.05)	13.97(0.03)	13.86(0.03)	-	1
16/05/93	49123.83	-	15.94(0.09)	14.60(0.04)	14.11(0.05)	-	1
16/05/93	49123.84	-	15.94(0.09)	14.60(0.04)	14.04(0.05)	-	1
17/05/93	49124.88	-	-	-	14.17(0.02)	-	3
27/05/93	49134.40	-	16.75(0.04)	15.23(0.01)	14.87(0.02)	14.51(0.01)	6
30/05/93	49137.40	-	-	15.30(0.01)	14.79(0.02)	-	6
14/06/93	49152.70	-	16.89(0.07)	15.81(0.03)	15.44(0.03)	-	5
21/06/93	49159.70	-	16.93(0.07)	15.88(0.03)	15.60(0.04)	-	5
01/07/93	49169.43	-	17.02(0.04)	16.21(0.02)	16.05(0.02)	16.01(0.02)	6
07/07/93	49176.15	-	17.29(0.10)	16.42(0.06)	16.29(0.05)	-	1
10/07/93	49178.40	-	17.31(0.04)	16.52(0.02)	16.35(0.02)	16.32(0.03)	3
11/07/93	49179.40	-	17.30(0.04)	16.56(0.02)	16.41(0.03)	16.34(0.03)	3
13/07/93	49181.40	-	17.38(0.04)	16.59(0.02)	16.44(0.03)	16.45(0.03)	3
23/08/93	49223.84	-	17.81(0.05)	17.55(0.03)	17.68(0.04)	-	3
10/09/93	49241.70	19.40(0.09)	18.22(0.09)	18.00(0.05)	18.19(0.05)	18.19(0.05)	5
18/11/93	49309.52	-	19.05(0.12)	19.06(0.06)	19.36(0.06)	19.16(0.07)	5
13/12/94	49332.57	-	-	19.70(0.07)	20.06(0.07)	-	5
15/12/94	49336.54	-	-	19.93(0.06)	19.92(0.05)	-	3
14/01/94	49367.45	-	19.64(0.09)	20.26(0.10)	-	-	3
06/05/94	49478.67	-	21.49(0.20)	-	-	-	5
09/05/94	49481.83	-	21.38(0.15)	21.51(0.10)	-	-	3
14/05/94	49486.85	-	21.45(0.20)	21.52(0.20)	-	-	2
04/06/94	49507.79	-	21.73(0.22)	21.73(0.12)	-	-	3
06/06/94	49509.88	-	21.72(0.20)	21.94(0.30)	21.70(0.20)	-	2
07/09/94	49602.63	-	22.45(0.40)	22.47(0.40)	-	-	5
07/09/94	49602.63	-	-	-	>21.91	>21.3	5
08/09/94	49603.58	-	22.88(0.40)	22.59(0.40)	-	-	5
08/09/94	49603.58	-	-	-	>22.02	>21.41	5
28/09/94	49624.67	-	23.00(0.30)	-	-	-	3
29/05/95	49866.67	-	>22.60	-	-	>21.5	6
				SN 1994D continues			
07/06/94	49510.54	-	15.67(0.02)	15.25(0.02)	15.14(0.02)	15.40(0.03)	3
08/06/94	49512.46	-	15.64(0.02)	15.24(0.02)	15.24(0.02)	15.44(0.03)	3
09/06/94	49513.46	-	-	15.35(0.02)	15.34(0.02)	-	3
13/06/94	49516.51	16.25(0.02)	15.75(0.01)	15.43(0.01)	15.42(0.01)	15.58(0.01)	2
14/06/94	49517.60	-	-	-	15.47(0.01)	-	2
25/06/94	49529.47	-	15.99(0.03)	15.69(0.03)	15.79(0.03)	16.12(0.03)	5
13/07/94	49546.51	-	16.26(0.03)	16.14(0.04)	16.20(0.03)	16.59(0.04)	5
08/01/95	49725.78	-	18.62(0.04)	19.03(0.04)	-	-	3
28/01/95	49745.85	-	19.11(0.09)	19.47(0.06)	-	-	5

Table A1

Date	Julian Day +2,400,000	U	B	V	R	I	tel.
				SN 1994D			
04/02/95	49752.85	-	19.07(0.03)	-	-	-	2
05/02/95	49753.79	-	19.03(0.03)	19.60(0.02)	-	-	2
20/02/95	49768.87	-	19.46(0.10)	19.97(0.10)	-	-	1
27/02/95	49776.30	-	19.75(0.08)	-	-	-	6
28/02/95	49776.46	-	19.79(0.15)	-	-	-	7
24/04/95	49831.67	-	20.56(0.14)	-	-	-	5
24/04/95	49831.67	-	-	>20.50	-	-	5
28/05/95	49865.67	-	20.91(0.20)	-	-	-	6
28/05/95	49865.67	-	-	>20.54	-	-	6
				SN 1994M			
14/05/94	49486.56	-	17.28(0.01)	16.84(0.01)	16.83(0.01)	17.25(0.01)	2
				SN 1994ae			
23/12/94	49709.85	-	15.02(0.05)	14.20(0.03)	13.94(0.03)	13.96(0.03)	1
13/01/95	49730.33	-	16.14(0.01)	15.17(0.01)	14.89(0.01)	14.67(0.01)	4
28/01/95	49745.77	-	16.34(0.04)	15.60(0.03)	15.40(0.03)	15.33(0.03)	5
05/02/95	49753.70	-	16.53(0.02)	15.83(0.02)	15.74(0.02)	15.71(0.02)	2
20/02/95	49768.79	-	16.69(0.05)	16.20(0.05)	16.12(0.05)	16.18(0.04)	1
27/02/95	49776.27	-	-	16.38(0.02)	-	-	6
27/02/95	49775.46	-	16.90(0.07)	16.28(0.05)	16.26(0.05)	16.56(0.04)	7
28/02/95	49776.46	-	16.90(0.07)	16.30(0.05)	16.37(0.06)	16.63(0.05)	7
31/03/95	49807.54	-	-	-	-	17.35(0.04)	3
20/04/95	49827.68	-	-	17.39(0.07)	17.63(0.07	18.00(0.06)	1
24/04/95	49831.67	-	17.80(0.06)	17.77(0.05)	17.89(0.05)	-	5
29/05/95	49866.67	-	18.46(0.07)	18.39(0.07)	18.82(0.05)	-	6
19/01/96	50101.77	-	21.45(0.20)	21.65(0.15)	-	-	2
21/02/96	50135.67	-	21.89(0.30)	22.09(0.17)	-	-	5
13/05/96	50216.67	-	>22.70	>22.80	-	-	5
				SN 1995D continues			
20/02/95	49768.78	-	13.39(0.01)	13.44(0.01)	13.47(0.02)	13.68(0.03)	1
27/02/95	49776.30	-	-	13.64(0.01)	13.75(0.01)	-	6
30/03/95	49806.59	-	-	15.24(0.01)	-	-	3
19/04/95	49827.68	-	16.74(0.12)	15.82(0.10)	15.64(0.10)	15.59(0.10)	1
25/04/95	49831.67	-	16.80(0.12)	15.97(0.11)	15.93(0.10)	15.71(0.10)	5
29/05/95	49867.67	-	17.40(0.06)	16.87(0.06)	16.88(0.04)	17.10(0.05)	6
22/11/95	50044.62	-	19.86(0.15)	20.13(0.10)	-	-	7
23/11/95	50045.58	-	19.65(0.14)	-	-	-	7
25/12/95	50077.85	-	20.08(0.10)	20.48(0.10)	-	-	2
19/01/96	50101.67	-	20.79(0.22)	20.84(0.12)	21.69(0.15)	21.10(0.20)	5
01/02/96	50114.67	-	21.11(0.09)	21.50(0.08)	-	-	1
01/02/96	50114.67	-	-	21.32(0.08)	-	-	1

Table A1

Date	Julian Day +2,400,000	U	B	V	R	I	tel.
				SN 1995D			
15/02/96	50128.56	-	21.13(0.20)	21.24(0.20)	-	-	7
16/02/96	50129.60	-	-	-	22.26(0.30)	-	7
16/02/96	50129.57	-	-	21.24(0.20)	-	-	7
18/02/96	50131.68	-	20.86(0.25)	21.27(0.10)	22.12(0.10)	-	2
21/02/96	50134.67	-	21.31(0.30)	21.36(0.15)	22.15(0.20)	21.04(0.10)	5
19/04/96	50192.67	-	22.16(0.50)	22.30(0.22)	23.39(0.50)	-	5
10/02/97	50489.67	-	-	>23.0	-	-	3
				SN 1995ac			
02/10/95	49992.67	-	17.24(0.02)	17.26(0.02)	17.19(0.02)	17.32(0.02)	3
13/10/95	50004.64	-	17.93(0.15)	17.53(0.06)	17.50(0.06)	17.79(0.15)	3
14/11/95	50035.67	-	20.25(0.08)	19.19(0.07)	18.59(0.06)	18.47(0.07)	6
09/06/96	50243.83	-	>23.49	22.79(0.20)	-	-	3
				SN 1995bd			
18/01/96	50100.67	-	18.19(0.01)	17.12(0.01)	-	-	2
				SN 1996bo			
24/10/96	50380.65	-	16.33(0.03)	16.05(0.03)	15.79(0.03)	-	5
19/11/96	50406.64	18.46(0.08	17.81(0.08)	16.60(0.04)	16.21(0.03)	16.09(0.04)	5
				SN 1997bp			
08/04/97	50547.49	-	14.19(0.02)	14.02(0.02)	13.91(0.02)	-	7
17/04/97	50555.73	14.92(0.04)	14.47(0.04)	14.01(0.03)	13.99(0.03)	14.47(0.03)	5
18/04/97	50556.68	15.06(0.04)	14.54(0.04)	14.01(0.03)	14.01(0.03)	14.50(0.03)	5
19/04/97	50557.65	15.10(0.05)	14.64(0.05)	14.12(0.03)	14.12(0.03)	14.62(0.03)	5
26/04/97	50565.74	16.06(0.06)	15.47(0.05)	14.58(0.03)	14.43(0.03)	14.81(0.03)	5
13/05/97	50581.67	-	16.93(0.01)	15.43(0.01)	14.93(0.01)	14.59(0.01)	2
02/01/98	50815.88	-	20.11(0.14)	20.07(0.08)	20.79(0.09)	20.44(0.09)	5
02/02/98	50846.81	-	20.66(0.15)	20.65(0.10)	-	-	8
26/03/98	50898.75	-	-	-	21.85(0.20)	-	5
29/05/98	50962.64	-	22.17(0.20)	22.16(0.15)	-	-	8
				SN 1997br			
17/04/97	50555.75	13.58(0.03)	14.18(0.03)	13.93(0.03)	13.74(0.03)	13.65(0.03)	5
19/04/97	50557.66	13.64(0.03)	14.13(0.03)	13.87(0.03)	13.70(0.03)	13.62(0.03)	5
13/05/97	50581.77	-	16.03(0.01)	14.64(0.01)	14.25(0.01)	-	2
09/08/97	50670.38	-	-	-	17.24(0.05)	-	1
22/03/98	50894.79	-	21.26(0.18)	21.06(0.15)	21.63(0.17)	-	1
29/05/98	50962.67	-	21.94(0.20)	21.82(0.15)	22.04(0.19)	-	8

Table A1

Date	Julian Day +2,400,000	U	B	V	R	I	tel.
				SN 1999aa			
16/03/99	51254.67	16.86(0.07)	16.51(0.06)	15.76(0.02)	15.66(0.03)	15.86(0.04)	5
17/03/99	51255.57	16.91(0.07)	16.61(0.06)	15.80(0.03)	15.67(0.03)	15.84(0.04)	5
12/04/99	51281.46	18.27(0.05)	17.98(0.05)	17.10(0.04)	16.80(0.04)	16.73(0.05)	8
				SN 1999dk			
25/08/99	51415.67	14.94(0.07)	15.06(0.05)	14.93(0.04)	14.92(0.04)	15.30(0.04)	1
02/09/99	51423.67	15.62(0.07)	15.45(0.06)	15.14(0.04)	15.23(0.05)	15.78(0.05)	1
05/09/99	51426.67	16.12(0.08)	15.82(0.07)	15.38(0.04)	15.49(0.05)	15.95(0.05)	1
14/09/99	51435.78	17.24(0.15)	16.75(0.05)	15.85(0.03)	15.68(0.03)	15.92(0.03)	8
17/09/99	51438.67	17.54(0.20)	17.11(0.05)	16.01(0.03)	15.70(0.03)	15.80(0.03)	8
08/10/99	51459.56	19.10(0.15)	18.12(0.03)	16.63(0.03)	16.58(0.02)	16.63(0.02)	9
				SN 2000cx			
27/07/00	51753.90	-	13.44(0.02)	13.24(0.03)	13.35(0.03)	13.77(0.02)	6
18/11/00	51866.55	18.31(0.02)	17.86(0.01)	17.76(0.01)	17.80(0.02)	18.21(0.02)	1

Appendix B

Confirmed SNe

Images[1] and spectra[2] of the 22 spectroscopically confirmed SNe (see Tab. 3.10). Spectra provided by Valenti (2003).

[1]North up, Est left

[2]Wavelenght in [Å], Flux in [ergs cm^{-2} sec^{-1} $Å^{-1}$ + const].

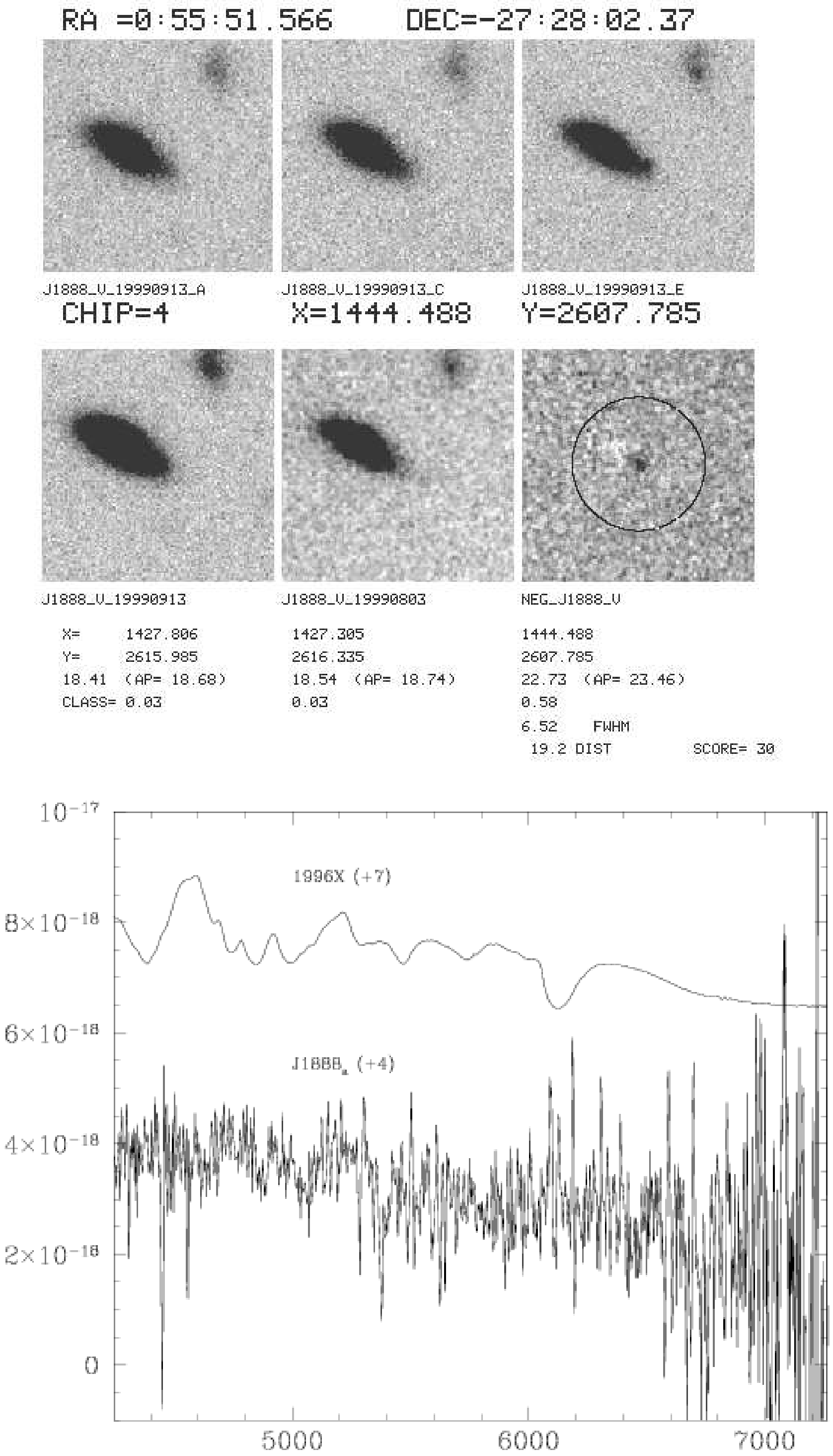

Figure B.1: SN J1888_A, type Ia, $z = 0.42$. The spectrum is compared to that of SN 1996X (Ia) 7 days past maximum. This objects was not formally announced because of the low quality spectrum and the uncertain preliminary classification (the objects was faint and at that epoch only the 3.6m telescope at ESO-La Silla was available for spectroscopic observations). However the following photometric follow-up showed a light curve consistent with that of a type Ia SN.

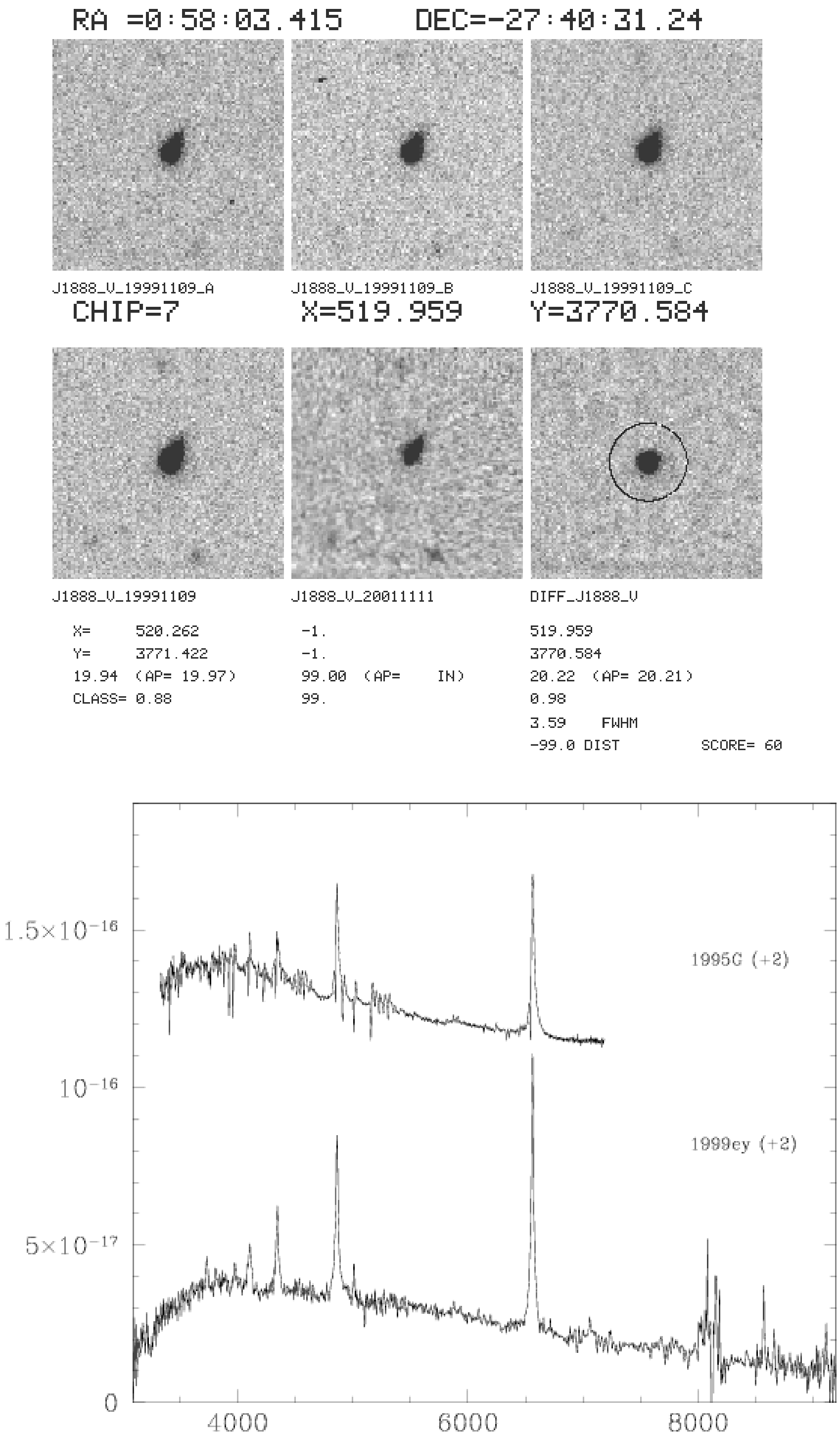

Figure B.2: SN 1999ey, type IIn, $z = 0.09$. The spectrum is compared to that of SN 1995G (IIn) 2 days past maximum.

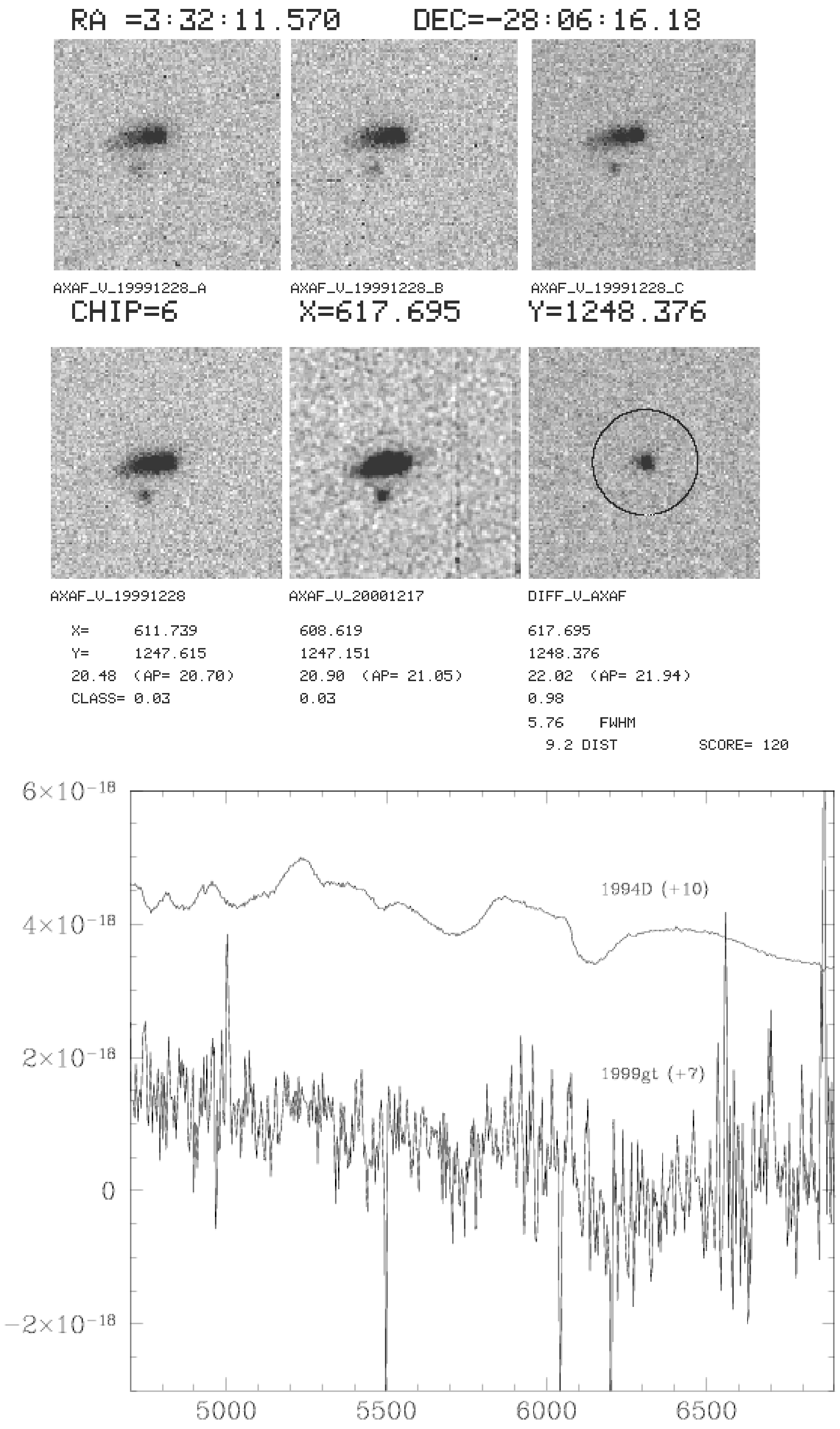

Figure B.3: SN 1999gt, type Ia, $z = 0.27$. The spectrum is compared to that of SN 1994D (Ia) 10 days after maximum.

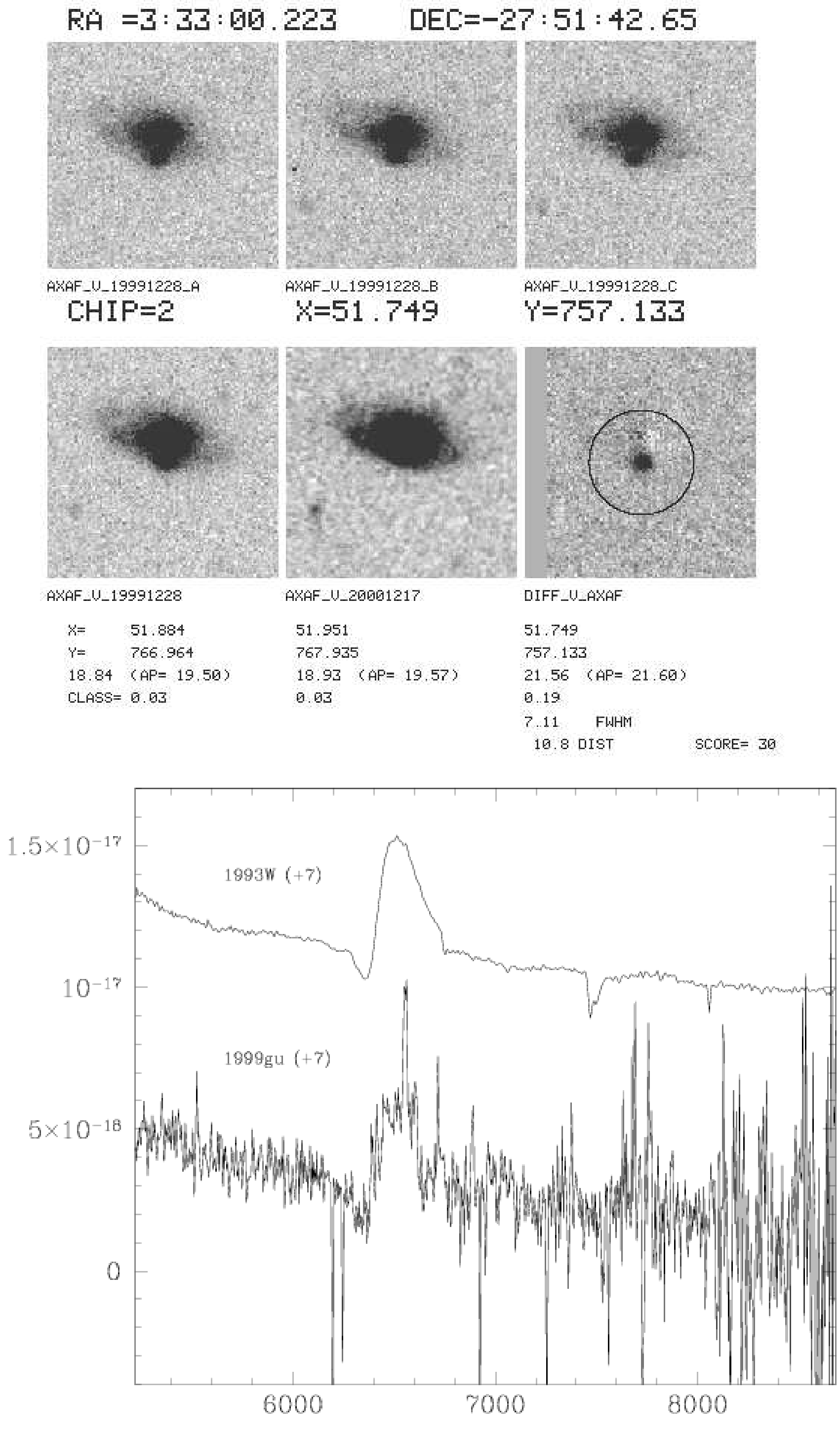

Figure B.4: SN 1999gu, type II, $z = 0.15$. The spectrum is compared to that of SN 1993W (II) a week past maximum.

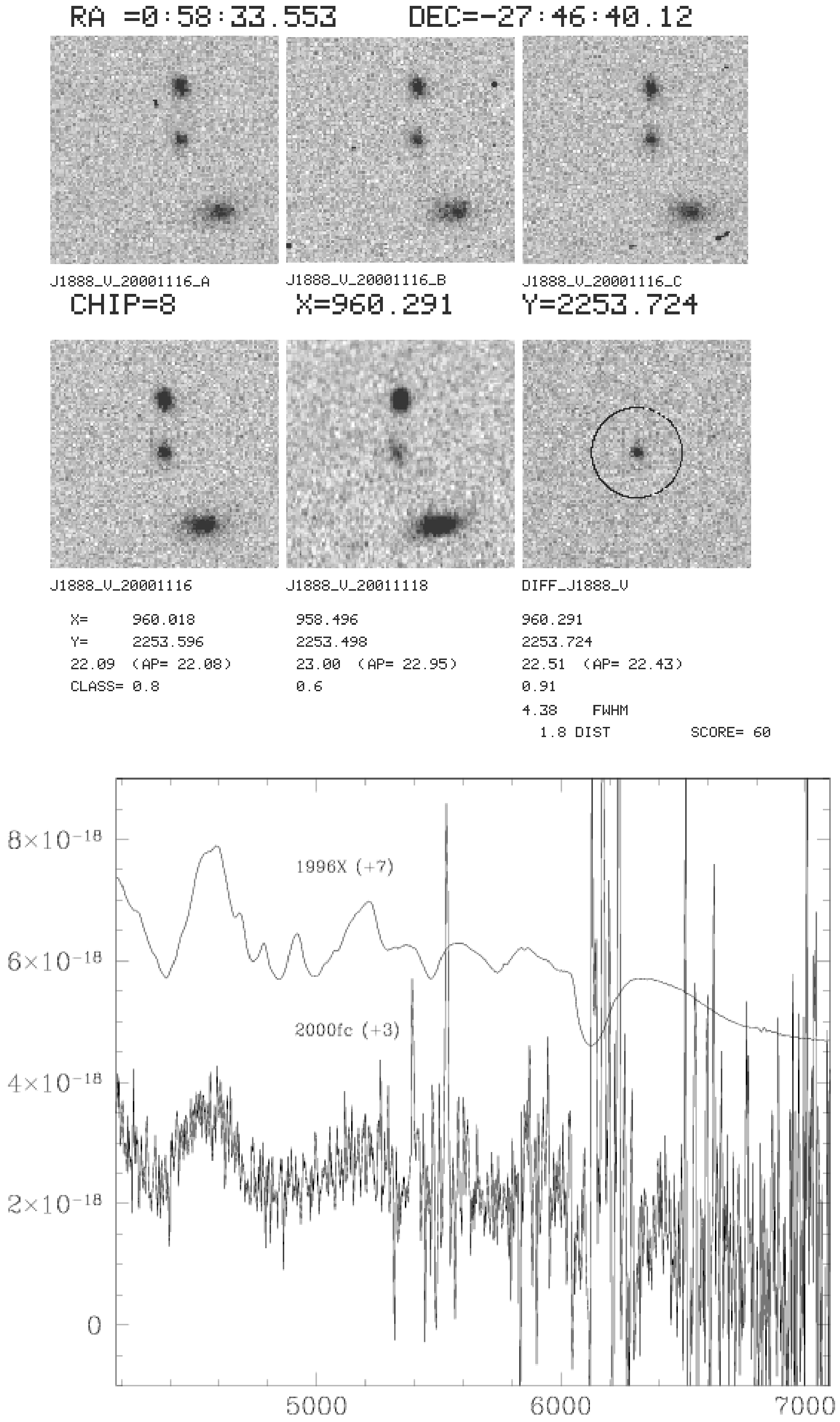

Figure B.5: SN 2000fc, type Ia, $z = 0.43$. The spectrum is compared to that of SN 1996X (Ia) a week past maximum.

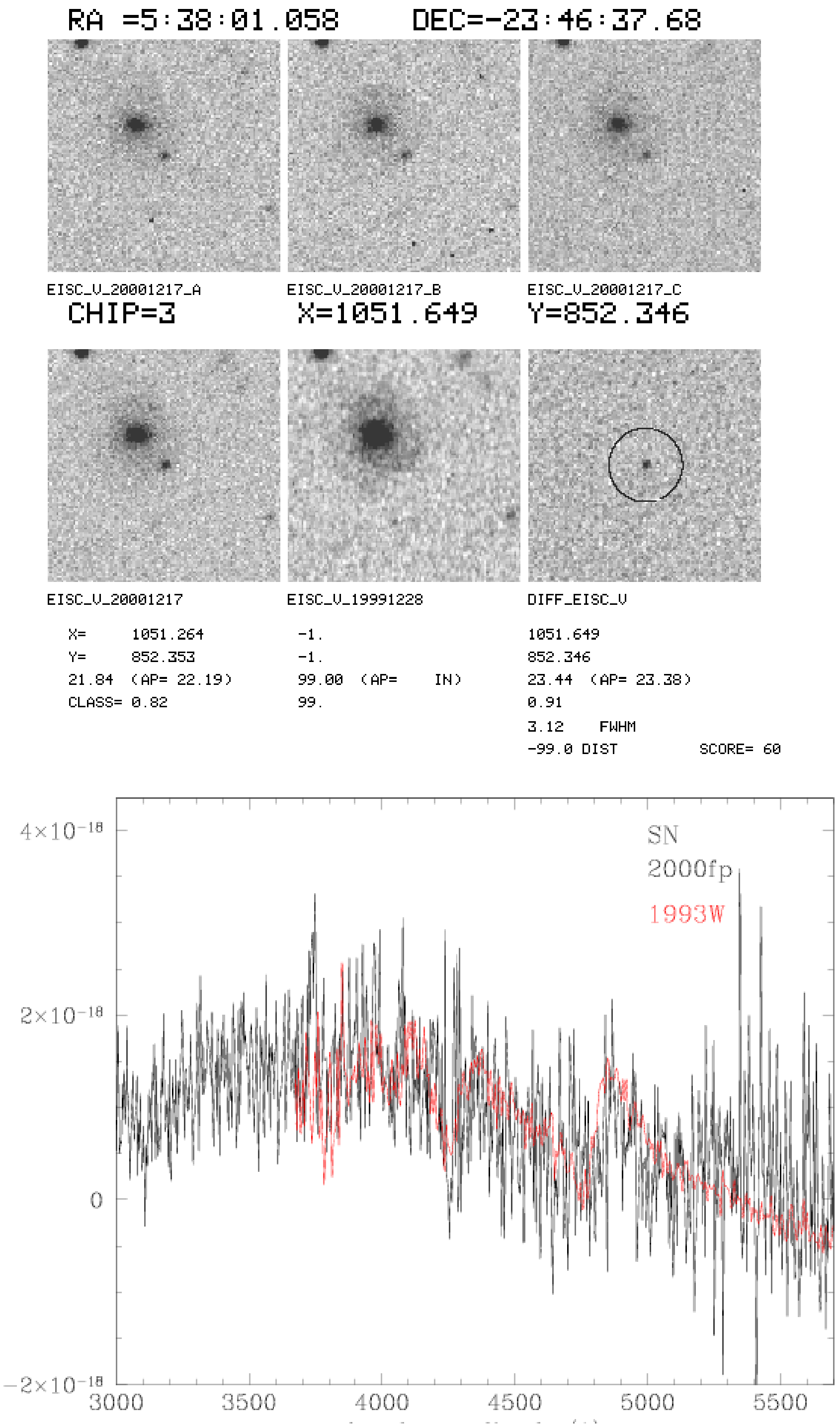

Figure B.6: SN 2000fp, type II, $z = 0.30$. The spectrum is compared to that of SN 1993W (II) 2 days past maximum.

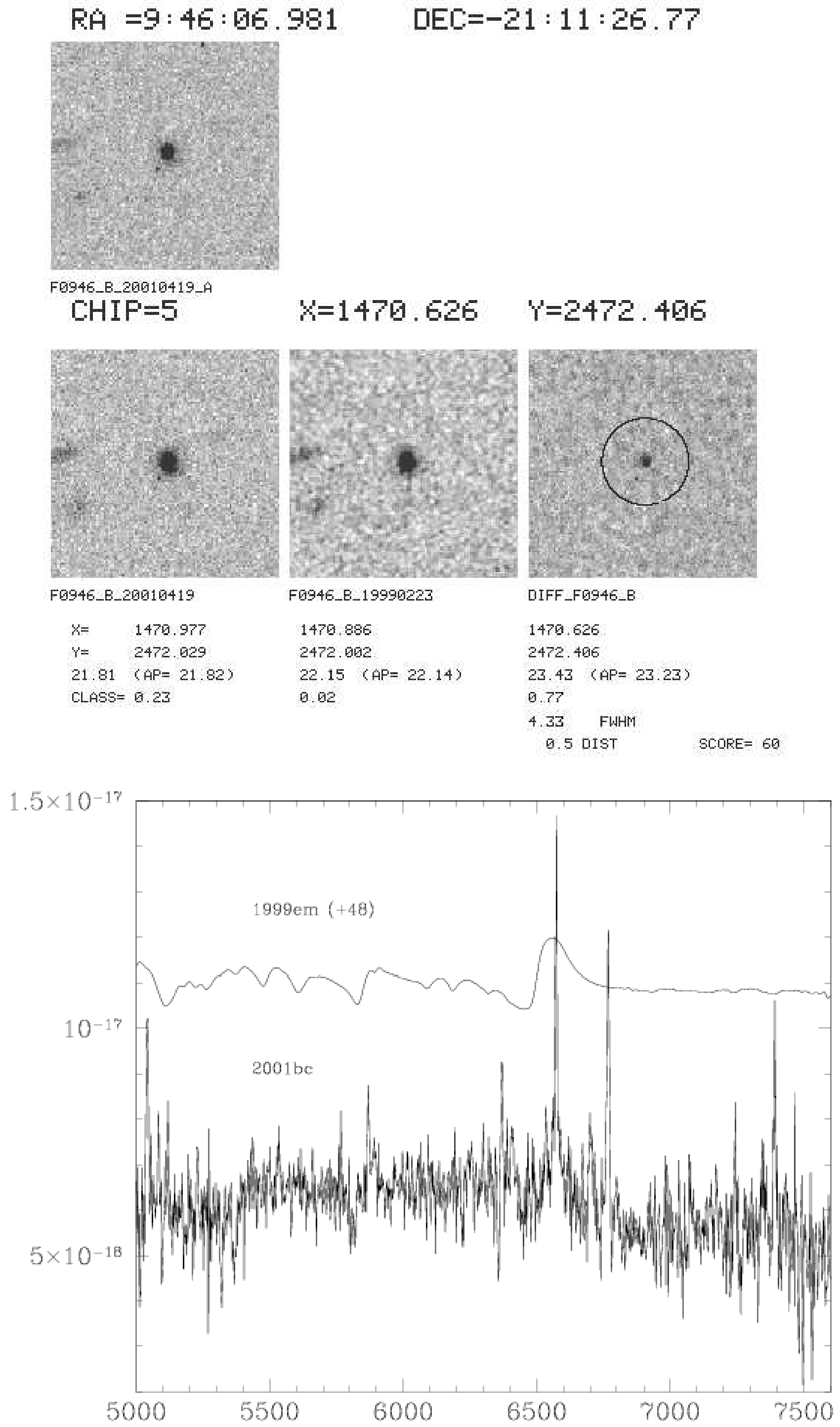

Figure B.7: SN 2001bc, type II, $z = 0.19$. The spectrum (comtaminated by the host galaxy) is compared to that of SN 1999em (IIP) 48 days past maximum.

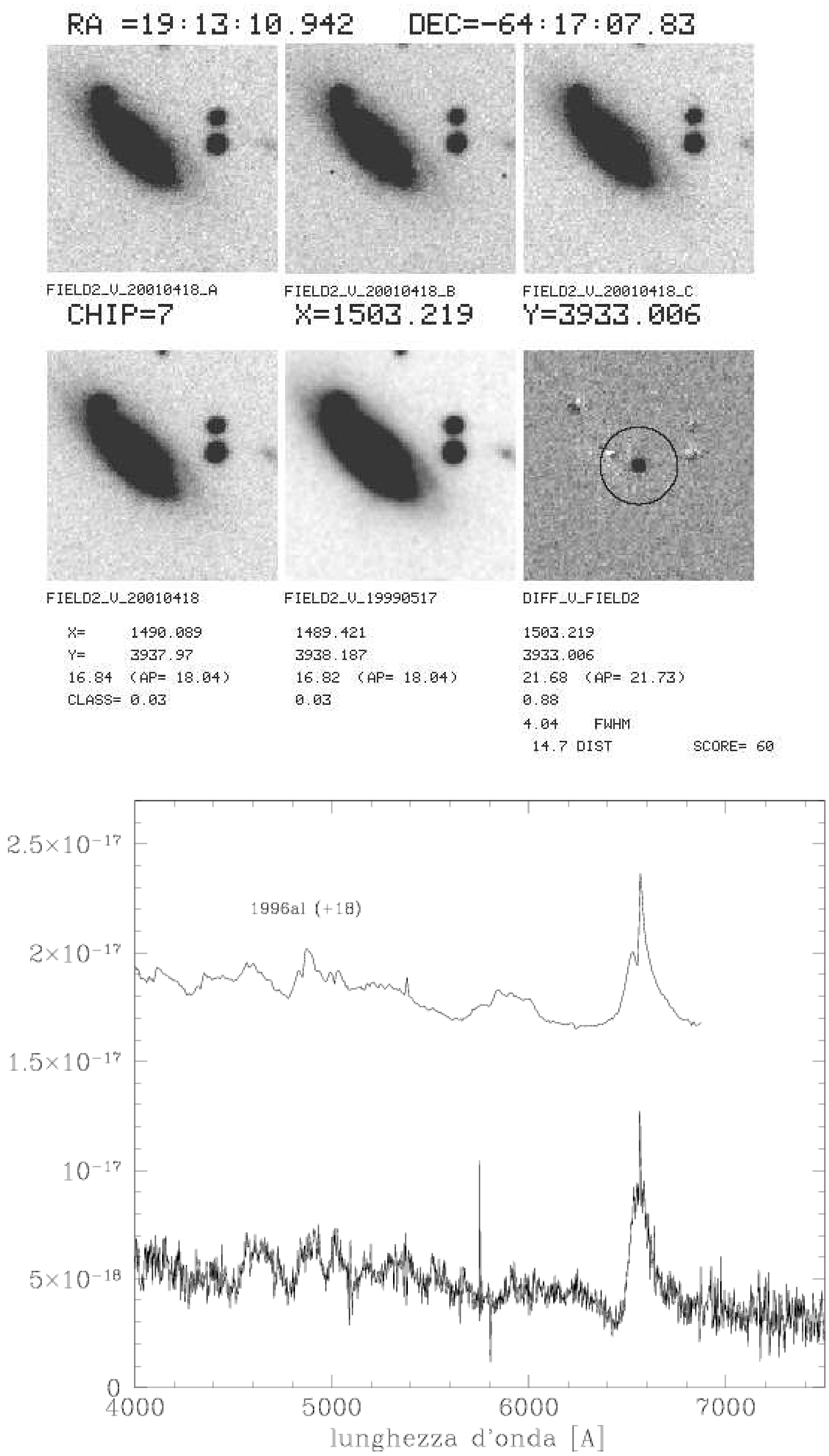

Figure B.8: SN 2001bd, type II, $z = 0.10$. The spectrum is compared to that of SN 1996al (IIL) 18 days past maximum.

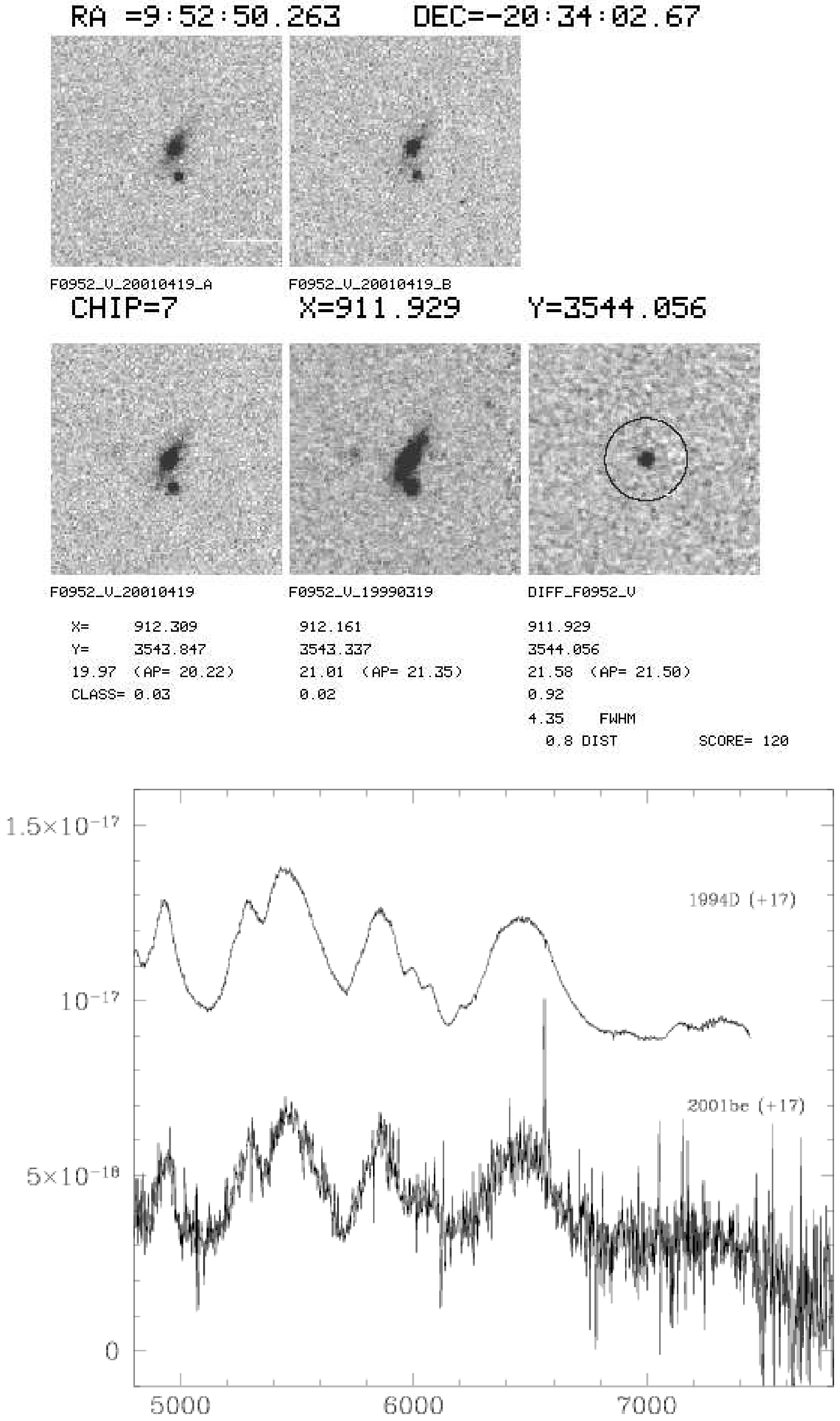

Figure B.9: SN 2001be, type Ia, $z = 0.24$. The spectrum is compared to that of SN 1994D (Ia) 17 days past maximum.

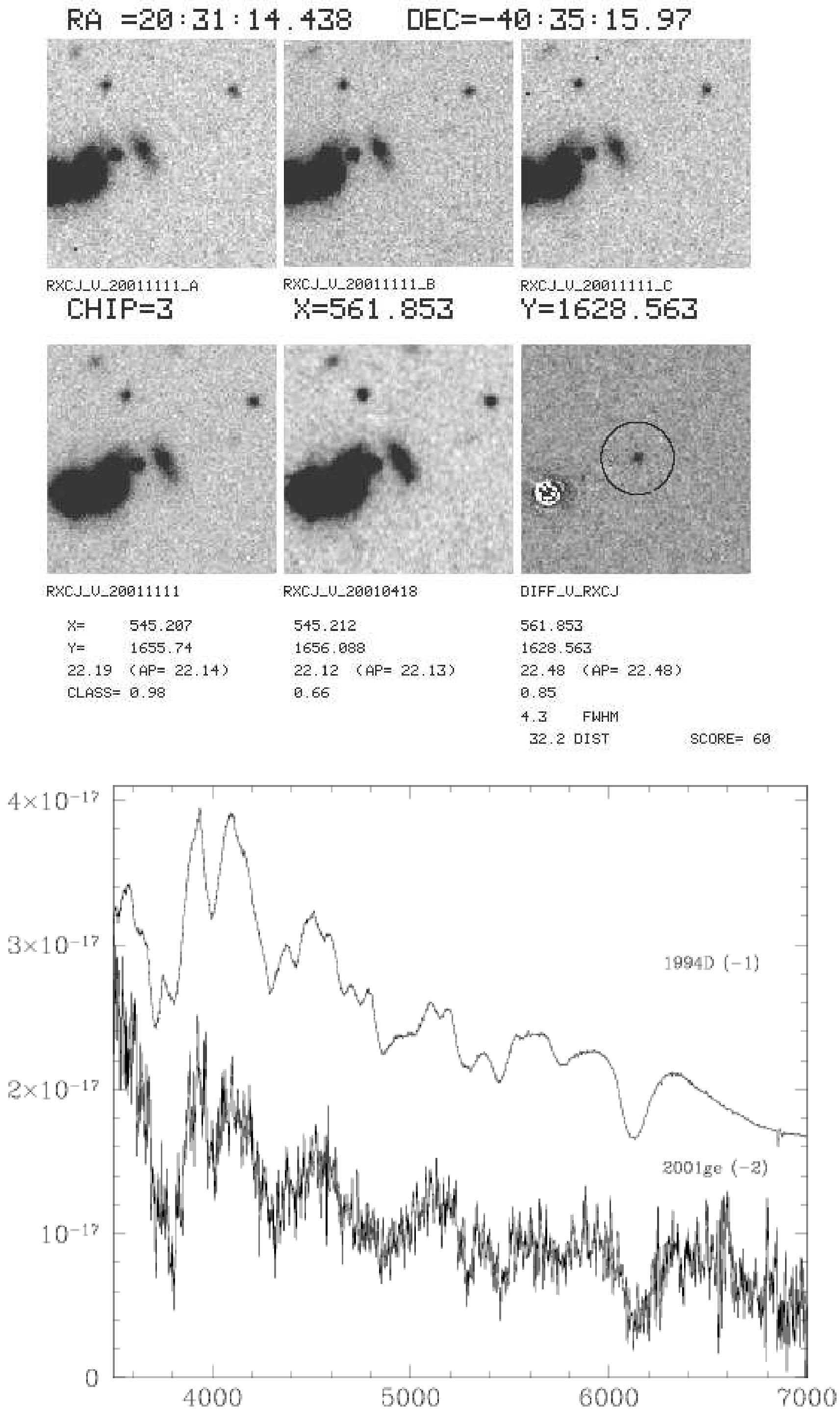

Figure B.10: SN 2001ge, type Ia, $z = 0.22$. The spectrum (contaminated by the host galaxy) is compared to that of SN 1994D (Ia) 1 day before maximum.

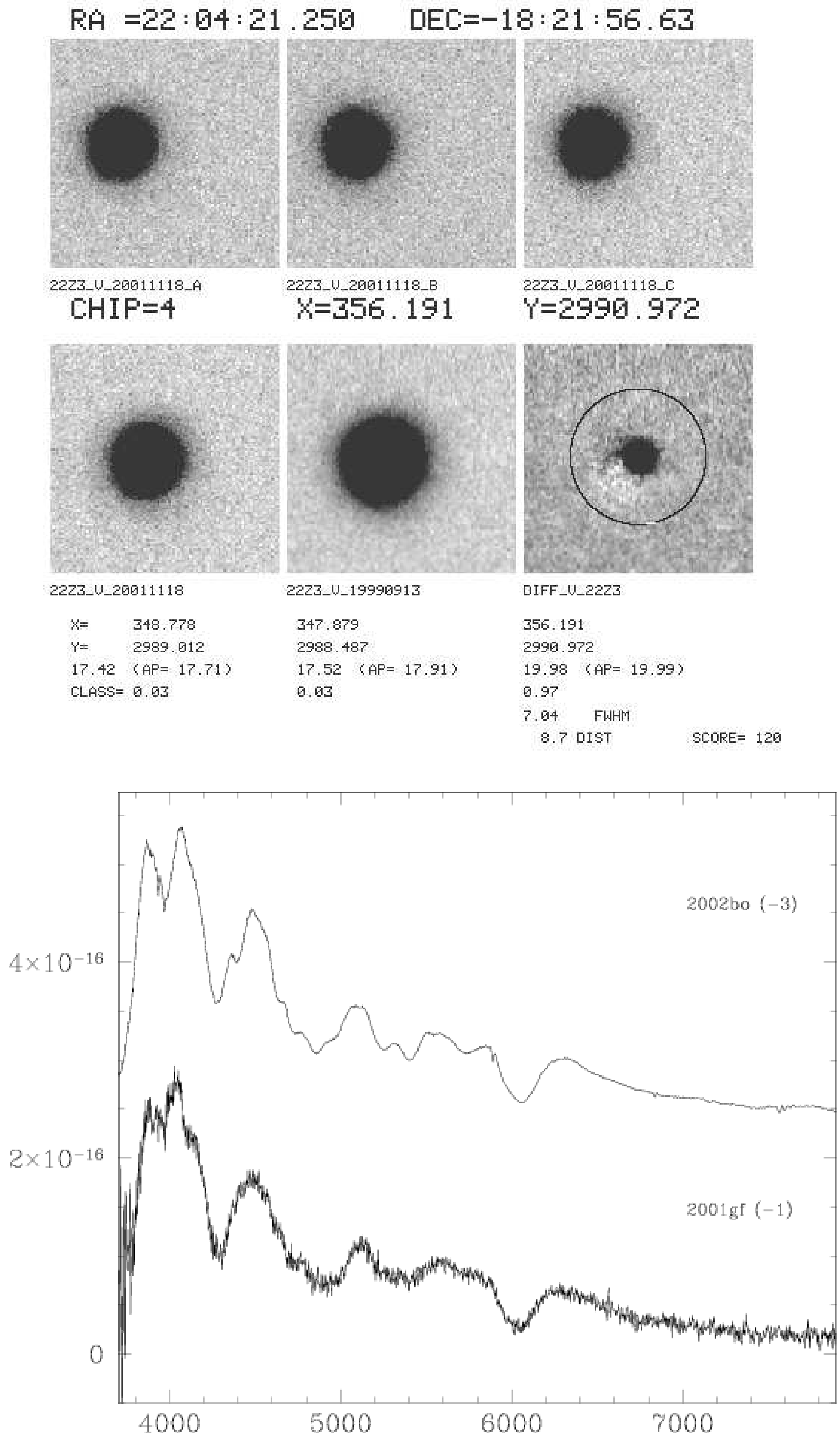

Figure B.11: SN 2001gf, type Ia, $z = 0.13$. The spectrum is compared to that of SN 2002bo (Ia) close 3 days before maximum.

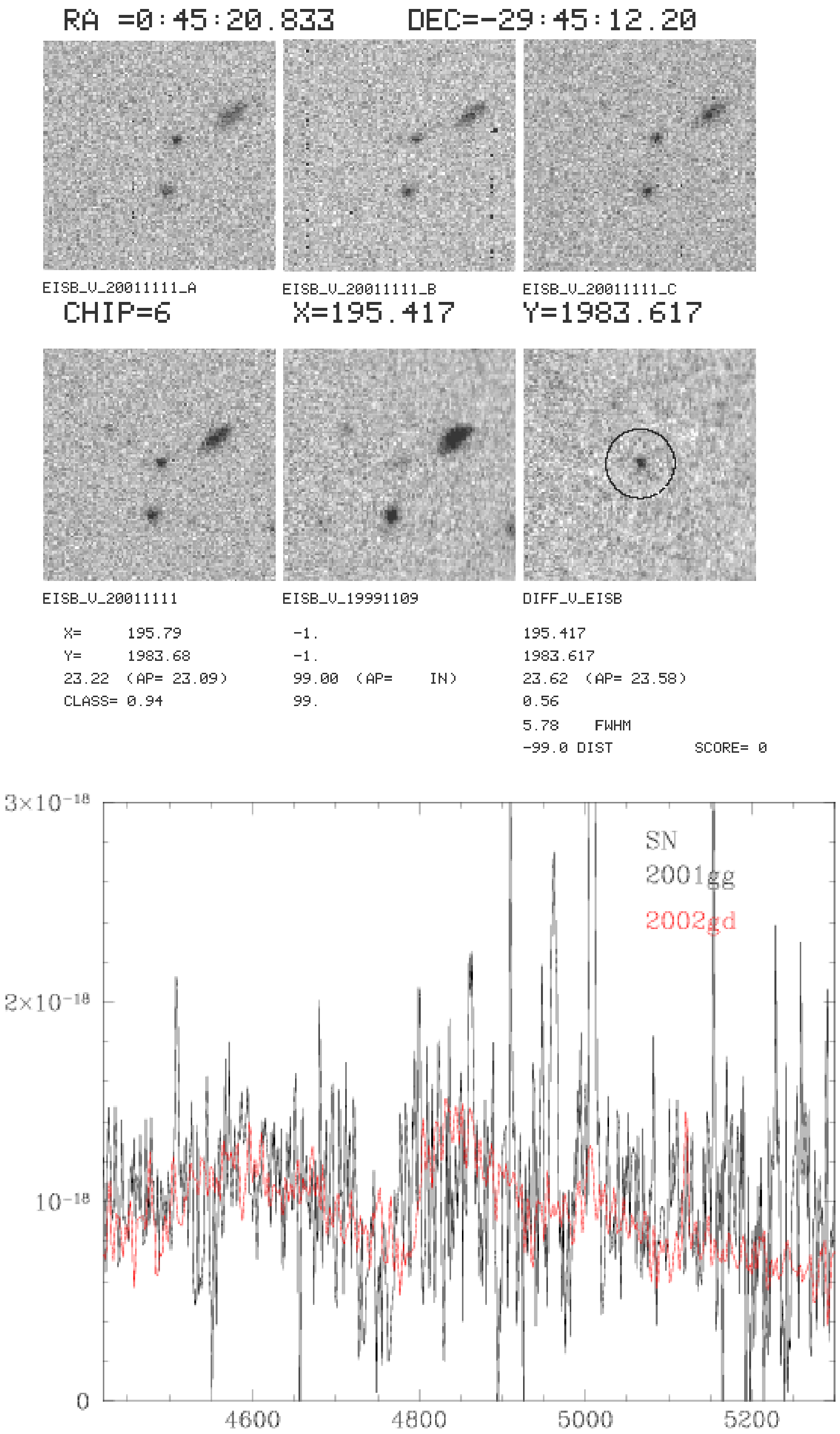

Figure B.12: SN 2001gg, type II, $z = 0.61$. The spectrum (the most noisy) is compared to that of SN 2002gd (II) 9 days past maximum.

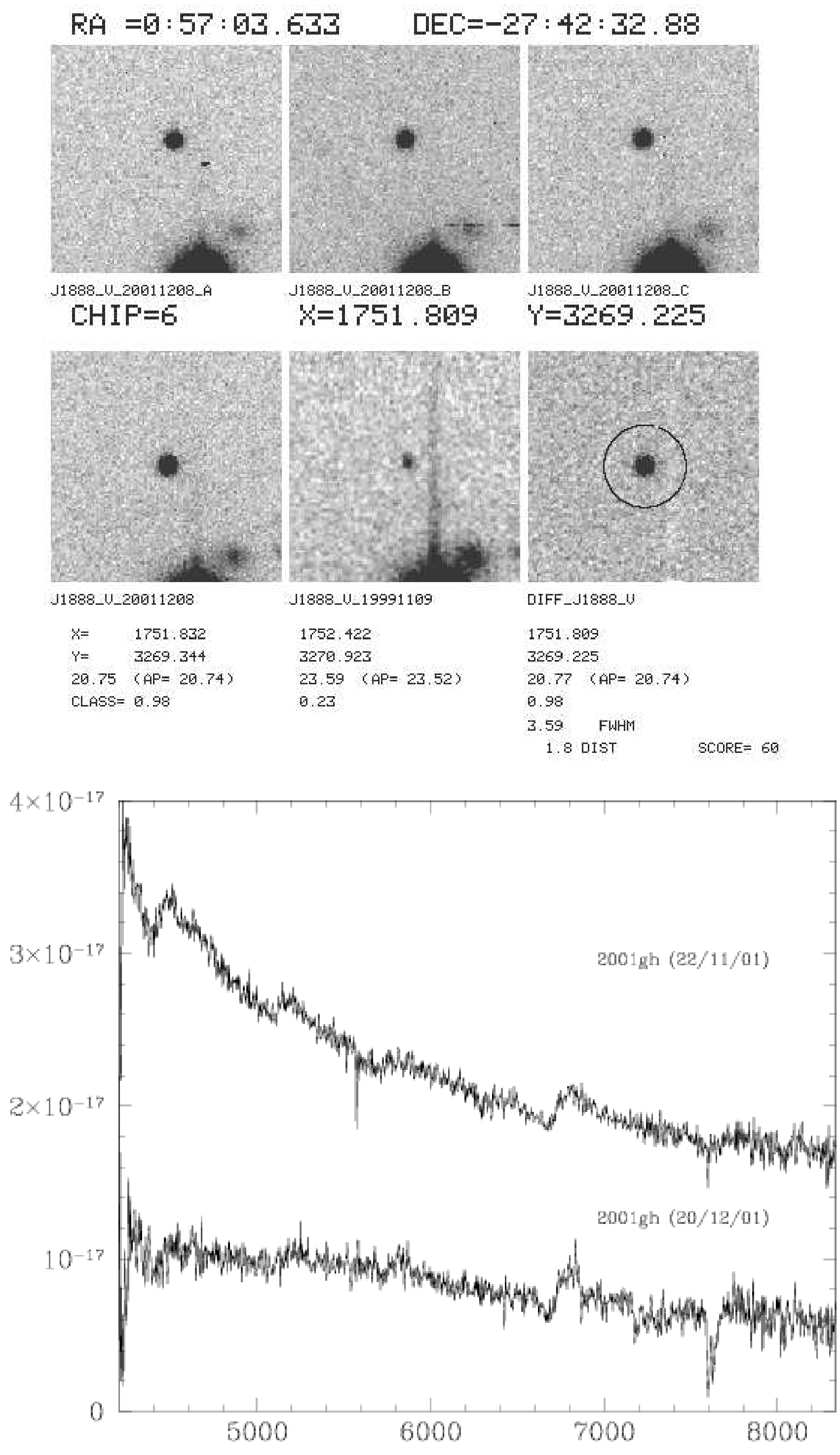

Figure B.13: SN 2001gh, type II, z = 0.16. Two spectra taken in different epochs are shown. It was not possible to find a comparison type II spectrum with similar He lines and blue continuum.

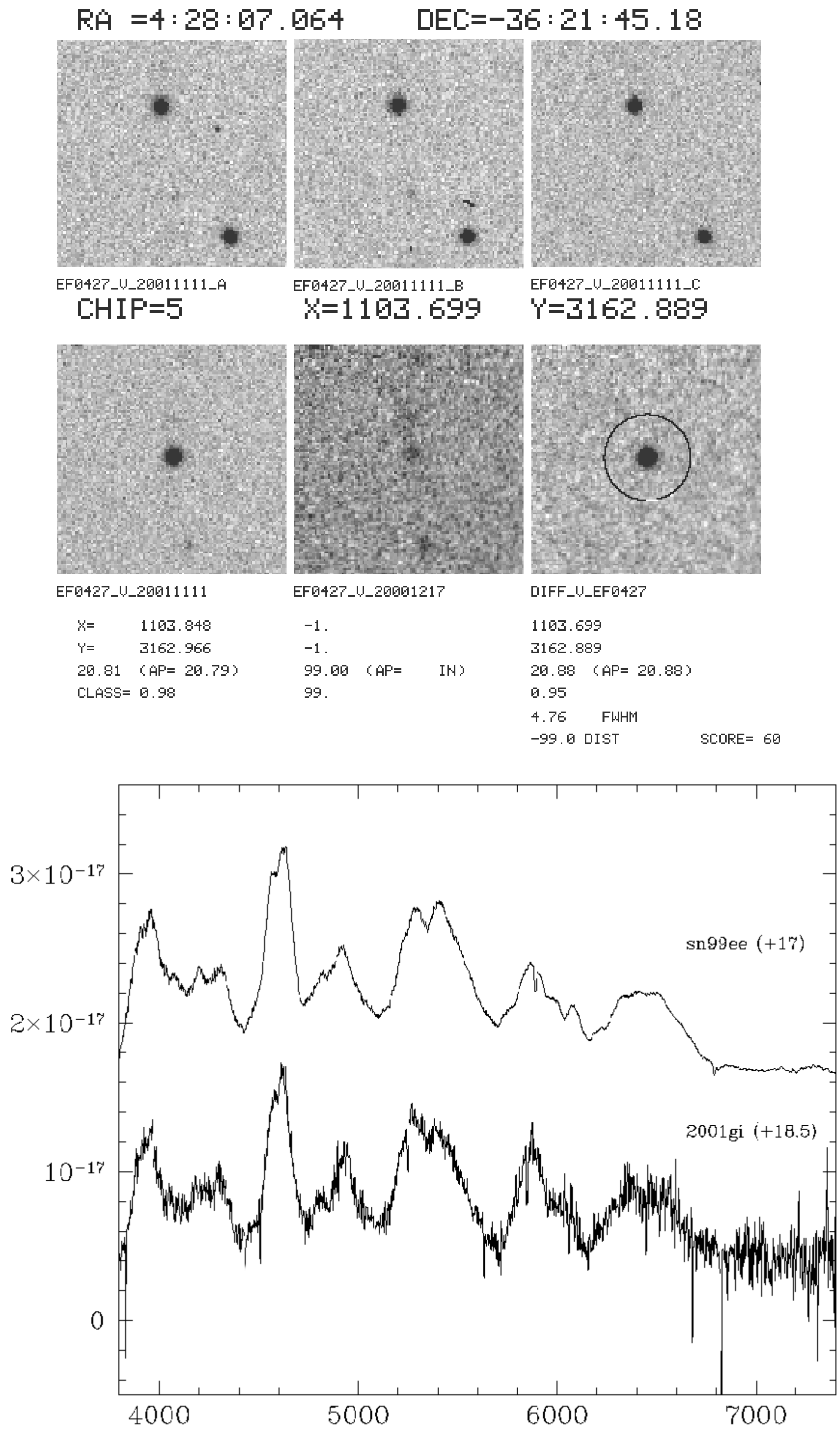

Figure B.14: SN 2001gi, type Ia, $z = 0.20$. The spectrum is compared to that of SN 1999ee (Ia) 17 days past maximum.

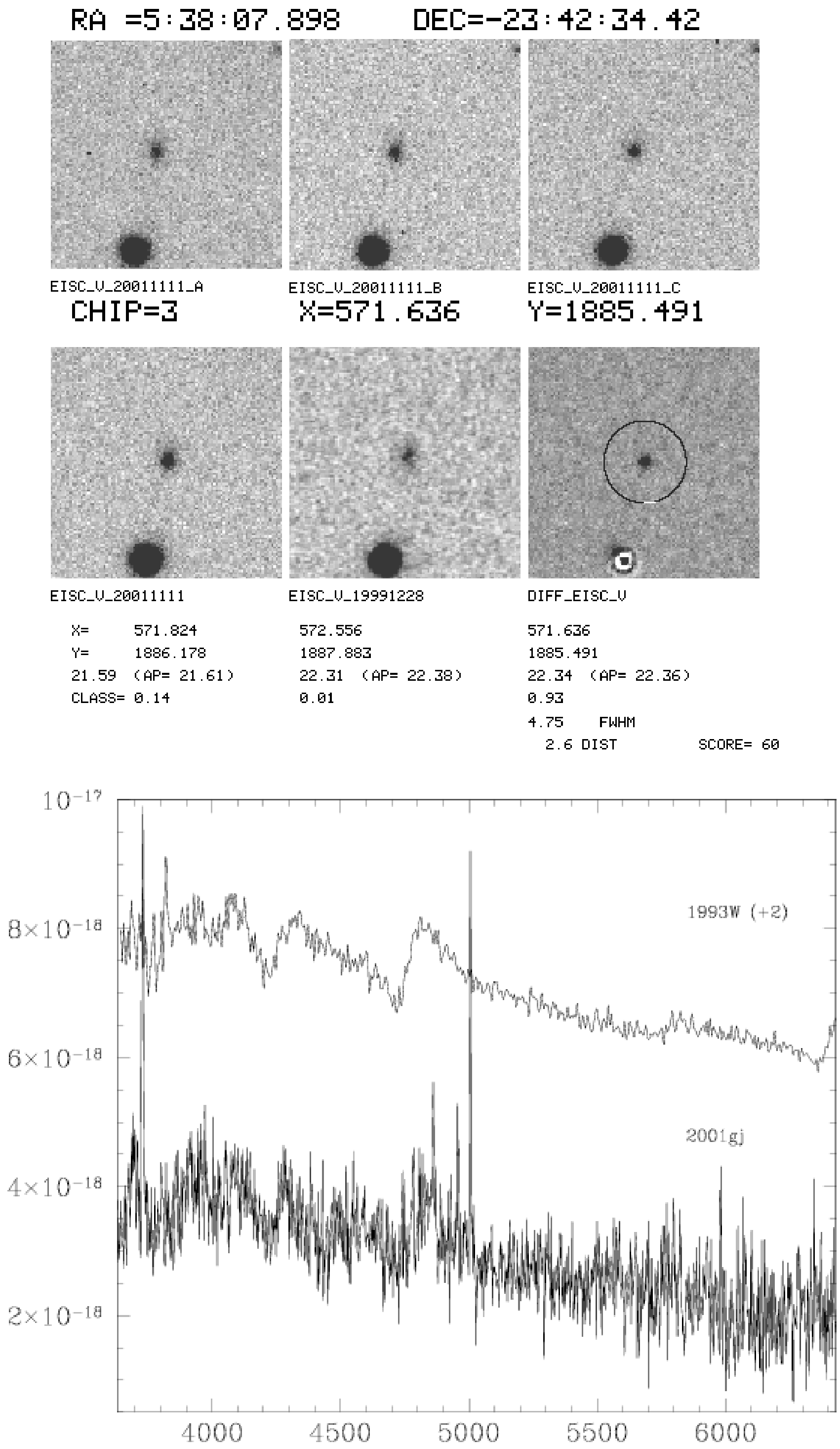

Figure B.15: SN 2001gj, type II, $z = 0.27$. The spectrum is compared to that of SN SN 1993W (II) 2 days past maximum.

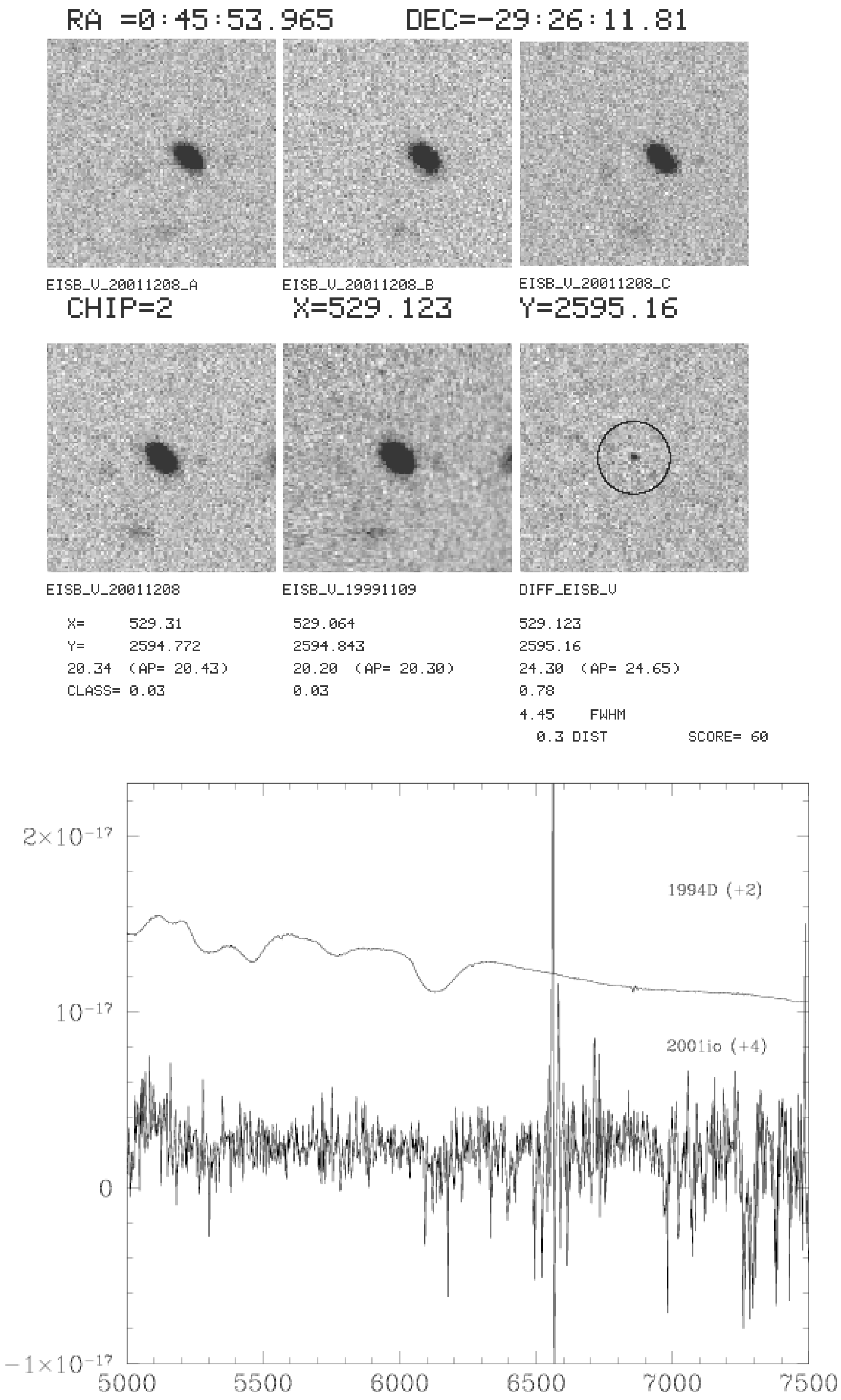

Figure B.16: SN 2001io, type Ia, $z = 0.19$. The spectrum is compared to that of SN 1994D (Ia) 2 days past maximum.

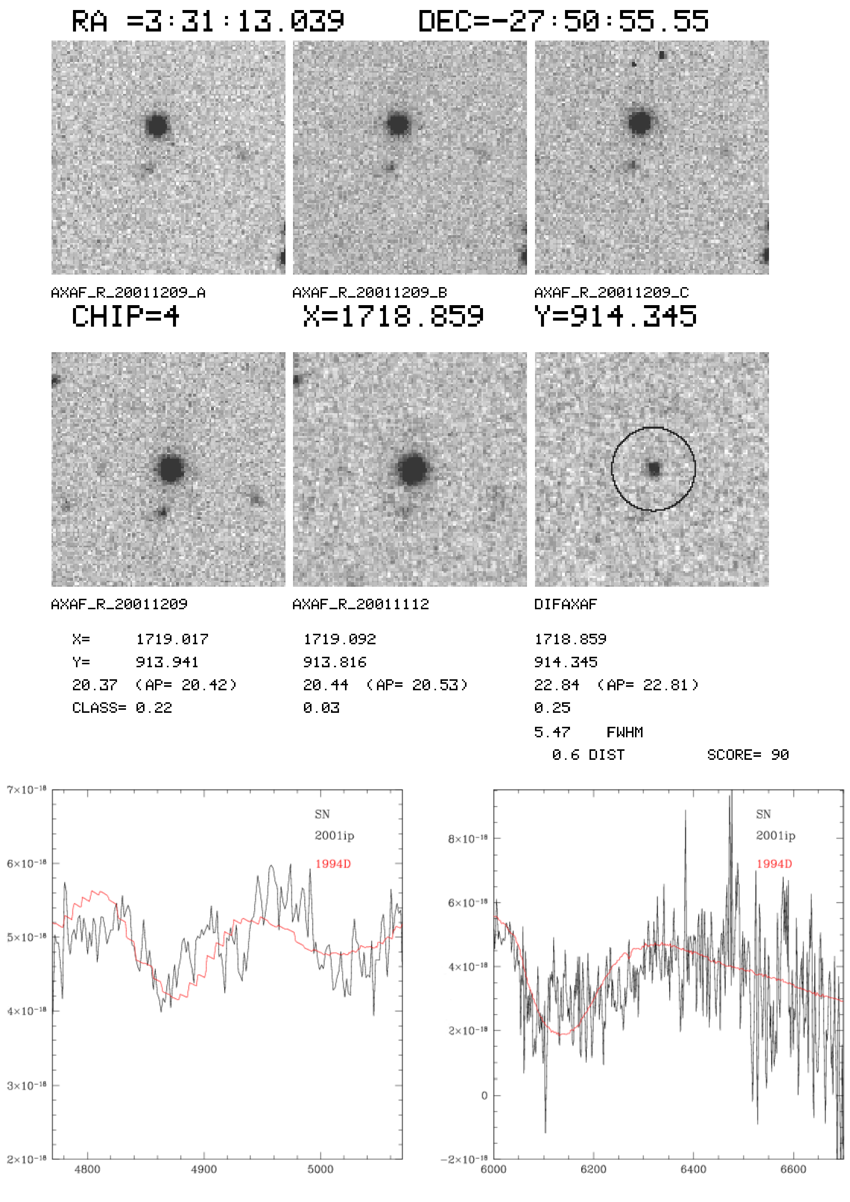

Figure B.17: SN 2001ip, type Ia, z = 054. The spectrum (contaminated by the host galaxy) is compared to that of SN 1994D (Ia) two days past B maximum. Two different wavelenght ranges are shown. It was not possible to find a comparison spectrum fitting all the spectral range. SN 2001ip spectrum is the noisy one.

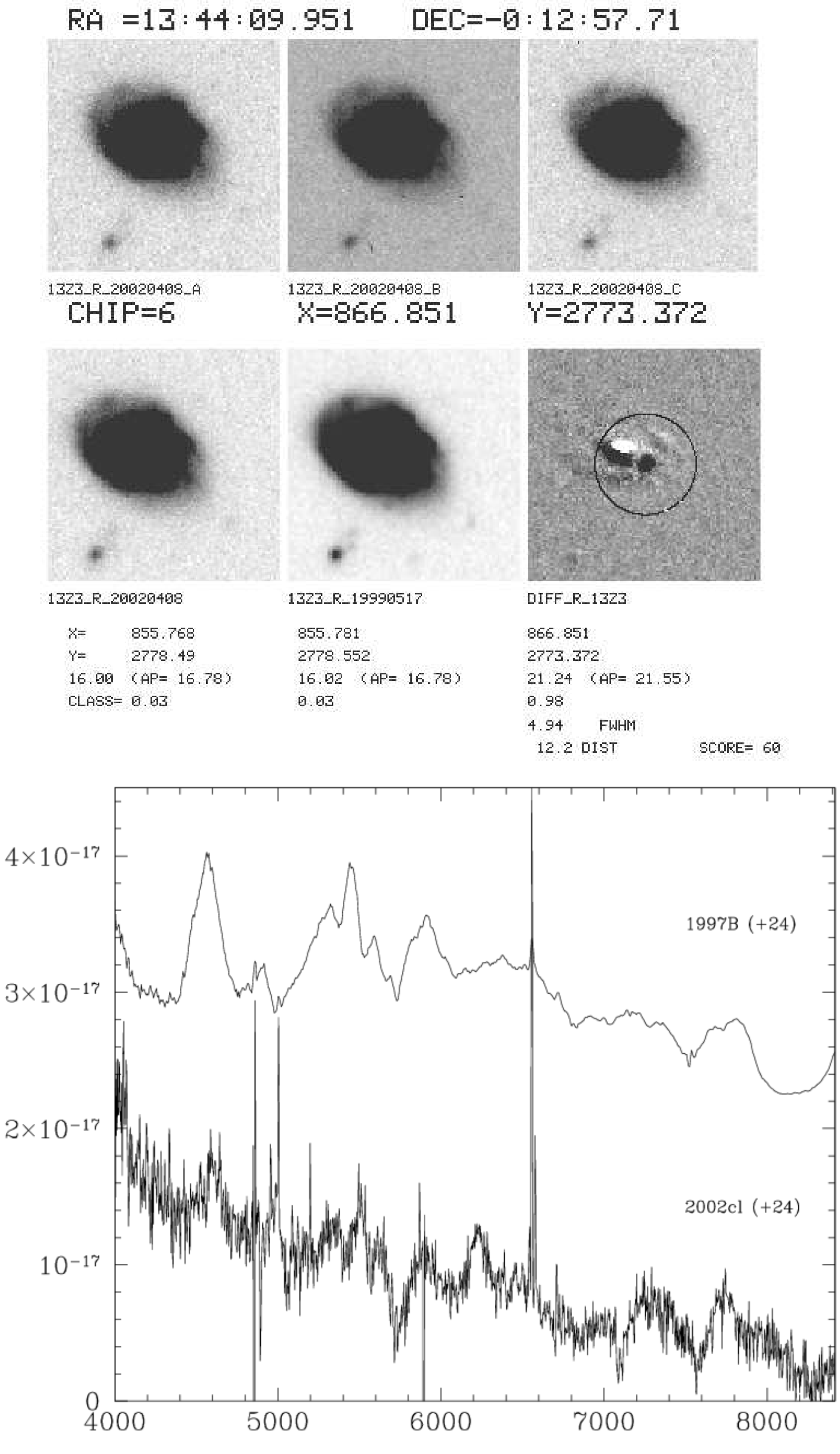

Figure B.18: SN 2002cl, type Ic, $z = 0.07$. The spectrum is compared to that of SN 1997B (Ic) 24 days past maximum.

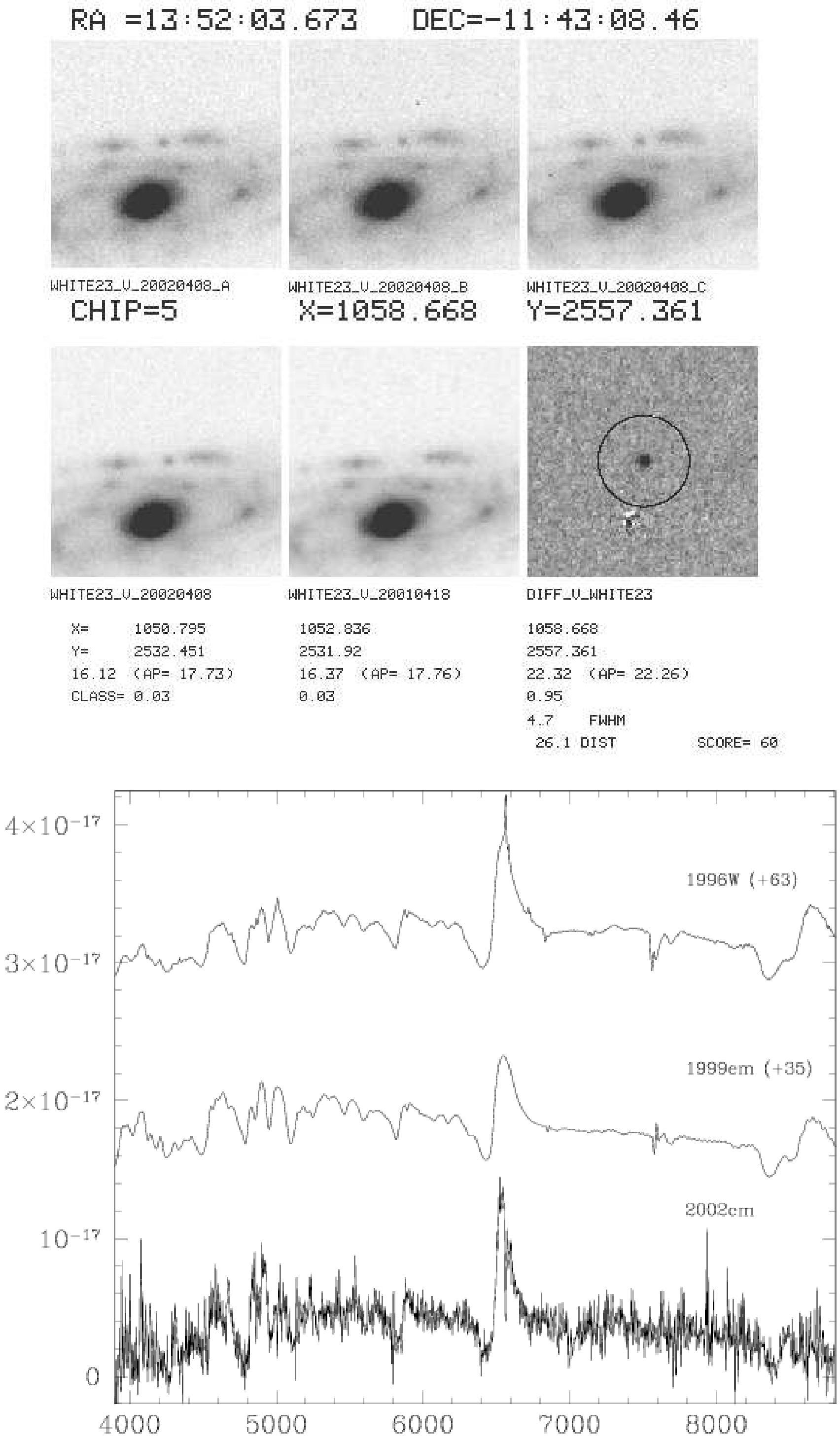

Figure B.19: SN 2002cm, type II, $z = 0.09$. The spectrum is compared to those of SN 1996W (IIP, 63 days post max.) and 1999em (IIP, 35 days post max.). Due to the slow spectral evolution of type IIP SNe at these epochs, the comparison is not useful to contrain about SN 2002cm phase.

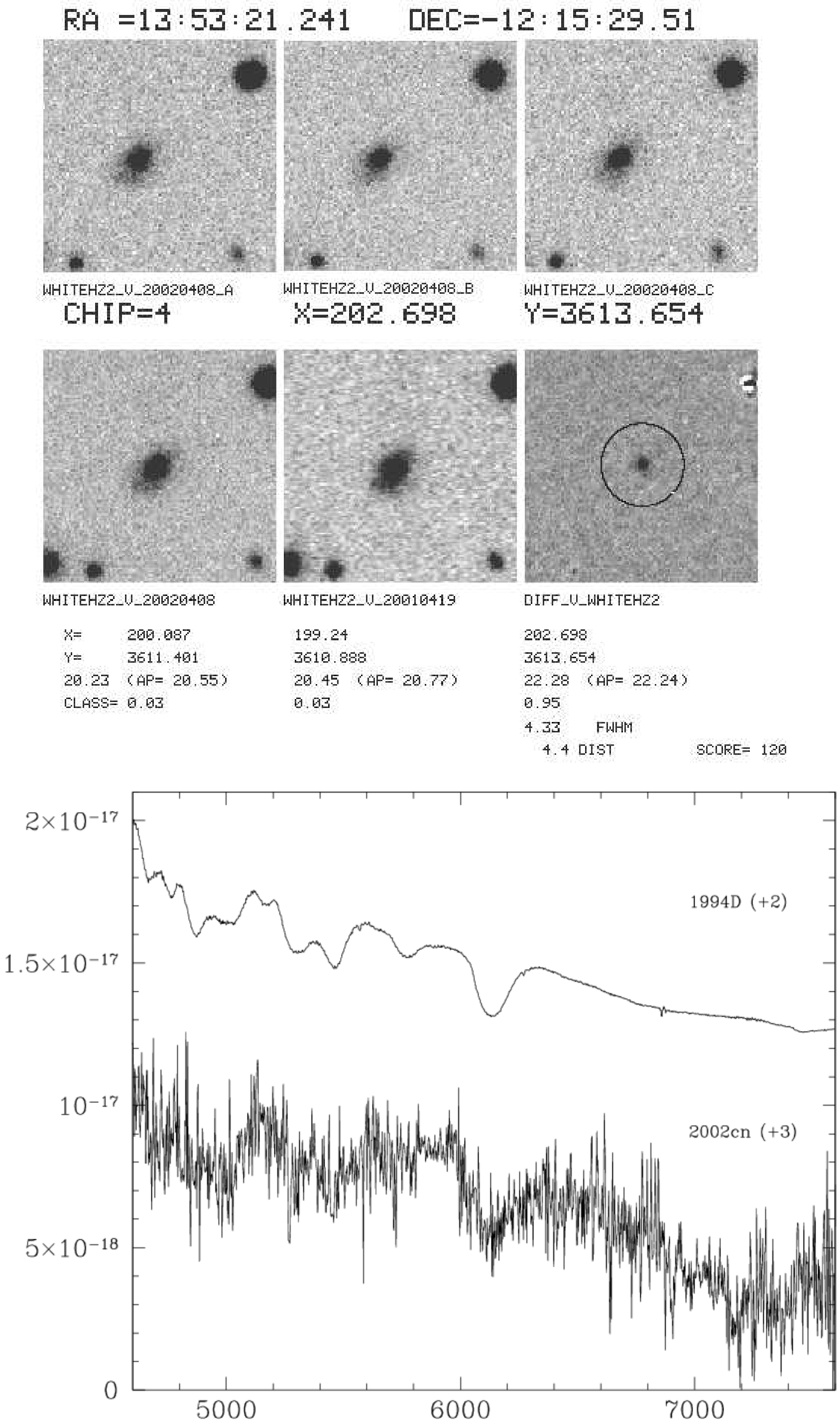

Figure B.20: SN 2002cn, type Ia, $z = 0.30$. The spectrum is compared to that of SN 1994D (Ia) 2 days past maximum.

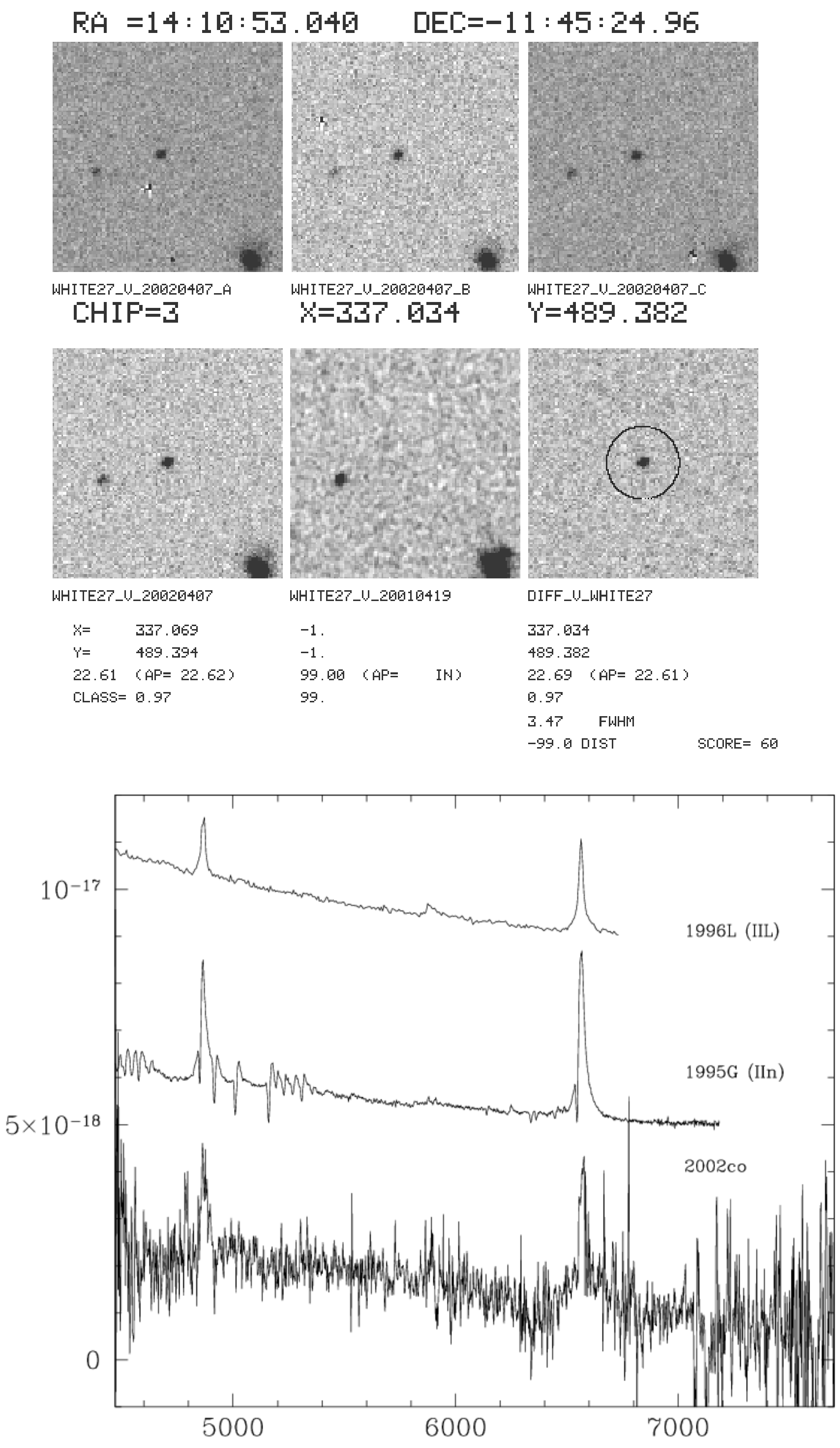

Figure B.21: SN 2002co, type II, $z = 0.32$. The spectrum is compared to those of SN 1996L (IIL) and 1995G (IIn) soon after maximum. SN 2002co is probably an intermediate type between types IIL and IIn.

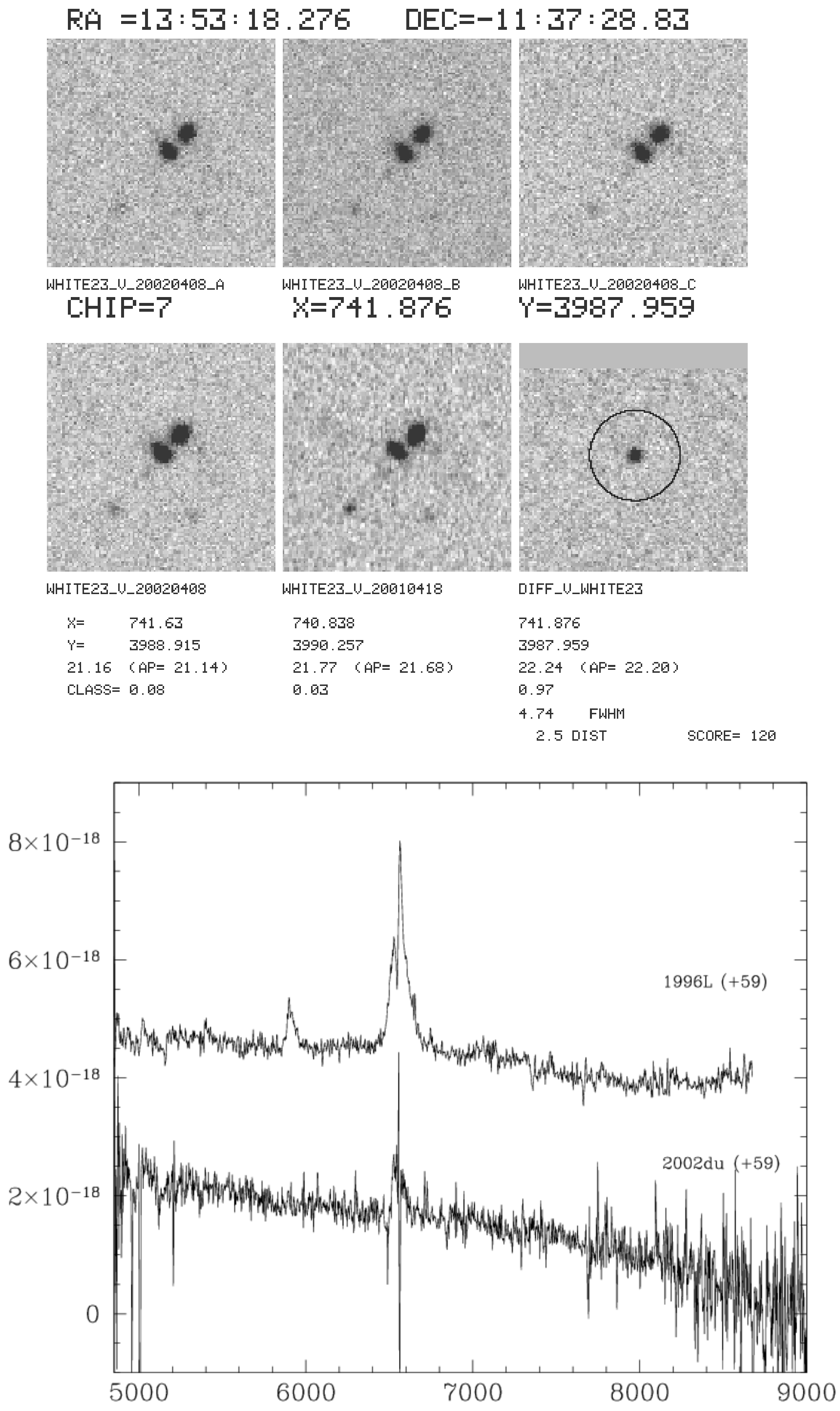

Figure B.22: SN 2002du, type II, $z = 0.21$. The spectrum is compared to that of SN 1996L (IIL) 56 days past maximum. SN 2002du seems an intermediate type between IIL–IIP.

Bibliography

Aguirre, A.: 1999, *ApJ* **525**, 583

Aguirre, A. and Haiman, Z.: 2000, *ApJ* **532**, 28

Alard, C.: 2000, *A&AS* **144**, 363

Alard, C. and Lupton, R. H.: 1998, *ApJ* **503**, 325

Aldering, G., Adam, G., Antilogus, P., Astier, P., Bacon, R., Bongard, S., Bonnaud, C., Copin, Y., Hardin, D., Henault, F., Howell, D. A., Lemonnier, J., Levy, J., Loken, S. C., Nugent, P. E., Pain, R., Pecontal, A., Pecontal, E., Perlmutter, S., Quimby, R. M., Schahmaneche, K., Smadja, G., and Wood-Vasey, W. M.: 2002, in *Survey and Other Telescope Technologies and Discoveries. Edited by Tyson, J. Anthony; Wolff, Sidney. Proceedings of the SPIE, Volume 4836, pp. 61-72 (2002).*, pp 61–72

Aldering, G., Knop, R., and Nugent, P.: 2000, *AJ* **119**, 2110

Baade, W. and Zwicky, F.: 1938, *ApJ* **88**, 411

Banerjee, S. K., Narlikar, J. V., Wickramasinghe, N. C., Hoyle, F., and Burbidge, G.: 2000, *AJ* **119**, 2583

Barbon, R., Benetti, S., Cappellaro, E., Patat, F., Turatto, M., and Iijima, T.: 1995, *A&AS* **110**, 513

Barbon, R., Ciatti, F., and Rosino, L.: 1973, *A&A* **29**, 57

Barris, B. J., Tonry, J. andBlondin, S., Challis, P., Chornock, R., Clocchiatti, A., Filippenko, A., Garnavich, P., Holland, S., Jha, S., kirshner, R., Krisciuna, K., Leibundgut, B., Li, W., Matheson, T., Miknaitis, G., Riess, A., Schimdt, B., Smith, R. C., Sollerman, J., Spyromilio, J., Stubbs, C., Suntzeff, N., Aussel, H., Chambers, K. C., Connelley, M. S., Donova, D., Henry, J. P., Kaiser, N., liu, M. C., Martin, E. L., and Wainscoat, R. J.: 2003, *astro-ph/0310843*

Benítez, N., Riess, A., Nugent, P., Dickinson, M., Chornock, R., and Filippenko, A. V.: 2002, *ApJL* **577**, L1

Benz, W., Cameron, A. G. W., Press, W. H., and Bowers, R. L.: 1990, *ApJ* **348**, 647

Bertin, E. and Arnouts, S.: 1996, *A&AS* **117**, 393

Blanton, M. R., Dalcanton, J., Eisenstein, D., Loveday, J., Strauss, M. A., SubbaRao, M., Weinberg, D. H., Anderson, J. E., Annis, J., Bahcall, N. A., Bernardi, M., Brinkmann, J., Brunner, R. J., Burles, S., Carey, L., Castander, F. J., Connolly, A. J., Csabai, I., Doi, M., Finkbeiner, D., Friedman, S., Frieman, J. A., Fukugita, M., Gunn, J. E., Hennessy, G. S., Hindsley, R. B., Hogg, D. W., Ichikawa, T., Ivezić, Ž., Kent, S., Knapp, G. R., Lamb, D. Q., Leger, R. F., Long, D. C., Lupton, R. H., McKay, T. A., Meiksin, A., Merelli, A., Munn, J. A., Narayanan, V., Newcomb, M., Nichol, R. C., Okamura, S., Owen, R., Pier, J. R., Pope, A., Postman, M., Quinn, T., Rockosi, C. M., Schlegel, D. J., Schneider, D. P., Shimasaku, K., Siegmund, W. A., Smee, S., Snir, Y., Stoughton, C., Stubbs, C., Szalay, A. S., Szokoly, G. P., Thakar, A. R., Tremonti, C., Tucker, D.: 2001, *AJ* **121**, 2358

Boles, T.: 2002, *IAUC* **8009**, 1

Bolzonella, M., Miralles, J.-M., and Pelló, R.: 2000, *A&A* **363**, 476

Bono, G., Caputo, F., Castellani, V., and Marconi, M.: 1999a, *ApJ* **512**, 711

Bono, G., Marconi, M., and Stellingwerf, R. F.: 1999b, *ApJS* **122**, 167

Botticella, M. T.: 2003, *graduation Thesis*

Bouchet, P., Lequeux, J., Maurice, E., Prevot, L., and Prevot-Burnichon, M. L.: 1985, *A&A* **149**, 330

Branch, D., Livio, M., Yungelson, L. R., Boffi, F. R., and Baron, E.: 1995, *PASP* **107**, 1019

Branch, D., Nugent, P., and Fisher, A.: 1997, *Thermonuclear Supernovae*, p. 715, Dordrecht: Kluwer

Brosch, N.: 1988, *in Dust in the Universe*, ed. M.E. Bailey & D.A. Williams (Cambridge: Cambridge Univ. Press), 502

Brosch, N. and Loinger, F.: 1991, *A&A* **249**, 327

Brown, W. R., Geller, M. J., Fabricant, D. G., and Kurtz, M. J.: 2001, *AJ* **122**, 714

Bruzual A., G. and Charlot, S.: 1993, *ApJ* **405**, 538

Burstein, D. and Heiles, C.: 1982, *BAAS* **14**, 662

Célérier, M.: 2000, *A&A* **353**, 63

Candia, P., Krisciunas, K., Suntzeff, N. B., González, D., Espinoza, J., Leiton, R., Rest, A., Smith, R. C., Cuadra, J., Tavenner, T., Logan, C., Snider, K., Thomas, M., West, A. A., González, G., González, S., Phillips, M. M., Hastings, N. C., and McMillan, R.: 2003, *PASP* **115**, 277

Capaccioli, M., Cappellaro, E., della Valle, M., D'Onofrio, M., Rosino, L., and Turatto, M.: 1990, *ApJ* **350**, 110

Cappellaro, E., Evans, R., and Turatto, M.: 1999, *A&A* **351**, 459

Cappellaro, E., Mazzali, P. A., Benetti, S., Danziger, I. J., Turatto, M., della Valle, M., and Patat, F.: 1997a, *A&A* **328**, 203

Cappellaro, E. and Turatto, M.: 2001, *The effect of binaries on stellar population studies*, editor D. Vanbeveren, ASSL series, vol. 264, p. 199 Kluwer Academic Publishers, Dordrecht

Cappellaro, E., Turatto, M., Benetti, S., Tsvetkov, D. Y., Bartunov, O. S., and Makarova, I. N.: 1993a, *A&A* **268**, 472

Cappellaro, E., Turatto, M., Benetti, S., Tsvetkov, D. Y., Bartunov, O. S., and Makarova, I. N.: 1993b, *A&A* **273**, 383

Cappellaro, E., Turatto, M., Tsvetkov, D. Y., Bartunov, O. S., Pollas, C., Evans, R., and Hamuy, M.: 1997b, *A&A* **322**, 431

Caputo, F., Marconi, M., and Musella, I.: 2000a, *A&A* **354**, 610

Caputo, F., Marconi, M., Musella, I., and Santolamazza, P.: 2000b, *A&A* **359**, 1059

Cardelli, J. A., Clayton, G. C., and Mathis, J. S.: 1989, *ApJ* **345**, 245

Clayton, G. C. and Cardelli, J. A.: 1988, *AJ* **96**, 695

Coleman, G. D., Wu, C.-C., and Weedman, D. W.: 1980, *ApJS* **43**, 393

Colgate, S. A.: 1979, *ApJ* **232**, 404

Colless, M., Dalton, G., Maddox, S., Sutherland, W., Norberg, P., Cole, S., Bland-Hawthorn, J., Bridges, T., Cannon, R., Collins, C., Couch, W., Cross, N., Deeley, K., De Propris, R., Driver, S. P., Efstathiou, G., Ellis, R. S., Frenk, C. S., Glazebrook, K., Jackson, C., Lahav, O., Lewis, I., Lumsden, S., Madgwick, D., Peacock, J. A., Peterson, B. A., Price, I., Seaborne, M., and Taylor, K.: 2001, *MNRAS* **328**, 1039

Combes, F.: 2003, *astro-ph/0308144*

Connolly, A. J., Szalay, A. S., Dickinson, M., Subbarao, M. U., and Brunner, R. J.: 1997, *ApJL* **486**, L11+

Contaldi, C. R. and CBI/BOOMERanG Collaboration: 2002, *Bulletin of the American Astronomical Society* **34**, 787

Cowie, L. L., Songaila, A., and Barger, A. J.: 1999, *AJ* **118**, 603

Croft, R. A. C., Weinberg, D. H., Bolte, M., Burles, S., Hernquist, L., Katz, N., Kirkman, D., and Tytler, D.: 2002, *Apj* **581**, 20

Cross, N., Driver, S. P., Couch, W., Baugh, C. M., Bland-Hawthorn, J., Bridges, T., Cannon, R., Cole, S., Colless, M., Collins, C., Dalton, G., Deeley, K., De Propris, R., Efstathiou, G., Ellis, R. S., Frenk, C. S., Glazebrook, K., Jackson, C., Lahav, O., Lewis, I., Lumsden, S., Maddox, S., Madgwick, D., Moody, S., Norberg, P., Peacock, J. A., Peterson, B. A., Price, I., Seaborne, M., Sutherland, W., Tadros, H., and Taylor, K.: 2001, *MNRAS* **324**, 825

Cumming, R. J., Lundqvist, P., Smith, L. J., Pettini, M., and King, D. L.: 1996, *MNRAS* **283**, 1355

Dahlén, T. and Fransson, C.: 1999, *A&A* **350**, 349

Davis, M., Newman, J. A., Faber, S. M., and Phillips, A. C.: 2001, in *Deep Fields*, pp 241–+

de Bernardis, P., Ade, P. A. R., Bock, J. J., Bond, J. R., Borrill, J., Boscaleri, A., Coble, K., Contaldi, C. R., Crill, B. P., De Troia, G., Farese, P., Ganga, K., Giacometti, M., Hivon, E., Hristov, V. V., Iacoangeli, A., Jaffe, A. H., Jones, W. C., Lange, A. E., Martinis, L., Masi, S., Mason, P., Mauskopf, P. D., Melchiorri, A., Montroy, T., Netterfield, C. B., Pascale, E., Piacentini, F., Pogosyan, D., Polenta, G., Pongetti, F., Prunet, S., Romeo, G., Ruhl, J. E., and Scaramuzzi, F.: 2002, *ApJ* **564**, 559

de Vaucouleurs, G., de Vaucouleurs, A., Corwin, H. G., Buta, R. J., Paturel, G., and Fouque, P.: 1991, *Third Reference Catalogue of Bright Galaxies*, Volume 1-3, XII, 2069 pp. 7 figs.. Springer-Verlag Berlin Heidelberg New York

Drell, P. S., Loredo, T. J., and Wasserman, I.: 2000, *ApJ* **530**, 593

Eck, C. R., Cowan, J. J., Roberts, D. A., Boffi, F. R., and Branch, D.: 1995, *ApJL* **451**, L53+

Efstathiou, G., Moody, S., Peacock, J. A., Percival, W. J., Baugh, C., Bland-Hawthorn, J., Bridges, T., Cannon, R., Cole, S., Colless, M., Collins, C., Couch, W., Dalton, G., de Propris, R., Driver, S. P., Ellis, R. S., Frenk, C. S., Glazebrook, K., Jackson, C., Lahav, O., Lewis, I., Lumsden, S., Maddox, S., Norberg, P., Peterson, B. A., Sutherland, W., and Taylor, K.: 2002, *MNRAS* **330**, L29

Ellis, R. S., Colless, M., Broadhurst, T., Heyl, J., and Glazebrook, K.: 1996, *MNRAS* **280**, 235

Evans, R. and Hazelbrook, N. S. W.: 2003, *IAUC* **8171**, 2

Evans, R. and McNaught, R. H.: 2003, *IAUC* **8150**, 2

Evans, R. and Quirk, S.: 2003, *IAUC* **8042**, 1

Evans, R., van den Bergh, S., and McClure, R. D.: 1989, *ApJ* **345**, 752

Falco, E. E., Impey, C. D., Kochanek, C. S., Lehár, J., McLeod, B. A., Rix, H.-W., Keeton, C. R., Muñoz, J. A., and Peng, C. Y.: 1999, *ApJ* **523**, 617

Ferrarese, L., Ford, H. C., Huchra, J., Kennicutt, R. C., Mould, J. R., Sakai, S., Freedman, W. L., Stetson, P. B., Madore, B. F., Gibson, B. K., Graham, J. A., Hughes, S. M., Illingworth, G. D., Kelson, D. D., Macri, L., Sebo, K., and Silbermann, N. A.: 2000, *ApJS* **128**, 431

Filippenko, A.: 2003, in *"From Twilight to Highlight: The Physics of Supernovae," ed. W. Hillebrandt and B. Leibundgut (Berlin: Springer-Verlag)*, pp 171–182

Filippenko, A. V.: 1988, *AJ* **96**, 1941

Filippenko, A. V.: 1989, *PASP* **101**, 588

Filippenko, A. V.: 1997, *ARA&A* **35**, 309

Filippenko, A. V., Matheson, T., and Barth, A. J.: 1994, *AJ* **108**, 2220

Fiorentino, G., Caputo, F., Marconi, M., and Musella, I.: 2002, *ApJ* **576**, 402

Fischer, E.: 2003, *astro-ph/0306459*

Fixsen, D. J., Dwek, E., Mather, J. C., Bennett, C. L., and Shafer, R. A.: 1998, *ApJ* **508**, 123

Folkes, S., Ronen, S., Price, I., Lahav, O., Colless, M., Maddox, S., Deeley, K., Glazebrook, K., Bland-Hawthorn, J., Cannon, R., Cole, S., Collins, C., Couch, W., Driver, S. P., Dalton, G., Efstathiou, G., Ellis, R. S., Frenk, C. S., Kaiser, N., Lewis, I., Lumsden, S., Peacock, J., Peterson, B. A., Sutherland, W., and Taylor, K.: 1999, *MNRAS* **308**, 459

Freedman, W. L. and Madore, B. F.: 1990, *ApJ* **365**, 186

Freedman, W. L., Madore, B. F., Gibson, B. K., Ferrarese, L., Kelson, D. D., Sakai, S., Mould, J. R., Kennicutt, R. C., Ford, H. C., Graham, J. A., Huchra, J. P., Hughes, S. M. G., Illingworth, G. D., Macri, L. M., and Stetson, P. B.: 2001, *ApJ* **553**, 47

Frieman, J. A., Huterer, D., Linder, E. V., and Turner, M. S.: 2003, *PhRvD* **67**, 83505

Fujita, S. S., Ajiki, M., Shioya, Y., Nagao, T., Murayama, T., Taniguchi, Y., Umeda, K., Yamada, S., Yagi, M., Okamura, S., and Komiyama, Y.: 2003, *ApJL* **586**, L115

Gal-Yam, A., Maoz, D., Dan, J., and Ibbetson, P.: 1998, *IAUC* **7055**, 1

Gal-Yam, A., Maoz, D., and Sharon, K.: 2002, *MNRAS* **332**, 37

Garnavich, P. M., Holland, S. T., Schmidt, B. P., Krisciunas, K., Smith, R. C., Suntzeff, N. B., Becker, A., Miceli, A., Miknaitis, G., Rest, A., Stubbs, C., Filippenko, A. V., Jha, S., Li, W., Challis, P., Kirshner, R. P., Matheson, T., Barris, B., Tonry, J. L., Riess, A. G., Leibundgut, B., Sollerman, J., Spyromilio, J., Clocchiatti, A., Pompea, S., and High-Z Supernova Search Team: 2002, *Bulletin of the American Astronomical Society* **34**, 1233

Garnavich, P. M., Jha, S., Challis, P., Clocchiatti, A., Diercks, A., Filippenko, A. V., Gilliland, R. L., Hogan, C. J., Kirshner, R. P., Leibundgut, B., Phillips, M. M., Reiss, D., Riess, A. G., Schmidt, B. P., Schommer, R. A., Smith, R. C., Spyromilio, J., Stubbs, C., Suntzeff, N. B., Tonry, J., and Carroll, S. M.: 1998, *ApJ* **509**, 74

Geller, M. J., Kurtz, M. J., Wegner, G., Thorstensen, J. R., Fabricant, D. G., Marzke, R. O., Huchra, J. P., Schild, R. E., and Falco, E. E.: 1997, *AJ* **114**, 2205

Gilliland, R. L. and Phillips, M. M.: 1998, *IAUC* **6810**, 1

Giovanelli, R., Dale, D. A., Haynes, M. P., Hardy, E., and Campusano, L. E.: 1999, *ApJ* **525**, 25

Glazebrook, K., Ellis, R., Colless, M., Broadhurst, T., Allington-Smith, J., and Tanvir, N.: 1995, *MNRAS* **273**, 157

Gnedin, N. Y. and Hamilton, A. J. S.: 2002, *MNRAS* **334**, 107

Höflich, P., Straniero, O., Limongi, M., Dominguez, I., and Chieffi, A.: 2001, in *Revista Mexicana de Astronomia y Astrofisica Conference Series*, pp 157–162

Hamuy, M., Maza, J., Phillips, M. M., Suntzeff, N. B., Wischnjewsky, M., Smith, R. C., Antezana, R., Wells, L. A., Gonzalez, L. E., Gigoux, P., Navarrete, M., Barrientos, F., Lamontagne, R., della Valle, M., Elias, J. E., Phillips, A. C., Odewahn, S. C., Baldwin, J. A., Walker, A. R., Williams, T., Sturch, C. R., Baganoff, F. K., Chaboyer, B. C., Schommer, R. A., Tirado, H., Hernandez, M., Ugarte, P., Guhathakurta, P., Howell, S. B., Szkody, P., Schmidtke, P. C., and Roth, J.: 1993a, *AJ* **106**, 2392

Hamuy, M., Phillips, M., Suntzeff, N., and Maza, J.: 2003a, in *IAUC*, pp 2–+

Hamuy, M., Phillips, M. M., Maza, J., Suntzeff, N. B., Schommer, R. A., and Aviles, R.: 1995, *AJ* **109**, 1

Hamuy, M., Phillips, M. M., Suntzeff, N. B., Maza, J., Gonzalez, L. E., Roth, M., Krisciunas, K., Morrel, N., Green, E. M., Persson, S. E., and McCarthy, P. J.: 2003b, *astro-ph/0306270*

Hamuy, M., Phillips, M. M., Suntzeff, N. B., Schommer, R. A., Maza, J., Antezan, A. R., Wischnjewsky, M., Valladares, G., Muena, C., Gonzales, L. E., Aviles, R., Wells, L. A., Smith, R. C., Navarrete, M., Covarrubias, R., Williger, G. M., Walker, A. R., Layden, A. C., Elias, J. H., Baldwin, J. A., Hernandez, M., Tirado, H., Ugarte, P., Elston, R., Saavedra, N., Barrientos, F., Costa, E., Lira, P., Ruiz, M. T., Anguita, C., Gomez, X., Ortiz, P., della Valle, M., Danziger, J., and 48 coauthors: 1996c, *AJ* **112**, 2408

Hamuy, M., Phillips, M. M., Suntzeff, N. B., Schommer, R. A., Maza, J., and Aviles, R.: 1996a, *AJ* **112**, 2391

Hamuy, M., Phillips, M. M., Suntzeff, N. B., Schommer, R. A., Maza, J., and Aviles, R.: 1996b, *AJ* **112**, 2398

Hamuy, M., Phillips, M. M., Wells, L. A., and Maza, J.: 1993b, *PASP* **105**, 787

Hansen, L., Jorgensen, H. E., Norgaard-Nielsen, H. U., Ellis, R. S., and Couch, W. J.: 1989, *A&A* **211**, L9

Hardin, D., Afonso, C., Alard, C., Albert, J. N., Amadon, A., Andersen, J., Ansari, R., Aubourg, É., Bareyre, P., Bauer, F., Beaulieu, J. P., Blanc, G., Bouquet, A., Char, S., Charlot, X., Couchot, F., Coutures, C., Derue, F., Ferlet, R., Glicenstein, J. F., Goldman, B., Gould, A., Graff, D., Gros, M., Haissinski, J., Hamilton, J. C., de Kat, J., Kim, A., Lasserre, T., Lesquoy, É., Loup, C., Magneville, C., Mansoux, B., Marquette, J. B., Maurice, É., Milsztajn, A., Moniez, M., Palanque-Delabrouille, N., Perdereau, O., Prévot, L., Regnault, N., Rich, J., Spiro, M., Vidal-Madjar, A., Vigroux, L., Zylberajch, S., and The EROS Collaboration: 2000, *A&A* **362**, 419

Hardin, D., Walton, N. A., Ellis, R. S., Irwin, M., McMahon, R. G., Hook, I., Ruiz-Lapuente, P., Mendez, J., Visco, A., Astier, P., Balland, C., Blanc, G., Blanchard, A., Fabbro, S., Hammer, F., Letessier-Selvon, A., Levy, J. M., Mouchet, M., Pain, R., Rich, J., Shahmaneche, K., and Taillet, R.: 1999, *IAUC* **7182**, 1

Hatano, K., Branch, D., Nomoto, K., Deng, J. S., Maeda, K., Nugent, P., and Aldering, G.: 2001, *Bulletin of the American Astronomical Society* **33**, 838

Hippelein, H., Maier, C., Meisenheimer, K., Wolf, C., Fried, J. W., von Kuhlmann, B., Kümmel, M., Phleps, S., and Röser, H.-J.: 2003, *A&A* **402**, 65

Ho, L. C. and Filippenko, A. V.: 1995, *ApJ* **444**, 165

Höeflich, P., Khokhlov, A., Wheeler, J. C., Phillips, M. M., Suntzeff, N. B., and Hamuy, M.: 1996, *ApJL* **472**, L81+

Hogg, D. W. and Turner, E. L.: 1998, *PASP* **110**, 727

Holz, D. E.: 1998, *ApJL* **506**, L1

Howell, D. A.: 2001, *ApJL* **554**, L193

Howell, D. A., Wang, L., and Wheeler, J. C.: 2000, *ApJ* **530**, 166

Humason, M. L. and Gates, H. S.: 1960, *PASP* **72**, 208

Hurst, G. M., Armstrong, M., and Arbour, R.: 2000, *IAUC* **7470**, 1

Iben, I.: 1997, *Scenarios for Type Ia supernovae*, in Thermonuclear Supernovae, pp. 111-26; Ruiz-Lapuente P., Canal R., and Isern J., eds.; Dordrecht: Kluwer

Iben, I. and Renzini, A.: 1984, *Phys. Rep.* **105**, 329

Iben, I. and Tutukov, A. V.: 1984, *ApJS* **54**, 335

Ivanov, V. D., Hamuy, M., and Pinto, P. A.: 2000, *APJ* **542**, 588

Jacoby, G. H., Branch, D., Clardullo, R., Davies, R. L., Harris, W. E., Pierce, M. J., Pritchet, C. J., Tonry, J. L., and Welch, D. L.: 1992, *PASP* **104**, 599

Kantowski, R., Vaughan, T., and Branch, D.: 1995, *ApJ* **447**, 35

Kennicutt, R. C.: 1983, *ApJ* **272**, 54

Kennicutt, R. C.: 1998, *ARA&A* **36**, 189

Kennicutt, R. C., Stetson, P. B., Saha, A., Kelson, D., Rawson, D. M., Sakai, S., Madore, B. F., Mould, J. R., Freedman, W. L., Bresolin, F., Ferrarese, L., Ford, H., Gibson, B. K., Graham, J. A., Han, M., Harding, P., Hoessel, J. G., Huchra, J. P., Hughes, S. M. G., Illingworth, G. D., Macri, L. M., Phelps, R. L., Silbermann, N. A., Turner, A. M., and Wood, P. R.: 1998, *ApJ* **498**, 181

Kim, A., Goobar, A., and Perlmutter, S.: 1996, *PASP* **108**, 190

Kirshner, R. P., Aguilera, C., Barris, B., Becker, A., Challis, P., Chornock, R., Clocchiatti, A., Covarrubias, R., Filippenko, A. V., Garnavich, P. M., Holland, S., Jha, S., Krisciunas, K., Leibundgut, B., Li, W. D., Matheson, T., Miceli, A., Miknaitis, G., Rest, A., Riess, A. G., Schmidt, B. P., Smith, R. C., Sollerman, J., Spyromilio, J., Stubbs, C., Suntzeff, N. B., Tonry, J. L., and The ESSENCE Team: 2003, *American Astronomical Society Meeting* **202**, 0

Knop, R. A., Aldering, G., Amanullah, R., Astier, P., Blanc, G., Burns, M. S., Conley, A., Deustua, S. E., Doi, M., Ellis, R., Fabbro, S., Folatelli, G., Fruchter, A. S., Garavini, G., Garmond, S., Garton, K., Gibbons, R., Goldhaber, G., Goobar, A., Groom, D. E., Hardin, D., Hook, I., Howell, D. A., Kim, A. G., Lee, B. C., Lidman, C., Mendez, J., Nobili, S., Nugent, P. E., Pain, R., Panagia, N., Pennypacker, C. R., Perlmutter, S., Quimby, R., Raux, J., Regnault, N., Ruiz-Lapuente, P., Sainton, G., Schaefer, B., Schahmaneche, K., Smith, E., Spadafora, A. L., Stanishev, V., Sullivan, M., Walton, N. A., Wang, L., Wood-Vasey, W. M., and Yasuda, N.: 2003, *ApJ* **598**, 102

Kobayashi, C., Tsujimoto, T., and Nomoto, K.: 2000, *ApJ* **539**, 26

Kroupa, P.: 2003, *astro-ph/0309598*

Kroupa, P. and Weidner, C.: 2003, *astro-ph/0308356*

Kuijken, K., Bender, R., Cappellaro, E., Muschielok, B., Baruffolo, A., Cascone, E., Iwert, O., Mitsch, W., Nicklas, H., Valentijn, E. A., Baade, D., Begeman, K. G., Bortolussi, A., Boxhoorn, D., Christen, F., Deul, E. R., Geimer, C., Greggio, L., Harke, R., Häfner, R., Hess, G., Hess, H.-J., Hopp, U., Ilijevski, I., Klink, G., Kravcar, H., Lizon, J. L., Magagna, C. E., Müller, P., Niemeczek, R., de Pizzol, L., Poschmann, H., Reif, K., Rengelink, R., Reyes, J., Silber, A., and Wellem, W.: 2002, *The Messenger* **110**, 15

Kulkarni, S. R., Frail, D. A., Wieringa, M. H., Ekers, R. D., Sadler, E. M., Wark, R. M., Higdon, J. L., Phinney, E. S., and Bloom, J. S.: 1998, *Nature* **395**, 663

Kuo, C.-L., Ade, P., Bock, J. J., Daub, M. D., Goldstein, J., Holzapfel, W. L., Lange, A. E., Newcomb, M., Peterson, J. B., Ruhl, J., Runyan, M. C., and Torbet, E.: 2002, *Bulletin of the American Astronomical Society* **34**, 1324

Landolt, A. U.: 1992, *AJ* **104**, 340

Lanzetta, K. M., Yahata, N., Pascarelle, S., Chen, H., and Fernández-Soto, A.: 2002, *ApJ* **570**, 492

Lee, M. G., Park, C., Lee, J., Lee, S., Park, C. G., Jeon, Y.-B., and Bolte, M.: 1999, *IAUC* **7237**, 3

Leibundgut, B.: 2000, *A&AAR* **10**, 179

Leibundgut, B.: 2001, *ARA&A* **39**, 67

Leibundgut, B., Schommer, R., Phillips, M., Riess, A., Schmidt, B., Spyromilio, J., Walsh, J., Suntzeff, N., Hamuy, M., Maza, J., Kirshner, R. P., Challis, P., Garnavich, P., Smith, R. C., Dressler, A., and Ciardullo, R.: 1996, *ApJL* **466**, L21+

Lewis, G. F. and Ibata, R. A.: 2001, *MNRAS* **324**, L25

Li, W., Filippenko, A. V., Chornock, R., Berger, E., Berlind, P., Calkins, M. L., Challis, P., Fassnacht, C., Jha, S., Kirshner, R. P., Matheson, T., Sargent, W. L. W., Simcoe, R. A., Smith, G. H., and Squires, G.: 2003a, *astro-ph/0301428*

Li, W., Filippenko, A. V., Chornock, R., and Jha, S.: 2003b, *American Astronomical Society Meeting* **202**, 0

Li, W., Filippenko, A. V., and Riess, A. G.: 2001, *ApJ* **546**, 719

Li, W. D., Qiu, Y. L., Qiao, Q. Y., Ma, J., Hu, J. Y., Wang, L., and Wheeler, J. C.: 1996, *IAUC* **6379**, 1

Lilly, S. J., Le Fevre, O., Hammer, F., and Crampton, D.: 1996, *ApJL* **460**, L1+

Lin, H., Kirshner, R. P., Shectman, S. A., Landy, S. D., Oemler, A., Tucker, D. L., and Schechter, P. L.: 1996, *ApJ* **464**, 60

Linder, E. V.: 2003, in *American Institute of Physics Conference Series*, pp 193–207

Linder, E. V. and Huterer, D.: 2003, *PhRvD* **67**, 81303

Lira, P.: 1996, *Master's thesis*, MS thesis. Univ. Chile (1996)

Loveday, J., Peterson, B. A., Efstathiou, G., and Maddox, S. J.: 1992, *ApJ* **390**, 338

Mörtsell, E., Gunnarsson, C., and Goobar, A.: 2001, *ApJ* **561**, 106

Madau, P., della Valle, M., and Panagia, N.: 1998a, *MNRAS* **297**, L17+

Madau, P., Ferguson, H. C., Dickinson, M. E., Giavalisco, M., Steidel, C. C., and Fruchter, A.: 1996, *MNRAS* **283**, 1388

Madau, P., Pozzetti, L., and Dickinson, M.: 1998b, *ApJ* **498**, 106

Madgwick, D. S., Hewett, P., Mortlock, D., and Wang, L.: 2003, *astro-ph/0310887*

Madgwick, D. S., Lahav, O., Baldry, I. K., Baugh, C. M., Bland-Hawthorn, J., Bridges, T., Cannon, R., Cole, S., Colless, M., Collins, C., Couch, W., Dalton, G., De Propris, R., Driver, S. P., Efstathiou, G., Ellis, R. S., Frenk, C. S., Glazebrook, K., Jackson, C., Lewis, I., Lumsden, S., Maddox, S., Norberg, P., Peacock, J. A., Peterson, B. A., Sutherland, W., and Taylor, K.: 2002, *MNRAS* **333**, 133

Madore, B. F. and Freedman, W. L.: 1991, *PASP* **103**, 933

Marzke, R. O., da Costa, L. N., Pellegrini, P. S., Willmer, C. N. A., and Geller, M. J.: 1998, *ApJ* **503**, 617

Marzke, R. O., Huchra, J. P., and Geller, M. J.: 1994, *ApJ* **428**, 43

Maza, J., Hamuy, M., Suntzeff, N. B., Phillips, M. M., and Aviles, R.: 1993, *Bulletin of the American Astronomical Society* **25**, 1340

Maza, J., Wischnjewsky, M., Torres, C., Gonzalez, I., Costa, E., and Wroblewski, H.: 1981, *PASP* **93**, 239

Milgrom, M.: 1983, *ApJ* **270**, 371

Milgrom, M.: 1988, *ApJ* **333**, 689

Minkowski, R.: 1939, *ApJ* **89**, 156

Mochkovitch, R., Guerrero, J., and Segretain, L.: 1997, *The merging of white dwarfs*, in Thermonuclear Supernovae, pp. 187-204; Ruiz-Lapuente P., Canal R., and Isern J., eds.; Dordrecht: Kluwer

Mochkovitch, R. and Livio, M.: 1990, *A&A* **236**, 378

Monet, D. B. A., Canzian, B., Dahn, C., Guetter, H., Harris, H., Henden, A., Levine, S., Luginbuhl, C., Monet, A. K. B., Rhodes, A., Riepe, B., Sell, S., Stone, R., Vrba, F., and Walker, R.: 1998, *VizieR Online Data Catalog* **1252**, 0

Muller, R. A., Newberg, H. J. M., Pennypacker, C. R., Perlmutter, S., Sasseen, T. P., and Smith, C. K.: 1992, *ApJL* **384**, L9

Nobili, S., Goobar, A., Knop, R., and Nugent, P.: 2003, *A&A* **404**, 901

Nomoto, K., Iwamoto, K., and Kishimoto, N.: 1997, *Science* **276**, 1378

Nomoto, K., Thielemann, F.-K., and Yokoi, K.: 1984, *ApJ* **286**, 644

Norgaard-Nielsen, H. U., Hansen, L., Jorgensen, H. E., Aragon Salamanca, A., and Ellis, R. S.: 1989, *Nature* **339**, 523

Pain, R., Fabbro, S., Sullivan, M., Ellis, R. S., Aldering, G., Astier, P., Deustua, S. E., Fruchter, A. S., Goldhaber, G., Goobar, A., Groom, D. E., Hardin, D., Hook, I. M., Howell, D. A., Irwin, M. J., Kim, A. G., Kim, M. Y., Knop, R. A., Lee, J. C., Lidman, C., McMahon, R. G., Nugent, P. E., Panagia, N., Pennypacker, C. R., Perlmutter, S., Ruiz-Lapuente, P., Schahmaneche, K., Schaefer, B., and Walton, N. A.: 2002, *ApJ* **577**, 120

Pain, R., Hook, I. M., Deustua, S., Gabi, S., Goldhaber, G., Groom, D., Kim, A. G., Kim, M. Y., Lee, J. C., Pennypacker, C. R., Perlmutter, S., Small, I. A., Goobar, A., Ellis, R. S., McMahon, R. G., Glazebrook, K., Boyle, B. J., Bunclark, P. S., Carter, D., and Irwin, M. J.: 1996, *ApJ* **473**, 356

Parodi, B. R., Saha, A., Sandage, A., and Tammann, G. A.: 2000, *ApJ* **540**, 634

Pearson, T. J., Mason, B. S., Readhead, A. C. S., Shepherd, M. C., Sievers, J. L., Udomprasert, P. S., Cartwright, J. K., Farmer, A. J., Padin, S., Myers, S. T., Bond, J. R., Contaldi, C. R., Pen, U.-L., Prunet, S., Pogosyan, D., Carlstrom, J. E., Kovac, J., Leitch, E. M., Pryke, C., Halverson, N. W., Holzapfel, W. L., Altamirano, P., Bronfman, L., Casassus, S., May, J., and Joy, M.: 2003, *ApJ* **591**, 556

Percival, W. J., Baugh, C. M., Bland-Hawthorn, J., Bridges, T., Cannon, R., Cole, S., Colless, M., Collins, C., Couch, W., Dalton, G., De Propris, R., Driver, S. P., Efstathiou, G., Ellis, R. S., Frenk, C. S., Glazebrook, K., Jackson, C., Lahav, O., Lewis, I., Lumsden, S., Maddox, S., Moody, S., Norberg, P., Peacock, J. A., Peterson, B. A., Sutherland, W., and Taylor, K.: 2001, *MNRAS* **327**, 1297

Perlmutter, S., Aldering, G., della Valle, M., Deustua, S., Ellis, R. S., Fabbro, S., Fruchter, A., Goldhaber, G., Groom, D. E., Hook, I. M., Kim, A. G., Kim, M. Y., Knop, R. A., Lidman, C., McMahon, R. G., Nugent, P., Pain, R., Panagia, N., Pennypacker, C. R., Ruiz-Lapuente, P., Schaefer, B., and Walton, N.: 1998, *Nature* **391**, 51

Perlmutter, S., Aldering, G., Goldhaber, G., Knop, R. A., Nugent, P., Castro, P. G., Deustua, S., Fabbro, S., Goobar, A., Groom, D. E., Hook, I. M., Kim, A. G., Kim, M. Y., Lee, J. C., Nunes, N. J., Pain, R., Pennypacker, C. R., Quimby, R., Lidman, C., Ellis, R. S., Irwin, M., McMahon, R. G., Ruiz-Lapuente, P., Walton, N., Schaefer, B., Boyle, B. J., Filippenko, A. V., Matheson, T., Fruchter, A. S., Panagia, N., Newberg, H. J. M., Couch, W. J., and The Supernova Cosmology Project: 1999, *ApJ* **517**, 565

Perlmutter, S., Gabi, S., Goldhaber, G., Goobar, A., Groom, D. E., Hook, I. M., Kim, A. G., Kim, M. Y., Lee, J. C., Pain, R., Pennypacker, C. R., Small, I. A., Ellis, R. S., McMahon, R. G., Boyle, B. J., Bunclark, P. S., Carter, D., Irwin, M. J., Glazebrook, K., Newberg, H. J. M., Filippenko, A. V., Matheson, T., Dopita, M., Couch, W. J., and The Supernova Cosmology Project: 1997, *ApJ* **483**, 565

Perlmutter, S., Muller, R. A., Newberg, H. J. M., Pennypacker, C. R., Sasseen, T. P., and Smith, C. K.: 1992, in *ASP Conf. Ser. 34: Robotic Telescopes in the 1990s*, pp 67–71

Perlmutter, S. and Schmidt, B.: 2003, *Measuring Cosmology with Supernovae*, astro-ph/0303428, In Supernovae & Gamma Ray Bursts, K. Weiler, Ed., Springer, Lecture Notes in Physics, in press

Phillips, M. M.: 1993, *ApJL* **413**, L105

Phillips, M. M., Lira, P., Suntzeff, N. B., Schommer, R. A., Hamuy, M., and Maza, J.: 1999, *AJ* **118**, 1766

Piersanti, L., Gagliardi, S., Iben, I. J., and Tornambé, A.: 2003, *ApJ* **583**, 885

Poznanski, D., Gal-Yam, A., Maoz, D., Filippenko, A. V., Leonard, D. C., and Matheson, T.: 2002, *PASP* **114**, 833

Press, W., Teukolsky, S., Vetterling, W. T., and Flannery, B. P.: 1992, *Numerical Recipes in Fortran 77, The Art of Scientific Computing*, 2nd Ed., Cambridge University Press

Pskovskii, I. P.: 1977, *AZh* **54**, 1188

Puckett, T. and Newton, J.: 2000, *IAUC* **7446**, 1

Ragazzoni, R., Giallongo, E., Pasian, F., Pedichini, F., Fontana, A., Marconi, G., Speziali, R., Turatto, M., Danziger, J., Cremonese, G., Smareglia, R., Gallieni, D., Anaclerio, E., and Lazzarini, P. G.: 2000, in *Proc. SPIE Vol. 4008, p. 439-446, Optical and IR Telescope Instrumentation and Detectors, Masanori Iye; Alan F. Moorwood; Eds.*, pp 439–446

Rasio, F. A. and Shapiro, S. L.: 1995, *ApJ* **438**, 887

Ratcliffe, A., Shanks, T., Parker, Q. A., and Fong, R.: 1998, *MNRAS* **293**, 197

Reiss, D. J.: 2000, *Ph.D. Thesis*

Reiss, D. J., Germany, L. M., Schmidt, B. P., and Stubbs, C. W.: 1998, *AJ* **115**, 26

Renzini, A.: 1996, *Searching for Type Ia supernova progenitors*, In Supernovae and Supernova Remnants; pp. 77-85, ed. R McCray, Z Wang, Cambridge Univ. Press

Renzini, A. and da Costa, L. N.: 1997, *The Messenger* **87**, 23

Riello, M.: 2002, in *the proceedings of the "Workshop on Variability with Wide Field Imagers", Mem. S.A.It.*

Riess, A. G.: 2000, *PASP* **112**, 1284

Riess, A. G., Filippenko, A. V., Challis, P., Clocchiatti, A., Diercks, A., Garnavich, P. M., Gilliland, R. L., Hogan, C. J., Jha, S., Kirshner, R. P., Leibundgut, B., Phillips, M. M., Reiss, D., Schmidt, B. P., Schommer, R. A., Smith, R. C., Spyromilio, J., Stubbs, C., Suntzeff, N. B., and Tonry, J.: 1998, *AJ* **116**, 1009

Riess, A. G., Filippenko, A. V., Li, W., and Schmidt, B. P.: 1999a, *AJ* **118**, 2668

Riess, A. G., Filippenko, A. V., Liu, M. C., Challis, P., Clocchiatti, A., Diercks, A., Garnavich, P. M., Hogan, C. J., Jha, S., Kirshner, R. P., Leibundgut, B., Phillips, M. M., Reiss, D., Schmidt, B. P., Schommer, R. A., Smith, R. C., Spyromilio, J., Stubbs, C., Suntzeff, N. B., Tonry, J., Woudt, P., Brunner, R. J., Dey, A., Gal, R., Graham, J., Larkin, J., Odewahn, S. C., and Oppenheimer, B.: 2000, *ApJ* **536**, 62

Riess, A. G., Kirshner, R. P., Schmidt, B. P., Jha, S., Challis, P., Garnavich, P. M., Esin, A. A., Carpenter, C., Grashius, R., Schild, R. E., Berlind, P. L., Huchra, J. P., Prosser, C. F., Falco, E. E., Benson, P. J., Briceño, C., Brown, W. R., Caldwell, N., dell'Antonio, I. P., Filippenko, A. V., Goodman, A. A., Grogin, N. A., Groner, T., Hughes, J. P., Green, P. J., Jansen, R. A., Kleyna, J. T., Luu, J. X., Macri, L. M., McLeod, B. A., McLeod, K. K., McNamara, B. R., McLean, B., Milone, A. A. E., Mohr, J. J., Moraru, D., Peng, C., Peters, J., Prestwich, A. H., Stanek, K. Z., Szentgyorgyi, A., and Zhao, P.: 1999b, *AJ* **117**, 707

Riess, A. G., Nugent, P. E., Gilliland, R. L., Schmidt, B. P., Tonry, J., Dickinson, M., Thompson, R. I., Budavári, T., Casertano, S., Evans, A. S., Filippenko, A. V., Livio, M., Sanders, D. B., Shapley, A. E., Spinrad, H., Steidel, C. C., Stern, D., Surace, J., and Veilleux, S.: 2001, *ApJ* **560**, 49

Riess, A. G., Press, W. H., and Kirshner, R. P.: 1995, *ApJL* **438**, L17

Riess, A. G., Press, W. H., and Kirshner, R. P.: 1996a, *ApJ* **473**, 88

Riess, A. G., Press, W. H., and Kirshner, R. P.: 1996b, *ApJ* **473**, 588

Rifatto, A.: 1990, in *ASSL Vol. 165: Dusty Objects in the Universe*, pp 277–+

Rosa-González, D., Terlevich, E., and Terlevich, R.: 2002, *MNRAS* **332**, 283

Rowan-Robinson, M.: 1985, *The Cosmological Distance Ladder*, W.H. Freeman and Company, New York

Ruiz-Lapuente, P. and Canal, R.: 1998, *ApJL* **497**, L57+

Ruiz-Lapuente, P., Canal, R., and Burkert, A.: 1997, *SNe Ia: on the binary progenitors and expected statistics*, in Thermonuclear Supernovae, pp. 205-30; Ruiz-Lapuente P., Canal R., and Isern J., eds.; Dordrecht: Kluwer

Ruiz-Lapuente, P., Cappellaro, E., Turatto, M., Gouiffes, C., Danziger, I. J., della Valle, M., and Lucy, L. B.: 1992, *ApJL* **387**, L33

Rust, B. W.: 1974, *Ph.D. Thesis*

Sadat, R., Blanchard, A., Guiderdoni, B., and Silk, J.: 1998, *A&A* **331**, L69

Salpeter, E. E.: 1955, *ApJ* **121**, 161

Salvo, M. E., Cappellaro, E., Mazzali, P. A., Benetti, S., Danziger, I. J., Patat, F., and Turatto, M.: 2001, *MNRAS* **321**, 254

Sandage, A. and Tammann, G. A.: 1993, *ApJ* **415**, 1

Schaefer, B. E.: 2000, *IAUC* **7391**, 1

Schaefer, B. E., Snyder, J. A., Hernandez, J., Roscherr, B., Deng, M., Ellman, N., Bailyn, C., Rengstorf, A., Smith, D., Levine, A., Barthelmy, S., Butterworth, P., Hurley, K., Cline, T., Meegan, C., Kouveliotou, C., Kippen, R. M., Park, H.-S., Williams, G. G., Porrata, R., Bionta, R., Hartmann, D., Band, D., Frail, D., Kulkarni, S., Bloom, J., Djorgovski, S., Sadava, D., Chaffee, F., Harris, F., Abad, C., Adams, B., Andrews, P., and 37 coauthors: 1999, *ApJL* **524**, L103

Schlegel, D. J., Finkbeiner, D. P., and Davis, M.: 1998, *ApJ* **500**, 525

Schlegel, E. M. and Petre, R.: 1993, *ApJL* **412**, L29

Schmidt, B. P., Suntzeff, N. B., Phillips, M. M., Schommer, R. A., Clocchiatti, A., Kirshner, R. P., Garnavich, P., Challis, P., Leibundgut, B., Spyromilio, J., Riess, A. G., Filippenko, A. V., Hamuy, M., Smith, R. C., Hogan, C., Stubbs, C., Diercks, A., Reiss, D., Gilliland, R., Tonry, J., Maza, J., Dressler, A., Walsh, J., and Ciardullo, R.: 1998, *ApJ* **507**, 46

Schmidt, M.: 1959, *ApJ* **129**, 243

Schwartz, M., Li, W. D., Filippenko, A. V., Modjaz, M., and Treffers, R. R.: 2000, *IAUC* **7514**, 2

Scodeggio, M., Olsen, L. F., da Costa, L., Slijkhuis, R., Benoist, C., Deul, E., Erben, T., Hook, R., Nonino, M., Wicenec, A., and Zaggia, S.: 1999, *A&AS* **137**, 83

Slipher, V. M.: 1917, *The Observatory* **40**, 304

Spergel, D. N., Verde, L., Peiris, H. V., Komatsu, E., Nolta, M. R., Bennett, C. L., Halpern, M., Hinshaw, G., Jarosik, N., Kogut, A., Limon, M., Meyer, S. S., Page, L., Tucker, G. S., Weiland, J. L., Wollack, E., and Wright, E. L.: 2003, *ApJS* **148**, 175

Steidel, C. C., Adelberger, K. L., Giavalisco, M., Dickinson, M., and Pettini, M.: 1999, *ApJ* **519**, 1

Stetson, P. B.: 1998, *PASP* **110**, 1448

Stone, R. C., Pier, J. R., and Monet, D. G.: 1999, *AJ* **118**, 2488

Strolger, L.-G., Smith, R. C., Candia, P., Soderberg, A., Challis, P., Corvarrubias, R., Krick, J., Athey, A., Phillips, M. M., Knopp, R., and Conely, A.: 2000, *IAUC* **7404**, 1

Sullivan, M., Ellis, R., Nugent, P., Smail, I., and Madau, P.: 2000a, *MNRAS* **319**, 549

Sullivan, M., Treyer, M. A., Ellis, R. S., Bridges, T. J., Milliard, B., and Donas, J.: 2000b, *MNRAS* **312**, 442

Tammann, G. A., Loeffler, W., and Schroeder, A.: 1994, *ApJS* **92**, 487

Tonry, J. L., Blakeslee, J. P., Ajhar, E. A., and Dressler, A.: 2000, *ApJ* **530**, 625

Tonry, J. L., Schmidt, B. P., Barris, B., Candia, P., Challis, P., Clocchiatti, A., Coil, A. L., Filippenko, A. V., Garnavich, P., Hogan, C., Holland, S. T., Jha, S., Kirshner, R. P., Krisciunas, K., Leibundgut, B., Li, W., Matheson, T., Phillips, M. M., Riess, A. G., Schommer, R., Smith, R. C., Sollerman, J., Spyromilio, J., Stubbs, C. W., and Suntzeff, N. B.: 2003, *ApJ* **594**, 1

Treffers, R. R., Peng, C. Y., Filippenko, A. V., Richmond, M. W., Barth, A. J., and Gilbert, A. M.: 1997, *IAUC* **6627**, 1

Tripp, R. and Branch, D.: 1999, *ApJ* **525**, 209

Tully, R. B. and Fisher, J. R.: 1988, *Annales de Geophysique*

Turatto, M.: 2000, *Memorie della Societa Astronomica Italiana* **71**, 573

Turatto, M., Cappellaro, E., Benetti, S., and Danziger, I. J.: 1993, *MNRAS* **265**, 471

Turatto, M., Suzuki, T., Mazzali, P. A., Benetti, S., Cappellaro, E., Danziger, I. J., Nomoto, K., Nakamura, T., Young, T. R., and Patat, F.: 2000, *ApJL* **534**, L57

Tyson, J. A. and LSST Collaboration: 2002, *Bulletin of the American Astronomical Society* **34**, 1317

Udalski, A.: 2000, *Acta Astronomica* **50**, 279

Uenishi, T., Nomoto, K., and Hachisu, I.: 2003, *astro-ph/0309433*

Umeda, H., Nomoto, K., Kobayashi, C., Hachisu, I., and Kato, M.: 1999, *APJL* **522**, L43

Valdes, F.: 1997, in *ASP Conf. Ser. 125: Astronomical Data Analysis Software and Systems VI*, pp 455–+

Valdes, F. G.: 1998, in *ASP Conf. Ser. 145: Astronomical Data Analysis Software and Systems VII*, pp 53–+

Valenti, S.: 2003, *graduation Thesis*

Vishwakarma, R. G.: 2002, *MNRAS* **331**, 776

Wambsganss, J., Cen, R., Xu, G., and Ostriker, J. P.: 1997, *ApJL* **475**, L81+

Wang, L., Goldhaber, G., Aldering, G., and Perlmutter, S.: 2003, *astro-ph/0302341, ApJ, in press*

Weidner, C. and Kroupa, P.: 2003, *astro-ph/0310860*

Whelan, J. and Iben, I. J.: 1973, *ApJ* **186**, 1007

Williams, A., Woodings, S., Martin, R., Verveer, A., and Biggs, J.: 1998, *IAUC* **6805**, 2

Wilson, O. C.: 1939, *ApJ* **90**, 634

Wittman, D. M., Tyson, J. A., Bernstein, G. M., Lee, R. W., dell'Antonio, I. P., Fischer, P., Smith, D. R., and Blouke, M. M.: 1998, in *Proc. SPIE Vol. 3355, p. 626-634, Optical Astronomical Instrumentation, Sandro D'Odorico; Ed.*, pp 626–634

Wolf, C., Meisenheimer, K., Rix, H.-W., Borch, A., Dye, S., and Kleinheinrich, M.: 2003, *A&A* **401**, 73

Wood-Vasey, W. M.: 2002, in *IAUC 8019*, pp 2–+

Wood-Vasey, W. M., Aldering, G., Lee, B. C., Loken, S., Nugent, P., Perlmutter, S., Quimby, R., Siegrist, J., Wang, L., Knop, R. A., Antilogus, P., Astier, P., Hardin, D., Pain, R., Copin, Y., Smadja, G., Adam, G., Bacon, R., Lemmonier, J., Pecontal, E., Kessler, R., and Nearby Supernova Factory Collaboration: 2002, *Bulletin of the American Astronomical Society* **34**, 1205

Woosley, S. E. and Weaver, T. A.: 1986, *ARA&A* **24**, 205

Yungelson, L. R. and Livio, M.: 2000, *ApJ* **528**, 108

Zucca, E., Zamorani, G., Vettolani, G., Cappi, A., Merighi, R., Mignoli, M., Stirpe, G. M., MacGillivray, H., Collins, C., Balkowski, C., Cayatte, V., Maurogordato, S., Proust, D., Chincarini, G., Guzzo, L., Maccagni, D., Scaramella, R., Blanchard, A., and Ramella, M.: 1997, *A&A* **326**, 477

Curriculum Vitae

Altavilla Giuseppe

Place and date of birth:	Manduria (Taranto), Feb. 4th 1974
Nationality:	Italian
Address (work):	Osservatorio Astronomico di Padova Vicolo dell'osservatorio, 5 35122 Padova Italy phone: +39 049 8293411 fax: +39 049 8759840 E-mail altavilla@pd.astro.it

Education and qualifications

Sept. 1988 - Jul. 1993

Liceo Scientifico Statale "Archimede" (Roma)
(High School, specialising in Sciences)
Final grade: 60/60

Oct. 1993 - Jun. 2000

University of Padova, Italy
Degree title: Astronomy
Final grade: 100/110
Dissertation: "Supernovae Ia light curve morphology and absolute magnitude calibration"

Supervisors: Prof. R. Barbon,
Prof. E. Cappellaro

Appointments:

Sept. 2000 - present

University of Padua
PhD Student

Padova Astronomical Observatory
Research Fellow

Additional training:

National School of Astrophysics: May 20-25, 2001 (Sirolo, Ancona)
- Solar system minor planets
- Stellar structure, evolution and variability

Oct. 15-19, 2001 (Trieste)
- Chemical evolution of galaxies
- High resolution spectroscopy

Jun. 3-7, 2002 (Cetraro, Cosenza)
- Turbolences in space plasmas
- Galaxies and galaxy systems

May 11-17, 2003 (Marciana Marina, Livorno)
- The Local Group Galaxies
- The new generation telescopes

Congresses:

Jan. 30-31, 2000
Astronomical Observatory of Capodimonte, Italy
"VST Science"
oral contribution:"SN rate at VST"

Apr. 10-15, 2000
Astronomical Observatory of Rome, Italy
Monteporzio Catone
XLIV congress of the Italian Astronomical Society (SAIt)

Jul. 29-31, 2002
Garching, Germany
"From Twilight to Highlight, the Physics of Supernovae"

ESO/MPA/MPE Workshop
poster + proceedings

Sept. 16-20, 2002
Lampedusa Island, Italy
" Workshop on Variability with Wide Field Imagers"
oral contribution + proceedings

March 10-15, 2003
Ringberg Castle at Lake Tegernsee, Germany
"The Physics of Type Ia Supernova Explosions"
RTN Workshop and Winter School,
oral contribution: SN Ia calibration & the Hubble Constant

Apr. 22-26, 2003
Valencia, Spain
"Supernovae, 10 years of SN1993J"
IAU Colloquium 192
poster + proceedings

Sept. 25-27, 2003
ECT*, Villa Tambosi, Trento, Italy
"Thermonuclear Supernovae and Cosmology"
ECT*/RTN Workshop and School

Experience

Telescope & instruments: - Asiago 1.82m + AFOSC
- ESO/MPG 2.2m + WFI
- Danish 1.54m + DFOSC
- NTT + SOFI
- VLT + FORS1/2

Image processing & data reduction: IRAF
ISIS

Informatics: Unix, Linux
MS Windows

Languages: Italian: mother tongue
English: good

Publications

– – – – – – **refereed** –

2003, MNRAS, 338, 939
Photometry and spectroscopy of the Type IIP SN 1999em
from outburst to dust formation.
Elmhamdi, Abouazza;
Danziger, I. J.; Chugai, N.; Pastorello, A.; Turatto, M.;
Cappellaro, E.; Altavilla, G.; Benetti, S.; Patat, F.; Salvo, M.

2003, MNRAS, 338, 711
Peculiar, low-luminosity Type II supernovae: low-energy
explosions in massive progenitors?
Zampieri, L.;
Pastorello, A.; Turatto, M.; Cappellaro, E.;Benetti, S.; Altavilla, G.;
Mazzali, P.; Hamuy, M.

2002, ApJ, 566, 1005
Direct Analysis of Spectra of Type Ib Supernovae
Branch, D;
Benetti, S.; Kasen, D.; Baron, E.;
Jeffery, D. J.; Hatano, K.; Stathakis, R. A.;
Filippenko, A. V.; Matheson, T.; Pastorello, A.; Altavilla, G.;
Cappellaro, E.; Rizzi, L.; Turatto, M.; Li, W.; Leonard, D. C.;
Shields, J. C.

MNRAS submitted
Cepheid Calibration of type Ia Supernovae and the Hubble constant
Altavilla, G.;
Fiorentino, G.; Marconi, M.; Musella, I.; Cappellaro, E.; Barbon, R.;
Benetti, S.; Pastorello, A.; Riello, M.; Turatto, M.; Zampieri, L.

2004, MNRAS, 347, 74
Low luminosity Type II Supernovae: spectrocopic and
photometric evolution
Pastorello, A.;
Zampieri, L.; Turatto, M.; Cappellaro, E.; Benetti, S.; Meikle, W.P.S.;
Branch, D.; Baron, E.; Patat, F.; Armstrong, M.; Altavilla, G.;
Salvo, M.; Riello, M.

MNRAS accepted
Supernova 2002bo: inadequacy of the single parameter description
Benetti, S.;
Meikle, W.P.S.; Stehle, M.; Altavilla, G,; Desidera, S.; Folatelli, G.;
Goobar, A.; Mendez, J.; Navasardyan, H.; Pastorello, A.;Patat, F.;
Riello, M.; Ruiz-Lapuente, P.; Tsvetkov, D., Turatto, M., Mazzali, P.;
Hillebrandt W.

– –

StRESS: *S*outhern In*t*ermediate *R*edshift *E*SO *S*N *S*earch,
Global SNe Rate Estimate

Altavilla, G.;
Riello, M.; Botticella, M.T.; Valenti, S.; Cappellaro, E.
To appear in the proceedings of the IAU Colloquium 192
"Supernovae, 10 years of SN1993J",
Valencia 2003, Springer Verlag

2003 MmSAI 74 526

Core-collapse supernovae and evidence for black hole formation.
Zampieri, L.;
Pastorello, A.; Turatto, M.; Cappellaro, E.; Benetti, S.;
Altavilla, G.; Mazzali, P.; Hamuy, M.

2003 fthp.conf 216

Peculiar, Low Luminosity Type II Supernovae:
Site of Black Hole Formation?
Zampieri, L.;
Pastorello, A.; Turatto, M.; Cappellaro, E.;
Benetti, S.; Altavilla, G.; Mazzali, P.; Hamuy, M.
From Twilight to Highlight: The Physics of Supernovae.
Proceedings of the ESO/MPA/MPE Workshop held in Garching,
Germany, 29-31 July 2002, p. 216.

2003 fthp.conf 395

An Intermediate Redshift Supernova Search at ESO:
Preliminary Results.
Altavilla, G.;
Riello, M.; Cappellaro, E.; Benetti, S.;Pastorello, A.; Patat, F.;
Prevedello, M.; Turatto, M.; Zampieri, L.
From Twilight to Highlight: The Physics of Supernovae.
Proceedings of the ESO/MPA/MPE Workshop held in Garching,
Germany, 29-31 July 2002, p. 395.

2003 fthp.conf 400

An Intermediate Redshift Supernova Search at ESO:
Reduction Tools and Efficiency Tests.
Riello, M.;
Altavilla, G.; Cappellaro, E.; Benetti, S.;
Pastorello, A.; Patat, F.; Prevedello, M.; Turatto, M.; Zampieri, L.

"An Intermediate Redshift Supernova Search at ESO: SN Rate first estimate"

Altavilla G.
To appear in the proceedings of the
"Workshop on Variability with Wide Field Imagers",
Lampedusa 2002, Mem. S.A.It

IAUC circulars:

IAUC 8207 Supernova 2003ie IN NGC 4051
Benetti, S.; Navasardyan, H.; Pastorello, A.; Botte, V.; Ciroi, S.; Altavilla, G.;Elias-Rosa, N.; Riello, M.; Turatto, M.; Zampieri, L.; Cappellaro, E.

IAUC 8187 Supernova 2003hg in NGC 7771
Elias-Rosa, N.; Benetti, S.; Marmo, C.; Pastorello, A.; Altavilla, G.; Navasardyan, H.; Riello, M.; Turatto, M.; Zampieri, L.; Cappellaro, E.

IAUC8019 Supernova 2002hy in NGC 3464
Benetti, S.; Altavilla, G.; Pastorello, A.; Riello, M.; Turatto, M.; Zampieri, L.; Cappellaro, E.

IAUC7987 Supernova 2002gd in NGC 7537
Benetti, S.; Altavilla, G.; Pastorello, A.; Riello, M.; Turatto, M.; Zampieri, L.; Cappellaro, E.; Germany, L.

IAUC7965 Supernovae 2002en, 2002eo, 2002es, and 2002eu
Pastorello, A.; Benetti, S.; Altavilla, G.; Della Valle, A.; Giro, E.; Riello, M.; Turatto, M.; Cappellaro, E.

IAUC7963 Supernova 2002ej in NGC 6324
Desidera, S.; Giro, E.; Della Valle, A.; Benetti, S.; Altavilla, G.; Pastorello, A.; Turatto, M.; Cappellaro, E.

IAUC7919 Supernova 2002dj in NGC 5018
Riello, M.; Benetti, S.; Altavilla, G.; Pastorello, A.; Turatto, M.; Cappellaro, E.; O'Toole, S.

IAUC7921 Supernova 2002dm in IC 5017
Turatto, M.; Riello, M.; Altavilla, G.; Benetti, S.; Pastorello, A.; Cappellaro, E.

IAUC7922 Supernova 2002dg
Riello, M.; Benetti, S.; Altavilla, G.; Pastorello, A.; Turatto, M.; Cappellaro, E.

IAUC7929 Supernova 2002du
Altavilla, G.

IAUC7894 Supernovae 2002cj, 2002ck, 2002cp, 2002cs
Riello, M.; Benetti, S.; Altavilla, G.; Pastorello, A.; Turatto, M.; Cappellaro, E.; Ruiz-Lapuente, P.; Matheson, T.; Calkins, M.; Chornock, R.

IAUC7901	Supernova 2002cv in NGC 3190 Turatto, M.; Desidera, S.; Benetti, S.; Altavilla, G.; Pastorello, A.; Riello, M.; Cappellaro, E.
IAUC7885	Supernovae 2002cl, 2002cm, 2002cn, 2002co Altavilla, G.; Benetti, S.
IAUC7844	Supernova 2002bh in UGC 5286 Benetti, S.; Altavilla, G.; Pastorello, A.; Turatto, M.; Desidera, S.; Cappellaro, E
IAUC7848	Supernova 2002bo in NGC 3190 Benetti, S.; Altavilla, G.; Pastorello, A.; Riello, M.; Turatto, M.; Cappellaro, E.; Tomov, T.; Mikolajewski, M.
IAUC7828	Supernova 2002an in NGC 2575 Benetti, S.; Altavilla, G.; Pastorello, A.; Turatto, M.; Desidera, S.; Giro, E.; Cappellaro, E.
IAUC7787	Supernovae 2001is and 2001it Benetti, S.; Altavilla, G.; Pastorello, A.; Turatto, M.; Desidera, S.; Giro, E.; Cappellaro, E.
IAUC7789	Supernova 2002A in UGC 3804 Benetti, S.; Altavilla, G.; Pastorello, A.; Turatto, M.; Desidera, S.; Brunino, R.; De Checchi, M.; Villanova, S.; Cappellaro, E.
IAUC7776	Supernova 2001ie in UGC 5542 Cappellaro, E.; Benetti, S.; Altavilla, G.; Pastorello, A.; Turatto, M.; Desidera, S.; Zamanov, R.
IAUC7779	Supernova 2001if near MCG +06-6-43 Benetti, S.; Altavilla, G.; Pastorello, A.; Turatto, M.; Desidera, S.; Giro, E.; Pernechele, C.; Bortolussi, A.; Cappellaro, E.
IAUC7780	Supernovae 2001io and 2001ip Altavilla, G.; Benetti, S.; Pastorello, A.; Riello, M.; Turatto, M.; Zampieri, L.; Cappellaro, E.; Clocchiatti, A.; Contreras, C.; Danziger, I.J.; Mazzali, P.; Patat, F.
IAUC7748	Supernova 2001fh in PGC 66592 Benetti, S.; Altavilla, G.; Cappellaro, E.; Pastorello, A.; Turatto, M.; Desidera, S.; Giro, E.
IAUC7762	Supernovae 2001ge, 2001gf, 2001gg, 2001gh, 2001gi, 2001gj Altavilla, G.; Benetti, S.; Cappellaro, E.; Pastorello, A.; Riello, M.; Turatto, M.; Zampieri, L.; Clocchiatti, A.; Contreras, C.; Danziger, I.J.; Mazzali, P.; Patat, F.

IAUC7709 V4740 Sagittarii
Patat, F.; Contreras, C.; Prieto, J.; Altavilla, G.; Benetti, S.; Cappellaro, E.; Pastorello, A.; Turatto, M.

IAUC7714 Supernova 2001ed in NGC 706
Benetti, S.; Altavilla, G.; Cappellaro, E.; Pastorello, A.; Turatto, M.; Contreras, C.; Prieto, J.; Clocchiatti, A.; Patat, F.

IAUC7680 Supernovae 2001dh, (2001dj) and 2001dl
Patat, F.; Contreras, C.; Prieto, J.; Altavilla, G.; Benetti, S.; Cappellaro, E.; Pastorello, A.; Turatto, M.

IAUC7693 Supernova 2001dr in NGC 4932
Benetti, S.; Altavilla, G.; Cappellaro, E.; Pastorello, A.; Turatto, M.; Della Valle, A.

IAUC7663 Supernova 2001cz in NGC 4679
Pastorello, A.; Altavilla, G.; Benetti, S.; Cappellaro, E.; Turatto, M.

IAUC7643 Supernova 2001cl in NGC 7260
Benetti, S.; Altavilla, G.; Cappellaro, E.; Pastorello, A.; Turatto, M.; Pritchard, J.

IAUC7615 Supernovae 2001bc, 2001bd, 2001be
Cappellaro, E.; Altavilla, G.; Benetti, S.; Pastorello, A.; Turatto, M.; Clocchiatti, A.; Danziger, I. J.; Mazzali, P.; Patat, F.

IAUC7639 Supernova 2001bg in NGC 2608
Benetti, S.; Altavilla, G.; Cappellaro, E.; Pastorello, A.; Turatto, M.; Cosentino, R.; Zacchei, A.; Danziger, I. J.; Patat, F.

IAUC7537 Supernova 2000fc in Anonymous Galaxy
Turatto, M.; Altavilla, G.; Benetti, S.; Cappellaro, E.; Pastorello, A.; Clocchiatti, A.

IAUC7545 Supernova 2000fe in UGC 4870
Benetti, S.; Altavilla, G.; Cappellaro, E.; Desidera, S.; Fantinel, D.; Giro, E.; Lessio, L.; Pastorello, A.; Pernechele, C.; Turatto, M.

IAUC7549 Supernova 2000fp in Anonymous Galaxy
Clocchiatti, A.; Arevalo, P.; Rada, C.; Barrientos, F.; Minniti, D.; Courbin, F.; Turatto, M.; Altavilla, G.; Benetti, S.; Cappellaro, E.; Pastorello, A.; Leibundgut, B.; Spyromilio, J.

IAUC7481 Supernova 2000da in UGC 5, Supernova 2000db in NGC 3949, Supernova 2000de in NGC 4384
Pastorello, A.; Giro, E.; Altavilla, G.; Benetti, S.

IAUC7391	Supernova 1998bu in NGC 3368 Cappellaro, E.; Benetti, S.; Pastorello, A.; Turatto, M.; Altavilla, G.; Rizzi, L.
IAUC7367	Supernova 2000H in IC 454 Pastorello, A.; Altavilla, G.; Cappellaro, E.; Turatto, M.; Benetti, S.